

# Sheffield Hallam University

*The use of MALDI-MS for imaging drug disposition in respiratory disease models.*

FLINDERS, Bryn.

Available from the Sheffield Hallam University Research Archive (SHURA) at:

<http://shura.shu.ac.uk/19652/>

## A Sheffield Hallam University thesis

This thesis is protected by copyright which belongs to the author.

The content must not be changed in any way or sold commercially in any format or medium without the formal permission of the author.

When referring to this work, full bibliographic details including the author, title, awarding institution and date of the thesis must be given.

Please visit <http://shura.shu.ac.uk/19652/> and <http://shura.shu.ac.uk/information.html> for further details about copyright and re-use permissions.

Learning and Information Services  
Adsett Centre, City Campus  
Sheffield S1 1WD

102 019 780 3



Sheffield Hallam University  
Learning and Information Services  
Adsett Centre, City Campus  
Sheffield S1 1WB

**REFERENCE**

ProQuest Number: 10694533

All rights reserved

INFORMATION TO ALL USERS

The quality of this reproduction is dependent upon the quality of the copy submitted.

In the unlikely event that the author did not send a complete manuscript and there are missing pages, these will be noted. Also, if material had to be removed, a note will indicate the deletion.



ProQuest 10694533

Published by ProQuest LLC (2017). Copyright of the Dissertation is held by the Author.

All rights reserved.

This work is protected against unauthorized copying under Title 17, United States Code  
Microform Edition © ProQuest LLC.

ProQuest LLC.  
789 East Eisenhower Parkway  
P.O. Box 1346  
Ann Arbor, MI 48106 – 1346

The use of MALDI-MS for imaging drug disposition in  
respiratory disease models.

Bryn Flinders

A thesis submitted in partial fulfilment of the requirements of Sheffield Hallam  
University for the degree of Doctor of Philosophy

September 2013

## **Acknowledgements**

First and foremost I would like to thank my supervisor Professor Malcolm Clench, for giving me the opportunity to undertake this project and for his help and support.

This PhD was supported by a MRC case studentship in collaboration with GlaxoSmithKline and Sheffield Hallam University.

I would like to thank my industrial supervisors Josie Morrell, Dr Peter Marshall and Lisa Ranshaw from GlaxoSmithKline (Stevenage) for their support throughout this project.

Also I would like to thank Dr Simona Francese and Dr Akram Khan for their help and advice.

I would also like to thank members of the mass spectrometry group at Sheffield Hallam University, many thanks to Dr Paul Trim, Laura Cole, Leesa Ferguson, Dr Marie-Claude Djidja, Dr Philippa Hart, Dr Jill Newton, Christopher Mitchell, Robert Bradshaw and Afnan Baturba for their friendship, help and support throughout.

I would also like to take this opportunity to thank Dr Andrew McEwen from Quotient Bioresearch Ltd for his permission to use some of the WBA data in this thesis.

Also I would like to thank Professor Ron Heeren and Ivo Klinkert from FOM Institute AMOLF for their permission and help to use the Volume Explorer software to generate data included in this thesis.

Last but not least I would like to thank my parents for their love, encouragement and support over the last three years.

## **Abstract**

Matrix-assisted laser desorption/ionisation-mass spectrometry imaging (MALDI-MSI) has been extensively applied to monitoring the distribution of pharmaceutical compounds in tissues. The main aim of the work reported in this thesis is to monitor the distribution of respiratory compounds in the lungs following inhaled delivery.

Glucocorticoids that contain multiple carbonyl functionalities are not easily protonated/de-protonated to form charged species due to the poor ionisation efficiencies of the carbonyl functionalities. Derivatisation with hydrazine based reagents has been proposed as a solution to this problem. These reagents have been employed for the in-solution and on-tissue derivatisation of a range of glucocorticoids to form their respective hydrazones improving their mass spectral ionisation efficiency and detection.

MALDI-MSI has been used to screen a set of respiratory compounds in order to determine their on-tissue limit of detection. The distribution of a Tiotropium Bromide was monitored throughout the lungs following inhaled delivery. High spatial resolution imaging enabled a detailed view of the distribution of Tiotropium in the trachea and major airways.

Quantitative mass spectrometry imaging is a new field that has recently gained a lot of attention especially in pharmaceutical research. The ability to obtain quantitative information as well as the distribution of pharmaceutical compounds and associated metabolites offers a distinct advantage over traditional quantitative methods such as LC-MS/MS and QWBA. The current methods of generating quantification information from MALDI-MS images has been evaluated, which led to development of a method for the preparation of standards for use in the quantification of drugs in tissue sections.

MALDI-MSI has been used to acquire data from serial sections obtained at equal intervals through control mouse lung tissue, homogenate registration markers were incorporated in order to aid the final 3D image construction. Using two 3D imaging software packages were used to reconstruct the images were stacked together to enable the 3D distribution of a particular endogenous species throughout the lungs to be displayed.

# Table of contents

|  |          |
|--|----------|
| <b>1. Introduction</b> .....                                       | <b>1</b> |
| 1.1. Introduction to respiratory conditions.....                   | 2        |
| 1.1.1. Asthma .....  | 2        |
| 1.1.1.1. Burden of asthma.....                                     | 2        |
| 1.1.1.2. Causes of asthma .....                                    | 3        |
| 1.1.1.3. Pathogenesis of asthma.....                               | 4        |
| 1.1.2. Chronic Obstructive Pulmonary Disease .....                 | 6        |
| 1.1.2.1. Burden of COPD .....                                      | 6        |
| 1.1.2.2. Causes of COPD.....                                       | 6        |
| 1.1.2.3. Pathogenesis of COPD .....                                | 7        |
| 1.2. Pharmaceutical treatment strategies .....                     | 11       |
| 1.2.1. $\beta_2$ -adrenoreceptor agonists .....                    | 11       |
| 1.2.1.1. $\beta_2$ -adrenoreceptor agonists target.....            | 11       |
| 1.2.1.2. Structures of the $\beta_2$ -adrenoreceptor agonists..... | 12       |
| 1.2.1.3. Mechanism of action .....                                 | 14       |
| 1.2.2. Glucocorticoids .....                                       | 16       |
| 1.2.2.1. Structures of glucocorticoids .....                       | 16       |
| 1.2.2.2. Mechanism of action .....                                 | 17       |
| 1.2.3. Anticholinergic bronchodilators .....                       | 20       |
| 1.2.3.1. Structures of anticholinergic bronchodilators .....       | 20       |
| 1.2.3.2. Anticholinergic bronchodilator target.....                | 21       |
| 1.2.3.3. Mechanism of action .....                                 | 22       |
| 1.3. Introduction to mass spectrometry .....                       | 23       |
| 1.3.1. Ionisation sources .....                                    | 23       |
| 1.3.1.1. Matrix-assisted laser desorption/ionisation .....         | 23       |
| 1.3.1.1.1. Ionisation processes .....                              | 25       |
| 1.3.1.1.2. MALDI matrices.....                                     | 27       |
| 1.3.2. Secondary ion mass spectrometry .....                       | 30       |
| 1.3.3. Electrospray ionisation .....                               | 33       |
| 1.3.4. Desorption electrospray ionisation.....                     | 35       |
| 1.3.5. Laser ablation electrospray ionisation .....                | 37       |
| 1.4. Mass analysers .....  | 39       |
| 1.4.1. Time-of-Flight.....   | 39       |
| 1.4.1.1. Linear time-of-flight mode .....                          | 39       |
| 1.4.1.2. Reflectron time-of-flight mode .....                      | 40       |

|  |    |
|--|----|
| 1.4.2. Quadrupole .....  | 41 |
| 1.5. Hybrid Mass Spectrometers .....   | 42 |
| 1.5.1. Quadrupole time-of-flight mass spectrometer.....                        | 42 |
| 1.5.2. Tandem time-of-flight mass spectrometer .....                           | 45 |
| 1.5.3. Quadrupole-ion mobility separation-time-of-flight mass spectrometer.... | 46 |
| 1.6. Mass Spectrometry Imaging.....  | 48 |
| 1.6.1. Microprobe Imaging Mode .....   | 48 |
| 1.6.2. Microscope Imaging Mode .....   | 48 |
| 1.6.3. Raster Imaging Mode.....  | 49 |
| 1.7. Matrix application/deposition for MALDI-MSI .....                         | 51 |
| 1.7.1. Airbrush.....   | 52 |
| 1.7.2. Suncollect .....  | 53 |
| 1.7.3. ImagePrep .....   | 54 |
| 1.7.4. Portrait.....   | 55 |
| 1.7.5. Sublimation.....  | 56 |
| 1.7.6. ChIP chemical inkjet printer .....                                      | 58 |
| 1.7.7. HTX TM-Sprayer.....   | 59 |
| 1.8. Scope of thesis.....  | 61 |
| 1.9. References.....   | 63 |

**2. Use of hydrazine based reagents for improved sensitivity of glucocorticoids by MALDI-MSI..... 76**

|  |    |
|--|----|
| 2.1. Introduction.....   | 77 |
| 2.1.1. Purpose of derivatisation.....  | 77 |
| 2.1.2. Derivatisation reagents .....   | 78 |
| 2.1.2.1. 2,4-Dinitrophenylhydrazine (DNPH) .....   | 78 |
| 2.1.2.2. 4-Dimethylamino-6-(4-methoxy-1-naphthyl)-1,3,5-tetrazine-2-hydrazine (DMNTH)..... | 79 |
| 2.1.2.3. Girard's reagents.....  | 81 |
| 2.1.3. Other applications of derivatisation in mass spectrometry.....                      | 82 |
| 2.1.4. Aims and objectives .....   | 82 |
| 2.2. Methods .....   | 84 |
| 2.2.1. Information.....  | 84 |
| 2.2.2. Materials .....   | 84 |
| 2.2.3. Instrumentation .....   | 84 |
| 2.2.4. Tissue preparation.....   | 85 |
| 2.2.5. Derivatisation of glucocorticoids using DNPH.....                                   | 85 |

|  |     |
|--|-----|
| 2.2.5.1. In-solution derivatisation procedure.....                     | 85  |
| 2.2.5.2. On-tissue derivatisation procedure .....                      | 86  |
| 2.2.6. Derivatisation of glucocorticoids using Girard's reagent P..... | 86  |
| 2.2.6.1. In-solution derivatisation procedure .....                    | 86  |
| 2.2.7. Derivatisation of glucocorticoids using DMNTH .....             | 87  |
| 2.2.7.1. In-solution derivatisation procedure.....                     | 87  |
| 2.2.7.2. On-tissue derivatisation procedure .....                      | 87  |
| 2.2.8. Data processing.....  | 89  |
| 2.3. Results and Discussion .....                                      | 90  |
| 2.3.1. MALDI-MS analysis of glucocorticoids.....                       | 90  |
| 2.3.2. In-solution derivatisation using DNPH.....                      | 91  |
| 2.3.3. In-solution derivatisation using Girard's reagent P.....        | 94  |
| 2.3.4. In-solution derivatisation using DMNTH.....                     | 96  |
| 2.3.5. On-tissue derivatisation using DNPH.....                        | 99  |
| 2.3.6. On-tissue derivatisation using DMNTH.....                       | 101 |
| 2.4. Conclusion.....   | 106 |
| 2.5. References.....   | 108 |

|  |            |
|--|------------|
| <b>3. Monitoring the distribution of respiratory compounds in the lungs by MALDI-MSI .....</b> | <b>112</b> |
| 3.1. Introduction.....   | 113        |
| 3.1.1. Traditional methods of drug analysis in tissue sections .....                           | 113        |
| 3.1.1.1. Whole Body Autoradiography.....   | 113        |
| 3.1.1.2. Liquid Chromatography-Tandem Mass Spectrometry .....                                  | 114        |
| 3.1.2. Mass Spectrometry Imaging .....   | 115        |
| 3.1.2.1. Matrix-Assisted Laser Desorption/Ionisation.....                                      | 115        |
| 3.1.2.2. MALDI-MSI in monitoring drug distribution.....  | 115        |
| 3.1.3. Aims and objectives .....   | 117        |
| 3.2. Methods .....   | 118        |
| 3.2.1. Information.....  | 118        |
| 3.2.2. Materials .....   | 118        |
| 3.2.3. Dose preparation and administration .....   | 118        |
| 3.2.4. Tissue preparation.....   | 119        |
| 3.2.5. Matrix deposition.....  | 119        |
| 3.2.6. Instrumentation .....   | 120        |
| 3.2.6.1. MALDI-LIFT MS/MS imaging.....   | 120        |

|  |            |
|--|------------|
| 3.2.6.2. MALDI-MS and MS/MS imaging .....  | 120        |
| 3.2.6.3. MALDI-IMS-MS imaging.....   | 121        |
| 3.3. Results and Discussion .....  | 122        |
| 3.3.1. Respiratory compound feasibility study .....  | 122        |
| 3.3.2. MALDI-MS and MS/MS imaging of Tiotropium in lung tissue sections.   | 131        |
| 3.3.2.1. MALDI-MS and MS/MS images .....   | 131        |
| 3.3.2.2. MALDI-IMS-MS images.....  | 132        |
| 3.3.2.3. MALDI-LIFT-MS/MS images.....  | 133        |
| 3.3.3. High spatial resolution imaging of Tiotropium in lung tissue sections...  | 134        |
| 3.3.3.1. MALDI-IMS-MS images.....  | 134        |
| 3.3.3.2. MALDI-LIFT-MS/MS images.....  | 135        |
| 3.3.3.3. MALDI-MS/MS images .....  | 136        |
| 3.4. Conclusion.....   | 137        |
| 3.5. References.....   | 138        |
| <br>   |            |
| <b>4. Development of methodology for the quantification of pharmaceuticals<br/>in tissue sections by MALDI-MSI .....</b> | <b>141</b> |
| 4.1. Introduction.....   | 142        |
| 4.1.1. Traditional methods for the quantitation of drugs in tissue sections.....   | 142        |
| 4.1.1.1. Quantitative Whole Body Autoradiography .....   | 142        |
| 4.1.1.2. Tissue homogenization followed by LC-MS/MS .....  | 143        |
| 4.1.2. Quantitation by MALDI-MSI .....   | 143        |
| 4.1.3. Previous examples of quantitation by MALDI-MSI.....   | 145        |
| 4.1.4. Quantitative MSI software .....   | 148        |
| 4.1.5. Aims and objectives .....   | 148        |
| 4.2. Methods .....   | 149        |
| 4.2.1. Information.....  | 149        |
| 4.2.2. Materials .....   | 149        |
| 4.2.3. Matrix deposition.....  | 149        |
| 4.2.4. Sample preparation.....   | 150        |
| 4.2.4.1. On-tissue standard preparation.....   | 150        |
| 4.2.4.2. Homogenate standard preparation .....   | 150        |
| 4.2.4.3. Homogenate standard section preparation .....   | 151        |
| 4.2.4.4. Homogenate standard array preparation.....  | 152        |
| 4.2.5. Instrumentation .....   | 154        |
| 4.2.5.1. MALDI-LIFT-MS/MS imaging .....  | 154        |

|  |            |
|--|------------|
| 4.2.5.2. MALDI-MS and MS/MS imaging .....  | 155        |
| 4.3. Results and Discussion .....  | 156        |
| 4.3.1. On-tissue standards .....   | 156        |
| 4.3.2. Homogenate standards .....  | 160        |
| 4.3.3. Homogenate standard sections .....  | 162        |
| 4.3.4. Homogenate standard array .....   | 164        |
| 4.4. Conclusion.....   | 168        |
| 4.5. References .....  | 170        |
| <br>   |            |
| <b>5. Development of methodology for monitoring the three-dimensional distribution of endogenous species in the lungs by MALDI-MSI .....</b> | <b>173</b> |
| 5.1. Introduction.....   | 174        |
| 5.1.1. Traditional 3D imaging techniques .....   | 174        |
| 5.1.2. Current approaches to 3D-MSI .....  | 174        |
| 5.1.3. Previous examples 3D-MSI .....  | 175        |
| 5.1.3.1. 3D MALDI-MSI.....   | 175        |
| 5.1.3.2. 3D LAESI-MSI.....   | 179        |
| 5.1.3.3. 3D DESI-MSI.....  | 180        |
| 5.1.3.4. 3D SIMS-MSI.....  | 181        |
| 5.1.4. Aims and objectives .....   | 182        |
| 5.2. Methods .....   | 183        |
| 5.2.1. Information.....  | 183        |
| 5.2.2. Materials .....   | 183        |
| 5.2.3. Tissue Preparation .....  | 183        |
| 5.2.4. Matrix Application .....  | 184        |
| 5.2.5. Instrumentation .....   | 184        |
| 5.2.6. Data Processing .....   | 185        |
| 5.3. Results and Discussion .....  | 186        |
| 5.4. Conclusion.....   | 194        |
| 5.5. References .....  | 195        |
| <br>   |            |
| <b>6. Conclusion and suggestions for future work .....</b>   | <b>198</b> |
| 6.1. Introduction.....   | 199        |
| <br>   |            |
| <b>7. Appendices .....</b>   | <b>203</b> |
| 7.1. Publications .....  | 204        |

|   |     |
|---|-----|
| 7.2. Conferences – Poster presentations ..... | 204 |
| 7.3. Conferences – Oral presentations.....    | 206 |
| 7.4. Conferences attended .....               | 206 |

## List of figures

### 1. Introduction

- 1.1. Map showing the global prevalence of clinical asthma (Masoli et al., 2004) 3
- 1.2. Diagram showing the difference between normal lung tissue and that following an asthmatic episode ([www.nhlbi.nih.gov](http://www.nhlbi.nih.gov))..... 5
- 1.3. Diagram showing the difference between normal lung tissue and that afflicted with Chronic Obstructive Pulmonary Disease ([www.nhlbi.nih.gov](http://www.nhlbi.nih.gov)) ..... 8
- 1.4. Scheme showing the inflammation mechanism of COPD (Image adapted from Barnes and Hansel 2004)..... 9
- 1.5. Computed tomography (CT) scans showing the cross-section of healthy lungs on the left and emphysematous lungs on the right (Barker and Lai 2008)10
- 1.6. Proposed structure of the  $\beta_2$ -adrenoreceptor which consists of seven  $\alpha$ -helices spanning the membrane, amino acid residues important in agonist binding are circled (Image adapted from Sears and Lotvall 2005) ..... 12
- 1.7. Structures of the  $\beta_2$ -adrenoreceptor agonists A) Salbutamol, B) Formoterol and C) Salmeterol..... 13
- 1.8. Diagram illustrating the different interactions of the three  $\beta_2$ -adrenoreceptor agonists with the  $\beta_2$ -adrenoreceptor (Johnson 2001) ..... 13
- 1.9. Diagram showing the effect of Beta 2-Adrenergic receptor agonists on promoting smooth muscle relaxation (Adapted from Barnes 2004c) ..... 15
- 1.10. Structures of the synthetic corticosteroids A) Dexamethasone, B) Beclomethasone Dipropionate, C) Fluticasone Propionate and D) Budesonide17
- 1.11. Simplified structure of the glucocorticoid receptor, showing the corticosteroid binding domain at the C-terminal region of the receptor and the DNA binding domain in the middle of the receptor with the “zinc fingers” (Barnes 1998) ..... 18
- 1.12. Schemes showing the two processes by which corticosteroids facilitate their anti-inflammatory action. Trans-activation is the production of anti-inflammatory mediators and trans-repression is the inhibition of the production of pro-inflammatory mediators (Barnes 2010) ..... 19
- 1.13. Structures of A) the short-acting anticholinergic bronchodilator Ipratropium and B) the long-acting anticholinergic bronchodilator Tiotropium ..... 20
- 1.14. Scheme showing the location of the three muscarinic receptors. The  $M_1$  receptors are located in the parasympathetic ganglion, the  $M_2$  receptors are located at the cholinergic nerve terminals and the  $M_3$  receptors are located on the airway smooth muscle and mucus glands (Barnes 2004d) ..... 21
- 1.15. Diagram showing the mechanism of action of anticholinergic bronchodilators (Image adapted from [www.pharmacologycorner.com](http://www.pharmacologycorner.com))..... 22

|  |    |
|--|----|
| 1.16. Simplified schematic of a mass spectrometer showing the three main components in blue .....  | 23 |
| 1.17. Schematic representation of the matrix-assisted laser desorption/ionisation process, showing the analyte (green dots) embedded within the matrix (blue dots) the laser is then fired at this mixture causing desorption and subsequent ionization in the gas phase of both matrix and analyte molecules that are sampled by the mass spectrometer ( <a href="http://www.chm.bris.ac.uk">www.chm.bris.ac.uk</a> ) ..... | 24 |
| 1.18. Schematic representation of the secondary ion mass spectrometry process, showing the primary ion beam (blue dots) which strikes the sample causing the production of secondary ions ( <a href="http://www.mse.engin.umich.edu">www.mse.engin.umich.edu</a> ) .....   | 31 |
| 1.19. Schematic representation of an electrospray ionisation source. Showing the formation of a Taylor cone at the tip of the capillary and the production of a spray of charged droplets due to an applied electric potential (Image adapted from Kebarle 2000).....  | 33 |
| 1.20. Diagram showing the ion evaporation method and the charge residue method of ion formation in ESI (El-Anead et al., 2009).....  | 34 |
| 1.21. Schematic representation of the desorption electrospray ionisation source, showing the spray of charged droplets (red dots) that is directed towards the sample the impact of the charged particles results in the production of gaseous ions of analytes originally on the sample surface that are sampled by the mass spectrometer (Takats et al., 2004).....  | 35 |
| 1.22. Schematic representation of the laser ablation electrospray ionisation source, showing the production of ablated material (red dots) which are intercepted by the electrospray plume (black dots) and post-ionised to form ions (green dots) that are sampled by the mass spectrometer (Image adapted from Shrestha et al., 2010) .....  | 38 |
| 1.23. Schematic of a time-of-flight mass analyser operated in linear mode, ions are produced and accelerated by an applied potential (accelerating voltage) into the field-free flight tube where the ions separated based on their velocity. Lighter ions (blue dots) travel faster than larger ions (red dots) and therefore reach the detector first (Image adapted from Castleberry et al., 2008).....                   | 39 |
| 1.24. Schematic of a time-of-flight mass analyser operated in reflectron mode, ions (blue dots) with more kinetic energy and velocity will penetrate the reflectron more deeply than those with lower kinetic energy (red dots) resulting in the ions reaching the second detector at the same time (Image adapted from Castleberry et al., 2008) .....  | 40 |
| 1.25. Schematic representation of a quadrupole mass analyser, the red ion is of the correct mass-to-charge and is able to traverse the quadrupole whilst the blue is of a different mass-to-charge and is neutralised on the metal rods ( <a href="http://www.chm.bris.ac.uk">www.chm.bris.ac.uk</a> ) .....   | 41 |
| 1.26. Schematic of a Hybrid Quadrupole Time-of-Flight with an orthogonal MALDI ion source (Baldwin et al., 2001) .....   | 42 |

|   |    |
|---|----|
| 1.27. Schematic of the ion modulator of the Time-of-Flight mass analyser from a hybrid instrument (Chernushevich et al., 2001).....   | 44 |
| 1.28. Schematic of the MALDI-LIFT-TOF/TOF mass spectrometer showing the MALDI ion source, the first TOF with timed ion selector, the LIFT and the second TOF with gridless reflector (Suckau et al., 2003).....   | 45 |
| 1.29. Schematic of the Waters MALDI HDMS SYNAPT G2 system, this instrument has a quadrupole orthogonal acceleration time-of-flight geometry and is equipped with an ion mobility separation device located between the quadrupole and the time-of-flight analysers. The “triwave” ion mobility separation device consists of three regions the trap, ion mobility separation and transfer regions (Waters Corporation, Manchester, UK)..... | 46 |
| 1.30. Schematics of the two approaches to mass spectrometry imaging. Microprobe mode A) collects mass spectra from an array of designated sampling positions to reconstruct an image after completion of the experiment. In microscope mode B) magnified images of ion distributions are directly acquired using a position sensitive detector (Luxemborg et al., 2004).....  | 49 |
| 1.31. Diagram showing the conventional spot-to-spot (left) and the raster (right) acquisition modes (Simmons 2008).....   | 50 |
| 1.32. Image of the Iwata Eclipse HP-CS airbrush used for manual matrix deposition ( <a href="http://www.iwata-medea.com">www.iwata-medea.com</a> ).....   | 52 |
| 1.33. Image of the Sunchrom Suncollect automated matrix sprayer (Image from <a href="http://www.sunchrom.de">www.sunchrom.de</a> ).....   | 53 |
| 1.34. Image of the Bruker ImagePrep™ matrix deposition device (Image from <a href="http://www.bdal.com">www.bdal.com</a> ).....   | 54 |
| 1.35. Image of the Labcyte Portrait® 630 Reagent Multi-Spotter instrument (Image from <a href="http://www.labcyte.com">www.labcyte.com</a> ).....   | 55 |
| 1.36. Image of sublimation equipment used to apply the matrix onto tissue samples. The image shows the tissue sample on a MALDI plate mounted to the underside of the condenser and the matrix powder in the bottom part of the apparatus (Hankin et al., 2007).....  | 57 |
| 1.37. Image of the Shimadzu CHIP-1000 chemical inkjet printer (Image from <a href="http://www.ssi.shimadzu.com">www.ssi.shimadzu.com</a> ).....   | 58 |
| 1.38. Image of the HTX TM-Sprayer (Image from <a href="http://www.htximaging.com">www.htximaging.com</a> ).....   | 59 |

## **2. Use of hydrazine based reagents for improved sensitivity of glucocorticoids by MALDI-MSI**

|   |    |
|---|----|
| 2.1. Structure of the hydrazine based reagent 2,4-Dinitrophenylhydrazine (DNPH).....  | 78 |
| 2.2. Scheme showing the reaction between steroids and DNPH to form the respective hydrazone derivative (Brombacher et al., 2003)..... | 79 |

|  |    |
|--|----|
| 2.3. Diagram showing the functional groups of the derivatisation reagent 4-Dimethylamino-6-(4-methoxy-1-naphthyl)-1, 3, 5-triazine-2-hydrazine (DMNTH) and their functions .....   | 80 |
| 2.4. Structures of the derivatisation reagents Girard's reagent P (left) and Girard's reagent T (right) .....  | 81 |
| 2.5. Equipment setup for the incubation of the reactive matrix coated tissue ...   | 88 |
| 2.6. MALDI-Mass Spectrum showing Fluticasone Propionate (500 ng/μl) mixed with the matrix CHCA. The spectra shows the presence of matrix related peaks and the expanded region shows the sodium adduct of Fluticasone Propionate ( $[M+Na]^+$ ) at m/z 523.1964 .....  | 90 |
| 2.7. MALDI-MS spectrum showing Fluticasone Propionate (500 ng/μl) following 1 hour reaction with the reactive matrix DNPH at room temperature. The spectrum shows the presence of the radical cation ( $[M]^+$ ) of Fluticasone Propionate at m/z 500.1402, the sodium adduct ( $[M+Na]^+$ ) at m/z 523.0986, the potassium adduct ( $[M+K]^+$ ) at m/z 539.0763 and the protonated hydrazone derivative ( $[M_D+H]^+$ ) at m/z 681.1208 .....             | 91 |
| 2.8. MALDI-MS showing Fluticasone Propionate (500 ng/μl) following 1 hour reaction with a mixture of the reactive matrix DNPH and CHCA at room temperature. The spectrum shows the presence of the radical cation ( $[M]^+$ ) of Fluticasone Propionate at m/z 500.1022, the sodium adduct ( $[M+Na]^+$ ) at m/z 523.0709, the potassium adduct ( $[M+K]^+$ ) at m/z 539.0473 and the protonated hydrazone derivative ( $[M_D+H]^+$ ) at m/z 681.0750..... | 92 |
| 2.9. ESI-MS spectrum showing Fluticasone Propionate following derivatisation with Girard's reagent P at a temperature of 70°C for 30 minute. The spectrum shows the protonated hydrazone derivative at m/z 634.2.....  | 94 |
| 2.10. ESI-MS/MS spectrum showing the product ions at m/z 527.1 and m/z 555.0, derived from the precursor ion of the protonated hydrazone derivative at m/z 634.1.....  | 95 |
| 2.11. Simplified scheme showing the fragmentation of Steroidal Girard P Hydrazones and the formation of the six membered dihydropyridazinone ring and the five membered dihydropyrazole ring (Griffiths et al., 2008) .....  | 96 |
| 2.12. MALDI-MS spectrum showing Fluticasone Propionate (500 ng/μl) following a 48 hour incubation with the reactive matrix DMNTH at room temperature. The spectrum shows the presence of the protonated un-reacted DMNTH ( $[M+H]^+$ ) at m/z 311.1621 and the protonated hydrazone derivative ( $[M_D+H]^+$ ) at m/z 793.3123.....  | 96 |
| 2.13. MALDI-MS spectrum showing Fluticasone Propionate (500 ng/μl) following 48 hour reaction with a mixture of the reactive matrix DMNTH and CHCA at room temperature. The spectrum shows the presence of the protonated hydrazone derivative ( $[M_D+H]^+$ ) at m/z 793.2853.....  | 97 |
| 2.14. Optical images showing the spiked tissue section A) before and B) after reactive matrix deposition. MALDI-MS images showing the distribution of C) the radical cation ( $[M]^+$ ) of Fluticasone Propionate at m/z 500.2 and D) the  |    |

|  |     |
|--|-----|
| protonated hydrazone derivative ( $[M_D+H]^+$ ) of Fluticasone Propionate at m/z 681.2 .....   | 99  |
| 2.15. Optical images showing the spiked tissue section A) before and B) after reactive matrix deposition. MALDI-MS images showing the distribution of the protonated hydrazone derivative of Fluticasone Propionate at m/z 793 C) before and D) after normalisation against the distribution of E) a reactive matrix related peak at m/z 589 .....   | 101 |
| 2.16. Optical images showing the spiked tissue section A) before and B) after reactive matrix deposition. MALDI-MS images showing the distribution of the protonated hydrazone derivative of Fluticasone Propionate at m/z 793 C) before and D) after normalisation against the distribution of E) a reactive matrix related peak at m/z 589 .....   | 102 |
| 2.17. Optical images showing the spiked tissue section A) before and B) after reactive matrix deposition. MALDI-MS images showing the distribution of the protonated hydrazone derivatives of C) Fluticasone Propionate at m/z 793, D) Beclomethasone Dipropionate at m/z 813, E) Budesonide at m/z 723, F) Dexamethasone at m/z 685 all images were normalised against the distribution of G) a reactive matrix related peak at m/z 589 ..... | 104 |

### **3. Monitoring the distribution of respiratory compounds in the lungs by MALDI-MSI**

|   |     |
|---|-----|
| 3.1. Whole body autoradiograms showing the distribution of $^{14}C$ -testosterone throughout the whole body section of a rat following intravenous administration, sacrificed 5 minutes and 2 hours post dose ..... | 114 |
| 3.2. MALDI-MS spectrum showing Tiotropium ( $[M]^+$ ) at m/z 392.116 at a concentration of 100 ng/ $\mu$ l .....  | 122 |
| 3.3. MALDI-LIFT-MS/MS spectrum showing the product ions at m/z 152.042 and m/z 170.113, derived from the precursor ion of Tiotropium at m/z 392 at a concentration of 100 ng/ $\mu$ l .....                         | 123 |
| 3.4. MALDI-LIFT-MS/MS image showing the distribution of the product ion at m/z 152, derived from the precursor ion of Tiotropium at m/z 392 (200 $\mu$ m spatial resolution) .....                                  | 124 |
| 3.5. ESI-MS/MS spectrum showing the product ions at m/z 152.2 and 170.2, derived from the precursor ion of Tiotropium at m/z 392.2 (100 ng/ml) .....  | 125 |
| 3.6. MALDI-MS spectrum showing Ambroxol (100 ng/ $\mu$ L) analysed using the matrix 2,5-Dihydroxybenzoic acid (DHB). The spectrum shows the presence of a peak at m/z 379.025 .....                                 | 126 |
| 3.7. MALDI-LIFT-MS/MS spectrum showing the product ions at m/z 115.736 and 263.955, derived from the precursor ion of Ambroxol at m/z 379.025 (100 ng/ $\mu$ l) .....   | 127 |
| 3.8. MALDI-LIFT-MS/MS image showing the distribution of the product ion at m/z 262, derived from the precursor ion of Ambroxol at m/z 379 .....   | 128 |

|   |     |
|---|-----|
| 3.9. ESI-MS/MS spectrum showing the product ions at m/z 116.2 and 264.0, derived from the precursor ion of Ambroxol at m/z 379.1 (1 µg/ml).....   | 129 |
| 3.10. MALDI-MS and MALDI-MS/MS Images showing the distribution of A) product ions at m/z 152 and 170, B) product ions at m/z 152 and 170, C) product ions at m/z 152 and 170, D) tiotropium ([M] <sup>+</sup> ) at m/z 392 and E) product ion at m/z 152 (Spatial resolution 100 µm).....   | 131 |
| 3.11. MALDI-Mass Spectrometry Images showing the distribution of Tiotropium ([M] <sup>+</sup> ) at m/z 392 (green) in relation to endogenous species (red) such as A) phosphocholine at m/z 184, B) unidentified species at m/z 241, C) unidentified species at m/z 478, D) heme group of haemoglobin at m/z 616, E) unidentified species at m/z 710, F) unidentified species at m/z 772, F) unidentified species at m/z 380, G) unidentified species at m/z 872 and H) choline at m/z 104 (Spatial resolution 100 µm)..... | 132 |
| 3.12. MALDI-LIFT-Tandem Mass Spectrometry Images showing the distribution of the product ion at m/z 152, derived from the precursor ion of Tiotropium at m/z 392. Consecutive sections showing A)section 11, B)section 12, C)section 15, D)section 16, E)section 17 and F)section 18 (Spatial resolution 200 µm)  | 133 |
| 3.13. MALDI-IMS-Mass Spectrometry Images showing the distribution of Tiotropium ([M] <sup>+</sup> ) at m/z 392 (green) in relation to the endogenous species at m/z 872 (red). (30 µm spatial resolution).....  | 134 |
| 3.14. MALDI-LIFT-MS/MS images showing the distribution of the product ion at m/z 152, derived from the precursor ion of Tiotropium at m/z 392 throughout A) the major airway and B) the trachea (30 µm spatial resolution).....   | 135 |
| 3.15. MALDI-MS/MS images showing A) the distribution of the product ion at m/z 152, derived from the precursor ion of Tiotropium at m/z 392. The distribution of the compound is localised in the trachea immediately after intratracheal dosing. The expanded images show B) the data presented prior to smoothing and C) following smoothing (50 µm spatial resolution).....  | 136 |

#### **4. Development of methodology for the quantification of pharmaceuticals in tissue sections by MALDI-MSI**

|  |     |
|--|-----|
| 4.1. Whole body autoradiogram showing the distribution of a radio-labelled compound throughout the whole body section of a rat. The highlighted region shows the spiked whole blood standards used for quantitation ( <a href="http://www.biospacelab.com">www.biospacelab.com</a> ) ..... | 142 |
| 4.2. Diagram showing the production of the frozen homogenate standards for sectioning using pipette tips as a mold and B) an optical image showing a frozen homogenate standard mounted to a cryostat stage.....   | 152 |
| 4.3. Optical image showing the Tiotropium homogenate standards (100 - 0.1 ng/µl) embedded in frozen the gelatin .....  | 153 |
| 4.4. MALDI-LIFT MS/MS images showing A) the distribution of the product ion at m/z 152, derived from the precursor ion of Tiotropium at m/z 392 within the   |     |

|  |     |
|--|-----|
| deposited standards and B) the distribution of the product ion at m/z 166, derived from the precursor ion of the internal standard Ipratropium at m/z 332 within the deposited standards .....                               | 156 |
| 4.5. Calibration curve showing the exported filter data from the MALDI-LIFT MS/MS image showing the Tiotropium standards spotted onto the control tissue section .....   | 157 |
| 4.6. Calibration curve showing the exported filter data from the MALDI-LIFT MS/MS image showing the Tiotropium standards spotted onto the control tissue section following normalisation against the internal standard ..... | 158 |
| 4.7. MALDI-LIFT MS/MS image showing the distribution of the product ion at m/z 166, derived from the precursor ion of Ipratropium at m/z 332 within the mixed homogenate standards (200 µm spatial resolution) .....         | 160 |
| 4.8. Calibration curve showing the exported filter data from the MALDI-LIFT-MS/MS image showing the distribution of Ipratropium within the mixed homogenate standards .....  | 161 |
| 4.9. MALDI-LIFT MS/MS image showing the distribution of the product ion at m/z 166, derived from the precursor ion of Ipratropium at m/z 332 within the homogenate standard sections (200 µm spatial resolution) .....       | 162 |
| 4.10. Calibration curve showing the exported filter data from the MALDI-LIFT MS/MS image showing the three replicates of Ipratropium homogenate standard sections .....  | 163 |
| 4.11. MALDI-MS/MS image showing the distribution of the product ions at m/z 152 (left) and 170 (right), derived from the precursor ion of Tiotropium at m/z 392 (150 µm spatial resolution) .....                            | 164 |
| 4.12. Calibration curve produced from region of interest analysis on the distribution of the product ion at m/z 172, derived from the precursor ion of Tiotropium at m/z 392 .....   | 165 |
| 4.13. MALDI-MS/MS image showing the distribution of the product ions at m/z 107 (left) and 135 (right), derived from the precursor ion of Fenoterol at m/z 303 (150 µm spatial resolution) .....                             | 166 |
| 4.14. Calibration curve Graph produced from region of interest analysis on the distribution of the product ion at m/z 107, derived from the precursor ion of Fenoterol at m/z 303 .....                                      | 167 |

**5. Development of methodology for monitoring the three-dimensional distribution of endogenous species in the lungs by MALDI-MSI**

|   |     |
|---|-----|
| 5.1. 3D MALDI-MS image of myelin basic protein in the corpus callosum of a mouse brain. The yellow volume corresponds to the outline of the entire corpus callosum from 264 optical images (Crecelius et al., 2005) ..... | 175 |
| 5.2. 3D MALDI-MS images of the substantia nigra and interpeduncular nucleus. The images show the distribution of PEP-19 (green) which is localised  |     |

|   |     |
|---|-----|
| in both regions and a protein with m/z 7416 (red) localised in the substansia nigra (Seely and Caprioli 2012).....  | 176 |
| 5.3. Co-registered MALDI-MS images and MRI of a whole mouse head. The MALDI-MSI images (colour scale) of A) the astrocytic phosphoprotein (Pea15) and B) the fatty acid binding protein 5 (Fabp5) are co-registered with the MRI data (grey scale) and an optical image (Sinha et al., 2008).....   | 177 |
| 5.4. 3D reconstruction of MALDI-MS images of (A) the neuropeptide <i>C. borealis</i> tachykinin-related peptide (CabTRP 1a) and (B) lipid PC 38:6 acquired from the brain of a crab (Chen et al., 2009).....  | 177 |
| 5.5. 3D images showing the co-registration of from optical imaging, H&E imaging, and MSI based on the position of the fiducial markers. (A) co-registration of MSI data (gray), optical imaging data of the tumor boundary (yellow mesh) and the hypoxic region (red). (B) co-registration of MSI data of actin (grey) and tdTomato (red) and H&E imaging data (yellow mesh) (Chughtai et al., 2012)..... | 178 |
| 5.6. Optical images of <i>Aphelandra squarrosa</i> leaves (A) before and (B) after analysis. (C) 3D LAESI-MS images showing the distribution of kaempferol/luteolin (yellow/orange scale) which follow the variegation pattern and chlorophyll (blue scale) accumulated in the mesophyll layers (Nemes et al., 2009) .....  | 179 |
| 5.7. 3D DESI-MS images of the mouse brain showing (A) PS 18:0/22:6 in green, (B) ST 24:1 in red and (C) PI 18:0/22:6 in blue. The same views are shown for the transparent overlaid distributions of the lipids (D) PS 18:0/22:6 and ST 24:1 and (E) PS 18:0/22:6 and PI 18:0/22:6 (Eberlin et al., 2010).....  | 180 |
| 5.8. 3D visualisation of SIMS depth profiling of HeLa-M cells prepared by the formalin fixation freeze-drying (left) and the hydrated freeze fracture (right). The images show phosphocholine at m/z 184 (green) localised in the cell membrane and adenine at m/z 136 or guanine at m/z 156 localised in the nucleus (Fletcher et al., 2011) .....   | 181 |
| 5.9. 3D SIMS-MS images of a rat heart showing the distribution of an endogenous species at m/z 145 (red), sodium at m/z 23 (green) and potassium at m/z 39 (blue) from different angles (Fornai et al., 2012).....  | 182 |
| 5.10. Optical images showing the control mouse lung tissue embedded in gelatin prior to freezing .....  | 184 |
| 5.11. MALDI-MS spectra obtained from the control mouse lung tissue (blue spectrum) and the registration markers (red spectrum).....   | 186 |
| 5.12. MALDI-MS images showing the distribution of various endogenous species in the control mouse lung tissue section (150 $\mu$ m spatial resolution). .....   | 187 |
| 5.13. MALDI-MS/MS images showing the distribution of the product ion at m/z 124, derived from the precursor ion of phosphocholine at m/z 184 (150 $\mu$ m spatial resolution) .....   | 188 |

|  |     |
|--|-----|
| 5.14. 2D MALDI-MS images showing the distribution of phosphocholine at m/z 184 following normalization against the protonated CHCA matrix at m/z 190, through the first 16 control mouse lung tissue sections .....  | 189 |
| 5.15. 3D MALDI-MS images produced using Image J software showing the distribution of phosphocholine at m/z 184 following normalization against the protonated CHCA matrix at m/z 190, throughout the control mouse lung tissue from different angles.....  | 190 |
| 5.16. 3D MALDI-MS images produced using Volume Explorer software showing the distribution of phosphocholine at m/z 184 following normalization against the protonated CHCA matrix at m/z 190, throughout the control mouse lung tissue from different angles.....  | 191 |
| 5.17. 3D MALDI-MS images showing the distribution of A) a possible phosphatidylcholine at m/z 756.5, B) the heme group of hemoglobin at m/z 616.2 C) another possible phosphatidylcholine m/z 760, D) an overlay of the phosphatidylcholine at m/z 756.5 and the heme group at m/z 616 and E) an overlay of all three endogenous species ..... | 192 |

## **List of tables**

### **1. Introduction**

1.1. Some of the commonly used MALDI matrices including their structure and the analyte classes they have been applied to ..... 29

### **2. Use of hydrazine based reagents for improved sensitivity of glucocorticoids by MALDI-MSI**

2.1. A table summarising the results from the in-solution derivatisation of the glucocorticoids with the hydrazine based derivatisation reagents ..... 98

### **3. Monitoring the distribution of respiratory compounds in the lungs by MALDI-MSI**

3.1. A table summarising the results from the feasibility study on a range of respiratory compounds and the determined on tissue limit of detection ..... 130

## Abbreviations and units

|                  |   |
|------------------|---|
| µl               | microlitre  |
| µm               | micrometer  |
| 9-AA             | 9-aminoacridine   |
| ADE              | acoustic droplet ejection   |
| AP               | atmospheric pressure  |
| APCI             | atmospheric pressure chemical ionisation                            |
| CabTRP           | <i>cancer borealis</i> tachykinin-related peptide                   |
| CAD              | collision activated dissociation                                    |
| CBP              | CREB-binding protein  |
| CEC              | capillary electrochromatography                                     |
| CHCA             | alpha-cyano-4-hydroxycinnamic acid                                  |
| CID              | collision induced dissociation                                      |
| CMC              | carboxymethylcellulose  |
| COPD             | chronic obstructive pulmonary disease                               |
| CT               | computerised topography   |
| DAN              | 1,5-diaminonaphthalene  |
| DC               | direct current  |
| DESI             | desorption electrospray ionisation                                  |
| DHB              | 2,5-dihydroxybenzoic acid   |
| DMNTH            | 4-dimethylamino-6-(4-methoxy-1-naphthyl)-1,3,5-triazine-2-hydrazine |
| DNPH             | 2,4-dinitrophenylhydrazine  |
| DP               | declustering potential  |
| ESI              | electrospray ionisation   |
| FDA              | Food and Drug Administration  |
| FEV <sub>1</sub> | forced expiratory volume  |
| FP               | focusing potential  |

|           |  |
|-----------|--|
| FTICR     | Fourier transform ion cyclotron resonance                |
| GR        | glucocorticoid receptor                                  |
| GTMA      | glycidyltrimethylammonium chloride                       |
| HAT       | histone acetyl transferase                               |
| HDAC's    | histone deacetylases                                     |
| HDI       | high definition imaging                                  |
| HDMS      | high definition mass spectrometry                        |
| HPLC      | high performance liquid chromatography                   |
| hsp90     | heat shock protein                                       |
| HV        | high vacuum  |
| Hz        | hertz  |
| IgE       | Immunoglobulin-E   |
| IL-8      | interleukin-8  |
| IMS       | ion mobility separation                                  |
| IRD       | ion release delay  |
| IRW       | ion release width  |
| ITO       | indium tin oxide   |
| LAESI     | laser ablation electrospray ionisation                   |
| LC        | liquid chromatography                                    |
| LDI       | laser desorption ionisation                              |
| LTB4      | leukotriene-B4   |
| m/z       | mass-to-charge ratio                                     |
| MALDESI   | matrix-assisted laser desorption electrospray ionisation |
| MALDI     | matrix-assisted laser desorption/ionisation              |
| MBP       | myelin basic protein                                     |
| ME-SIMS   | matrix enhanced-secondary ion mass spectrometry          |
| MetA-SIMS | metal assisted- secondary ion mass spectrometry          |

|                     |  |
|---------------------|--|
| mg                  | milligram                                |
| ml                  | millilitre                               |
| MLCK                | myosin light chain kinase                |
| MRI                 | magnetic resonance imaging               |
| MRM                 | multiple reaction monitoring             |
| MS                  | mass spectrometry                        |
| MS/MS               | tandem mass spectrometry                 |
| MSI                 | mass spectrometry imaging                |
| Nd:YAG              | neodymium-doped yttrium aluminium garnet |
| Nd:YVO <sub>4</sub> | neodymium-doped vanadate                 |
| ng                  | nanogram                                 |
| NMR                 | nuclear magnetic resonance               |
| OCT                 | optimal cutting temperature              |
| PC                  | phosphatidylcholine                      |
| PEG                 | polyethylene glycol                      |
| PET                 | Positron emission tomography             |
| pg                  | picogram                                 |
| PKA                 | protein kinase A                         |
| PS                  | phosphatidylserine                       |
| QWBA                | quantitative whole body autoradiography  |
| RF                  | radio frequency                          |
| ROI                 | region of interest                       |
| SA                  | sinapinic acid                           |
| SIMS                | secondary ion mass spectrometry          |
| SRIGs               | stacked ring ion guides                  |
| SRM                 | single reaction monitoring               |
| ST                  | sulfatide                                |

|         |                            |
|---------|----------------------------|
| TFA     | trifluoroacetic acid       |
| TLC     | thin-layer chromatography  |
| TOF     | time-of-flight             |
| TOF/TOF | tandem time-of-flight      |
| WBA     | whole body autoradiography |
| WHO     | World Health Organisation  |

## 1.1: Introduction to respiratory conditions

### 1.1.1: Asthma

Asthma is a chronic inflammatory disease which may be caused by exposure to environmental allergens. Asthma is characterised by intermittent and variable airflow obstruction and airway hyper-responsiveness to allergens. This leads to wheezing, breathlessness, coughing and chest tightness. These symptoms are reversed with treatment (Caramori and Adcock 2003). Airflow obstruction can be caused by several factors e.g. vasodilatation, increased luminal secretion or smooth muscle contractions which can cause bronchospasms (Baker and Lai 2008).

#### 1.1.1.1: Burden of asthma

According to the World Health Organisation (WHO), in 2011 approximately 300 million people suffered from asthma and it claimed the lives of 255,000 people worldwide ([www.who.int](http://www.who.int)). Asthma UK estimates that there are currently 5.4 million people in the United Kingdom that have asthma ([www.asthma.org.uk](http://www.asthma.org.uk)).

Asthma is more prevalent in developed countries (such as the United Kingdom and the United States). However, asthma is becoming increasingly prevalent in developing countries (such as South America and Asia) due to increased urbanization and the adoption of western lifestyles (Braman 2006). This is illustrated in the diagram shown in Figure 1.1.

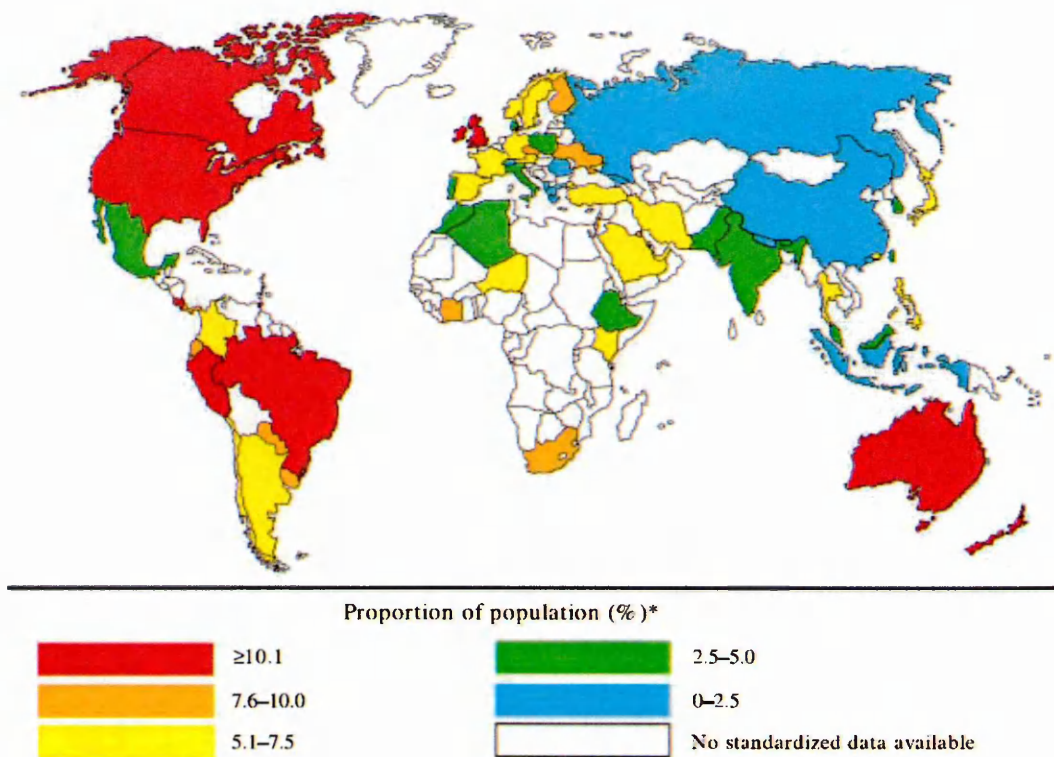


**Figure 1.1:** Map showing the global prevalence of clinical asthma (Masoli et al., 2004).

#### 1.1.1.2: Causes of asthma

There are many factors that are associated with the development of asthma, it is thought that in the case of genetically susceptible people if they are exposed to a particular allergen during a point in their life (usually childhood) this results in the production of immunoglobulin-E (IgE). It is upon re-exposure to that particular allergen that the person will present with the symptoms of asthma (Bourke 2007).

There have been many environmental factors that have been associated with the development of asthma, people that live in modern, urban and economically developed societies such as western parts of the world or countries that have adopted western culture are likely to develop asthma.

Other environmental factors can be separated into two groups:

- Outdoor environmental allergens - it is thought that atmospheric pollution such as vehicle exhaust emissions can trigger an asthmatic episode, however the most common outdoor allergens are pollen and fungal spores (Bourke 2007).
- Indoor environmental allergens – people tend to spend most of their time indoors and hence are greatly exposed to allergens that are derived from pets (such as fur or flakes of skin) and house dust mites (Barker and Lai 2008).

There are other factors that play a part in the development of asthma: respiratory infections like influenza can increase airway responsiveness in people, smoking can increase the production of IgE, diet such as eggs or milk can result in an asthmatic episode and drugs such as aspirin can induce bronchoconstriction (Barker and Lai 2008, Bourke 2007).

#### 1.1.1.3: Pathogenesis of asthma

An asthmatic attack /episode starts by the inhalation of an allergen (early phase reaction) to which the subject has become sensitized, the allergen interacts with the IgE antibody that has bound to the receptors of inflammatory cells (such as mast cells). This results in the activation of the inflammatory cells which degranulate and release mediators (such as histamine, prostaglandins and leukotrienes) this then results in smooth muscle contraction, increased luminal secretions and increased vascular permeability resulting in mucosal oedema (Bourke 2007), as shown in Figure 1.2.

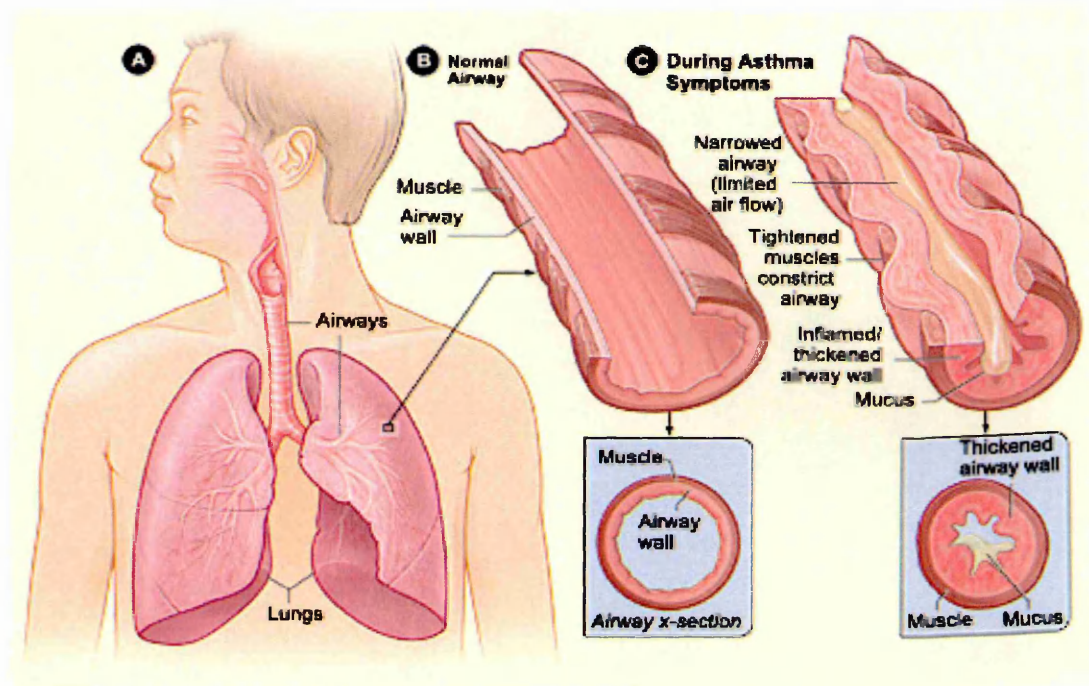


**Figure 1.2:** Diagram showing the difference between normal lung tissue and that following an asthmatic episode ([www.nhlbi.nih.gov](http://www.nhlbi.nih.gov)).

The inflammatory response (late phase reaction) of asthma is mediated through T-helper lymphocytes commonly Th2 cells, which produce cytokines and up-regulate the production of IgE and eosinophil and mast cell function (Bourke 2007). Once activated T cells attract eosinophils which release tissue damaging proteins and leukotrienes, which results in mucus hypersecretion, mucosal edema and bronchospasm (Baker and Lai 2008).

### 1.1.2: Chronic Obstructive Pulmonary Disease

Chronic obstructive pulmonary disease (COPD) clinically describes chronic bronchitis and emphysema two co-existing diseases that cause progressive and irreversible damage to the lungs. COPD is a disabling condition with symptoms that progress gradually, leading to breathlessness, wheezing, excess coughing and sputum production. At present there is no cure and non-pharmacological /pharmacological treatments merely alleviate symptoms and slow the progression of the disease.

#### 1.1.2.1: Burden of COPD

According to the World Health Organisation (WHO) in 2011 approximately 210 million people had COPD. The disease claimed the lives of more than 3 million people in 2011, which was equal to 5 % of all the deaths globally that year. COPD is currently the fourth leading cause of death worldwide, however based on current trends it is estimated that by 2030 chronic obstructive pulmonary disease will be the third leading cause of death worldwide ([www.who.int](http://www.who.int)).

#### 1.1.2.2: Causes of COPD

Cigarette smoking is the main cause of COPD, however only 15% of smokers develop COPD indicating that additional factors have an influence on the development of COPD (Maskell and Miller 2009). The additional factors that have been identified include: vehicle exhaust fumes and occupational exposure to dust or fumes from coal mining, paint spraying, cotton processing and farming. These factors all contribute to a reduced forced expiratory volume (FEV<sub>1</sub>) and an increased risk of developing COPD (Bourke 2007).

An imbalance between proteases and anti-proteases can be the result of a genetic deficiency in the anti-proteases such as  $\alpha$ 1-antitrypsin, which accounts for 2 % of COPD cases (Maskell and Millar 2009). Normally there is a balance between proteases and antiproteases, however a deficiency in anti-proteases could lead to the development of emphysema early on in life (Bourke 2007).

Also an imbalance between oxidants and anti-oxidants can be the result of cigarette smoke and air pollution which both contain unstable reactive oxygen species. Oxidants are also endogenously produced by neutrophils and macrophages during the inflammatory response. Oxidants cause damage to anti-proteases, increase mucus secretion and activate transcription factors that produce pro-inflammatory mediators (Hansel and Barnes 2004, Maskell and Millar 2009).

#### 1.1.2.3: Pathogenesis of COPD

Briefly COPD is commonly caused by long term exposure to cigarette smoke, COPD is characterised by airway inflammation/scarring and increased luminal mucus secretion (chronic bronchitis) and destruction of the lung parenchyma (emphysema) resulting in a loss in lung elasticity and elastic recoil, resulting in a reduced airflow which is not fully reversible (Baker and Lai 2008). This is illustrated in Figure 1.3.

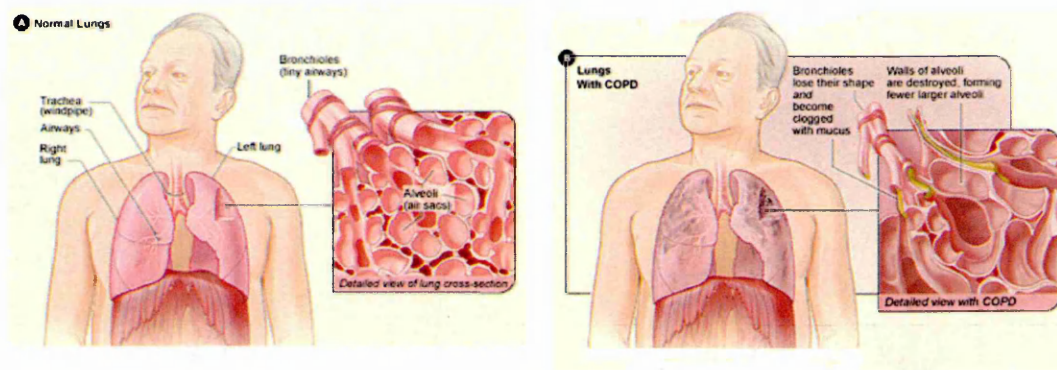


**Figure 1.3:** Diagram showing the difference between normal lung tissue and that afflicted with Chronic Obstructive Pulmonary Disease ([www.nhlbi.nih.gov](http://www.nhlbi.nih.gov)).

The inflammation mechanism in COPD is complex and is illustrated in Figure 1.4, it is thought that cigarette smoke or other inhaled irritants induce an inflammatory response in the respiratory epithelium and lung parenchyma. Macrophages, epithelial cells and CD8-T lymphocytes are stimulated to release neutrophil chemotaxins such as interleukin-8 (IL-8) and leukotriene-B4 (LTB4). Macrophages can cause damage directly by releasing proteases and indirectly by release of chemicals called cytokines that attract neutrophils; cytokines alter the permeability of the blood vessel walls, attracting neutrophils that pass through the blood vessel wall to the site of inflammation, in addition fluid leaks from blood into the surrounding tissue causing them to become oedematous and swollen (Maskell and Millar 2009, Hansel and Barnes 2004). Neutrophils also release proteases that begin to break down the parenchyma (emphysema) and promote mucus hypersecretion (chronic bronchitis).

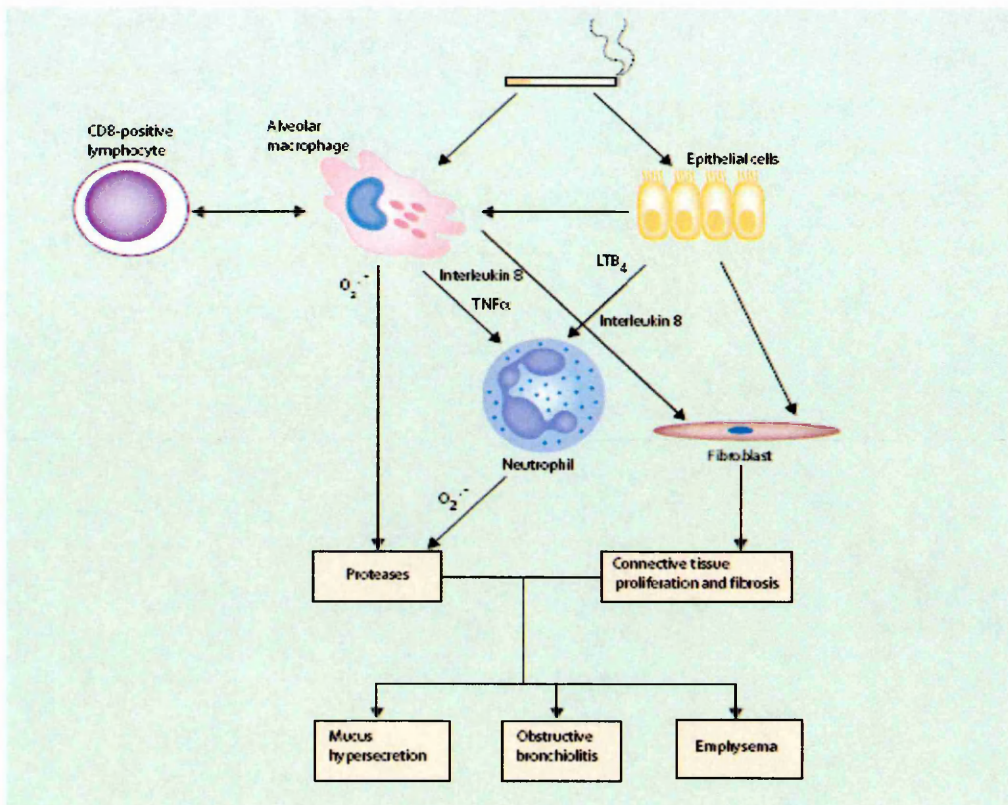


**Figure 1.4:** Scheme showing the inflammation mechanism of COPD (Image adapted from Barnes and Hansel 2004).

Mucus hypersecretion is characteristic of chronic bronchitis. Cigarette smoke and other inhaled irritants result in mucus production through reflex activation of sensory nerves, however as the process becomes chronic there is an increased amount of goblet cells, enlargement of submucosal bronchial glands and thickened smooth muscle resulting in excessive coughing.

Emphysema is characterised by enlargement of the airspaces and destruction of the lung parenchyma resulting in the production of large holes or bullae resulting in gas exchange abnormalities. This is illustrated in Figure 1.5, which shows computerised tomography (CT) scans of a cross-section of healthy lungs and emphysematous lungs.

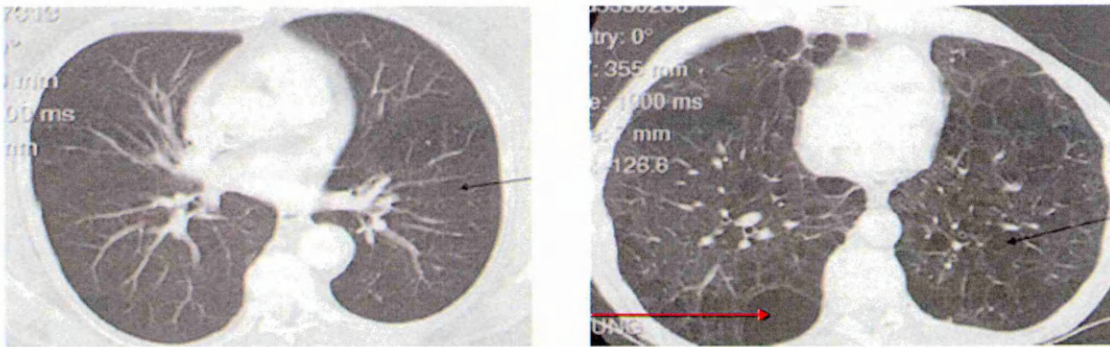


**Figure 1.5:** *Computed tomography (CT) scans showing the cross-section of healthy lungs on the left and emphysematous lungs on the right (Barker and Lai 2008).*

The healthy lung cross-section shows the lung tissue as a heterogenous grey colour and the structure of the lungs is rounded and even. In comparison with that of the emphysematous lung which shows black staining from carbon deposits caused by cigarette smoke and air pollution, also the lungs have large holes also known as bullae caused by proteolysis of the lung parenchyma (indicated by the red arrow). The emphysematous lungs also show the lungs are not rounded and even meaning a loss in elastic recoil resulting in a difficulty to breathe (Barker and Lai 2008, Bourke 2007).

## 1.2: Pharmaceutical treatment strategies

### 1.2.1: $\beta_2$ -adrenoreceptor agonists

#### 1.2.1.1: $\beta_2$ -adrenoreceptor agonists target

The  $\beta_2$ -adrenoreceptor is a single polypeptide glycoprotein complex that is embedded within the plasma membrane (Page and Barnes 2004). This receptor belongs to a seven-transmembrane domain family of receptors which are also known as G-protein coupled receptors (Johnson 2001). It is found in high concentrations throughout the respiratory tract and bronchial smooth muscle with approximately 30-40,000 receptors per cell (Sears and Lotvall 2005). G-protein coupled receptors are also found in the epithelium, in vascular smooth muscle and in submucosal glands. This could explain the regulation of mucus secretion observed following  $\beta_2$ -adrenoreceptor agonist administration (Barnes 2004b).

The  $\beta_2$ -adrenoreceptor is composed of 413 amino acid residues that are arranged into seven-membrane spanning alpha helices with an extracellular N-terminus and an intracellular C-terminus and three intracellular loops (Clark *et al.*, 1993, Sears and Lotvall 2005) as shown in Figure 1.6. These helices group together to form a hydrophobic binding site, which is accessible to compounds via the extracellular aqueous biophase (Anderson *et al.*, 1994).

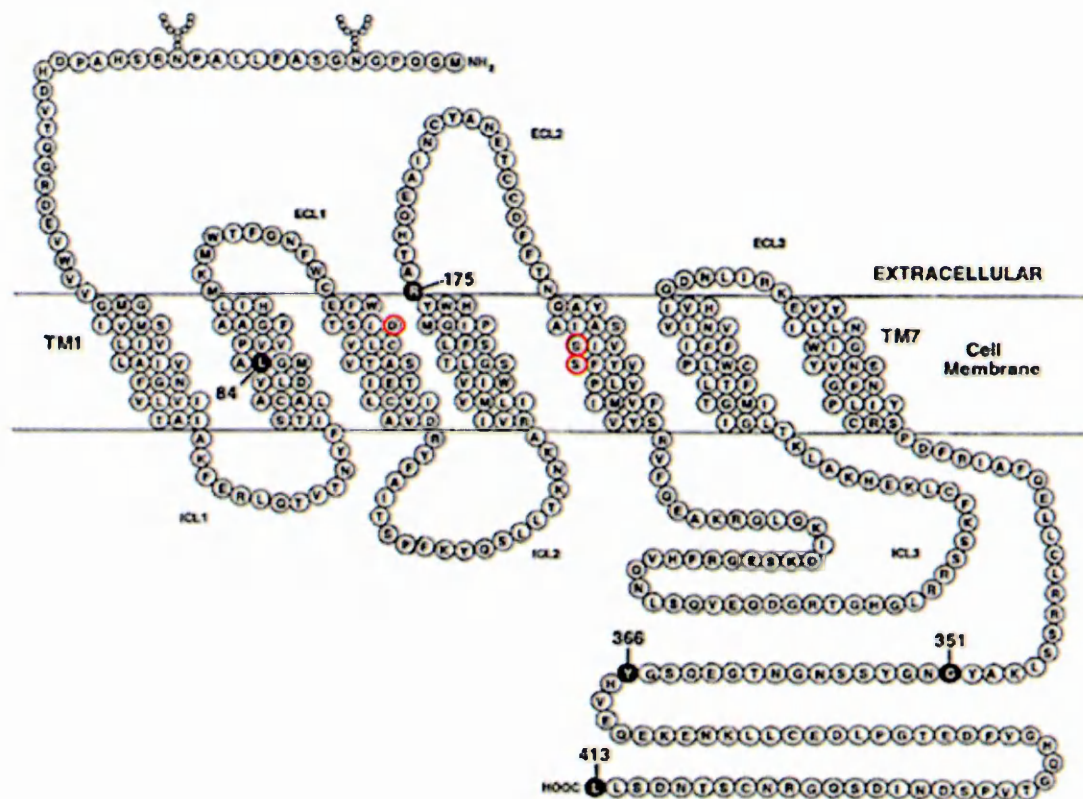


**Figure 1.6:** Proposed structure of the  $\beta_2$ -adrenoreceptor which consists of seven  $\alpha$ -helices spanning the membrane, amino acid residues important in agonist binding are circled (Image adapted from Sears and Lotvall 2005).

### 1.2.1.2: Structures of $\beta_2$ -adrenoreceptor agonists

Salbutamol (Figure 1.7A) is a short-acting  $\beta_2$ -adrenoreceptor agonist that consists of the catechol nucleus (benzene ring with two hydroxyl groups at positions 3 and 4) and an amino side chain that is responsible for the direct interaction with the active site of the receptor. Formoterol (Figure 1.7B) is a long-acting  $\beta_2$ -adrenoreceptor agonist and is a formamide substituted phenoethanolamine. Salmeterol (Figure 1.7C) is also a long-acting  $\beta_2$ -adrenoreceptor agonist it is a saligenin derivative of phenylethanolamine (Anderson *et al.*, 1994).

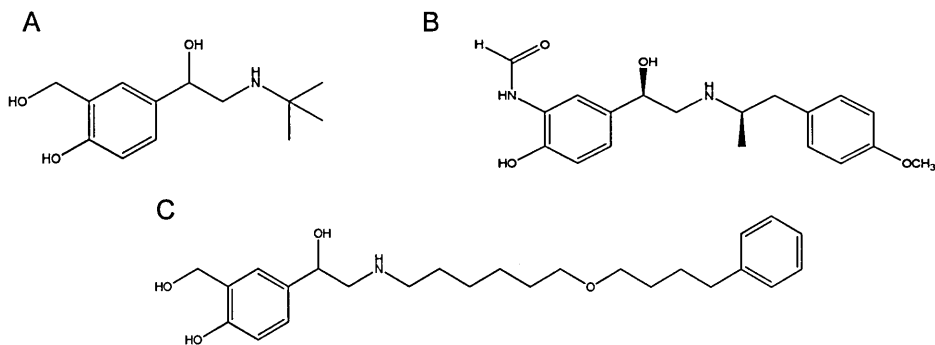


**Figure 1.7:** Structures of the  $\beta_2$ -adrenoreceptor agonists A) salbutamol, B) formoterol and C) salmeterol.

The structures of the  $\beta_2$ -adrenoreceptor agonists determine how they enter the active site of the  $\beta_2$ -adrenoreceptor and the agonistic duration of action. The mechanism of interaction for each of the compounds described above is illustrated in Figure 1.8.

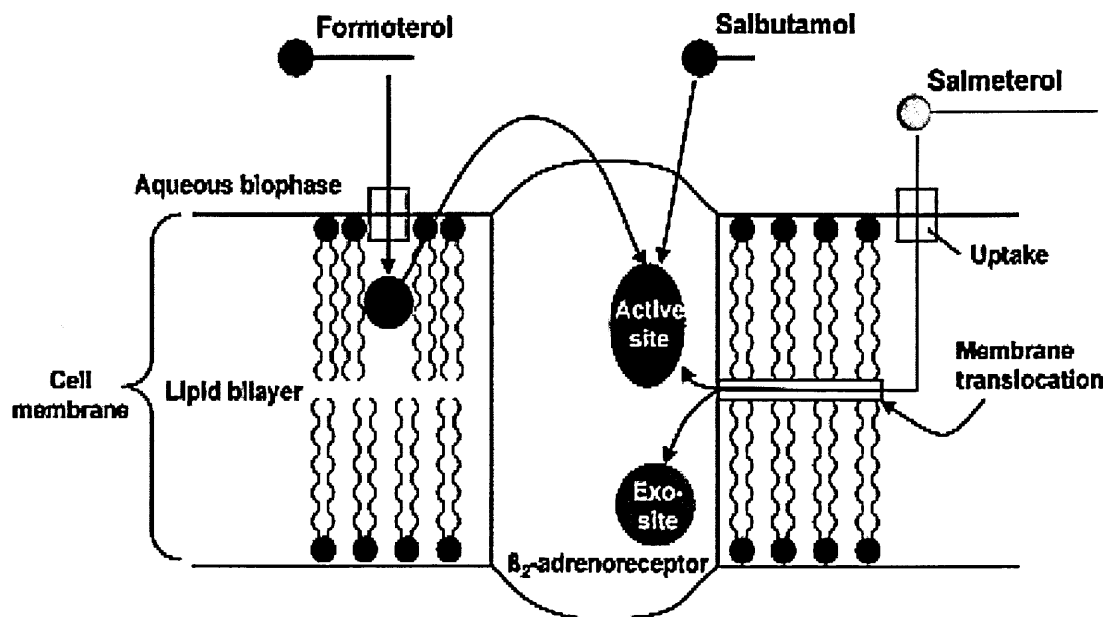


**Figure 1.8:** Diagram illustrating the different interactions of the three  $\beta_2$ -adrenoreceptor agonists with the  $\beta_2$ -adrenoreceptor (Johnson 2001).

Salbutamol is a hydrophilic compound and interacts directly with the active site of a  $\beta$ -adrenoreceptor, resulting in a rapid onset of action (Johnson 2001).

Bronchodilation occurs within 2-3 minutes and peak bronchodilation is achieved at 15 minutes post inhalation. Salbutamol is however, only a short acting  $\beta_2$ -adrenoreceptor agonist, as it only weakly binds to the active site of the receptor resulting in a duration of action of around 4-6 hours (Sears and Lotvall 2005).

Another  $\beta_2$ -adrenoreceptor agonist, formoterol is partially lipophilic and is taken up by the cell membrane to form a depot. From here the compound diffuses into the receptor and interacts with the active site and consequently has a prolonged duration of action of up to 12 hours (Sears and Lotvall 2005).

In contrast, salmeterol is highly lipophilic due to the long side-chain within the compounds structure and as a result it enters the cell membrane and laterally diffuses into the receptor, however this process is slow and can take up to 30 minutes (Johnson 2001). The binding of salmeterol to the active site is a unique process that involves the binding of the side-chain to a secondary binding site called the "exo-site". The saligenin head of the compound can freely engage and disengage from the active site due to the oxygen within the compound acting as a hinge or fulcrum. Whilst the onset of action is relatively slow this unique method by which salmeterol interacts with the active site of the receptor, enables a prolonged duration of action of up to 12 hours.

#### 1.2.1.3: Mechanism of action

$B_2$ -adrenoreceptor agonists are used to stimulate bronchial smooth muscle relaxation through activation of adenylyl cyclase (Baker and Lai 2008). Activation of adenylyl cyclase is facilitated by the receptor-associated guanine nucleotide regulatory protein ( $G_s$  protein). This is composed of  $\alpha$ ,  $\beta$  and  $\gamma$  subunits. In a resting state the  $\alpha$ -subunit binds GDP and exists as a heterotrimer with the  $\beta$  and  $\gamma$  subunits (Johnson 2001). However on receptor activation the GDP is

released allowing GTP to bind to the  $\alpha$ -subunit, which dissociates from the  $\beta$  and  $\gamma$  subunits and interacts with adenylyl cyclase that converts ATP into cAMP (Johnson and Druey 2002). Production of cAMP subsequently leads to the activation of cAMP-dependant protein kinase A (PKA), which then causes the inactivation (by phosphorylation) of myosin light chain kinase (MLCK). Inactivated MLCK precludes interaction with the contractile protein myosin, thereby promoting smooth muscle relaxation as shown in Figure 1.9 (Caramori and Adcock 2003).  $\beta_2$ -adrenoreceptor agonists can also promote smooth muscle relaxation by activation of pathways which reduces  $\text{Ca}^{2+}$  levels, this causes a reduction of  $\text{Ca}^{2+}$  dependant actin-myosin leading to relaxation of smooth muscle within the airway (Caramori and Adcock 2003).

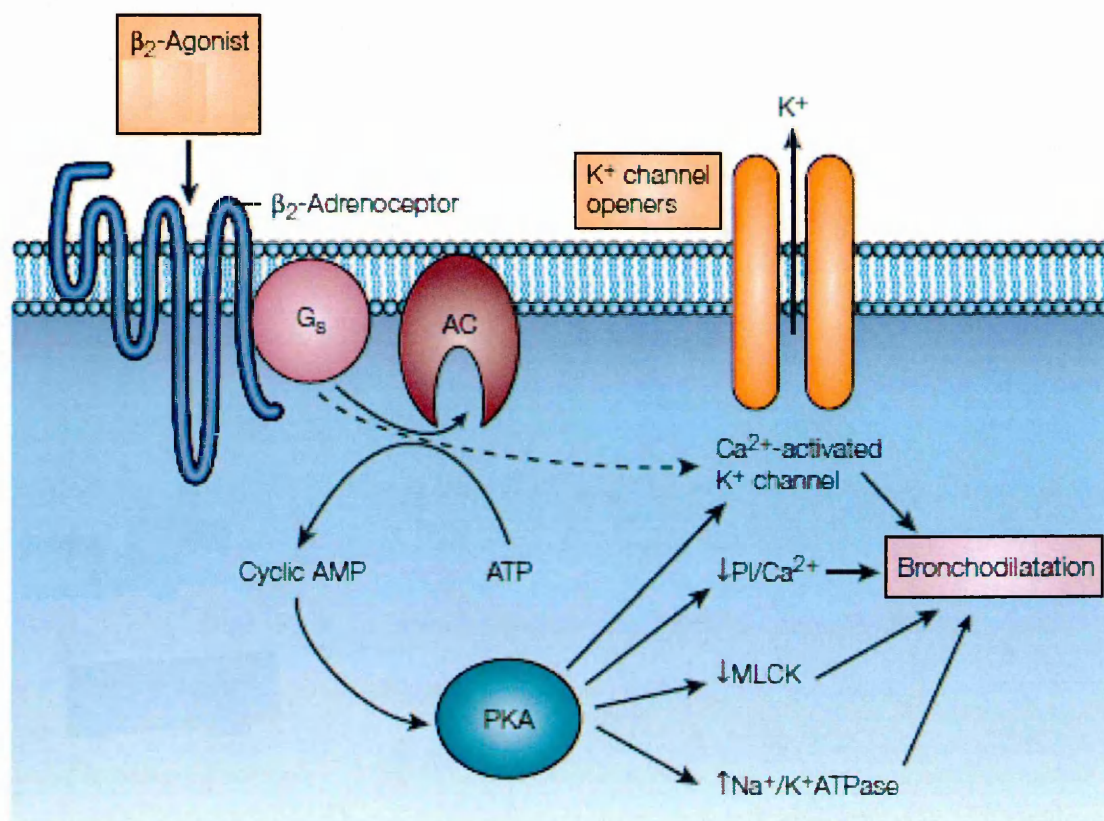


**Figure 1.9:** Diagram showing the effect of Beta 2-Adrenergic receptor agonists on promoting smooth muscle relaxation (Adapted from Barnes 2004c).

### 1.2.2: Corticosteroids

Corticosteroids (or glucocorticoids) are the mainstay of asthma management treatment and are commonly called preventers as these compounds treat the underlying disease process by reducing the number of inflammatory cells in the airways (such as eosinophils, T lymphocytes and mast cells) thus providing a resistance to severe attacks. Corticosteroids are also used in the treatment of COPD (Calverley 2000), however because of the damage caused by the disease to the lungs their anti-inflammatory effect is minimal and barely increases the patients forced expiratory volume (Baker and Lai 2008).

#### 1.2.2.1: Structures of corticosteroids

All modern corticosteroids used in the management of asthma are synthetic analogues of natural corticosteroids such as cortisone and hydrocortisone, first isolated from the adrenal glands in the late 1930's and successfully used in anti-inflammatory treatment in the mid 1940's (Gupta *et al.*, 2004).

Structural modifications by way of the addition or modifications of various functional groups helped to improve the anti-inflammatory action and reduce some of the observed systemic side effects. Dexamethasone (Figure 1.10A) was introduced in the 1950's and is derived from triamcinolone by the replacement of the 16 $\alpha$ -hydroxyl group with a methyl group, this further improved the anti-inflammatory action and devoid of any side effects.

The major breakthrough came with the inhalation of topically active corticosteroids for the management of asthma, which negates any associated systemic side effects. Beclomethasone dipropionate (Figure 1.10B) which is a derivative of beclomethasone, was one of the first of inhaled topically active corticosteroids. Fluticasone propionate (Figure 1.10C) is a derivative of

fluticasone. Budesonide (Figure 1.10D) introduced in early 1980's is a non-halogenated corticosteroid.

The role of particular functional groups and the history of the production of modern synthetic corticosteroids were reviewed by (Gupta *et al.*, 2004).

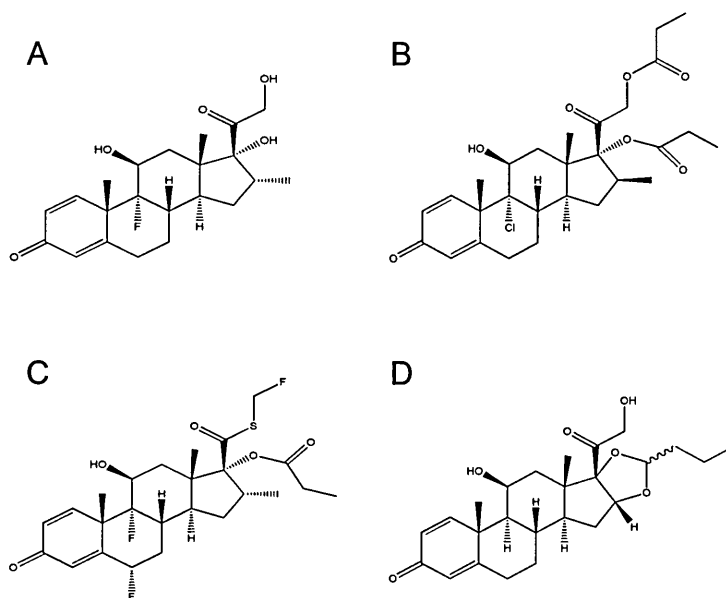


**Figure 1.10:** Structures of the synthetic corticosteroids A) dexamethasone, B) beclomethasone dipropionate, C) fluticasone propionate and D) budesonide.

#### 1.2.2.2: Mechanism of action

Corticosteroids illicit an anti-inflammatory response by crossing the cell membrane and binding to the intracellular glucocorticoid receptor (GR) as shown in the schematic in Figure 1.11. In their dormant state glucocorticoid receptors are bound in an oligomeric complex to chaperone proteins such as the 90 KDa heat shock protein (hsp90). This prevents the receptor from moving into the nucleus (Pelaia *et al.*, 2003).

The binding of the corticosteroid to the C-terminal end of the dormant glucocorticoid receptor, results in allosteric changes to the structure of the receptors causing the chaperone proteins to detach. The loss of the chaperone proteins reveals nuclear localisation signals on the glucocorticoid receptor and

allows the active steroid-receptor complex to translocate into the nucleus (Page and Barnes 2004).

Once in the nucleus the activated steroid-receptor complex can homodimerise and bind to the "glucocorticoid response elements" of the target DNA (Umland *et al.*, 2002). The binding is mediated through what are known as "zinc fingers" which consist of a zinc ion tetrahedrally coordinated to four cysteine residues located on the glucocorticoid receptor (Barnes 1998).

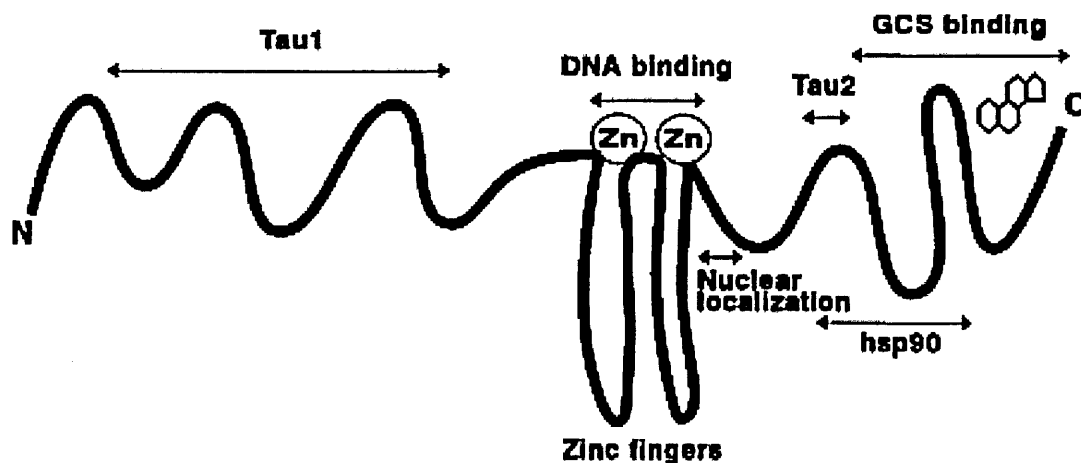


**Figure 1.11:** Simplified structure of the glucocorticoid receptor, showing the corticosteroid binding domain at the C-terminal region of the receptor and the DNA binding domain in the middle of the receptor with the "zinc fingers" (Barnes 1998).

This results in the unwinding of DNA and allows access of the CREB-binding protein (CBP), this forms a scaffold for the attachment of transcription factors and also has histone acetyl transferase (HAT) activity. Acetylation of histones permits unwinding of the local DNA and permits the RNA polymerase II to transcribe messenger RNA resulting in the production of anti-inflammatory proteins (Hansel and Barnes 2004). This increase in gene transcription of anti-inflammatory proteins is known as transactivation (Barnes 2010).

Corticosteroids can also exert their anti-inflammatory effect by blocking the transcription of pro-inflammatory mediators, which are activated by external stimuli. This process is known as transrepression (Barnes 2010). It involves the active steroid-receptor complex acting as a monomer which interacts with CBP, resulting in an inhibition of CBP-mediated histone acetyl transferase (HAT) activity thus preventing the unwinding of DNA and the production of pro-inflammatory mediators. In addition glucocorticoid receptors may also recruit histone deacetylases (HDAC's) to the CBP complex leading to tight nucleotide compaction and repression of the production of pro-inflammatory mediators (Hansel and Barnes 2004). The two processes of glucocorticoid anti-inflammatory action are summarised in Figure 1.12.

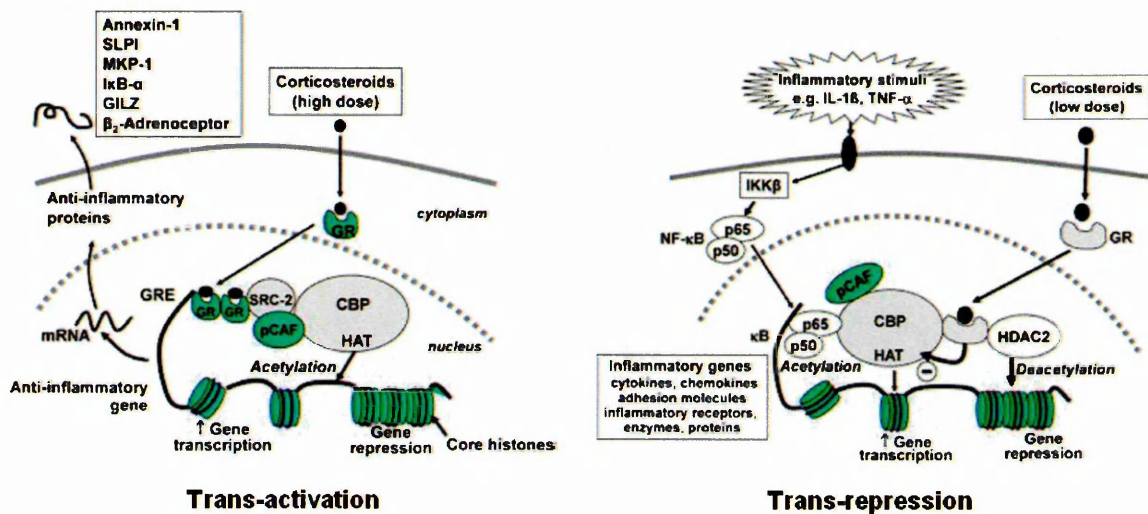


**Figure 1.12:** Schemes showing the two processes by which corticosteroids facilitate their anti-inflammatory action. Trans-activation is the production of anti-inflammatory mediators and trans-repression is the inhibition of the production of pro-inflammatory mediators (Barnes 2010).

### 1.2.3: Anticholinergic bronchodilators

Anticholinergic bronchodilators are commonly used in the management of COPD but have also been used in the management of asthma either alone or in combination with other bronchodilator agents. Anticholinergic bronchodilators are the most effective class of bronchodilator in patients with COPD, this is because the airway cholinergic vagal tone is the only reversible component of the disease (Barnes 2004d).

#### 1.2.3.1: Structures of anticholinergic bronchodilators

Modern anticholinergic bronchodilators are synthetic derivatives of atropine isolated from the berries of the deadly nightshade plant, *Atropa Belladonna* (Clark *et al.*, 1994). Anticholinergic bronchodilators such as ipratropium (Figure 1.13A), which is a quaternary methyl isopropyl derivative of atropine contains a positively charged quaternary nitrogen. This makes the compound poorly absorbable by the respiratory mucosal surface and prevents systemic absorption and therefore minimises the risks of any possible side effects (Page and Barnes 2004).

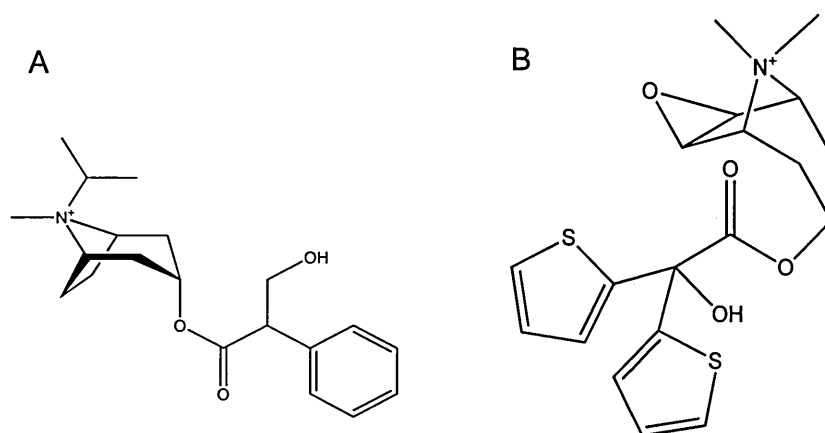


**Figure 1.13:** Structure of A) the short-acting anticholinergic bronchodilator ipratropium and B) the long-acting anticholinergic bronchodilator tiotropium.

### 1.2.3.2: Anticholinergic bronchodilator target

The target for anticholinergic bronchodilators are muscarinic receptors. There are three subtypes of muscarinic receptors located in the human airway designated  $M_1$ ,  $M_2$  and  $M_3$  receptors as shown in Figure 1.14. These receptors have specific functions in the parasympathetic nervous system and control the day-to-day function of the lungs and other organs. The  $M_1$  receptors are located in the parasympathetic ganglia, their function is the cholinergic neurotransmission through the parasympathetic ganglia. The  $M_2$  receptors (autoreceptors) are located on the postganglionic cholinergic nerves and provide negative feedback to inhibit the release of acetylcholine. Finally,  $M_3$  receptors are located on the bronchial smooth muscle and in the mucus glands, bronchoconstriction and mucus secretion is mediated through these receptors (Page and Barnes 2004, Hansel and Barnes 2004).

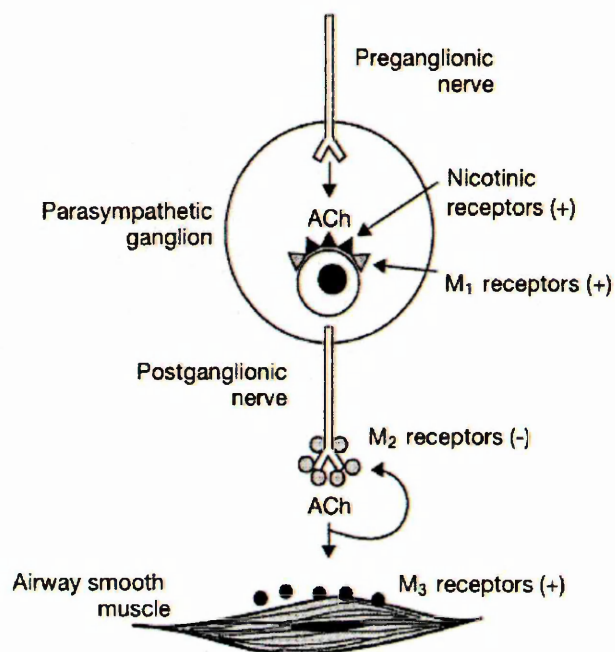


**Figure 1.14:** Scheme showing the location of the three muscarinic receptors. The  $M_1$  receptors are located in the parasympathetic ganglion, the  $M_2$  receptors are located at the cholinergic nerve terminals and the  $M_3$  receptors are located on the airway smooth muscle and mucus glands (Barnes 2004d).

### 1.2.3.3: Mechanism of action

Inhaled anticholinergic agents are muscarinic receptor antagonists that block the parasympathetic neurotransmitter acetylcholine which causes bronchoconstriction and mucus secretion. Acetylcholine is released by cholinergic nerve endings that innervate the lungs, which binds to muscarinic receptors in the smooth muscle and airway submucosal glands this causes bronchoconstriction and mucus secretion (Barnes 2004d). The mechanism of action of anticholinergic agents is shown in Figure 1.15, the anticholinergic agent binds to the muscarinic receptor and prevents acetylcholine from binding thus preventing bronchoconstriction and mucus secretion.

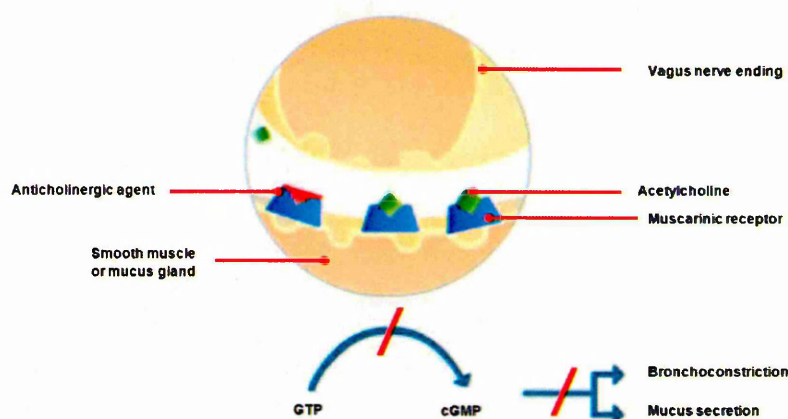


**Figure 1.15:** Diagram showing the mechanism of action of anticholinergic bronchodilators (Image adapted from [www.pharmacologycorner.com](http://www.pharmacologycorner.com)).

Tiotropium selectively blocks the  $M_1$  and  $M_3$  receptors and dissociates slowly, giving long-acting bronchodilation (~24 hours). This has the advantage of providing a once daily treatment with tiotropium. In contrast, ipratropium non-selectively blocks all three types of muscarinic receptors and dissociates from the receptors more quickly resulting in short-action bronchodilation (~4-6 hours).

### 1.3. Introduction to Mass Spectrometry

A mass spectrometer consists of an ion source for the creation of gas phase ions, a mass analyser for the separation of these ions according to their mass to charge ratio and a detector which “counts” the number of ions for each mass to charge ratio emerging from the mass analyser. The mass analyser and detector components are operated under high vacuum conditions; this is illustrated below in Figure 1.16.



**Figure 1.16:** Simplified schematic of a mass spectrometer showing the three main components in blue.

In some instances the mass spectrometer may have a sample introduction component at the front of the instrument for example automated sample introduction robotics followed by chromatographic separation. All modern mass spectrometers utilise computers for instrument control and data collection.

#### 1.3.1. Ionisation Sources

##### 1.3.1.1. Matrix-Assisted Laser Desorption/Ionisation

Matrix-assisted laser desorption/ionisation (MALDI) was initially developed by Karas, Hillenkamp and co-workers in the late 1980's (Karas *et al.*, 1985). Coincidentally around the same time a closely related technique was developed by Tanaka *et al.*, which involved mixing the analyte of interest with a suspension of ultrafine cobalt powder in glycerol (Tanaka *et al.*, 1988). Essentially MALDI is an extension of the laser desorption ionisation (LDI) technique that was introduced in the late 1960's. The advantages of LDI are it requires no special sample

preparation in comparison to MALDI, however due to the increased energy extensive fragmentation and a loss of chemical information is observed. Whilst MALDI is now the commonly used method LDI is still useful for the analysis of certain compounds such as fullerene and crude oil.

In profiling experiments the analyte is mixed with an excess solution of the matrix, which is a low molecular weight organic compound that absorbs the energy at the wavelength of the laser. The result is the formation of analyte-doped matrix crystals, the laser ablates the crystals which causes the excitation and heating of the matrix which causes desorption and ionisation in the gas phase.

The principle of the MALDI technique is illustrated below in Figure 1.17.

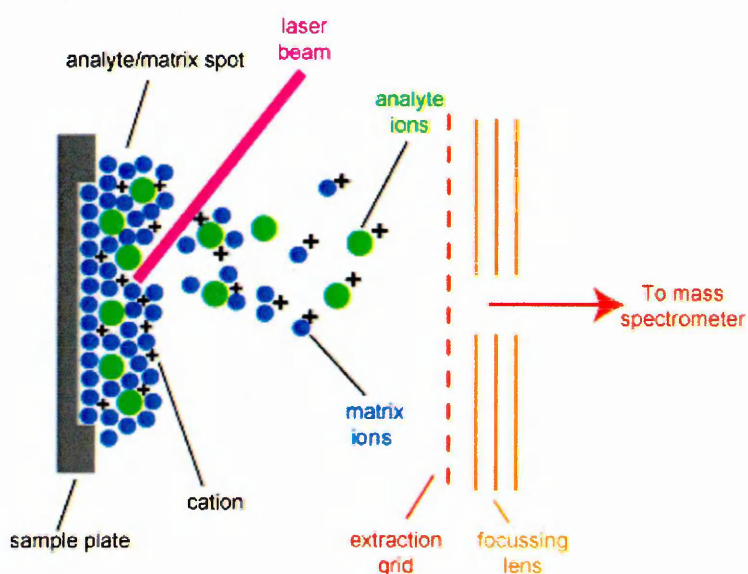


**Figure 1.17:** Schematic representation of the matrix-assisted laser desorption/ionisation process, showing the analyte (green dots) embedded within the matrix (blue dots) the laser is then fired at this mixture causing desorption and subsequent ionization in the gas phase of both matrix and analyte molecules that are sampled by the mass spectrometer ([www.chm.bris.ac.uk](http://www.chm.bris.ac.uk)).

MALDI was later developed into an imaging technique by (Spengler *et al.*, 1994). The initial work demonstrated the imaging of a dried mixture of the matrix 2,5-dihydroxybenzoic acid and the peptide substance P using the LAMMA 2000 scanning laser ion microprobe system the authors had developed. This concept was later extended for the analysis of tissue sections (Caprioli *et al.*, 1997). In imaging experiments the matrix is uniformly applied onto the surface of the sample, this causes the analytes within the tissue to migrate to the surface upon which the matrix and the analyte form co-crystals.

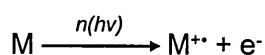
Whilst the use of MALDI is widely accepted in the scientific community, the underlying mechanism of the desorption and ionisation processes involved are not fully understood and are still under investigation. Current understanding of both the desorption and ionisation have been extensively reviewed (Dreisewerd 2003, Knochenmuss 2006).

#### 1.3.1.1.1 Ion formation in MALDI

The ionisation process in MALDI is generally thought to occur as a two step process; the primary ionisation occurs during or soon after the laser pulse followed by secondary reactions in the expanding plume of desorbed material (Knochenmuss 2006).

The formation of primary ions remains the most controversial aspect in MALDI and many theories have been proposed over the years.

The *multiphoton ionisation* is bar far the simplest explanation of ion formation resulting from laser excitation of the MALDI matrix, leading to the formation of a matrix radical cation (Zenobi and Knochenmuss 1998). This is represented by the following equation:

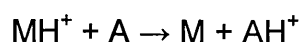


The *cluster model* originally called the “lucky survivor” model was introduced by (Karas *et al.*, 2000). It is thought that the analyte retains a charge upon incorporation into the solid matrix preparation, upon irradiation with the laser clusters are desorbed and in the gas phase neutral matrix and solvent molecules are lost. Extensive neutralisation is then thought to occur in the plume therefore the ions detected are the “lucky survivors” and explains the presence of singly charged ions (the only species to be observed in MALDI).

Following formation the initial primary ions then interact with neutral molecules in the expanding plume of desorbed material, these reactions result in the formation of secondary ions that are finally detected and observed in the mass spectrum. There are three types of secondary reactions that can occur these are known as proton, electron and cation transfer reactions.

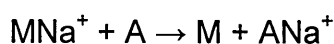
The *proton transfer* reaction is the most important secondary reaction in MALDI.

The proton transfer occurs between the protonated matrix and neutral analyte and is driven by the proton affinities of the analyte and matrix. The reaction is shown below:



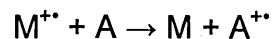
The *cation transfer* reaction is the more favourable mechanism for analytes with low proton affinity less than that of the matrix (Knochenmuss and Zenobi 2003).

This process is observed with the analysis of synthetic polymers and carbohydrates. The additions of sodium or potassium salts to the matrix can be used to promote the cationisation of certain analytes. This process is illustrated in the equation below:



The role of the matrix in the cationisation process has been investigated by (Zhang *et al.*, in 2004).

The *electron transfer* reaction is not very common but can occur when the ionisation potential of the matrix is greater than that of the analyte leads to the formation of analyte radical cations. The reaction is shown below:



#### 1.3.1.1.2. MALDI matrices

Several matrices have been developed for MALDI and MALDI imaging. The selection of the matrix is an important parameter to consider and the choice is based on the analyte of interest.

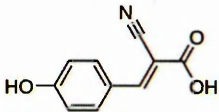
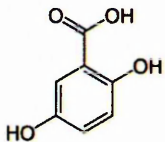
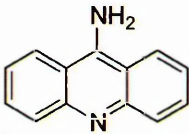
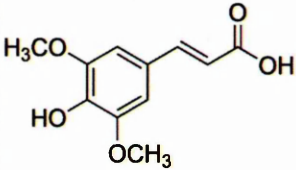
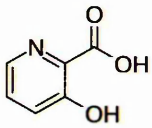
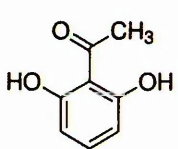
The most commonly used matrices are either benzoic or cinnamic acid derivatives. Sinapinic acid (SA) is routinely used for the analysis of high molecular weight compounds such as proteins whilst  $\alpha$ -cyano-4-hydroxycinnamic acid (CHCA) is more commonly used for low molecular weight compounds such as drugs, lipids and peptides (Bevis and Chait 1989, Bevis *et al.*, 1992, Schwatz et al., 2003). 2,5-dihydroxybenzoic acid (DHB) is commonly used in the analysis of drugs and lipids (Strupat *et al.*, 1991).

9-Aminoacridine (9-AA) was first introduced by Vermillion-Salsbury and Hercules in 2002 as a matrix for the analysis of acidic compounds in negative ion mode by MALDI-MS; 9-AA is a strong base and readily accepts protons in comparison to established matrices such as CHCA which is an acid that readily donates protons. The ionisation mechanism of 9-AA in negative ion mode is thought to occur by the abstraction of protons in an acid/base reaction leading to the formation of de-protonated species ( $[M-H]^-$ ).

It has been demonstrated by (Guo and Ze 2007) that a mixture of the acidic matrix CHCA and the basic matrix 9-AA, act as a binary matrix to reduce the

background noise associated with matrix adducts. This matrix preparation also enables switching between polarities without further sample preparation.

A summary of the most common MALDI matrices is shown below in Table 1.1, this is not an exhaustive list and new matrix candidates and matrix preparations are reported on a regular basis.

| Name                                      | Structure   | Application                          |
|---|---|--------------------------------------|
| Alpha-cyano-4-hydroxycinnamic acid (CHCA) |    | Proteins, peptides, lipids and drugs |
| 2, 5-Dihydroxybenzoic acid (DHB)          |    | Proteins, peptides, lipids and drugs |
| 9-Aminoacridine (9-AA)                    |    | Lipids and other small molecules     |
| Sinnapic acid (SA)                        |   | Proteins                             |
| 3-Hydroxypicolinic acid (HPA)             |  | Proteins and oligonucleotides        |
| 2, 4, 6-Trihydroxyacetophenone (THAP)     |  | Lipids, oligonucleotides and drugs   |
| 2,6-Dihydroxyacetophenone (DHA)           |  | Lipids                               |

**Table 1.1:** Some of the commonly used MALDI matrices including their structure and the analyte classes they have been applied to.

#### 1.4.2. Secondary Ion Mass Spectrometry

Secondary ion mass spectrometry (SIMS) is a surface analysis technique commonly used in materials research especially in the semiconductor industry (McPhail 2006). SIMS imaging is a complementary technique to MALDI-MSI and is capable of producing high spatial resolution images ( $<1 \mu\text{m}$ ).

In SIMS, a high energy primary ion beam is directed onto a sample surface which penetrates the surface region and induces a collision cascade. This results in the release of secondary ions in the form of neutral and charged secondary species.

There are two modes of operation called static SIMS which is used for surface analysis and dynamic SIMS which is used to analyse the samples depth profile.

Static SIMS uses a low primary ion dose, which minimises the interactions of the primary ions to the top monolayers of the sample resulting in minimal surface damage. Dynamic SIMS on the other hand utilises a high primary ion dose, which interacts with deeper layers of the sample, this cause the sputtering of the sample surface and enables the production of a depth profile.

This generation of secondary ions is illustrated in Figure 1.18.

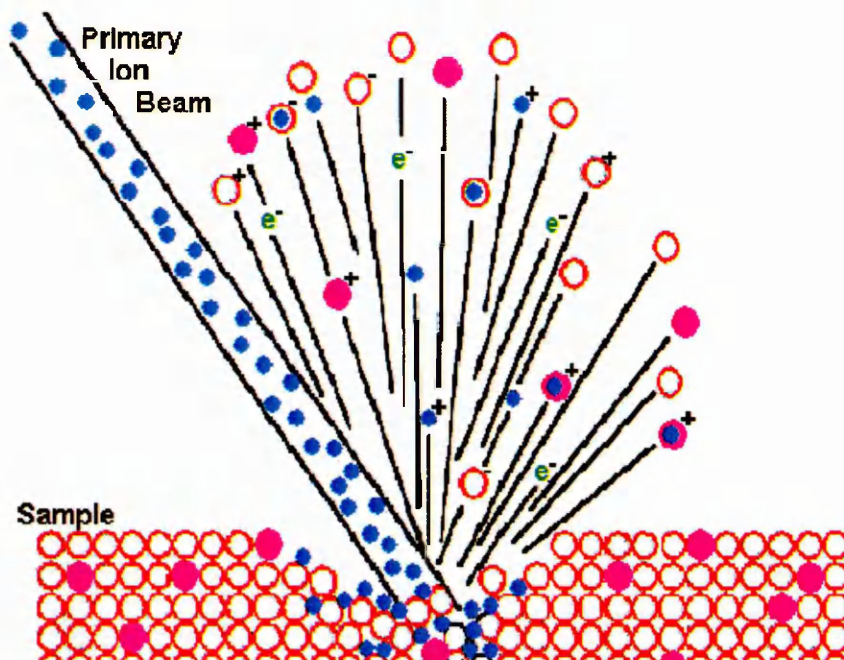


**Figure 1.18:** Schematic representation of the secondary ion mass spectrometry process, showing the primary ion beam (blue dots) which strikes the sample causing the production of secondary ions ([www.mse.engin.umich.edu](http://www.mse.engin.umich.edu)).

Application of a thin metal coating such as gold for Metal assisted-SIMS (Meta-SIMS) or the application of MALDI matrices for matrix enhanced-SIMS (ME-SIMS) have been developed to enhance the production of intact secondary ions and reduce fragmentation (McDonnell *et al.*, 2005, Altelaar *et al.*, 2007).

One of the main limitations of the SIMS technique is the ion source is usually coupled to time-of-flight or magnetic sector mass analysers and as a result the technique has low mass resolving power and no MS/MS capabilities (Prideaux and Stoeckli 2012).

In order to overcome these limitations several groups have investigated the connection of primary ion sources to commercially available instruments, an example by the Winograd group described the connection of a C<sub>60</sub> primary ion gun to an Applied Biosystems QSTAR instrument. This instrument demonstrated improved mass accuracy and resolving power (14,000), MS/MS

capabilities and capable of achieving a spatial resolution of around 30 $\mu$ m (Carado *et al.*, 2008).

Another example recently reported by Smith *et al.*, described the connection of a C<sub>60</sub> primary ion gun to a fourier transform ion cyclotron resonance mass spectrometer. This instrument demonstrated both high mass resolution (~100,000) and accuracy (1 ppm), MS/MS capabilities and capable of achieving a spatial resolution of around 40 $\mu$ m (Smith *et al.*, 2012).

### 1.4.3. Electrospray Ionisation

Electrospray ionisation (ESI) was first introduced by Dole and co-workers in 1968 and later coupled to a quadrupole mass analyser in 1984 by Yamashita and Fenn.

ESI is accomplished by passing a solution of analyte through a needle held at a high electrical potential into a chamber at atmospheric pressure. The high electric potential in the range of 3-6 kV is applied between the capillary and cone and causes an accumulation of positively charged ions at the tip of the capillary, to form what is known as a Taylor cone (Hoffmann and Stroobant 2007). When the imposed electric field is high enough the cone elongates, which then breaks and forms a spray of charged droplets (Gaskell 1997). A schematic of an ESI source is shown below in Figure 1.19.

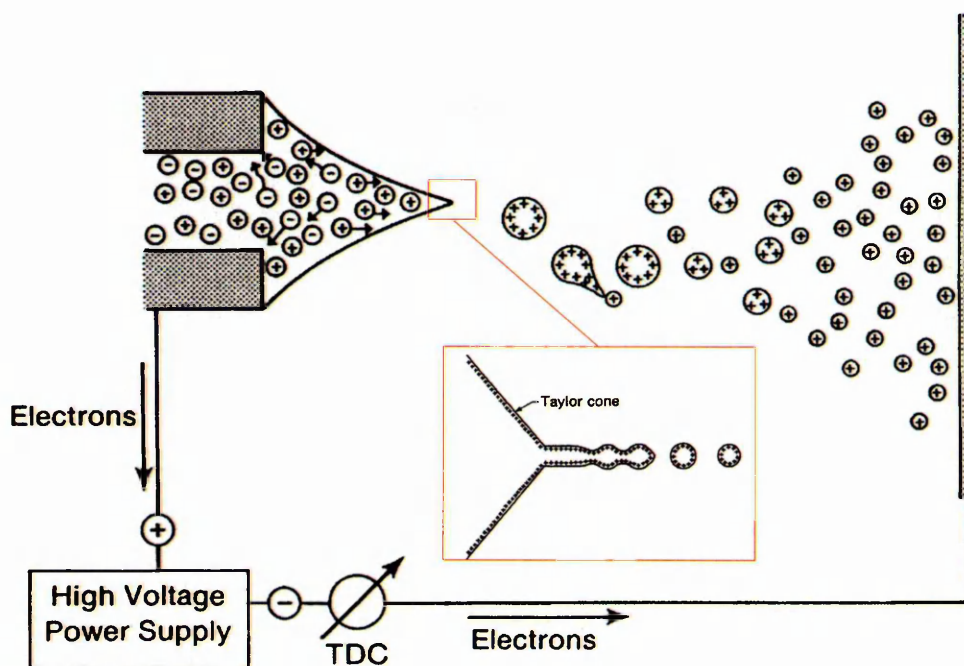


**Figure 1.19:** Schematic representation of an electrospray ionisation source. Showing the formation of a Taylor cone at the tip of the capillary and the production of a spray of charged droplets due to an applied electric potential (Image adapted from Kebarle 2000).

The solvent component of the droplet begins to evaporate with the aid of a stream of nitrogen gas and the diameter of the droplets is reduced, eventually the charge density becomes greater than the surface tension of the droplets. The point at which this occurs is known as the Rayleigh limit and at the point a process called Coulombic explosion occurs resulting in desorption of the ions into the gas phase. This process is known as the ion evaporation method and is more favourable for small molecular weight compounds (Baldwin 2005, El-Aneed *et al.*, 2009, Gaskell 1997). An alternative process known as the charge residue method can also occur, this results in the complete desolvation of droplets to form a single ion. This process is more favourable for large molecular weight compounds (Baldwin 2005, El-Aneed *et al.*, 2009). Both methods of ion formation are illustrated below in Figure 1.20.

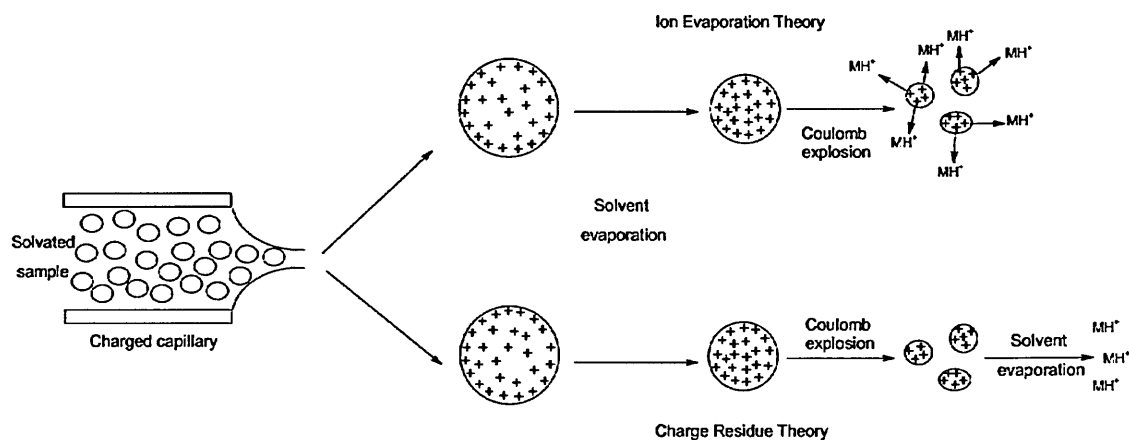


**Figure 1.20:** Diagram showing the two methods of ion formation in ESI. After the creation of a spray of charged droplets Coulombic explosion followed by desorption of ions from the surface can occur according to the ion evaporation method or the solvent can completely evaporate according to the charge residue method (El-Aneed *et al.*, 2009).

#### 1.4.4. Desorption Electrospray Ionisation

Desorption electrospray ionisation (DESI) is an ambient ionisation technique for mass spectrometry introduced by (Takats *et al.*, 2004).

The technique works by directing a spray of charged droplets produced from a pneumatically assisted electrospray onto a sample surface, the impact of these charged droplets produces a thin layer of solvent on the sample surface that extracts the analytes. It is upon the impact of subsequent charged droplets that causes the production of secondary microdroplets containing the dissolved analytes hence the term “droplet pickup” (Costa and Cooks 2008). A schematic of a DESI source is illustrated below in Figure 1.21.

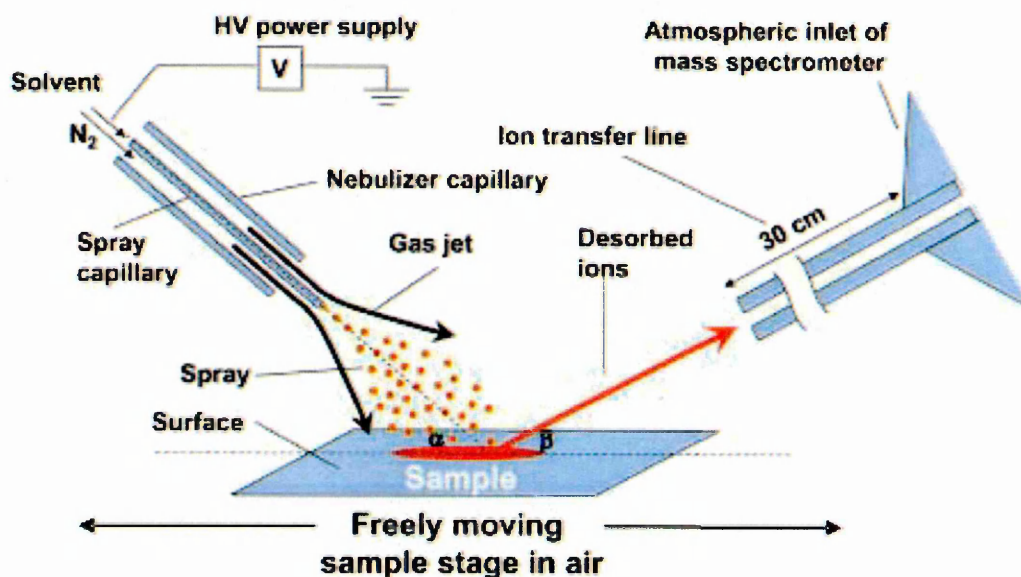


**Figure 1.21:** Schematic representation of the desorption electrospray ionisation source, showing the spray of charged droplets (red dots) that is directed towards the sample the impact of the charged particles results in the production of gaseous ions of analytes originally on the sample surface that are sampled by the mass spectrometer (Takats *et al.*, 2004).

DESI-MS was first demonstrated for the imaging of biological tissue sections by (Wiseman *et al.*, 2006). The first application of DESI-MS imaging to the

monitoring of the distribution of pharmaceutical compounds in tissue sections was later presented by (Wiseman *et al.*, 2008). In this work the distribution of the antipsychotic drug clozapine was monitored throughout rat brain, lung, kidney and testis tissue sections, the signal intensity of clozapine obtained from the images showed good correlation with quantitative data obtained from LC-MS/MS.

Kertesz *et al.*, demonstrated the use of DESI-MS/MS imaging to monitor the distribution of the drug propranolol throughout whole body tissue sections of a mouse, the resulting images were comparable with WBA distribution data.

The spatial resolution that can be achieved by DESI is 150-250  $\mu\text{m}$ . However Kertesz and Van Berkel demonstrated in 2008 that with optimised parameters such as the distance between the spray tip and sample and solvent flow rate, an imaging spatial resolution of approximately 40  $\mu\text{m}$  can be achieved.

#### 1.4.5. Laser Ablation Electrospray Ionisation

Laser ablation electrospray ionisation (LAESI) is a novel ion source originally developed by Akos Vertes and Peter Nemes in 2007 for producing ionised molecules for mass spectrometric analysis in normal atmospheric conditions from samples with a high water content e.g. plant tissues (Nemes and Vertes 2007).

The technique works by desorption of small portions of the sample into the gas phase and subsequent ionisation by an electrospray ion source. A mid infra-red laser (wavelength 2940 nm) is fired at the sample in order to excite the O-H bonds of the water molecules within the sample. This causes phase explosion leading to microscale ablation and ejection of neutral particulates. The particles are then intercepted by highly charged droplets from the ESI source, which captures a small amount of the emitted particles (Nemes *et al.*, 2009). From this point the gaseous ions are produced in a similar process to ESI and as a result the mass spectra exhibits multiply charged analyte peaks. Figure 1.22 shows the schematics of the LAESI ion source.

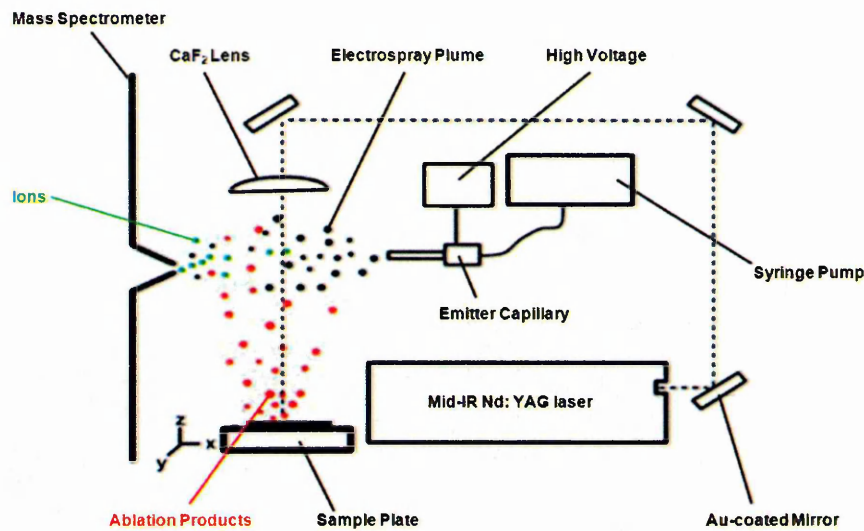


**Figure 1.22:** Schematic representation of the laser ablation electrospray ionisation source, showing the production of ablated material (red dots) which are intercepted by the electro spray plume (black dots) and post-ionised to form ions (green dots) that are sampled by the mass spectrometer (Image adapted from Shrestha et al., 2010).

Mass Spectrometric Imaging using LAESI has been used to monitor the distribution of endogenous proteins within biological tissue sections making the technique comparable to MALDI-MSI. Recently a commercial model based on the original research conducted by Vertes and Nemes has been produced by Protea Biosciences Inc., called the LAESI DP-1000 (<https://proteabio.com/LAESI>) and can currently be fitted onto Thermo and Waters instruments.

## 1.5: Mass Analysers

### 1.5.1: Time-of-Flight

#### 1.5.1.1: Linear time-of-flight mode

The concept of the time-of-flight (TOF) mass analyser was proposed by Stephens in 1946. The design of a linear TOF instrument was proposed by Wiley and McLaren in 1955 and later became the first commercial instrument. Ions formed in the MALDI source are accelerated towards the flight tube by a potential applied between the sample plate and the extraction grid, this imparts a constant kinetic energy on the ions as they enter the field-free flight tube. The ions will then separate according to their velocities, which will depend on their respective mass before reaching the detector (Hoffmann and Stroobant 2007). Briefly, lighter ions have shorter flight times than those of heavier ions (Castleberry *et al.*, 2008), this is illustrated below in Figure 1.23.

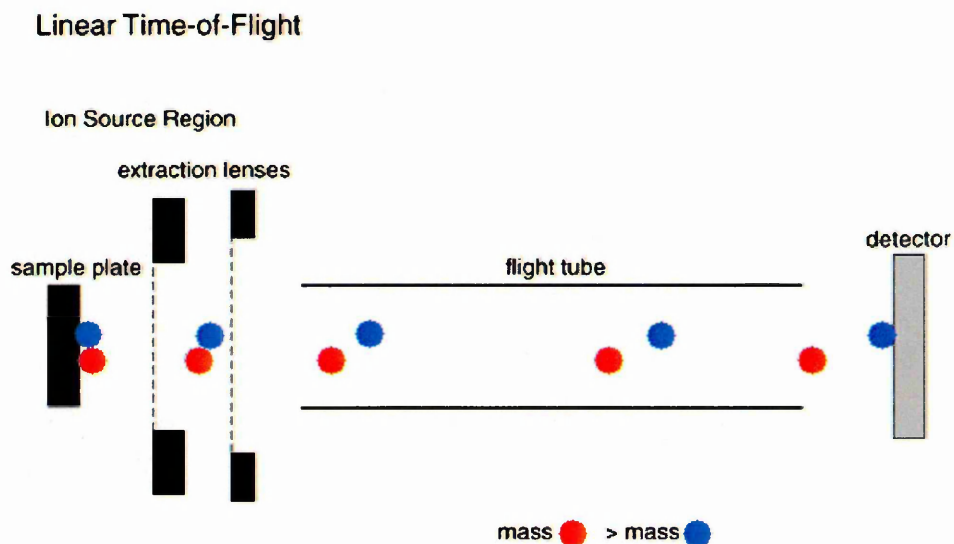


**Figure 1.23:** Schematic of a time-of-flight mass analyser operated in linear mode, ions are produced and accelerated by an applied potential (accelerating voltage) into the field-free flight tube where the ions separated based on their velocity. Lighter ions (blue dots) travel faster than larger ions (red dots) and therefore reach the detector first (Image adapted from Castleberry *et al.*, 2008).

### 1.5.1.2: Reflectron time-of-flight mode

Improvements in the mass resolution and reductions to the kinetic energy spread amongst ions with the same  $m/z$  value, can be achieved by using an ion mirror, or reflectron.

The reflectron was introduced by (Mamyrin *et al.*, 1973) and is composed of a series of ring electrodes that create an electric field by way of a linear voltage gradient. The principle behind reflectron mode is that ions with more kinetic energy will travel further into the reflectron than ions with lower kinetic energy. However because of this the ions will reach the detector at the same time (Hoffmann and Stroobant 2007). This is shown below in Figure 1.24.

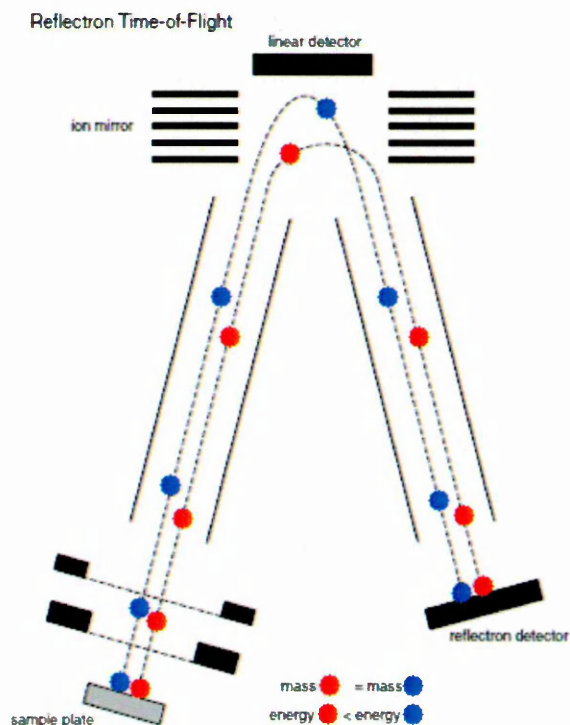


**Figure 1.24:** Schematic of a time-of-flight mass analyser operated in reflectron mode, ions (blue dots) with more kinetic energy and velocity will penetrate the reflectron more deeply than those with lower kinetic energy (red dots) resulting in the ions reaching the second detector at the same time (Image adapted from Castleberry *et al.*, 2008).

### 1.5.2. Quadrupole

The quadrupole component of the mass spectrometer acts as a mass filter, which consists of four parallel rods. These rods are connected in pairs, to which a radio frequency (RF) voltage along with a direct current (DC) voltage is applied.

The theory behind the quadrupole is that the ions are separated based on the stability of their trajectories in the oscillating electric fields that are applied to the rods (Hoffmann and Stroobant 2007). Basically a quadrupole works by allowing ions of a certain mass-to-charge ratio ( $m/z$ ) to travel between the metal rods and reach the detector for a given ratio of voltages, whilst other ions will collide with the metal rods and be neutralised, as illustrated in the schematic below in Figure 1.25.

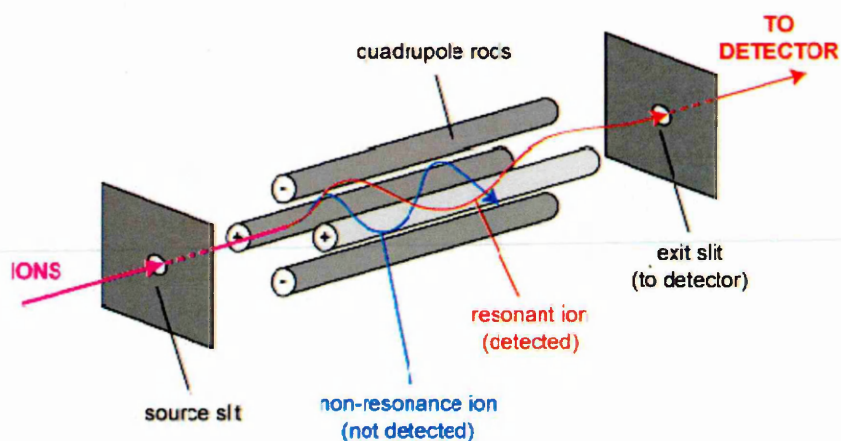


**Figure 1.25:** Schematic representation of a quadrupole mass analyser, the red ion is of the correct mass-to-charge and is able to traverse the quadrupole whilst the blue is of a different mass-to-charge and is neutralised on the metal rods ([www.chm.bris.ac.uk](http://www.chm.bris.ac.uk)).

## 1.6. Hybrid Mass Spectrometers

### 1.6.1: Quadrupole Time-of-Flight Mass Analyser

The majority of the MALDI-Mass Spectrometry data presented within this report was acquired using an Applied Biosystems/MDS Sciex Q-Star Pulsar-*i* hybrid quadrupole time-of-flight mass spectrometer fitted with an orthogonal MALDI ion source (Applied Biosystems, Foster City, California, USA). This instrument is an example of a “hybrid” mass spectrometer that combines two mass analysers (a quadrupole and time-of-flight) for improved sensitivity and mass resolution, this setup is illustrated below in Figure 1.26.

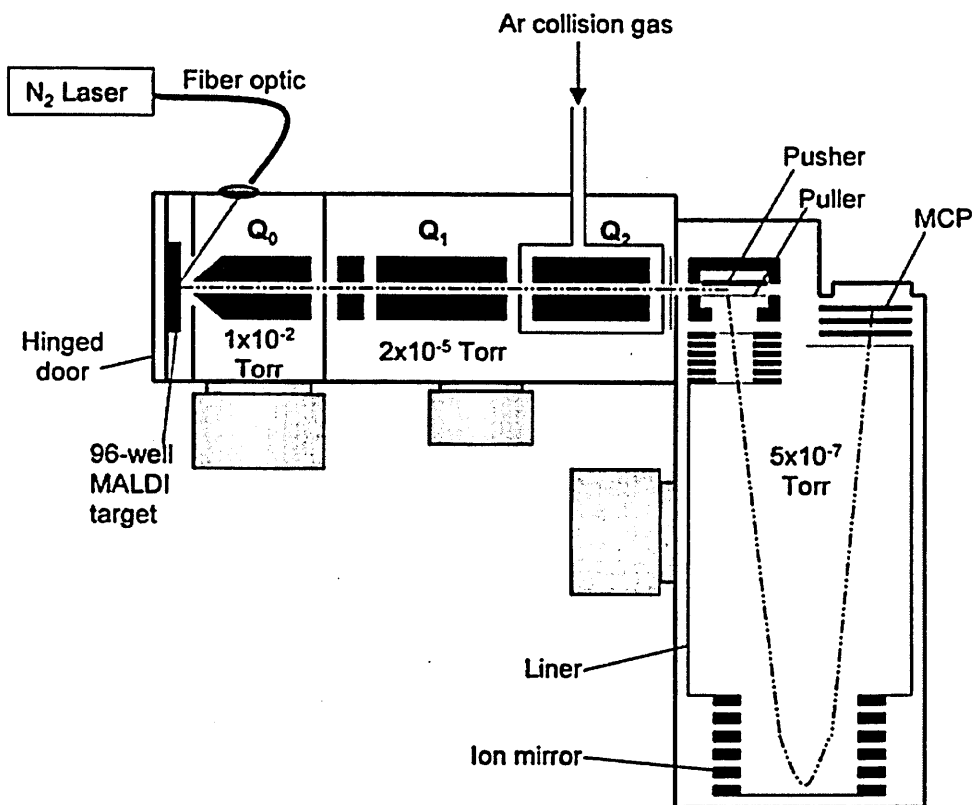


**Figure 1.26:** Schematic of a Hybrid Quadrupole Time-of-Flight with an orthogonal MALDI ion source (Baldwin et al., 2001).

The Q-Star Pulsar-*i* instrument consists of three quadrupoles ( $Q_0$ ,  $Q_1$  and  $Q_2$ ) followed by a reflectron time-of-flight mass analyser with orthogonal ion injection. Quadrupole ( $Q_0$ ) is operated in RF-only mode and is used to “cool” the

kinetic energy of the ions and focus them into quadrupole ( $Q_1$ ) (Chernushevich *et al.*, 2001).

For a conventional TOF-MS measurement, all three quadrupoles are both operated in RF-only mode and act as ion guides allowing the passage of ions with a wide range of  $m/z$  values, the ions are then focused into the orthogonal time-of-flight mass spectrometer for detection (Hoffmann and Stroobant 2007).

For TOF-MS/MS (product ion scan) measurements (the parameters are changed) the quadrupole ( $Q_1$ ) is used as a mass filter to select a particular ion of interest, by adjusting the offset voltages of the quadrupoles. The ions of interest are accelerated into the second quadrupole which acts as a quadrupole collision cell ( $Q_2$ ) where they collide with a neutral gas (argon or nitrogen) and undergo collision induced dissociation. The product ions are then focused into the orthogonal time-of-flight mass spectrometer and detected (Chernushevich *et al.*, 2001).

In order to achieve orthogonal ion injection into the time-of-flight mass analyser an ion modulator is used, the schematic of this device is shown below in Figure 1.27. The basic principle of this device is that ions are accelerated into the device from the last quadrupole ( $Q_2$ ) and then using a pulsed electric field the ions are pushed orthogonally to their original trajectory into the acceleration column. From here the ions enter the field-free drift space where the ions undergo time-of-flight separation, an ion mirror corrects the energy and spread of ions before they reach the detector (Hoffmann and Stroobant 2007, Chernushevich *et al.*, 2001).

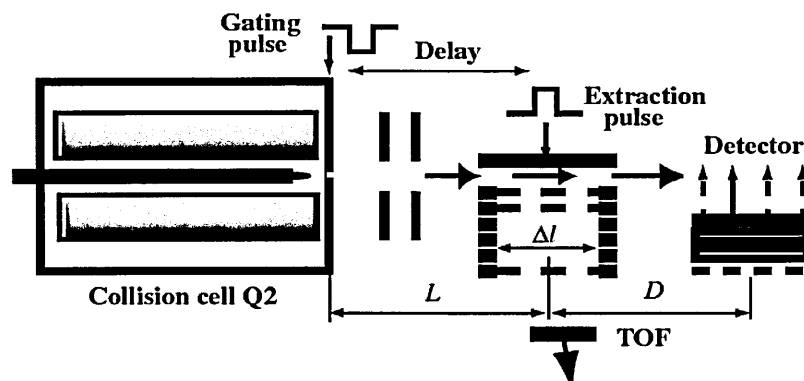


**Figure 1.27:** Schematic of the ion modulator of the Time-of-Flight mass analyser from a hybrid instrument (Chernushevich et al., 2001).

### 1.6.2. Tandem Time-of-Flight (TOF/TOF)

An example of a tandem time-of-flight (TOF/TOF) instrument and the one used to generate some of the data in this thesis is the Ultraflex series of mass spectrometers from Bruker Daltonics (Bruker, Bremen, Germany). The technology at the centre of this instrument is the LIFT cell that employs a potential lift to accelerate fragment ions.

This instrument is comprised of a short linear TOF analyser, a timed ion selector (TIS) to deliver ions into a collision cell, and a linear/reflector TOF analyser (Medzihradzsky *et al.*, 2000, Suckau *et al.*, 2003).

The schematic of the MALDI-LIFT-TOF/TOF mass spectrometer is shown below in Figure 1.28.

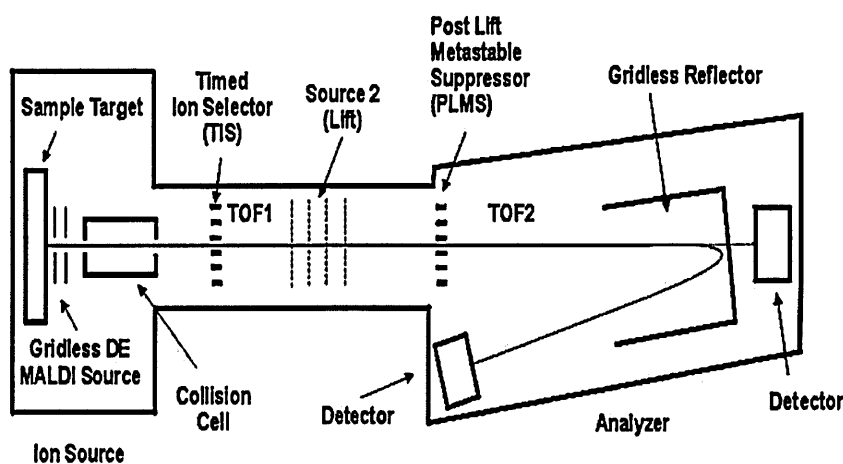


**Figure 1.28:** Schematic of the MALDI-LIFT-TOF/TOF mass spectrometer showing the MALDI ion source, the first TOF with timed ion selector, the LIFT and the second TOF with gridless reflector (Suckau *et al.*, 2003).

For MS/MS experiments the instrument works by operating the first TOF at low acceleration voltage (around 8 keV), the precursor ion of interest is selected using the time ion selector which delivers the precursor ion to a collision cell for fragmentation by collision induced dissociation (CID). The fragment ions are

then accelerated to around 20 keV using the LIFT cell into the second TOF which is a high resolving reflector TOF (Suckau *et al.*, 2003, Cotter *et al.*, 2007).

### 1.6.3. Quadrupole-Ion Mobility Separation-Time-of-Flight Mass Spectrometer

Ion mobility separation adds another dimension to mass spectrometric analysis, it separates ions based on their size/charge ratio in a drift tube containing a buffer gas under the influence of an electric field (Kanu *et al.*, 2008). Gas phase separation occurs due to the ions having differing collisional cross-sections and can separate isobaric species. The schematic of the MALDI HDMS SYNAPT G2 system is shown below in Figure 1.29.

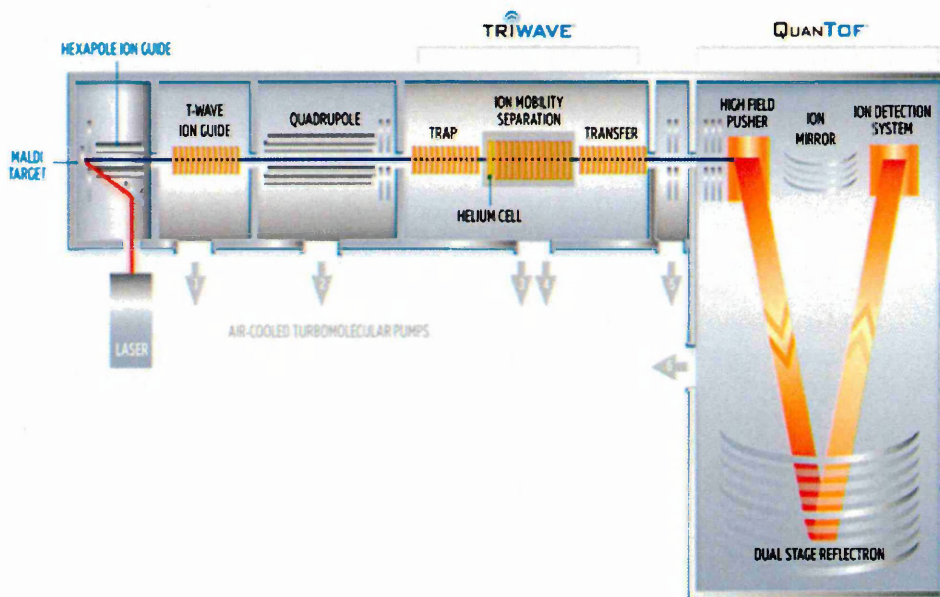


**Figure 1.29:** Schematic of the Waters MALDI HDMS SYNAPT G2 system, this instrument has a quadrupole orthogonal acceleration time-of-flight geometry and is equipped with an ion mobility separation device located between the quadrupole and the time-of-flight analysers. The “triwave” ion mobility separation device consists of three regions the trap, ion mobility separation and transfer regions (Waters Corporation, Manchester, UK).

The “Triwave” is the key technology at the centre of the SYNAPT HDMS system, it is comprised of three travelling wave enabled stacked ring ion guides (SRIGs). The trap cell is used to accumulate ions, which are released in packets into the ion mobility cell for mobility separation. Following this the mobility separated ions are transferred to the orthogonal acceleration time-of-flight analyser (Pringle *et al.*, 2007).

This technique has been employed in mass spectrometry imaging for the separation of ions from endogenous or matrix related isobaric species. One such application reported by (McLean *et al.*, 2007) utilised this technique for the separation of two spatially structured isobaric species in this case a peptide and a lipid resolved in a MALDI-IMS-MS imaging experiment (McLean *et al.*, 2007).

Another example reported by (Trim *et al.*, 2009) is the imaging of the distribution of the anticancer drug Vinblastine in whole body tissue sections of a rat. The MS and MS/MS imaging results obtained demonstrated the separation of Vinblastine from interfering isobaric species (e.g. lipids), resulting in a higher confidence in the data (Trim *et al.*, 2009).

New instruments that incorporate ion mobility separation technology have been developed. AB Sciex has introduced the SelexION™ an interchangeable ion mobility separation cell that can be fitted onto the AB Sciex 5500 and 6500 triple quadrupole or quadrupole ion trap mass spectrometers ([www.absciex.com](http://www.absciex.com)). Agilent Technologies have recently introduced the Agilent 6560 ion mobility Q-TOF LC-MS instrument that incorporates a drift tube based ion mobility cell ([www.chem.agilent.com](http://www.chem.agilent.com)).

## 1.7. Mass Spectrometry Imaging

### 1.7.1. Microprobe Imaging Mode

Microprobe mode is the most common approach to mass spectrometry imaging. It is accomplished by performing a programmable pattern of laser shots over the coated tissue section in an array to generate a full mass spectrum at each x, y co-ordinate (Khatib-Shahidi *et al.*, 2006). Once the entire tissue has been analysed imaging software is used to produce signal density maps of a selected molecular ion by plotting the x, y co-ordinates against the relative abundance and intensity of the selected m/z value (Reyzer *et al.*, 2007). The limitations of microprobe mode are that the achievable imaging resolution depends on the laser spot size and the acquisition time increases dramatically with increased resolution.

### 1.7.2. Microscope imaging mode

Microscope imaging mode was pioneered by Ron Heeren and co-workers at FOM Institute AMOLF (Amsterdam, The Netherlands). In microscope mode the sample is irradiated with a large diameter laser beam (~200  $\mu\text{m}$ ). The ions generated retain their spatial distribution until they reach a position sensitive detector (Altelaar *et al.*, 2007, Klerk *et al.*, 2009).

With this mode of acquisition the spatial resolution is determined by the quality of the ion optics and the resolving power of the detector, rather than the laser spot size (Luxembourg *et al.*, 2004).

Using this configuration a spatial resolution of 4  $\mu\text{m}$  has been achieved (Luxembourg *et al.*, 2004).

The advantages of the microscope mode are: the high spatial resolution is independent of the laser spot size and the amount of sampling points is reduced

thus reducing the acquisition time (Luxembourg *et al.*, 2004, Klerk *et al.*, 2009). However the ion optics and detection system required are more expensive and are only compatible with time-of-flight or magnetic sector analysers (Pol *et al.*, 2010).

A comparison between microprobe and microscope modes is illustrated in Figure 1.30.

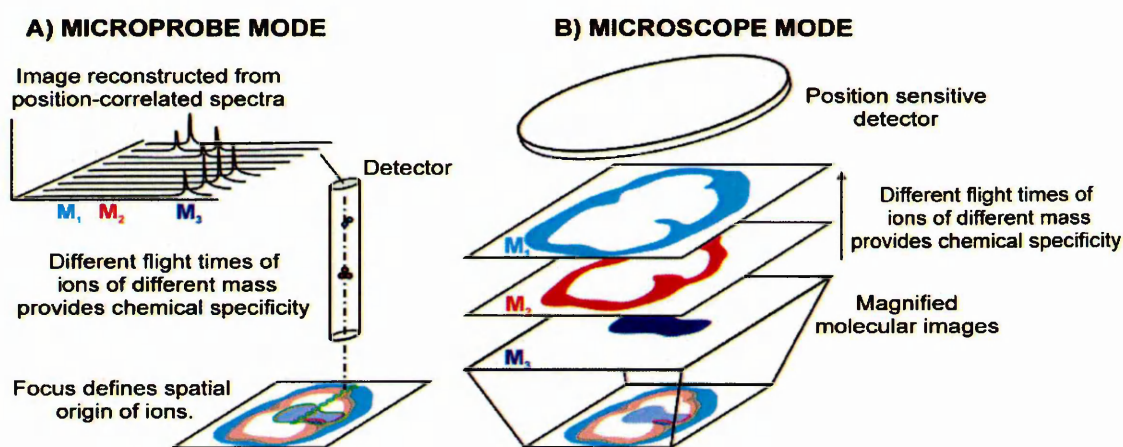


**Figure 1.30:** Schematics of the two approaches to mass spectrometry imaging. Microprobe mode A) collects mass spectra from an array of designated sampling positions to reconstruct an image after completion of the experiment. In microscope mode B) magnified images of ion distributions are directly acquired using a position sensitive detector (Luxembourg *et al.*, 2004).

### 1.7.3. Raster Imaging Mode

The majority of mass spectrometry images presented within this thesis were acquired in “raster” imaging mode developed by AB Sciex, this method of data acquisition is achieved by continuously firing the laser in rows across a sample as shown in Figure 1.31. In this acquisition method the generated data is placed into “bins” at selected intervals during the raster, these are based upon the selected spatial resolution and sampling speed (Trim *et al.*, 2010).

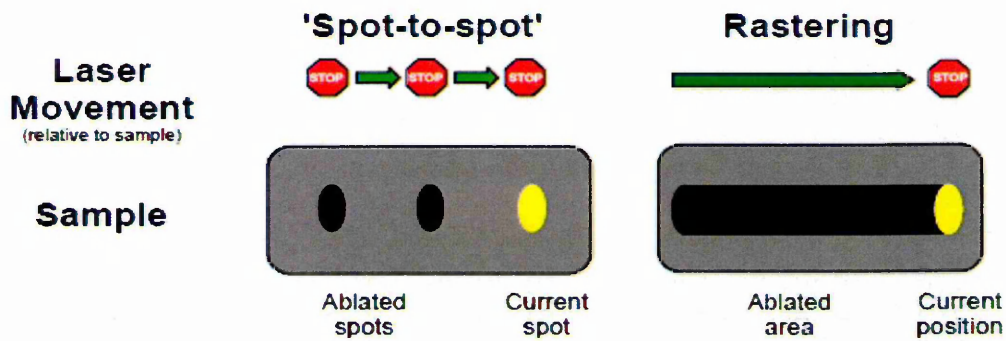


**Figure 1.31:** Diagram showing the conventional spot-to-spot (left) and the raster (right) acquisition modes (Simmons 2008).

For the conventional spot-to-spot method the main disadvantage is the acquisition time, which is increased with tissue size and image resolution, also the sensitivity is reduced by this method of acquisition because there are spaces between the laser shots that is not sampled. In contrast, the raster acquisition mode overcomes these disadvantages by decreasing the acquisition time without compromising the sensitivity and image resolution (Simmons 2008). Making this type of acquisition mode ideal for high throughput screening of multiple samples.

### 1.8. Matrix application/ deposition for MALDI Imaging

Matrix deposition is the most important step of the sample preparation procedure in a MALDI imaging experiment. This requires the matrix solution to be applied over the entire tissue sample prior to analysis. The matrix solution consists of the chosen matrix in a mixture of organic solvent (e.g. methanol or acetonitrile) and water with the addition of a strong acid (such as trifluoroacetic acid). The purpose of the organic solvent is to extract the analyte from the tissue section and evaporate, the analyte is then incorporated into the matrix crystals that form on the sample surface. The solvent to water ratio effects the formation and size of the matrix crystals, a higher solvent ratio leads to faster evaporation and produces smaller crystals. Several methods and instruments have been used for matrix application, which are discussed in the following section.

### 1.8.1. Airbrush

The use of a pneumatically assisted airbrush for matrix deposition is the simplest and cheapest method available. However, the use of this method requires skilful operation. For reproducible matrix application there are many parameters that need to be considered such as the distance and angle the airbrush is held from the sample, the amount of matrix applied per cycle, the number of cycles applied, the temperature and the humidity.

Probably the most important aspect to consider is the amount of matrix applied onto the sample, it is crucial that the sample is sufficiently wet to allow analyte extraction but not to over wet the sample, which can lead to analyte migration (Schwartz *et al.*, 2003).

An example of the kind of airbrush used for manual matrix deposition is shown below in Figure 1.32.

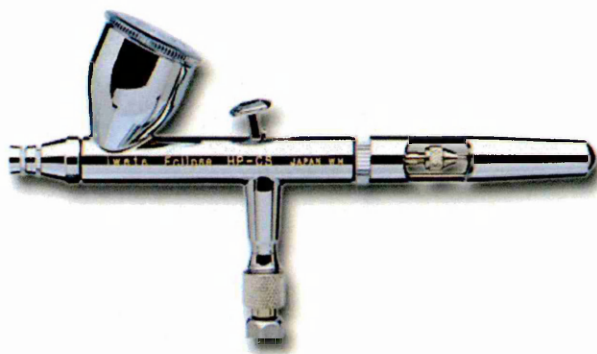


**Figure 1.32:** Image of the Iwata Eclipse HP-CS airbrush used for manual matrix deposition ([www.iwata-medea.com](http://www.iwata-medea.com)).

The advantages of using the airbrush application method are that it is fast, simple, cheap and with skilful operation can produce a homogenous matrix coverage. However the disadvantages are that there are limited environmental controls, the quality of the preparation differs from person to person and the droplet size is inconsistent (Kaletas *et al.*, 2009). Whilst this method may be

employed for matrix deposition, most laboratories have opted to use an automated matrix deposition device as they provide a more reproducible and homogenous matrix coating.

### 1.8.2. Suncollect

The Suncollect MALDI spotter (Sunchrom, Friedrichsdorf, Germany) is used to precisely spot HPLC fractions onto MALDI target plates or can be operated as an automated pneumatically assisted matrix sprayer.

This device has also been used to deposit enzymes such trypsin onto tissue samples for the purpose of in-situ protein digestion (Djidja *et al.*, 2010, Cole *et al.*, 2011). The Sunchrom Suncollect automated matrix sprayer is shown below in Figure 1.33.



**Figure 1.33:** Image of the Sunchrom Suncollect automated matrix sprayer (Image from [www.sunchrom.de](http://www.sunchrom.de)).

The advantages of the Suncollect automated matrix sprayer are that it produces an homogeneous matrix coating, it is automated and thus suitable for large areas and environmental factors (such as humidity and temperature) can be

controlled. However the disadvantages are the device is prone to clogging and the droplet size is not constant (Kaletas *et al.*, 2009).

### 1.8.3. ImagePrep

The Bruker ImagePrep matrix deposition device (Bruker Daltonics, Bremen, Germany) creates a matrix aerosol by vibrational vaporisation, which is gently deposited onto the sample (Schuerenberg *et al.*, 2007). The device has an optical sensor that monitors the scattered light from the crystalline matrix layer on the sample enabling control of all the relevant parameters (such as the matrix thickness, wetness and drying rate) in real time. The Imageprep matrix deposition device is shown below in Figure 1.34.

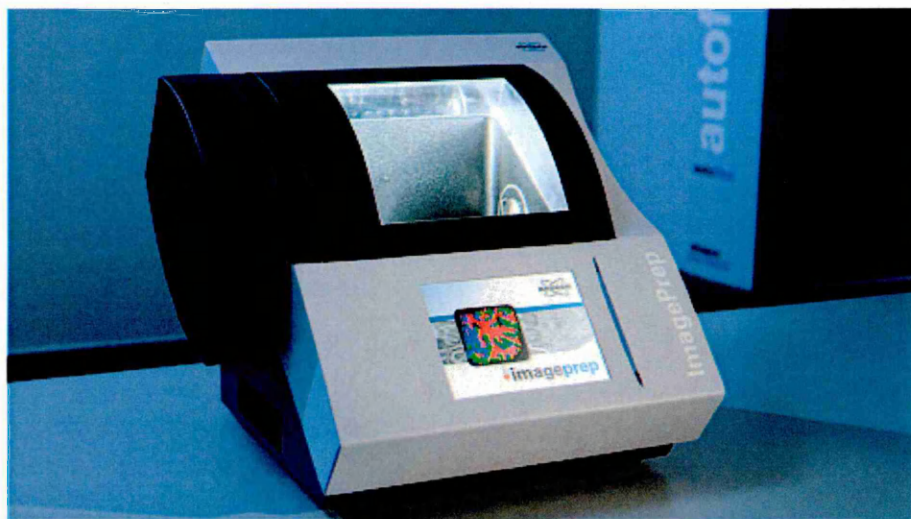


**Figure 1.34:** Image of the Bruker ImagePrep<sup>TM</sup> matrix deposition device (Image from [www.bdal.com](http://www.bdal.com)).

The advantages of the imageprep matrix deposition device are that the experimental conditions can be optimised and controlled, the device is automated and produces homogeneous matrix coverage. However the disadvantages are the device is slow, the spray foil is prone to clogging and it is expensive (Kaletas *et al.*, 2009).

#### 1.8.4. Portrait

The Labcyte Portrait® 630 Reagent Multi-Spotter (Labcyte Inc. California, USA) uses ultra-sound based acoustic droplet ejection (ADE) to deposit the matrix onto the sample in an array consisting of droplets of approximately 170 pl. The Portrait 630 reagent multi-spotter is a commercial version based on the acoustic spotter prototype device developed by (Aerni *et al.*, 2006).

A piezoelectric transducer converts radio frequency power into ultrasonic energy, which is then transmitted through the reagent reservoir causing the fluid to form a droplet that travels upwards onto the inverted sample above. The fluid is kept on the sample by surface tension. The portrait 630 reagent multi-spotter is shown below in Figure 1.35.

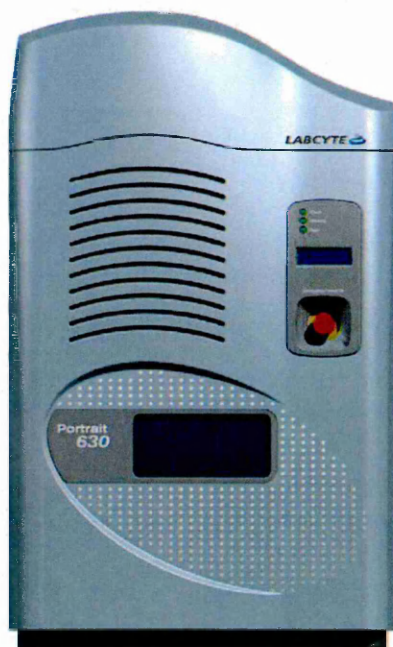


**Figure 1.35:** Image of the Labcyte Portrait® 630 Reagent Multi-Spotter instrument (Image from [www.labcyte.com](http://www.labcyte.com)).

The advantages of the portrait 630 reagent multi-spotter are that it produces uniform droplets with precise placement, it is automated and the absence of nozzles means it does not clog and has good reproducibility. However the

disadvantages are the instrument is slow and expensive and applies the matrix as droplets and the distance between them defines the spatial resolution (Kaletas *et al.*, 2009).

#### 1.8.5. Sublimation

Sublimation was introduced as a matrix deposition method by (Hankin *et al.*, 2007). In this study the sublimation method was used to apply the common MALDI matrix DHB onto mouse brain tissue sections, this enabled high spatial resolution images of phospholipids. The sublimation method was also used to deposit DHB onto a phospholipid standard, the results showed an improved signal intensity in comparison to the electrospray matrix deposition method.

The method employed by (Hankin *et al.*, 2007) involves attaching the sample to a condenser (maintained at 15°C) with double sided thermal conductive tape facing solid matrix powder. The matrix is then slowly heated to 120°C under low pressure (0.05 Torr) for 15-20 minutes, the matrix then sublimates and condenses on the sample surface. The equipment setup from matrix sublimation is shown in Figure 1.36.

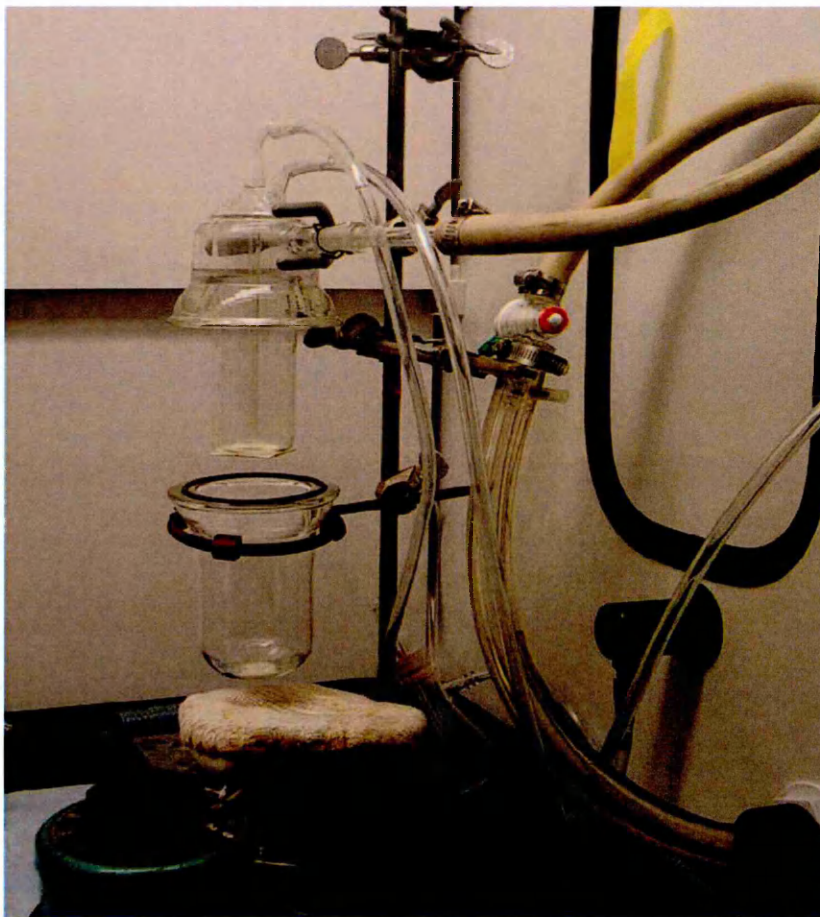


**Figure 1.36:** Image of sublimation equipment used to apply the matrix onto tissue samples. The image shows the tissue sample on a MALDI plate mounted to the underside of the condenser and the matrix powder in the bottom part of the apparatus (Hankin *et al.*, 2007).

Recently sublimation has been used to evaluate the use existing and novel matrices for high spatial resolution imaging of lipids in mouse brain and whole body fish tissue sections. In this study the matrix 1,5-diaminonaphthalene (DAN) gave the best results following sublimation (Thomas *et al.*, 2012).

The main advantage of sublimation deposition in comparison to the other matrix application techniques is it is a solvent free method and as a result eliminates the possibility of analyte diffusion (Hankin *et al.*, 2007, Murphy *et al.*, 2011). However there is limited analyte-matrix interaction and at present this method has only applied to lipids (Kaletas *et al.*, 2009).

The application of the sublimation matrix deposition method to proteins and peptides requires re-wetting of the surface to enable extraction and recrystallisation of analytes (Yang and Caprioli 2011).

#### 1.8.6. ChIP chemical inkjet printer

The ChIP-1000 chemical inkjet printer (Shimadzu Corporation, Tokyo, Japan) is a piezoelectric-based chemical ink-jet printer. The instrument uses piezo printing heads and nozzles that do not touch the sample surface, to deposit approximately 100 pl of the matrix onto the sample that dries to form a 100-250  $\mu\text{m}$  diameter spot. The ChIP-1000 chemical inkjet printer is shown below in Figure 1.38.



**Figure 1.37:** Image of the Shimadzu ChIP-1000 chemical inkjet printer (Image from [www.ssi.shimadzu.com](http://www.ssi.shimadzu.com)).

The advantages of the ChIP-1000 chemical inkjet printer are that it produces uniform droplets with precise placement which minimises cross-contamination, it is automated and has good reproducibility. However the disadvantages are

the instrument is slow, the nozzle tip is prone to clogging when concentrated matrix solutions are used and it is expensive (Kaletas *et al.*, 2009).

The adaptation of a desktop inkjet printer into an automated matrix deposition device was reported by (Baluya *et al.*, 2007). The desktop inkjet printer used had a six channel piezoelectric head that could deliver 3  $\mu$ l droplets of matrix onto a tissue section. A comparison of this device with other matrix deposition methods such as electrospray and airbrush methods showed that better quality and reproducible images could be obtained.

#### 1.8.7. HTX TM-Sprayer

The HTX TM-Sprayer (HTX Technologies, Carrboro, NC, USA) is another example of an automated matrix sprayer. It uses a heated spray nozzle to produce an aerosol of small droplets (20  $\mu$ m), the heated and pressurised matrix solution is able to penetrate further into the tissue sample to facilitate better analyte extraction and co-crystallisation whilst minimising delocalisation. The instrument also uses nitrogen to control the rate of solvent evaporation to prevent the creation of large matrix crystals. The HTX TM-Sprayer is shown below in Figure 1.39.



**Figure 1.38:** Image of the HTX TM-Sprayer (Image from [www.htximaging.com](http://www.htximaging.com)).

Other advantages of this instrument are it is capable of high flow rates (200  $\mu$ l/minute), it is fast (10-20 minutes per plate), produces a homogeneous and reproducible matrix coating and the stage is capable of holding up to 10 glass slides making it ideal for high throughput preparation.

### 1.9. Scope of this thesis

The main aim of the work reported in this thesis was the development of MALDI-MSI methods for monitoring the distribution of respiratory compounds in rodent lungs following inhaled delivery. In addition, developments to MALDI-MSI methodology and sample preparation strategies were also assessed with the aim of obtaining further information and enhancements to the field of MALDI-MSI.

**Chapter 2** presents the development and application of a method utilising hydrazine based reagents for the derivatisation of a range of glucocorticoids, in an attempt to improve their mass spectral ionisation efficiency and thus detection both in-solution and on-tissue.

**Chapter 3** describes the process of determining the feasibility of analysing a range of respiratory compounds by MALDI-MSI. The distribution of a selected respiratory compound was monitored throughout the lungs following inhaled delivery by MALDI-MSI. A comparison of the data obtained from the analysis of samples on different instruments is also presented.

**Chapter 4** evaluates the current methods for generating quantitative information from mass spectrometry images, the advantages and disadvantages of each method is discussed. Also presented is a novel method for the preparation of standards for the quantitation of drugs in tissue sections by MALDI-MSI.

**Chapter 5** introduces methodology to determine the three-dimensional distribution of endogenous species throughout the lungs by MALDI-MSI. The use of freely available software to produce a 3D reconstruction of a series of MALDI-MS images obtained through the sample is also presented.

**Chapter 6** summarises the work performed to generate this thesis and makes some conclusions along with recommendations for further studies.

## 1.10. References

AERNI, H.R., CORNETT, D.S. and CAPRIOLI, R.M., 2006. Automated acoustic matrix deposition for MALDI sample preparation. *Analytical Chemistry*, **78**(3), 827-834.

ALTELAAR, A.F.M., LUXEMBOURG, S.L., MCDONNELL, L.A., PIERSMA, S.R. and HEEREN, R.M., 2007. Imaging mass spectrometry at cellular length scales. *Nature Protocols*, **2**(5), 1185-1196.

ALTELAAR, A.F.M., TABAN, I.M., MCDONNELL, L.A., VERHAERT, P.D.E.M., DE LANGE, R.P.J., ADAN, R.A.H., MOOI, W.J., HEEREN, R.M.A. and PIERSMA, S.R., 2007. High-resolution MALDI imaging mass spectrometry allows localization of peptide distributions at cellular length scales in pituitary tissue sections. *International Journal of Mass Spectrometry*, **260**(2-3), 203-211.

ANDERSON, G., LINDEN, A. and RABE, K., 1994. Why are long-acting beta-adrenoceptor agonists long-acting? *European Respiratory Journal*, **7**(3), 569-578.

BAKER, E. and LAI, D., 2008. *Respiratory medicine*. Oxford: Wiley-Blackwell.

BALDWIN, M.A., MEDZIHRADESKY, K.F., LOCK, C.M., FISHER, B., SETTINERI, T.A. and BURLINGAME, A.L., 2001. Matrix assisted laser desorption/ionization coupled with quadrupole/orthogonal acceleration time-of-flight mass spectrometry for protein discovery, identification, and structural analysis. *Analytical Chemistry*, **73**(8), 1707-1725.

BALDWIN, M.A., 2005. Mass spectrometers for the analysis of biomolecules. *Methods in Enzymology*. Academic Press, 3-48.

BALUYA, D.L., GARRETT, T.J. and YOST, R.A., 2007. Automated MALDI matrix deposition method with inkjet printing for imaging mass spectrometry. *Analytical Chemistry*, **79**(17), 6862-6867.

BARNES, P.J., 1998. Anti-inflammatory actions of glucocorticoids: molecular mechanisms. *Clinical Science*, **94**(6), 557-572.

BARNES, P.J. and HANSEL, T.T., 2004a. Prospects for new drugs for chronic obstructive pulmonary disease. *The Lancet*, **364**(9438), 985-996.

BARNES, P.J., 2004b. Distribution of receptor targets in the lung. *Proceedings of the American Thoracic Society*, **1**(4), 345-351.

BARNES, P.J., 2004c. New drugs for asthma. *Nature Reviews Drug Discovery*, **3**(10), 831-844.

BARNES, P.J., 2004d. The role of anticholinergics in chronic obstructive pulmonary disease. *American Journal of Medicine Supplement*, **117**(12, supplement 1), 24-32.

BARNES, P.J., 2010. Mechanisms and resistance in glucocorticoid control of inflammation. *The Journal of Steroid Biochemistry and Molecular Biology*, **120**(2-3), 76-85.

BEAVIS, R.C. and CHAIT, B.T., 1989. Matrix-assisted laser-desorption mass spectrometry using 355 nm radiation. *Rapid Communications in Mass Spectrometry*, **3**(12), 432-435.

BEAVIS, R.C., CHAUDHARY, T. and CHAIT, B.T., 1992.  $\alpha$ -Cyano-4-hydroxycinnamic acid as a matrix for matrix assisted laser desorption mass spectrometry. *Organic Mass Spectrometry*, **27**(2), 156-158.

BOURKE, S.J., 2003. *Lecture notes on respiratory medicine*. 6th edn. Oxford: Blackwell.

BRAMAN, S.S., 2006. The global burden of asthma. *CHEST Journal*, **130**(1 supplement), 4S-12S.

CALVERLEY, P.M.A., 2000. Inhaled corticosteroids are beneficial in chronic obstructive pulmonary disease. *American Journal of Respiratory and Critical Care Medicine*, **161**(2), 341-342.

CARAMORI, G. and ADCOCK, I., 2003. Pharmacology of airway inflammation in asthma and COPD. *Pulmonary Pharmacology and Therapeutics*, **16**(5), 247-277.

CAPRIOLI, R.M., FARMER, T.B. and GILE, J., 1997. Molecular imaging of biological samples: Localization of peptides and proteins using MALDI-TOF MS. *Analytical Chemistry*, **69**(23), 4751-4760.

CARADO, A., PASSARELLI, M.K., KOZOLE, J., WINGATE, J.E., WINOGRAD, N. and LOBODA, A.V., 2008. C60 secondary ion mass spectrometry with a hybrid-quadrupole orthogonal time-of-flight mass spectrometer. *Analytical Chemistry*, **80**(21), 7921-7929.

CASTLEBERRY, C.M., CHOU, C. and LIMBACH, P.A., 2001. Matrix-assisted laser desorption/ionization time-of-flight mass spectrometry of oligonucleotides. *Current Protocols in Nucleic Acid Chemistry*. John Wiley & Sons, Inc.

CHERNUSHEVICH, I.V., LOBODA, A.V. and THOMSON, B.A., 2001. An introduction to quadrupole-time-of-flight mass spectrometry. *Journal of Mass Spectrometry*, **36**(8), 849-865.

CLARK, T.J.H., GODFREY, S. and LEE, T.H., *Asthma*. 3 edn. Chapman & Hall Medical.

COLE, L.M., DJIDJA, M., BLUFF, J., CLAUDE, E., CAROLAN, V.A., PALEY, M., TOZER, G.M. and CLENCH, M.R., 2011. Investigation of protein induction in tumour vascular targeted strategies by MALDI MSI. *Methods*, **54**(4), 442-453.

COSTA, A.B. and GRAHAM COOKS, R., 2008. Simulated splashes: Elucidating the mechanism of desorption electrospray ionization mass spectrometry. *Chemical Physics Letters*, **464**(1-3), 1-8.

COTTER, R.J., GRIFFITH, W. and JELINEK, C., 2007. Tandem time-of-flight (TOF/TOF) mass spectrometry and the curved-field reflectron. *Journal of Chromatography B*, **855**(1), 2-13.

DE HOFFMANN, E. and STROOBANT, V., 2007. *Mass spectrometry: principles and applications*. 3 edn. Chichester: Wiley.

DJIDJA, M., CLAUDE, E., SNEL, M.F., FRANCESE, S., SCRIVEN, P., CAROLAN, V. and CLENCH, M.R., 2010. Novel molecular tumour classification using MALDI-mass spectrometry imaging of tissue micro-array. *Analytical and Bioanalytical Chemistry*, **397**(2), 587-601.

DREISEWERD, K., 2003. The desorption process in MALDI. *Chemical reviews*, **103**(2), 395-426.

EL-ANEED, A., COHEN, A. and BANOUB, J., 2009. Mass spectrometry, review of the basics: Electrospray, MALDI, and commonly used mass analyzers. *Applied Spectroscopy Reviews*, **44**(3), 210-230.

GASKELL, S.J., 1997. Electrospray: Principles and practice. *Journal of Mass Spectrometry*, **32**(7), 677-688.

GUO, Z. and HE, L., 2007. A binary matrix for background suppression in MALDI-MS of small molecules. *Analytical and Bioanalytical Chemistry*, **387**(5), 1939-1944.

GUPTA, R., JINDAL, D.P. and KUMAR, G., 2004. Corticosteroids: the mainstay in asthma therapy. *Bioorganic & Medicinal Chemistry*, **12**(24), 6331-6342.

HANKIN, J.A., BARKLEY, R.M. and MURPHY, R.C., 2007. Sublimation as a method of matrix application for mass spectrometric imaging. *Journal of the American Society for Mass Spectrometry*, **18**(9), 1646-1652.

HANSEL, T.T. and BARNES, P.J., 2004. *An atlas of chronic obstructive pulmonary disease, COPD*. Boca Raton, Fla. ; London: Parthenon Pub. Group.

<http://proteabio.com/LAESI>

JOHNSON, M., 2001. Beta2-adrenoceptors: mechanisms of action of beta2-agonists. *Paediatric Respiratory Reviews*, **2**(1), 57-62.

JOHNSON, E.N. and DRUEY, K.M., 2002. Heterotrimeric G protein signaling: Role in asthma and allergic inflammation. *Journal of Allergy and Clinical Immunology*, **109**(4), 592-602.

KALETAS, B.K., VAN DER WIEL, I.M., STAUBER, J., DEKKER, L.J., GUZEL, C., KROS, J.M., LUIDER, T.M. and HEEREN, R.M.A., 2009. Sample preparation issues for tissue imaging by imaging MS. *Proteomics*, **9**(10), 2622-2633.

KANU, A.B., DWIVEDI, P., TAM, M., MATZ, L. and HILL, H.H., 2008. Ion mobility?mass spectrometry. *Journal of Mass Spectrometry*, **43**(1), 1-22.

KARAS, M., BACHMANN, D. and HILLENKAMP, F., 1985. Influence of the Wavelength in High-Irradiance Ultraviolet-Laser Desorption Mass-Spectrometry of Organic-Molecules. *Analytical Chemistry*, **57**(14), 2935-2939.

KARAS, M., GLÜCKMANN, M. and SCHÄFER, J., 2000. Ionization in matrix-assisted laser desorption/ionization: singly charged molecular ions are the lucky survivors. *Journal of Mass Spectrometry*, **35**(1), 1-12.

KEBARLE, P., 2000. A brief overview of the present status of the mechanisms involved in electrospray mass spectrometry. *Journal of Mass Spectrometry*, **35**(7), 804-817.

KERTESZ, V., VAN BERKEL, G.J., VAVREK, M., KOEPLINGER, K.A., SCHNEIDER, B.B. and COVEY, T.R., 2008. Comparison of drug distribution images from whole-body thin tissue sections obtained using desorption electrospray ionization tandem mass spectrometry and autoradiography. *Analytical Chemistry*, **80**(13), 5168-5177.

KERTESZ, V. and VAN BERKEL, G.J., 2008. Improved imaging resolution in desorption electrospray ionization-mass spectrometry. *Rapid Communications in Mass Spectrometry*, **22**(17), 2639-2644.

KHATIB-SHAHIDI, S., ANDERSSON, M., HERMAN, J.L., GILLESPIE, T.A. and CAPRIOLI, R.M., 2006. Direct molecular analysis of whole-body animal tissue sections by imaging MALDI mass spectrometry. *Analytical Chemistry*, **78**(18), 6448-6456.

KLERK, L.A., ALTELAAR, A.F.M., FROESCH, M., MCDONNELL, L.A. and HEEREN, R.M.A., 2009. Fast and automated large-area imaging MALDI mass spectrometry in microprobe and microscope mode. *International Journal of Mass Spectrometry*, **285**(1–2), 19-25.

KNOCHENMUSS, R. and ZENOBI, R., 2003. MALDI ionization: The role of in-plume processes. *Chemical reviews*, **103**(2), 441-452.

KNOCHENMUSS, R., 2006. Ion formation mechanisms in UV-MALDI. *The Analyst*, **131**(9), 966-986.

LUXEMBOURG, S.L., MIZE, T.H., MCDONNELL, L.A. and HEEREN, R.M.A., 2004. High-spatial resolution mass spectrometric imaging of peptide and protein distributions on a surface. *Analytical Chemistry*, **76**(18), 5339-5344.

MAMYRIN, B.A., KARATAEV, V.I., SHMIKK, D.V. and ZAGULIN, V.A., 1973. The mass-reflectron, a new nonmagnetic time-of-flight mass spectrometer with high resolution *Soviet Physics - JETP*, **37**(1), 45.

MASKELL, N. and MILLAR, A., 2009. *Oxford desk reference. Respiratory medicine*. Oxford: Oxford University Press.

MASOLI, M., FABIAN, D., HOLT, S., BEASLEY, R. and GLOBAL INITIATIVE FOR ASTHMA (GINA) PROGRAM, 2004. The global burden of asthma: executive summary of the GINA Dissemination Committee Report. *Allergy*, **59**(5), 469-478.

MCDONNELL, L.A., PIERSMA, S.R., ALTELAAR, A.F.M., MIZE, T.H., LUXEMBOURG, S.L., VERHAERT, P.D.E.M., VAN MINNEN, J. and HEEREN,

R.M.A., 2005. Subcellular imaging mass spectrometry of brain tissue. *Journal of Mass Spectrometry*, **40**(2), 160-168.

MCLEAN, J.A., RIDENOUR, W.B. and CAPRIOLI, R.M., 2007. Profiling and imaging of tissues by imaging ion mobility-mass spectrometry. *Journal of Mass Spectrometry*, **42**(8), 1099-1105.

MCPHAIL, D.S., 2006. Applications of secondary ion mass spectrometry (SIMS) in materials science. *Journal of Materials Science*, **41**(3), 873-903.

MEDZIHRADESKY, K.F., CAMPBELL, J.M., BALDWIN, M.A., FALICK, A.M., JUHASZ, P., VESTAL, M.L. and BURLINGAME, A.L., 2000. The characteristics of peptide collision-induced dissociation using a high-performance MALDI-TOF/TOF tandem mass spectrometer. *Analytical Chemistry*, **72**(3), 552-558.

MURPHY, R.C., HANKIN, J.A., BARKLEY, R.M. and BERRY, K.A.Z., 2011. MALDI imaging of lipids after matrix sublimation/deposition. *Biochimica Et Biophysica Acta-Molecular and Cell Biology of Lipids*, **1811**(11), 970-975.

NEMES, P. and VERTES, A., 2007. laser ablation electrospray ionization for atmospheric pressure, in vivo, and imaging mass spectrometry. *Analytical Chemistry*, **79**(21), 8098-8106.

NEMES, P., BARTON, A.A. and VERTES, A., 2009. three-dimensional imaging of metabolites in tissues under ambient conditions by laser ablation electrospray ionization mass spectrometry. *Analytical Chemistry*, **81**(16), 6668-6675.

PAGE, C.P. and BARNES, P.J., 2004. *Pharmacology and therapeutics of asthma and COPD*, Berlin, London, Springer.

PELAIA, G., VATRELLA, A., CUDA, G., MASELLI, R. and MARSICO, S.A., 2003. Molecular mechanisms of corticosteroid actions in chronic inflammatory airway diseases. *Life Sciences*, **72**(14), 1549-1561.

POL, J., STROHALM, M., HAVLICEK, V. and VOLNY, M., 2010. Molecular mass spectrometry imaging in biomedical and life science research. *Histochemistry and cell biology*, **134**(5), 423-443.

PRIDEAUX, B. and STOECKLI, M., 2012. Mass spectrometry imaging for drug distribution studies. *Journal of Proteomics*, **75**(16), 4999-5013.

PRINGLE, S.D., GILES, K., WILDGOOSE, J.L., WILLIAMS, J.P., SLADE, S.E., THALASSINOS, K., BATEMAN, R.H., BOWERS, M.T. and SCRIVENS, J.H., 2007. An investigation of the mobility separation of some peptide and protein ions using a new hybrid quadrupole/travelling wave IMS/oa-ToF instrument. *International Journal of Mass Spectrometry*, **261**(1), 1-12.

REYZER, M., HSIEH, Y., NG, K., KORFMACHER, W. and CAPRIOLI, R., 2003. Direct analysis of drug candidates in tissue by matrix-assisted laser desorption/ionization mass spectrometry. *Journal of Mass Spectrometry*, **38**(10), 1081-1092.

SCHUERENBERG, M., LUEBBERT, C., DEININGER, S., KETTERLINUS, R. and SUCKAU, D., 2007. MALDI tissue imaging: mass spectrometric localization of biomarkers in tissue slices. *Nature Methods*, **4**(5), iii-iv.

SCHWARTZ, S., REYZER, M. and CAPRIOLI, R., 2003. Direct tissue analysis using matrix-assisted laser desorption/ionization mass spectrometry: practical aspects of sample preparation. *Journal of Mass Spectrometry*, **38**(7), 699-708.

SEARS, M.R. and LÖTVALL, J., 2005. Past, present and future—adrenoceptor agonists in asthma management. *Respiratory medicine*, **99**(2), 152-170.

SHRESTHA, B., NEMES, P., NAZARIAN, J., HATHOUT, Y., HOFFMAN, E.P. and VERTES, A., 2010. Direct analysis of lipids and small metabolites in mouse brain tissue by AP IR-MALDI and reactive LAESI mass spectrometry. *Analyst*, **135**(4), 751-758.

SMITH, D.F., ROBINSON, E.W., TOLMACHEV, A.V., HEEREN, R.M.A. and PASA-TOLIC, L., 2011. C60 Secondary Ion Fourier Transform Ion Cyclotron Resonance Mass Spectrometry. *Analytical Chemistry*, **83**(24), 9552-9556.

SIMMONS, D.A., 2008. Improved MALDI-MS imaging performance using continuous laser rastering. *AB technical note*.

SPENGLER, B., HUBERT, M. and KAUFMANN, R., 1994. MALDI ion imaging and biological ion imaging with a new scanning UV-laser microprobe. *42<sup>nd</sup> American Society for Mass Spectrometry Conference*, Chicago, IL, USA.

STEPHENS W. E., 1946. A pulsed mass spectrometer with time dispersion. *Physical reviews*, **69** (11-12), 691.

STRUPAT, K., KARAS, M. and HILLENKAMP, F., 1991. 2,5-Dihydroxybenzoic acid: a new matrix for laser desorption—ionization mass spectrometry. *International Journal of Mass Spectrometry and Ion Processes*, **111**(0), 89-102.

SUCKAU, D., RESEMANN, A., SCHUERENBERG, M., HUFNAGEL, P., FRANZEN, J. and HOLLE, A., 2003. A novel MALDI LIFT-TOF/TOF mass spectrometer for proteomics. *Analytical and Bioanalytical Chemistry*, **376**(7), 952-965.

TAKÁTS, Z., WISEMAN, J.M., GOLOGAN, B. and COOKS, R.G., 2004. Mass spectrometry sampling under ambient conditions with desorption electrospray ionization. *Science*, **306**(5695), 471-473.

TANAKA, K., WAKI, H., IDO, Y., AKITA, S., YOSHIDA, Y., YOSHIDA, T. and MATSUO, T., 1988. Protein and polymer analyses up to  $m/z$  100 000 by laser ionization time-of-flight mass spectrometry. *Rapid Communications in Mass Spectrometry*, **2**(8), 151-153.

THOMAS, A., CHARBONNEAU, J.L., FOURNAISE, E. and CHAURAND, P., 2012. Sublimation of new matrix candidates for high spatial resolution imaging mass spectrometry of lipids: Enhanced information in both positive and negative polarities after 1,5-diaminonaphthalene deposition. *Analytical Chemistry*, **84**(4), 2048-2054.

TRIM, P.J., HENSON, C.M., AVERY, J.L., MCEWEN, A., SNEL, M.F., CLAUDE, E., MARSHALL, P.S., WEST, A., PRINCIVALLE, A.P. and CLENCH, M.R., 2008. Matrix-assisted laser desorption/ionization-ion mobility separation-mass spectrometry imaging of vinblastine in whole body tissue sections. *Analytical Chemistry*, **80**(22), 8628-8634.

TRIM, P.J., DJIDJA, M., ATKINSON, S.J., OAKES, K., COLE, L.M., ANDERSON, D.M.G., HART, P.J., FRANCESE, S. and CLENCH, M.R., 2010. Introduction of a 20 kHz Nd:YVO<sub>4</sub> laser into a hybrid quadrupole time-of-flight mass spectrometer for MALDI-MS imaging. *Analytical and Bioanalytical Chemistry*, **397**(8), 3409-3419.

UMLAND, S.P., SCHLEIMER, R.P. and JOHNSTON, S.L., 2002. Review of the molecular and cellular mechanisms of action of glucocorticoids for use in asthma. *Pulmonary Pharmacology & Therapeutics*, **15**(1), 35-50.

VERMILLION-SALSBURY, R.L. and HERCULES, D.M., 2002. 9-aminoacridine as a matrix for negative mode matrix-assisted laser desorption/ionization. *Rapid Communications in Mass Spectrometry*, **16**(16), 1575-1581.

WILEY, W.C. and MCLAREN, I.H., 1955. Time-of-flight mass spectrometer with improved resolution. *Review Scientific Instruments*, **26**(12), 1150-1157.

WISEMAN, J.M., IFA, D.R., SONG, Q. and COOKS, R.G., 2006. Tissue imaging at atmospheric pressure using desorption electrospray ionization (DESI) mass spectrometry. *Angewandte Chemie International Edition*, **45**(43), 7188-7192.

WISEMAN, J.M., IFA, D.R., ZHU, Y., KISSINGER, C.B., MANICKE, N.E., KISSINGER, P.T. and COOKS, R.G., 2008. Desorption electrospray ionization mass spectrometry: Imaging drugs and metabolites in tissues. *Proceedings of the National Academy of Sciences*, **105**(47), 18120-18125.

[www.asthma.org.uk](http://www.asthma.org.uk)

[www.bdal.com](http://www.bdal.com)

[www.chm.bris.ac.uk](http://www.chm.bris.ac.uk)

[www.htximaging.com](http://www.htximaging.com)

[www.iwata-medea.com](http://www.iwata-medea.com)

[www.mse.engin.umich.edu](http://www.mse.engin.umich.edu)

[www.nhlbi.nih.gov](http://www.nhlbi.nih.gov)

[www.labcyte.com](http://www.labcyte.com)

[www.pharmacologycorner.com](http://www.pharmacologycorner.com)

[www.sunchrom.de](http://www.sunchrom.de)

[www.who.int](http://www.who.int)

YAMASHITA, M. and FENN, J.B., 1984. Electrospray ion source. Another variation on the free-jet theme. *The Journal of physical chemistry*, **88**(20), 4451-4459.

YANG, J. and CAPRIOLI, R.M., 2011. Matrix sublimation/recrystallization for imaging proteins by mass spectrometry at high spatial resolution. *Analytical Chemistry*, **83**(14), 5728-5734.

ZENOBI, R. and KNOCHENMUSS, R., 1998. Ion formation in MALDI mass spectrometry. *Mass Spectrometry Reviews*, **17**(5), 337-366.

ZHANG, J. and ZENOBI, R., 2004. Matrix-dependent cationization in MALDI mass spectrometry. *Journal of Mass Spectrometry*, **39**(7), 808-816.

## Chapter 2

---

Use of hydrazine based reagents for improved sensitivity and detection of glucocorticoids by MALDI-MSI

## 2.1. Introduction

### 2.1.1. Purpose of derivatisation

One of the main aims of this research is to determine the distribution of corticosteroids in dosed rat lung tissue sections by MALDI-MSI. Corticosteroids contain multiple carbonyl functionalities which are not easily protonated/ deprotonated under mass spectrometry conditions, due to their low ionisation efficiencies. Derivatisation has been proposed as a solution to this problem by introduction of groups with fixed charges or with high proton affinity.

The most common derivatisation reactions of carbonyl compounds reported for analysis by “soft” ionisation mass spectrometry methods are based on the formation of oximes and hydrazones (Zaikin and Halket 2006). Other published methods involve the formation of Schiff’s bases, semicarbazones and thiosemicarbazones (Vaiken and Halket 2009).

Another benefit of derivatisation in “soft” ionisation mass spectrometry techniques such as MALDI-MS is that it can help prevent matrix-related ion suppression and isobaric overlay between matrix and analyte peaks by the introduction of groups with fixed charges or easily ionisable groups (Zaikin and Halket 2006).

Whilst there are many derivatisation reagents available there is not a preferred universal reagent. Thus the choice is ultimately determined by the analytes of interest for the method of analysis. There are several requirements to consider when choosing the ideal derivatisation reagent for use in “soft” ionisation mass spectrometry: 1) the reagent should be pre-charged or include a group having high proton affinity, 2) it must contain a suitable reactive group and 3) preferably should be commercially available or synthesised using inexpensive reagents (Cartwright *et al.*, 2005 and Zaikin and Halket 2006).

Careful consideration should be made when selecting the derivatisation reagent for example smaller reagents are suited for sterically hindered functional groups, the addition of a larger reagent can have the desired effect of moving the mass of the derivative into the less noisy region of the mass spectrum (Vaiken and Halket 2009).

### 2.1.2. Derivatisation reagents

#### 2.1.2.1. 2,4-Dinitrophenylhydrazine

2,4-Dinitrophenylhydrazine (DNPH) is the most commonly used hydrazine based reagent for the purpose of derivatising the carbonyl functionalities of aldehydes and ketones for liquid chromatographic separation followed by UV/vis or fluorescence spectroscopy (Vogel *et al.*, 2000). However the use of this reagent as a MALDI matrix requires caution. DNPH is reported to be explosive when dry (Sigma Aldrich MSDS). The structure of 2,4-dinitrophenylhydrazine is shown below in Figure 2.1.

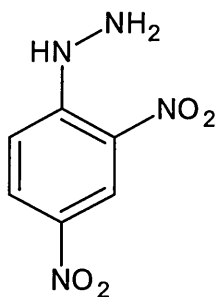


**Figure 2.1:** Structure of the hydrazine based reagent 2,4-Dinitrophenylhydrazine (DNPH).

DNPH has been characterised as a "reactive matrix" this is because it not only derivatises the carbonyl containing compounds but also assists in ionisation and detection by MALDI-MS. DNPH was utilised in this capacity for the derivatisation and analysis of corticosteroids (Brombacher *et al.*, 2003). The

reaction between DNPH and the carbonyl groups of corticosteroids is shown below in Figure 2.2.

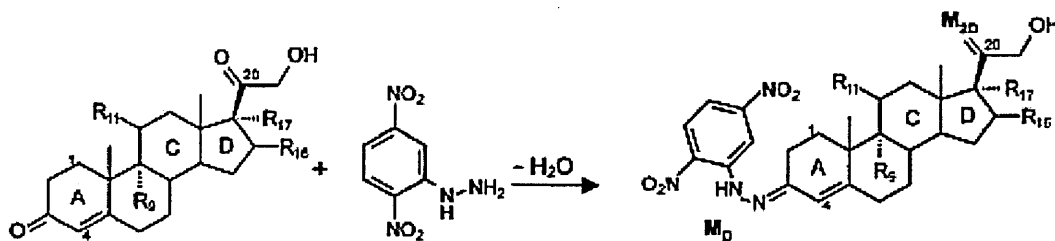


**Figure 2.2:** Scheme showing the reaction between steroids and DNPH to form the respective hydrazone derivative (Brombacher *et al.*, 2003).

The derivatisation of glucocorticoids using DNPH results in the formation of the radical cation ( $[M]^{+\bullet}$ ) via charge transfer reactions. The intact derivatised steroid is also observed in the form of a protonated derivatised molecule ( $[M_D+H]^+$ ) (Brombacher *et al.*, 2003).

DNPH has recently been used for the derivatization of phospholipids and their related oxidation products for analysis by MALDI-MS (Teuber *et al.*, 2012).

#### 2.1.2.2. 4-Dimethylamino-6-(4-methoxy-1-naphthyl)-1, 3, 5-triazine-2-hydrazine

4-Dimethylamino-6-(4-methoxy-1-naphthyl)-1, 3, 5-triazine-2-hydrazine (DMNTH) is a "tailor made" derivatisation reagent that combines a selective reactive functionality, stability and good spectroscopic properties in one compound (Mugo and Bottaro 2007). This reagent was developed by the Karst group at the University of Munster, Germany.

This reagent is synthesised by substitution reactions of cyanuric chloride, which acts as a base molecule to couple functional groups that have specific roles in the detection, reactivity and polarity of the derivatisation agent, this is illustrated in Figure 2.3.

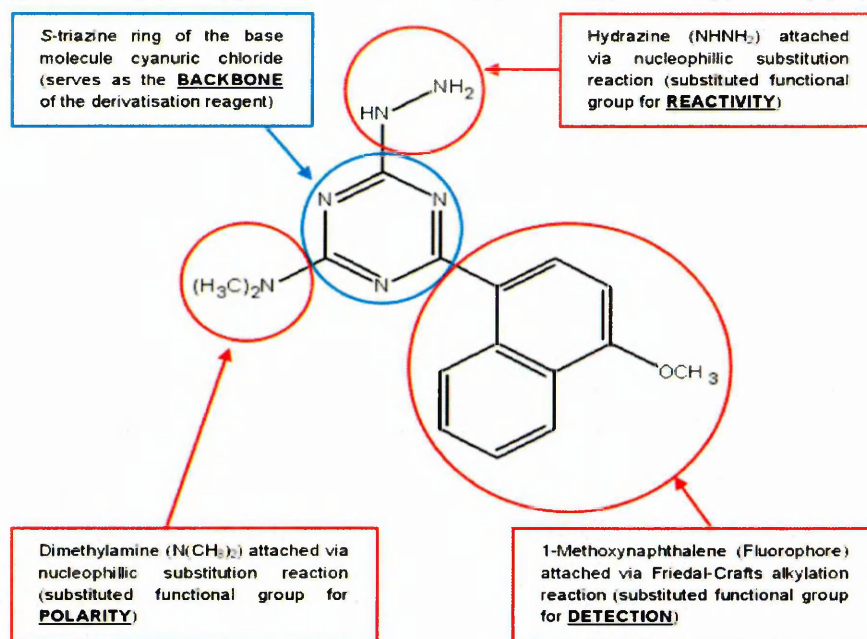


**Figure 2.3:** Diagram showing the functional groups of the derivatisation reagent 4-Dimethylamino-6-(4-methoxy-1-naphthyl)-1,3,5-triazine-2-hydrazine (DMNTH) and their functions.

There are several reports of the use of DMNTH as a derivatisation reagent. Examples are the derivatisation of carbonyl containing Friedel-Crafts alkyls followed by chromatographic separation and detection by atmospheric pressure chemical ionisation (APCI) mass spectrometry (Kempter *et al.*, 1999) and in water samples (Kempter and Karst 2000). The optimised parameters necessary for the separation of DMNTH derivatised carbonyl compounds by reversed phase capillary electrochromatography (CEC) were described by (Liu *et al.*, 2001).

Test tubes coated with DMNTH have been used for the determination of aldehydes in air samples followed by chromatographic separation and detection by UV-visible and fluorescence spectroscopy, the results were found to be comparable to the established method using the derivatisation reagent DNPH (Kempter *et al.*, 2002). The most recent application of DMNTH has been reported by (Mugo and Bottaro in 2007), for the derivatisation and analysis of a

range of carbonyl containing compounds by laser desorption ionisation-mass spectrometry (LDI-MS).

### 2.1.2.3. Girard's reagents

Girard's reagent P (1-(carboxymethyl) pyridinium chloride hydrazide) and Girard's reagent T (carboxymethyl) trimethylammonium chloride hydrazide) were first introduced by (Girard and Sandulesco in 1936).

Both reagents possess a permanently charged moiety which promotes a strong  $[M]^+$  ion for the derivative when analysed by mass spectrometry (Griffiths *et al.*, 2003). The structures of the Girard's reagents are shown below in Figure 2.4.

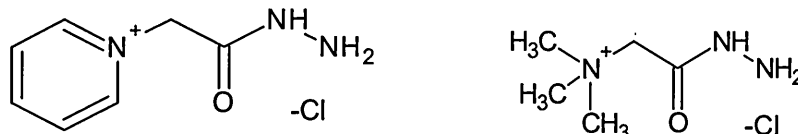


**Figure 2.4:** Structures of the derivatisation reagents Girard's reagent P (left) and Girard's reagent T (right).

Girard's reagents were first used by their discoverers to separate steroids such as esterone from urinary extracts (Wheeler 1962). Since then the Girard's reagents have been extensively used for the isolation and identification of steroids in biological fluids.

The potential of using Girard's reagents in doping control studies was demonstrated by (Shackleton *et al.*, in 1997). In this work Girard's reagent T was used for the derivatisation of testosterone esters that were extracted from plasma samples of volunteers, followed by high performance liquid chromatographic separation and analysis by ESI-MS.

Girard's reagent P was successfully employed for the derivatisation of neutral oxosteroids to facilitate improved analysis and detection by both ESI-MS and

MALDI-MS by (Griffiths *et al.*, 2003). Girard's reagent P was later used for the derivatisation of androgenic steroids (representative of those found during malpractice in the cattle industry) in spiked heifer urine followed by analysis by ESI-MS by (Kirk *et al.*, 2006).

Girard's reagent T has also been used in the derivatisation of oligosaccharides (Naven and Harvey 1996). Similarly Girard's reagent T was used with a derivatisation reagent called glycidyltrimethylammonium chloride (GTMA) for the derivatisation of oligosaccharides by (Gouw *et al.*, 2002).

### 1.3. Other applications of derivatisation in mass spectrometry

Recently a technique termed "reactive DESI" which involves the addition of reagents to the standard solvent spray for the purpose of derivatisating analytes present in the sample was introduced by (Eberlin *et al.*, 2011).

This technique has been utilised for the derivatisation of anabolic steroids, using hydroxylamine to form oximes which enabled their detection in urine samples (Huang *et al.*, 2007).

This method was utilised for the derivatisation of cortisone using a solvent spray containing the derivatisation reagent Girard's reagent T (Girod *et al.*, 2011a). Another study demonstrated the use of "Reactive DESI" for the derivatisation and imaging of malondialdehyde (MDA) (an oxidative stress marker) in injured rat spinal cord tissue samples. This was achieved by the addition of the derivatisation reagent to the solvent spray (Girod *et al.*, 2011b).

### 1.4. Aims and Objectives

The hydrazine based reagents DNPH, DMNTH and Girard's reagent P have been employed for the derivatisation of a range of glucocorticoids both in-solution and on-tissue to form their respective hydrazones and improve their

mass spectral ionisation efficiency and detection. Fluticasone propionate has been selected to demonstrate each example

## **2.2. Methods**

### **2.2.1. Information**

All animal studies were ethically reviewed and carried out in accordance with Animals (Scientific Procedures) Act 1986 and the GSK Policy on the Care, Welfare and Treatment of Laboratory Animals.

### **2.2.2. Materials**

The reagents  $\alpha$ -cyano-4-hydroxycinnamic acid (CHCA), fluticasone propionate, beclomethasone dipropionate, budesonide, trifluoroacetic acid (TFA) and ALUGRAM1 SIL G/UV254 precoated aluminum sheets were purchased from Sigma Aldrich<sup>®</sup> (Gillingham, Dorset, UK). The solvents methanol (MeOH), ethanol (EtOH) and acetonitrile (ACN) were purchased from Fisher Scientific (Loughborough, Leicestershire, UK). Girard's reagent P and dexamethasone was purchased from TCI Europe (Belgium). 2, 4-dinitrophenylhydrazine (DNPH) was purchased from Alfa Aesar<sup>®</sup> (Heysham, Lancashire, UK). 4-Dimethylamino-6-(4-methoxy-1-naphthyl)-1, 3, 5-triazine-2-hydrazine (DMNTH) was kindly donated by Professor Uwe Karst (University of Munster, Germany).

### **2.2.3. Instrumentation**

Mass spectra and images were acquired in positive ion mode on an Applied Biosystems/MDS Sciex hybrid quadrupole time-of-flight mass spectrometer (Q-Star Pulsar-*i*) with an orthogonal MALDI ion source (Applied Biosystems, Foster City, California, USA) and a high repetition Neodymium-doped yttrium vanadate (Nd: YVO<sub>4</sub>) laser (5 KHz) (Elforlight Ltd, Daventry, Northamptonshire, UK). Image acquisition was performed at a spatial resolution of 150  $\mu$ m x 150  $\mu$ m in

“Raster Image” mode; images were generated using the freely available Novartis Biomap 3.7.5.5 software ([www.maldi-msi.org](http://www.maldi-msi.org)).

Other mass spectrometry measurements were performed on a Thermo Finnigan MAT LCQ Classic Electrospray Ionisation-Mass Spectrometer (Thermo Finnigan, San Jose, California, USA).

#### 2.2.4. Tissue preparation

Frozen control rat lung tissue was sectioned using a Leica cryostat (Leica Microsystems, Wetzlar, Germany) to produce 12 µm thick sections, which were thaw mounted onto clean aluminium sheets.

#### 2.2.5. Derivatisation of glucocorticoids using DNPH

##### 2.2.5.1. In-solution derivatisation procedure

The derivatisation procedure involved the incubation of 10 µl of a test steroid (0.5 mg/ml in acetonitrile) and 10 µl of the solution of the DNPH matrix (1 mg/ml in acetonitrile with 0.3 % hydrochloric acid) in a 0.5 ml micro-centrifuge tube at room temperature for 30 minutes.

The derivatised steroids were then analysed using the Q-Star instrument operated in positive ion mode with an accumulation time of 0.7287 seconds (quoted as 4 decimal places from this point), declustering potential of 0, focusing potential of 20, second declustering potential of 15, collision gas of 3 arbitrary units and the scanning duration of 1 minute with a mass range of  $m/z$  150-1000.

### 2.2.5.2. On-tissue derivatisation procedure

Fluticasone proprionate ( $C_{25}H_{31}F_3O_5S$ , MW 500.57) standards (500, 100, 50, 25 and 5 ng/ $\mu$ l prepared in 70 % acetonitrile) were spotted (1  $\mu$ l) onto a control rat lung tissue section in triplicate. Then 1  $\mu$ l of a 4 mg/ml solution of DNPH in 50: 50 acetonitrile: water with 0.1 % TFA was applied onto the spiked areas (10 times per spot and allowed to dry between applications).

Using the Labcyte Portrait 630<sup>TM</sup> reagent multispotter (Labcyte, California, USA) as described by (Aerni *et al.*, 2006), the reactive matrix (4 mg/ml solution of DNPH in 50: 50 acetonitrile: water with 0.1 % TFA) was deposited onto the spiked lung tissue (20 cycles with 200  $\mu$ m distance between spots).

Imaging experiments were performed using the Q-Star instrument with the "Raster Image" mode set to the "slow" speed, the instrument was operated in positive ion mode with an accumulation time of 0.2943 seconds, declustering potential of 0, focusing potential of 20, second declustering potential of 15, collision gas of 3 arbitrary units, ion release delay (IRD) of 67.1 (the width of the pulse of ions released by the collision cell into the TOF), ion release width (IRW) of 29.1, duration of scanning of 2 minutes and a mass range of  $m/z$  150-700 with enhancement of  $m/z$  500.2.

### 2.2.6. Derivatisation of glucocorticoids using Girard's reagent P

#### 2.2.6.1. In-solution derivatisation procedure

The conversion of steroids into their respective Girard P hydrazones was performed using the method reported by (Kirk *et al.*, 2006). In summary, 300 mg of Girard's reagent P was weighed out and added to a 150 ml round bottom flask, to this 1 mg of the steroid was added along with 100 ml of methanol with 10 ml of glacial acetic acid. The reaction mixture was warmed using an oil bath

(70°C for 30 minutes), after which the reaction mixture was dried under a stream of nitrogen leaving a small amount of yellow oil, which was then reconstituted in 100 ml of a 10% methanol solution.

The derivatised steroids produced were analysed using a LCQ instrument operated in positive ion mode with a capillary temperature of 200°C, spray voltage of 4.50 kV and sheath gas flow (N<sub>2</sub>) 60 arbitrary units. The samples were introduced by direct infusion using the syringe pump on the instrument at a rate of 3 µl/minute<sup>-1</sup> and a mass range of 150-1000 was scanned. For tandem mass spectrometry experiments the collision energy was set to 32% in order to retain the precursor ions.

### 2.2.7. Derivatisation of glucocorticoids using DMNTH

#### 2.2.7.1. In-solution derivatisation procedure

The derivatisation procedure involved the incubation of 10 µl of a test steroid (2 mg/ml in acetonitrile) and 10 µl of the DMNTH matrix (5 mg/ml in 50: 50 acetonitrile: water with 0.1 % TFA) in a 0.5 ml micro-centrifuge tube at room temperature 48 hours.

The derivatised steroids were analysed using the Q-Star instrument operated in positive ion mode with an accumulation time of 0.728655 seconds, declustering potential (DP) of 0, focusing potential (FP) of 20, second declustering potential (DP2) of 15, collision gas (CAD) of 3 arbitrary units and the scanning duration of 1 minute with a mass range of *m/z* 250-900.

#### 2.2.7.2. On-tissue derivatisation procedure

Fluticasone Propionate standards (2000, 1000, 500, 250, 100, 50, 20 and 10 ng/µl prepared in 70 % acetonitrile) were spotted (1 µl) onto a control rat lung

tissue section. Using the Labcyte Portrait 630™ reagent multispotter, the reactive matrix (5 mg/ml solution of DMNTH in 50: 50 acetonitrile: water with 0.1 % TFA) was deposited onto the spiked lung tissue (25 cycles with 200 µm spot-to-spot distance).

Once the spiked tissue section had been coated with the reactive matrix, it was placed onto a polystyrene block and placed into a glass chamber containing 50 % methanol (Figure 2.5). The chamber lid was sealed using parafilm and incubated at 37°C with 5 % carbon dioxide for 48 hours in a Heraeus, Heracell incubator.

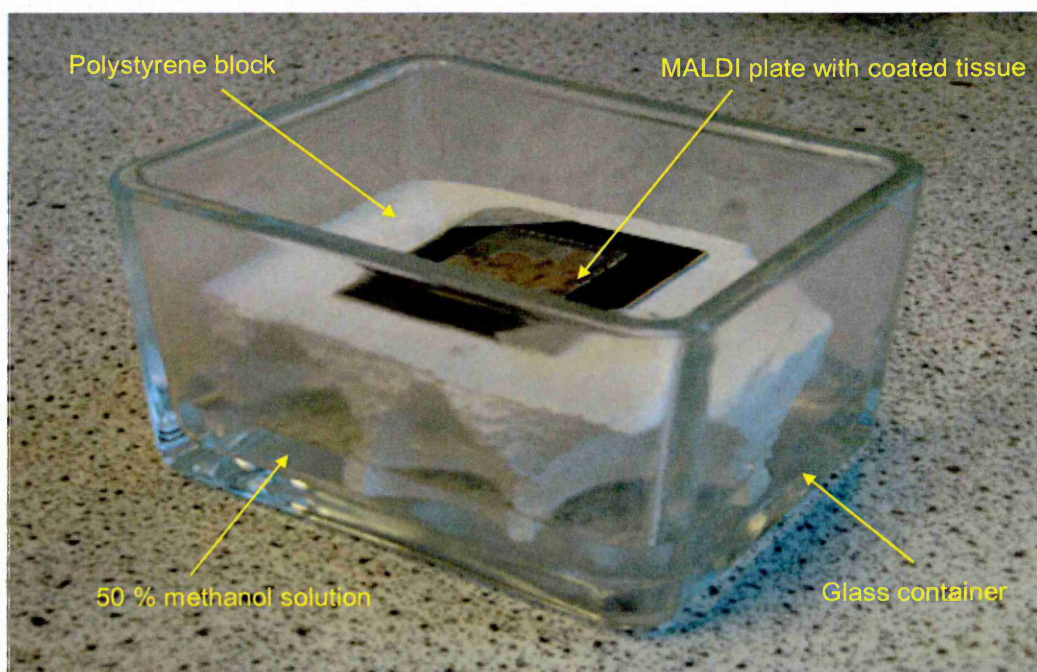


**Figure 2.5:** Equipment setup for the incubation of the reactive matrix coated tissue.

Following incubation the section was analysed using the Q-Star instrument with the “Raster Image” mode set to the "slow" speed, the instrument was operated in positive ion mode with an accumulation time of 0.4886 seconds, declustering potential (DP) of 0, focusing potential (FP) of 20, second declustering potential (DP2) of 15, collision gas (CAD) of 3 arbitrary units, ion release delay (IRD) of

84.5, ion release width (IRW) of 36.6, duration of scanning was 3 minutes and a mass range of  $m/z$  450-800 with enhancement of  $m/z$  793.2.

#### 2.2.8. Data processing

Mass spectra from Analyst were exported in the form text files and imported into mMass, an open source mass spectrometry software used for mass spectral processing (Strohalm *et al.*, 2010).

## 2.3. Results and Discussion

### 2.3.1. MALDI-MS analysis of glucocorticoids

To illustrate the challenge of analysing glucocorticoids with MALDI-MS, a solution of fluticasone propionate was mixed with the matrix CHCA and spotted onto a MALDI target plate. The resulting MALDI-MS spectrum is displayed below in Figure 2.6.

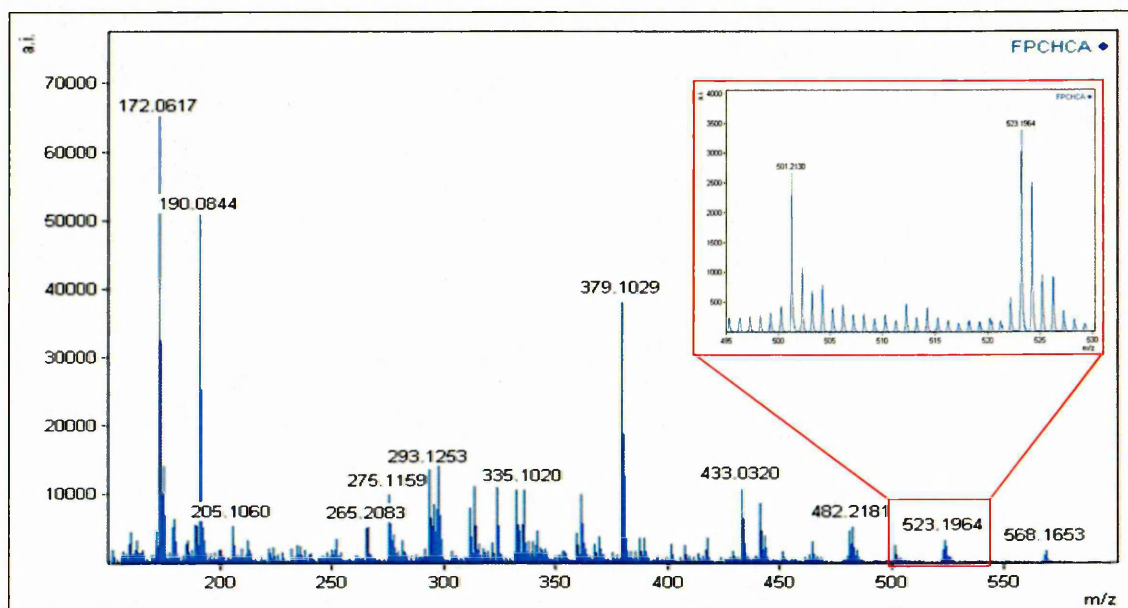


**Figure 2.6:** MALDI-MS spectrum showing fluticasone propionate (500 ng/ $\mu$ l) mixed with the matrix CHCA. The spectrum shows the presence of matrix related peaks and the expanded region shows the sodium adduct of Fluticasone propionate ( $[M+Na]^+$ ) at  $m/z$  523.1964.

The MALDI-MS spectrum displayed above in Figure 2.6 shows an abundance of CHCA matrix related peaks below 500 Da, the insert shows the sodium adduct ( $[M+Na]^+$ ) of Fluticasone propionate at  $m/z$  523.1964. As previously mentioned glucocorticoids are not easily analysed in mass spectrometry because they lack sites to which a proton can be attached and as a result they are ionised by the addition of metal ions such as sodium or potassium but with low efficiency.

### 2.3.2. In-solution derivatisation using DNPH

The MALDI-MS spectrum obtained for fluticasone propionate following derivatisation with DNPH is shown below in Figure 2.7.

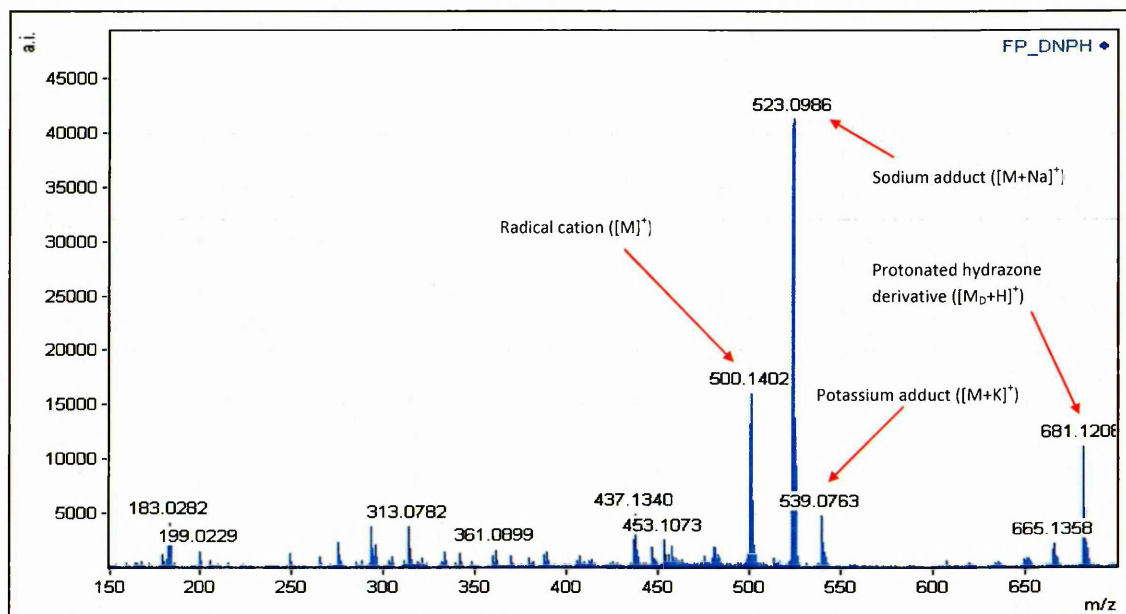


**Figure 2.7:** MALDI-MS spectrum showing fluticasone propionate (500 ng/ $\mu$ l) following 1 hour reaction with the reactive matrix DNPH at room temperature. The spectrum shows the presence of the radical cation ( $[M]^{+\bullet}$ ) of fluticasone propionate at  $m/z$  500.1402, the sodium adduct ( $[M+Na]^{+\bullet}$ ) at  $m/z$  523.0986, the potassium adduct ( $[M+K]^{+\bullet}$ ) at  $m/z$  539.0763 and the protonated hydrazone derivative ( $[M_D+H]^{+\bullet}$ ) at  $m/z$  681.1208.

The MALDI-MS spectrum obtained (Figure 2.7) shows a radical cation ( $[M]^{+\bullet}$ ) at 500.1402, the sodium adduct ( $[M+Na]^{+\bullet}$ ) at  $m/z$  523.0986 (the most abundant ion), the potassium adduct ( $[M+K]^{+\bullet}$ ) at  $m/z$  539.0763 and the protonated hydrazone derivative ( $[M_D+H]^{+\bullet}$ ) of fluticasone propionate at  $m/z$  681.1208. The spectrum also shows the presence of the protonated reactive matrix ( $[M+H]^{+\bullet}$ ) at  $m/z$  199.0229.

During the analysis of derivatised corticosteroids, budesonide and dexamethasone, (Brombacher *et al.*, 2003) observed the presence of a strong

sodium adduct ion signal ( $[M+Na]^+$ ) in addition to the radical cation and protonated hydrazone derivative. Also the intensity of the sodium adduct was found to be higher than that of the radical cation, which is also observed in the spectrum shown in Figure 2.7.

The MALDI-MS spectrum of fluticasone propionate following derivatisation with a mixture of CHCA and DNPH is shown below in Figure 2.8.

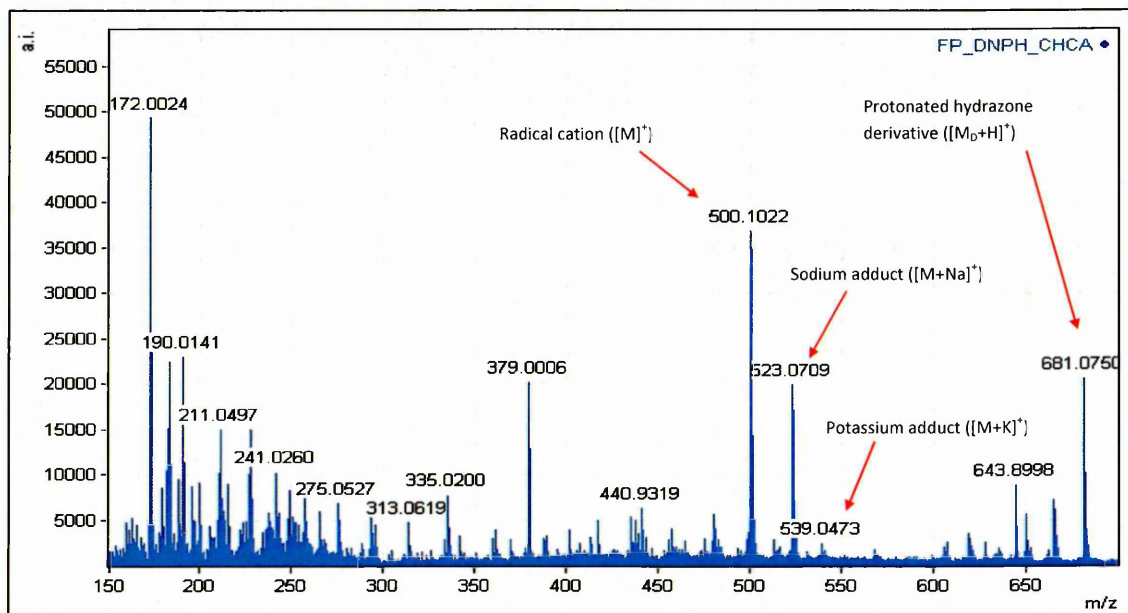


**Figure 2.8:** MALDI-MS showing fluticasone propionate (500 ng/ $\mu$ l) following 1 hour reaction with a mixture of the reactive matrix DNPH and CHCA at room temperature. The spectrum shows the presence of the radical cation ( $[M]^+$ ) of fluticasone propionate at  $m/z$  500.1022, the sodium adduct ( $[M+Na]^+$ ) at  $m/z$  523.0709, the potassium adduct ( $[M+K]^+$ ) at  $m/z$  539.0473 and the protonated hydrazone derivative ( $[M_D+H]^+$ ) at  $m/z$  681.0750.

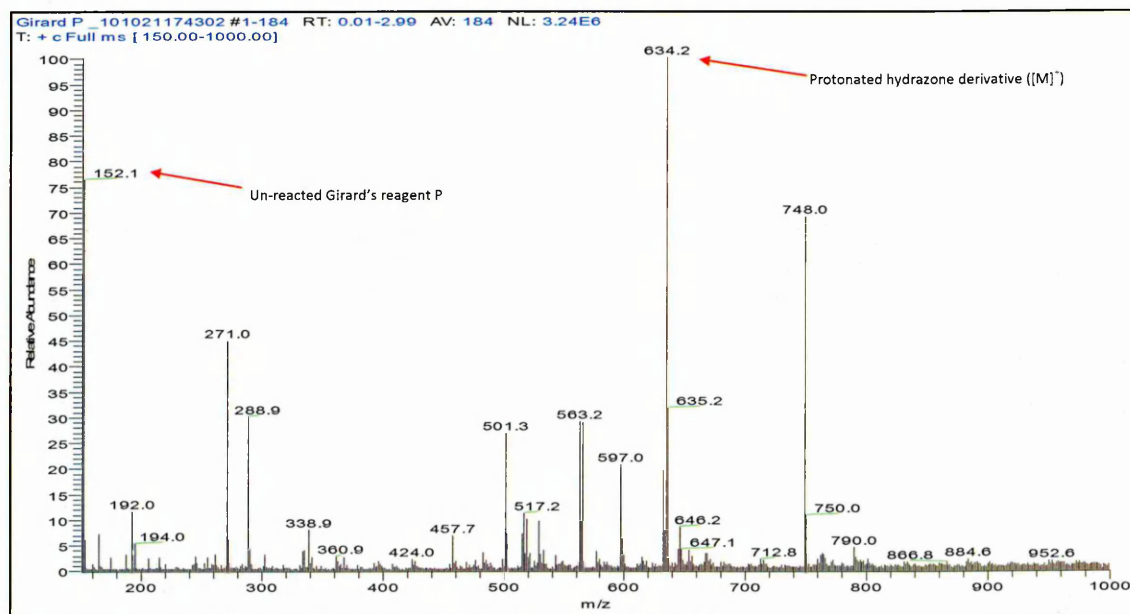
The MALDI-MS spectrum shown above in Figure 2.8 shows the radical cation ( $[M]^+$ ) at 500.1022 (the most abundant ion), the sodium adduct ( $[M+Na]^+$ ) at  $m/z$  523.0709, the potassium adduct ( $[M+K]^+$ ) at  $m/z$  539.0473 and the protonated hydrazone derivative ( $[M_D+H]^+$ ) of fluticasone propionate at  $m/z$  681.0750. The

spectrum also shows a high abundance of CHCA related adduct ions below 500 Da.

The spectrum shown in 2.8 highlights that the addition of CHCA to the DNPH has changed the ratio between the radical cation ( $[M]^+$ ) at  $m/z$  500 and sodium adduct ( $[M+Na]^+$ ) at  $m/z$  523 of fluticasone propionate. Also the spectrum shows the addition of CHCA appears to improve the intensity of the radical cation and the protonated hydrazone derivative ion by approximately a factor of 2.

### 2.3.3. In-solution derivatisation using Girard's reagent P

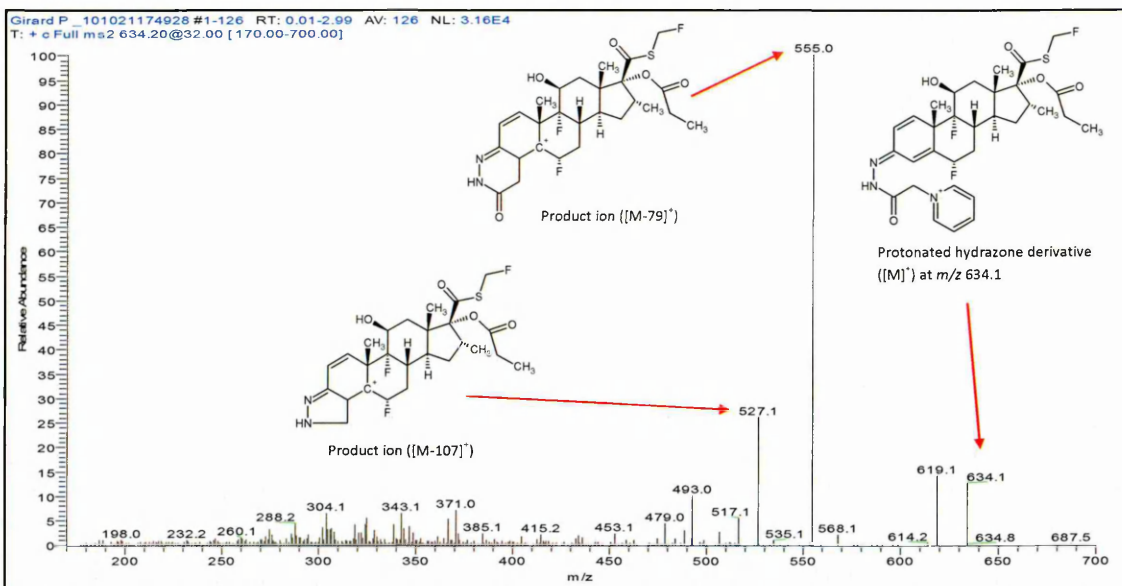
The ESI-MS spectrum of fluticasone propionate following derivatisation with Girard's reagent P is shown below in Figure 2.9.



**Figure 2.9:** ESI-MS spectrum showing fluticasone propionate following derivatisation with Girard's reagent P at a temperature of 70°C for 30 minute. The spectrum shows the protonated hydrazone derivative at  $m/z$  634.2.

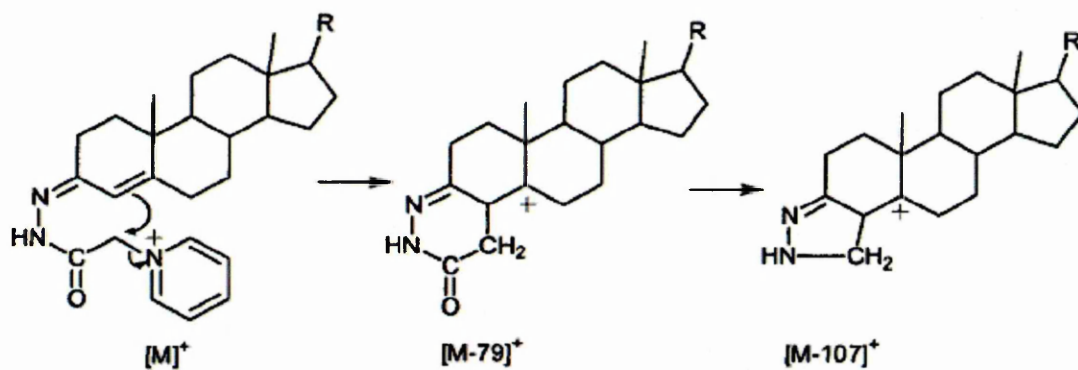
The ESI-MS spectrum depicted in Figure 2.9 shows the protonated hydrazone derivative of fluticasone propionate at  $m/z$  634.2 and a peak at  $m/z$  152.1 which fits for the un-reacted Girard's reagent P.

To confirm the peak at  $m/z$  634.1 is that of the protonated hydrazone derivative ( $[M]^+$ ) of fluticasone propionate a tandem mass spectrometry experiment was performed to generate a product ion scan. The ESI-MS/MS spectrum obtained is illustrated in Figure 2.10.



**Figure 2.10:** ESI-MS/MS spectrum showing the product ions at  $m/z$  527.1 and  $m/z$  555.0, derived from the precursor ion of the protonated hydrazone derivative at  $m/z$  634.1.

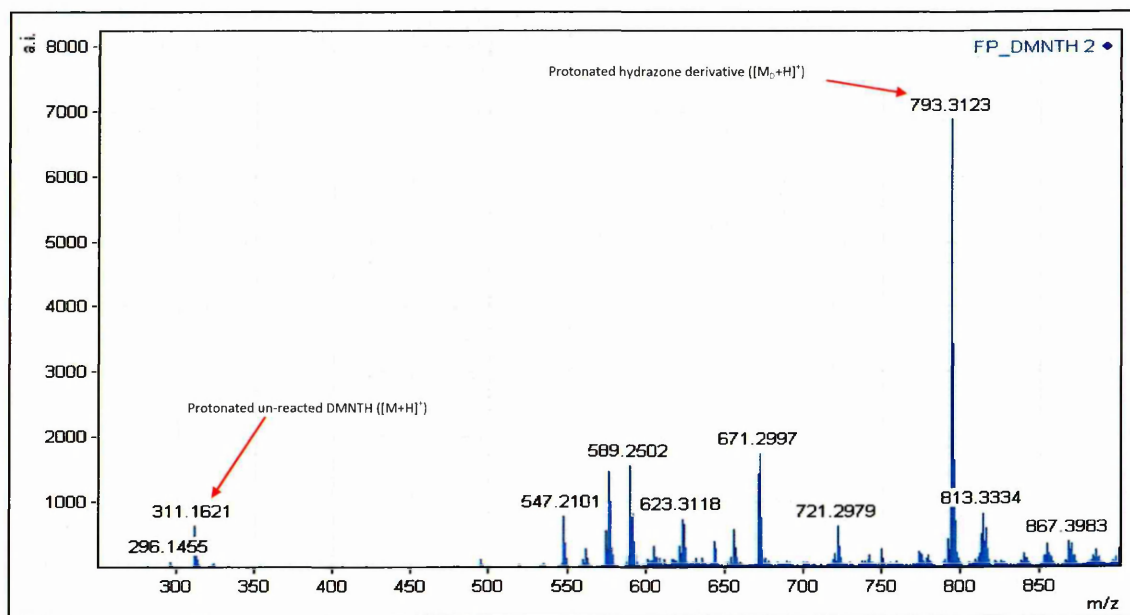
The ESI-MS/MS spectrum shown in Figure 2.10 shows the product ions at  $m/z$  527.1 and  $m/z$  555.0, derived from the precursor ion of the protonated hydrazone derivative of fluticasone propionate at  $m/z$  634.1 confirming the identity of the hydrazone derivative. The resulting product ions designated, ( $[M-79]^+$ ) at  $m/z$  555.0 is interpreted as the loss of the pyridine ring and a rearrangement to form the six membered dihydropyridazinone ring. The ion designated as ( $[M-107]^+$ ) at  $m/z$  527.1 is interpreted as the loss of the carbonyl group and a rearrangement to form the five membered dihydropyrazole ring. The assignment of the product ions is based upon the work reported by (Shackleton *et al.*, 1997) and is represented in the scheme in Figure 2.11.



**Figure 2.11:** Simplified scheme showing the fragmentation of Steroidal Girard P Hydrazones and the formation of the six membered dihydropyridazinone ring and the five membered dihydropyrazole ring (Griffiths et al., 2008).

#### 2.3.4. In-solution derivatisation using DMNTH

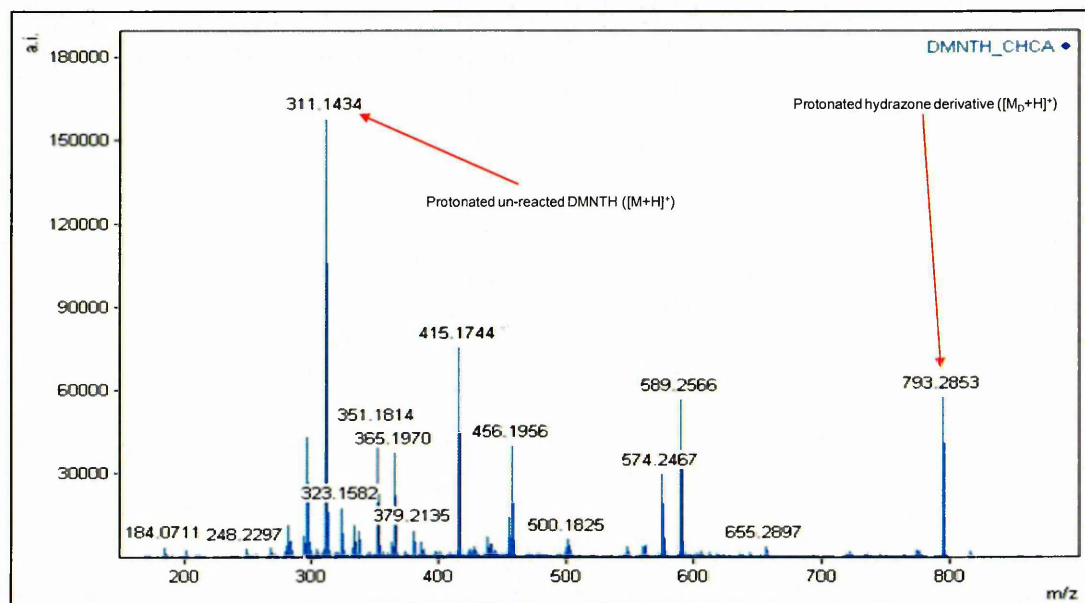
The MALDI-MS spectrum obtained for fluticasone propionate following derivatisation with DMNTH is shown below in Figure 2.12.



**Figure 2.12:** MALDI-MS spectrum showing fluticasone propionate (500 ng/ $\mu$ l) following a 48 hour incubation with the reactive matrix DMNTH at room temperature. The spectrum shows the presence of the protonated un-reacted DMNTH  $[M+H]^+$  at m/z 311.1621 and the protonated hydrazone derivative  $[M_D+H]^+$  at m/z 793.3123.

The MALDI-MS spectrum shown in Figure 2.12 shows the most abundant ion at  $m/z$  793.3123 which fits for the protonated hydrazone derivative ( $[M_D+H]^+$ ) of fluticasone propionate. Also present is the protonated un-reacted DMNTH ( $[M+H]^+$ ) ion at  $m/z$  311.1621.

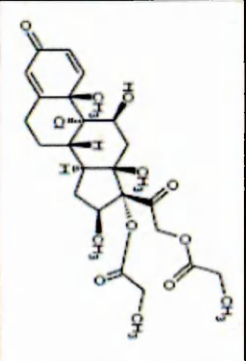
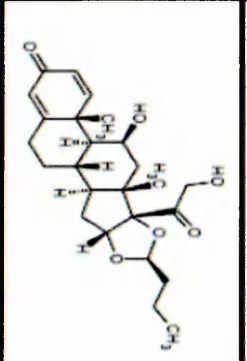
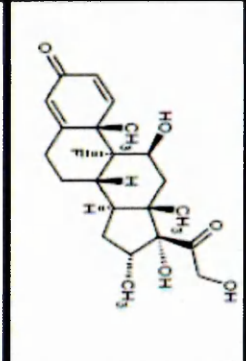
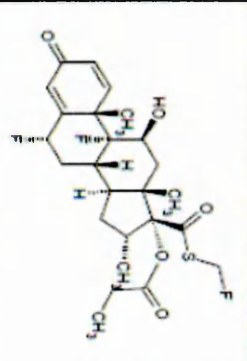
Derivatising fluticasone propionate with a mixture of CHCA and DMNTH gave a more complex spectrum (see Figure 2.13).



**Figure 2.13:** MALDI-MS spectrum showing fluticasone propionate (500 ng/ $\mu$ l) following 48 hour reaction with a mixture of the reactive matrix DMNTH and CHCA at room temperature. The spectrum shows the presence of the protonated hydrazone derivative ( $[M_D+H]^+$ ) at  $m/z$  793.2853.

The MALDI-MS spectrum shown in Figure 2.13 shows the protonated hydrazone derivative ( $[M_D+H]^+$ ) at  $m/z$  793.2853 of fluticasone propionate. The spectrum also shows the presence of protonated un-reacted DMNTH ( $[M+H]^+$ ) at  $m/z$  311.1434 which is the most abundant peak. The spectrum also shows the addition of CHCA improves the detection of the protonated hydrazone derivative by approximately a factor of 10.

The results obtained from the in-solution derivatisation of all the glucocorticoids with the three hydrazine based derivatisation is shown below in Table 2.1.

| Compound Name (IUPAC)   | Compound Structure  | DNPH   | Grid's reagent P     | DMNTH                                |
|---|---|--|----------------------|--------------------------------------|
| Beclomethasone Dipropionate<br><br>(8S,9R,10S,11S,13S,14S,16S,17R)-9-chloro-11-hydroxy-10,13,16-trimethyl-3-oxo-17-(2-(propionyloxy)acetyl)-cyclopenta[ <i>a</i> ]phenanthren-17-yl propionate)               |  | 520 (M <sup>+</sup> )<br>543 (M+Na) <sup>+</sup><br>539 (M+K) <sup>+</sup><br>701 (M <sub>2</sub> +H) <sup>+</sup> | 654 (M) <sup>+</sup> | 813 (M <sub>2</sub> +H) <sup>+</sup> |
| Budesonide<br><br>(16 $\beta$ ,17 $\beta$ -(butylidenebis(oxy))-11,21-dihydroxy-, (11 $\beta$ ,8,16 $\alpha$ -o)-pregna-1,4-diene-3,20-dione)   |   | 430 (M) <sup>+</sup><br>453 (M+Na) <sup>+</sup><br>469 (M+K) <sup>+</sup><br>611 (M <sub>2</sub> +H) <sup>+</sup>  | 564 (M) <sup>+</sup> | 723 (M <sub>2</sub> +H) <sup>+</sup> |
| Dexamethasone<br><br>(8S,9R,10S,11S,13S,14S,16R,17R)-9-Fluoro-11,17-dihydroxy-17-(2-hydroxyacetyl)-10,13,16-trimethyl-6,7,8,9,10,11,12,13,14,15,16,17-dodecahydro-3H-cyclopenta[ <i>a</i> ]phenanthren-3-one) |   | 392 (M) <sup>+</sup><br>415 (M+Na) <sup>+</sup><br>431 (M+K) <sup>+</sup><br>573 (M <sub>2</sub> +H) <sup>+</sup>  | 526 (M) <sup>+</sup> | 685 (M <sub>2</sub> +H) <sup>+</sup> |
| Futicasone Propionate<br><br>(S)-(fluoromethyl)-6 $\alpha$ ,9-difluoro-11 $\beta$ ,17-dihydroxy-16 $\alpha$ -methyl-3-oxoandrost-1,4-diene-17 $\beta$ -carbothioate, 17-propionate)                           |   | 500 (M) <sup>+</sup><br>523 (M+Na) <sup>+</sup><br>539 (M+K) <sup>+</sup><br>681 (M <sub>2</sub> +H) <sup>+</sup>  | 634 (M) <sup>+</sup> | 793 (M <sub>2</sub> +H) <sup>+</sup> |

**Table 2.1:** A table summarising the results from the in-solution derivatisation of the glucocorticoids with the hydrazine based derivatisation reagents.

### 2.3.5. On-tissue derivatisation using DNPH

Following the successful application of DNPH and DMNTH for the in-solution derivatisation of the range of glucocorticoids, the next step was to apply these reagents for on-tissue derivatisation experiments. The MALDI-MS images shown below in Figure 2.14 demonstrate the application of the reactive matrix DNPH for the derivatisation of fluticasone propionate on a control rat lung tissue section.

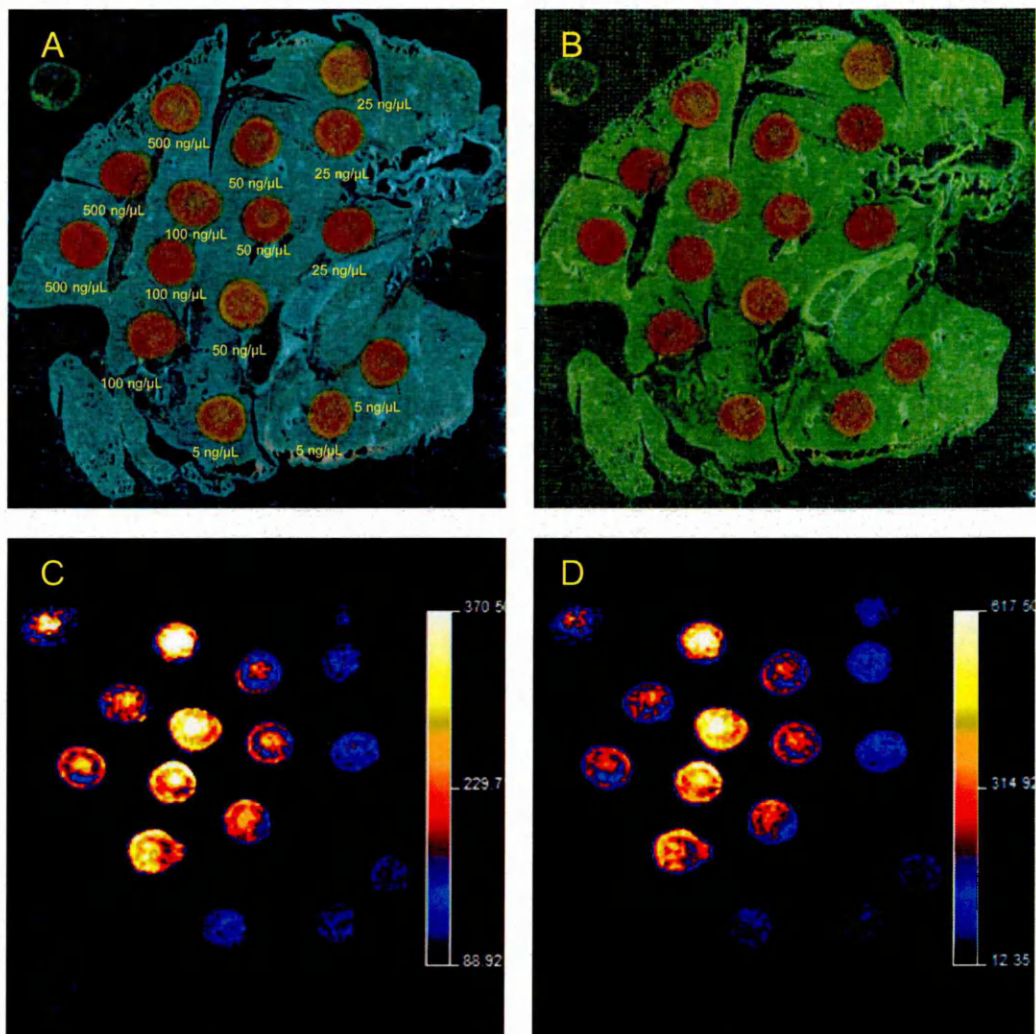


**Figure 2.14:** Optical images showing the spiked tissue section A) before and B) after reactive matrix deposition. MALDI-MS images showing the distribution of C) the radical cation ( $[M]^+$ ) of fluticasone propionate at  $m/z$  500.2 and D) the protonated hydrazone derivative ( $[M_D+H]^+$ ) of fluticasone propionate at  $m/z$  681.2.

The MALDI-MS images displayed in Figure 2.14 shows the distribution of the radical cation ( $[M]^{+\bullet}$ )  $m/z$  500.2 and the protonated hydrazone derivative ( $[M_D+H]^+$ )  $m/z$  681.2 of fluticasone propionate within the spiked areas of the lung tissue. However, the lack of linearity of the response with respect to concentration spiked needs to be investigated further. The cause may be related to the compound spiking methods and / or matrix application.

### 2.3.6. On-tissue derivatisation using DMNTH

The MALDI-MS images displayed below in Figure 2.15 shows the application of the reactive matrix DMNTH for the derivatisation of fluticasone propionate on a control rat lung tissue section without incubation prior to analysis.

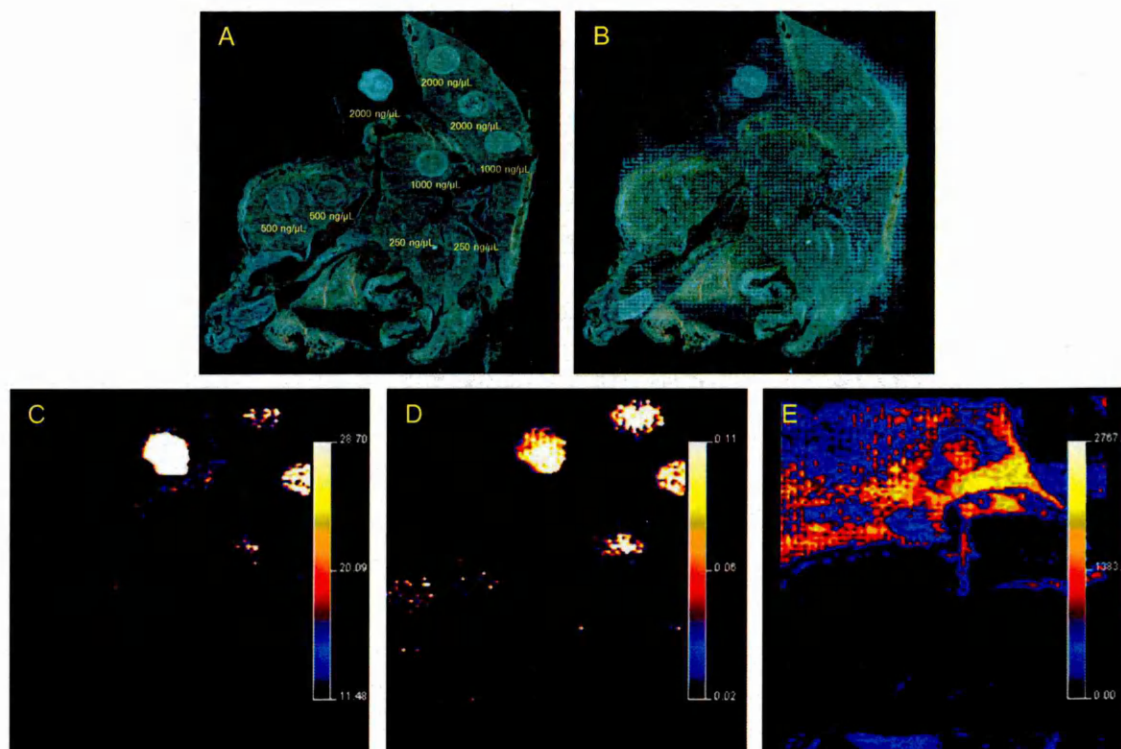


**Figure 2.15:** Optical images showing the spiked tissue section A) before and B) after reactive matrix deposition. MALDI-MS images showing the distribution of the protonated hydrazone derivative of fluticasone propionate at  $m/z$  793 C) before and D) after normalisation against the distribution of E) a reactive matrix related peak at  $m/z$  589.

The MALDI-MS Images shown in Figure 2.15 shows the distribution of the protonated hydrazone derivative ( $[M_D+H]^+$ ) at  $m/z$  793.2, the distribution of the reactive matrix related peak at  $m/z$  589.2 and the protonated hydrazone derivative ( $[M_D+H]^+$ ) at  $m/z$  793.2 following normalisation with the reactive matrix peak at  $m/z$  589.2. The distribution of the protonated hydrazone derivative ( $[M_D+H]^+$ ) at  $m/z$  793.2 is within the spiked areas of the tissue and the

normalised image shows that it is detectable down to 500 ng/ $\mu$ l following no incubation.

In contrast the MALDI-MS images presented below in Figure 2.16 shows the application of the reactive matrix DMNTH for the derivatisation of fluticasone propionate on a control rat lung tissue section. However this time the coated tissue section was incubated for 48 hours at 37°C prior to analysis, the reason for the incubation of the coated tissue is to maintain the derivatisation reaction on the sample surface.

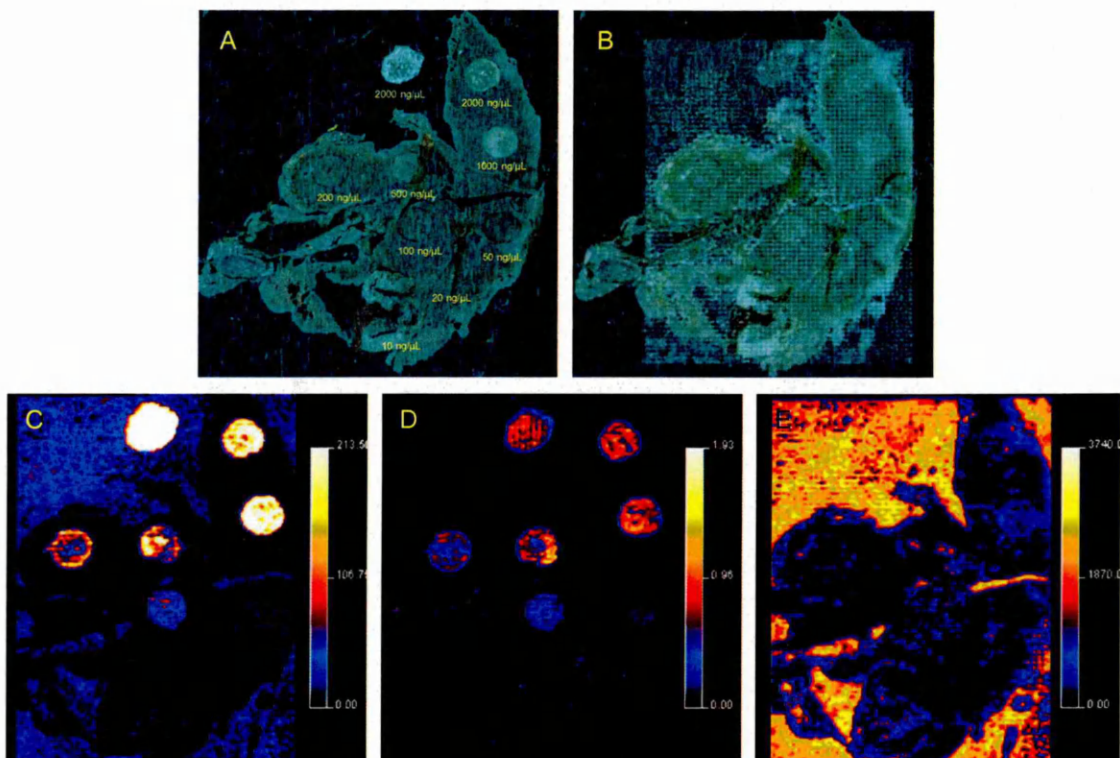


**Figure 2.16:** Optical images showing the spiked tissue section A) before and B) after reactive matrix deposition. MALDI-MS images showing the distribution of the protonated hydrazone derivative of fluticasone propionate at  $m/z$  793 C) before and D) after normalisation against the distribution of E) a reactive matrix related peak at  $m/z$  589.

The MALDI-MS Images shown in Figure 2.16 shows the distribution of the protonated hydrazone derivative ( $[M_D+H]^+$ ) at  $m/z$  793.2, the distribution of the

reactive matrix related peak at  $m/z$  589.2 and the protonated hydrazone derivative ( $[M_D+H]^+$ ) at  $m/z$  793.2 following normalisation with the reactive matrix peak at  $m/z$  589.2. The distribution of the protonated hydrazone derivative ( $[M_D+H]^+$ ) at  $m/z$  793.2 is within the spiked areas of the tissue and the normalised image shows that it is detectable down to 50 ng/ $\mu$ l following a 48 hour incubation at 37°C.

As the MALDI-MS images presented in Figures 2.15 and 2.16 show incubation of DMNTH coated samples at 37°C for 48 hours improves the detection of the protonated hydrazone derivative by a factor of 10.

The MALDI-MS presented below in Figure 2.17 shows the application of the reactive matrix DMNTH for the derivatisation of fluticasone propionate, beclomethasone dipropionate, budesonide and dexamethasone on a control rat lung tissue section. As in the previous experiment the coated tissue section was incubated at 37°C for 48 hours (prior to analysis).

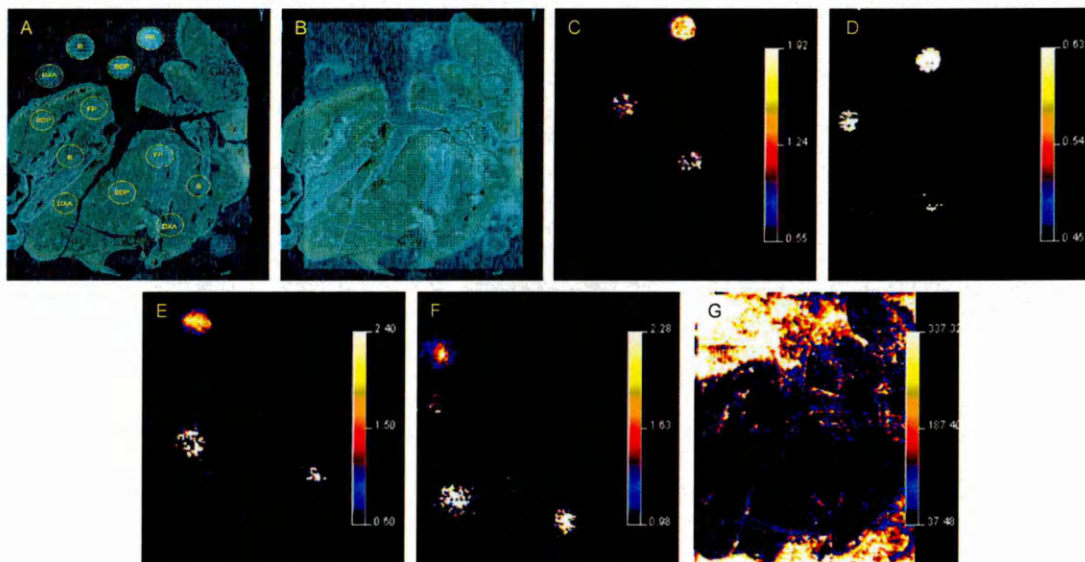


**Figure 2.17:** Optical images showing the spiked tissue section A) before and B) after reactive matrix deposition. MALDI-MS images showing the distribution of the protonated hydrazone derivatives of C) fluticasone propionate at  $m/z$  793, D) beclomethasone dipropionate at  $m/z$  813, E) budesonide at  $m/z$  723, F) dexamethasone at  $m/z$  685 all images were normalised against the distribution of G) a reactive matrix related peak at  $m/z$  589.

The MALDI-MS images shown in Figure 2.17 shows the distribution of the protonated hydrazone derivatives ( $[M_D+H]^+$ ) of the four steroids *on-tissue* following incubation for 48 hours at 37°C. The detection of the protonated hydrazone derivatives of fluticasone propionate at  $m/z$  793, beclomethasone dipropionate at  $m/z$  813, budesonide at  $m/z$  723 and dexamethasone at  $m/z$  685

was observed within the respective spiked areas on the tissue. This experiment shows DMNTH is capable of derivatising all the steroids under study on-tissue.

## 2.4. Conclusions

The use of hydrazine based reagents has successfully been employed for the derivatisation of glucocorticoids to form their respective hydrazones (both in-solution and on-tissue) and thus improve their mass spectral ionisation efficiency and detection.

Girard's reagent P was successfully used for the in-solution derivatisation of glucocorticoids, without a lengthy preparation time (~30 minutes). The quaternary nitrogen within the pyridine ring structure, produced a hydrazone derivative which was readily detected by mass spectrometry. Whilst the preparation time was only 30 minutes, Girard's reagent P was considered unsuitable for on-tissue experiments due to the high temperatures (~70°C) required to produce the hydrazone derivatives. The high temperatures would have a detrimental effect on the tissue and its constituents.

The use of DNPH for in-solution derivatisation of glucocorticoids was successful and the reaction with the glucocorticoids was found to be quick (~30 minutes), however it was found that the other glucocorticoids such as beclomethasone dipropionate and budesonide required a longer reaction time (~24 hours) in order to produce a detectable signal possibly due to the differences in the structures affecting the reaction kinetics.

The application of DNPH to the on-tissue experiments was also successful, the presence of the radical cation ( $[M]^+$ ) and the protonated hydrazone derivative ( $[M_D+H]^+$ ) of fluticasone propionate was observed in the spiked areas of the tissue sections. However further studies are required for the application of DNPH to on-tissue experiments to explain the apparent lack of linearity for the response with respect to concentration spiked onto the tissue section, which

could possibly be due to the application of the reactive matrix onto the spiked tissue section.

The tailor made reactive matrix DMNTH has successfully been applied to the in-solution derivatisation of glucocorticoids. It has been shown that a prolonged reaction (~48 hours) improves the detection of the protonated hydrazine derivative. The application of DMNTH to on-tissue experiments has also been successful, it has been shown that analysis of samples immediately after reactive matrix application results in the detection of the protonated hydrazone derivative ( $[M_D+H]^+$ ) of fluticasone propionate at concentration of 500 ng/ $\mu$ l. It was found that following incubation in a humid environment (37°C) results in the detection of the protonated hydrazone derivative ( $[M_D+H]^+$ ) of fluticasone propionate at a concentration of 50 ng/ $\mu$ l.

Further improvements in sensitivity and limits of detection were observed when CHCA was added to the reactive matrices DNPH or DMNTH.

Based on these observations, it is recommended to use Girard's reagent P for the in-solution derivatisation of corticosteroids. This is due to the quick reaction time and the well documented product ion formation, which results in easier tandem mass spectral interpretation and compound identification. For the on-tissue applications it is recommended to use the reactive matrix DMNTH, this is due to the presence of a strong protonated hydrazone derivative being the only species observed that is related to the derivatised corticosteroid, which is not the case with the reactive matrix DNPH.

## 2.5. References

AERNI, H.R., CORNETT, D.S. and CAPRIOLI, R.M., 2006. Automated acoustic matrix deposition for MALDI sample preparation. *Analytical Chemistry*, **78**(3), 827-834.

BROMBACHER, S., OWEN, S. and VOLMER, D., 2003. Automated coupling of capillary-HPLC to matrix-assisted laser desorption/ionization mass spectrometry for the analysis of small molecules utilizing a reactive matrix. *Analytical and Bioanalytical Chemistry*, **376**(6), 773-779.

CARTWRIGHT, A.J., JONES, P., WOLFF, J. and EVANS, E.H., 2005. Derivatisation of carboxylic acid groups in pharmaceuticals for enhanced detection using liquid chromatography with electrospray ionisation tandem mass spectrometry. *Rapid Communications in Mass Spectrometry*, **19**(8), 1058-1062.

EBERLIN, L.S., FERREIRA, C.R., DILL, A.L., IFA, D.R. and COOKS, R.G., 2011. Desorption electrospray ionization mass spectrometry for lipid characterization and biological tissue imaging. *Biochimica et Biophysica Acta (BBA) - Molecular and Cell Biology of Lipids*, **1811**(11), 946-960.

GIRARD, A. and SANDULESCO, G., 1936. Sur une nouvelle série de réactifs du groupe carbonyle, leur utilisation à l'extraction des substances cétoniques et à la caractérisation microchimique des aldéhydes et cétones. *Helvetica chimica acta*, **19**(1), 1095-1107.

GIROD, M., MOYANO, E., CAMPBELL, D.I. and COOKS, R.G., 2011. Accelerated bimolecular reactions in microdroplets studied by desorption electrospray ionization mass spectrometry. *Chemical Science*, **2**(3), 501-510.

GIROD, M., SHI, Y., CHENG, J. and COOKS, R.G., 2011. Mapping lipid alterations in traumatically injured rat spinal Cord by desorption electrospray ionization imaging mass spectrometry. *Analytical Chemistry*, **83**(1), 207-215.

GOUW, J.W., BURGERS, P.C., TRIKOUPIIS, M.A. and TERLOUW, J.K., 2002. Derivatization of small oligosaccharides prior to analysis by matrix-assisted laser desorption/ionization using glycidyltrimethylammonium chloride and Girard's reagent T. *Rapid Communications in Mass Spectrometry*, **16**(10), 905-912.

GRIFFITHS, W.J., LIU, S., ALVELIUS, G. and SJÖVALL, J., 2003. Derivatisation for the characterisation of neutral oxosteroids by electrospray and matrix-assisted laser desorption/ionisation tandem mass spectrometry: the Girard P derivative. *Rapid Communications in Mass Spectrometry*, **17**(9), 924-935.

HUANG, G., CHEN, H., ZHANG, X., COOKS, R.G. and OUYANG, Z., 2007. Rapid screening of anabolic steroids in urine by reactive desorption electrospray ionization. *Analytical Chemistry*, **79**(21), 8327-8332.

KEMPTER, C., ZUREK, G. and KARST, U., 1999. Determination of carbonyls using liquid chromatography-mass spectrometry with atmospheric pressure chemical ionization. *Journal of Environmental Monitoring*, **1**(4), 307-311.

KEMPTER, C., PÖTTER, W., BINDING, N., KLÄNING, H., WITTING, U. and KARST, U., 2000. Tailor-made derivatizing agents for carbonyl compounds using liquid chromatography. *Analytica Chimica Acta*, **410**(1-2), 47-64.

KEMPTER, C. and KARST, U., 2000. Determination of carbonyl compounds in waters using triazine-based hydrazine reagents and liquid chromatography. *Analyst*, **125**(3), 433-438.

KEMPTER, C., BERKHOUDT, T., TOLBÄ, L, G., EGMOSE, K. and KARST, U., 2002. Air monitoring of aldehydes by use of hydrazine reagents with a triazine backbone. *Analytical and Bioanalytical Chemistry*, **372**(5-6), 639-643.

KIRK, J.M., TARBIN, J. and KEELY, B.J., 2006. Analysis of androgenic steroid Girard P hydrazones using multistage tandem mass spectrometry. *Rapid Communications in Mass Spectrometry*, **20**(8), 1247-1252.

LIU, Z., ZOU, H. and YE, M., 2001. Separation of 4-dimethylamino-6-(4-methoxy-1-naphthyl)-1,3,5-triazine-2-hydrazine derivatives of carbonyl compounds by reversed-phase capillary electrochromatography. *Electrophoresis*, **22**(7), 1298-1304.

MUGO, S.M. and BOTTARO, C.S., 2007. Rapid on-plate and one-pot derivatization of carbonyl compounds for enhanced detection by reactive matrix LDI-TOF MS using the tailor-made reactive matrix, 4-dimethylamino-6-(4-methoxy-1-naphthyl)-1,3,5-triazine-2-hydrazine (DMNTH). *Journal of Mass Spectrometry*, **42**(2), 206-217.

NAVEN, T.J.P. and HARVEY, D.J., 1996. Cationic Derivatization of Oligosaccharides with Girard's T Reagent for Improved Performance in Matrix-assisted Laser Desorption/Ionization and Electrospray Mass Spectrometry. *Rapid Communications in Mass Spectrometry*, **10**(7), 829-834.

SHACKLETON, C.H.L., CHUANG, H., KIM, J., DE LA TORRE, X. and SEGURA, J., 1997. Electrospray mass spectrometry of testosterone esters: Potential for use in doping control. *Steroids*, **62**(7), 523-529.

STROHALM, M., KAVAN, D., NOVAK, P., VOLNY, M. and HAVLICEK, V., 2010. mMass 3: A Cross-Platform Software Environment for Precise Analysis of Mass Spectrometric Data. *Analytical Chemistry*, **82**(11), 4648-4651

VOGEL, M., BÜLDT, A. and KARST, U., 2000. Hydrazine reagents as derivatizing agents in environmental analysis – a critical review. *Fresenius' journal of analytical chemistry*, **366**(8), 781-791.

ZAIKIN, V.G. and HALKET, J.M., 2006. Derivatization in mass spectrometry - 8. Soft ionization mass spectrometry of small molecules. *European Journal of Mass Spectrometry*, **12**(2), 79-115.

ZAIKIN, V.G. and HALKET, J.M., 2009. *A handbook of derivatives for mass spectrometry*. IM Publishing.

## Chapter 3

---

Monitoring the distribution of respiratory compounds in the lungs by MALDI-MSI

### **3.1. Introduction**

#### **3.1.1. Traditional methods of drug analysis in tissue sections**

##### **3.1.1.1. Whole Body Autoradiography**

Whole Body Autoradiography (WBA) is a technique that monitors the spatial distribution of radiolabelled compounds within whole body tissue sections and is commonly used during the early stages of drug discovery and development (Trim *et al.*, 2009). This technique is also a mandatory procedure for drug approval by the Food and Drug Administration (FDA).

Briefly, the technique involves the administration of a radiolabelled compound (commonly  $^{14}\text{C}$  or  $^3\text{H}$ ) to a laboratory animal (usually a rat), which is sacrificed a defined time post dose based on the compound's known pharmacokinetics. The intact carcass is snap-frozen, embedded in a frozen carboxymethylcellulose, and cryosectioned (Solon and Kraus 2001). Whole-body sections are then exposed to a radioactivity detector (x-ray film or phosphor imaging plates) which allows the visualisation of the spatial distribution of the radiolabelled compound. An example of the data produced by this technique is illustrated by two whole body autoradiograms shown in Figure 3.1.

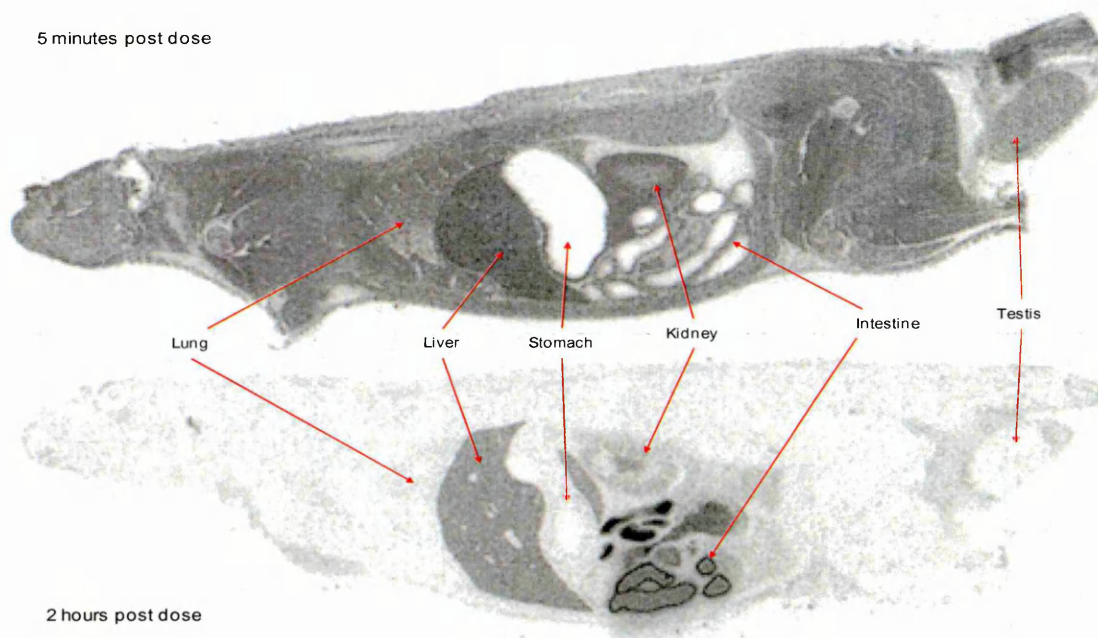


**Figure 3.1:** Whole body autoradiograms showing the distribution of <sup>14</sup>C-testosterone throughout the whole body section of a rat following intravenous administration, sacrificed 5 minutes and 2 hours post dose.

The advantages of this technique are parallel sample processing, standardised procedures, high sensitivity, and quantification (Stoeckli *et al.*, 2007). However, the disadvantages of this technique are that it requires the use of a radiolabelled candidate which is often expensive to synthesise and the inability to distinguish between the parent compound and metabolites.

#### 3.1.1.2. Liquid Chromatography-Tandem Mass Spectrometry

Liquid Chromatography-Tandem Mass Spectrometry (LC-MS/MS) can be used as a complement to WBA, it involves the excision of individual organs that are homogenised followed by extraction procedures. The extracts are then analysed by LC-MS/MS to determine the metabolites of a given compound, however during sample preparation the spatial distribution of the parent compound and metabolites is lost (Wang *et al.*, 2005).

### 3.1.2. Mass Spectrometry Imaging

#### 3.1.2.1. Matrix-Assisted Laser Desorption/Ionisation-Mass Spectrometry Imaging

Matrix-Assisted Laser Desorption/Ionisation-Mass Spectrometry Imaging (MALDI-MSI) is a label free technique that can simultaneously measure the distribution of both parent compound and metabolites throughout tissue sections.

The use of MALDI-MSI in pharmaceutical research has been on-going for over a decade and is currently being employed by some pharmaceutical companies as a complementary technique to QWBA and LC-MS/MS.

#### 3.1.2.2. MALDI-MSI in monitoring drug distribution

The first demonstration of the application of MALDI to directly study pharmaceutical compounds in animal tissue was reported by (Troendle *et al.*, in 1999). In this work the anticancer drug paclitaxel was detected in ovarian tumor xenografts and the antipsychotic drug spiperone was detected in spiked liver. However imaging experiments were not conducted in this work.

The first true MALDI-MSI experiment to monitor the distribution of pharmaceutical compounds in biological tissue sections was reported by (Reyzer *et al.*, 2003). In this work MALDI-MSI was applied to monitoring the distribution of a candidate antitumor drug (SCH226374) throughout a rat brain and tumour tissue sections.

Following these demonstrations the MALDI-MSI technique has been applied to monitoring the distribution of a wide range of pharmaceutical compounds throughout various tissues and is still used to this day (Prideaux and Stoeckli 2012).

The use of both MALDI-MSI and WBA techniques in mapping the distribution of the antipsychotic drug clozapine using these techniques was demonstrated by (Hsieh *et al.*, 2006). The resulting images revealed that the data from both techniques complemented each other.

MALDI-MSI was first applied to monitoring the distribution of a pharmaceutical compound throughout a whole-body tissue section in a mouse by (Rohner *et al.*, 2005). The resulting images showed the compound to be localised within the brain of the mouse.

This work was followed by a more in-depth study by (Stoeckli *et al.* 2007) and showed the distribution of an intra-tracheally administered compound throughout the whole-body tissue section of a rat. The images from MALDI-MSI and WBA show that after 5 minutes the compound is localised mainly within the trachea as expected and the stomach and after 1 hour the compound is localised within the nasal turbinates and the intestines.

The distribution of both parent compound and metabolites throughout whole-body tissue sections was reported by (Khatib-Shahidi *et al.* 2006) and showed the distribution of olanzapine and its metabolites throughout the whole-body tissue sections of a rat. These images showed high levels of olanzapine in the target organ (the brain) and two metabolites, *N*-desmethyloanzapine and 2-hydroxymethyl olanzapine which were detected within liver, kidney and bladder tissues indicating metabolism and excretion of the drug.

Recently, the use of ion mobility separation with MALDI-MS imaging to monitor the distribution of the anti-cancer drug vinblastine throughout the whole-body section of a rat following intravenous administration was demonstrated by (Trim *et al.*, 2009). These images showed that the distribution of vinblastine was within the liver and kidney. The utilisation of ion mobility separation allowed the

separation of vinblastine and its metabolites from interfering isobaric ions associated with endogenous species, thus increasing the confidence in the data obtained.

### 3.1.3. Aims and objectives

The aim of this study was to determine, for a set of respiratory compounds, the feasibility of analysing them by MALDI-MS imaging and to determine their on-tissue limit of detection. Then to monitor the distribution of a selected respiratory compound throughout the lungs following inhaled delivery by MALDI-MSI. A comparison of the datasets obtained from the analysis of samples on different instruments was also undertaken.

## **3.2. Methods**

### **3.2.1. Information**

All animal studies were ethically reviewed and carried out in accordance with Animals (Scientific Procedures) Act 1986 and the GSK Policy on the Care, Welfare and Treatment of Laboratory Animals.

### **3.2.2. Materials**

Alpha-cyano-4-hydroxycinnamic acid (CHCA), 2, 5-dihydroxybenzoic acid (DHB), ipratropium bromide, formoterol fumarate dihydrate and trifluoroacetic acid (TFA) were purchased from Sigma Aldrich (Gillingham, Dorset, UK). Methanol (MeOH) was purchased from Fisher Scientific (Loughborough, Leicestershire, UK). The respiratory compounds ambroxol, amiloride, budesonide, fluticasone furate, fluticasone propionate, flunisolide, formoterol, indacaterol, ipratropium bromide, lidocaine, nedocromil, salbutamol, tacrolimus and tiotropium bromide were kindly provided by GlaxoSmithKline (Stevenage, UK).

### **3.2.3. Dose preparation and administration**

The compound tiotropium was prepared by weighing out 1 mg of the compound into a large scintillation vial to which 4 ml of saline was added to make a 0.25mg/ml solution. 1 ml of the saline vehicle was placed into a large scintillation vial for use as a control. Three Wistar Han rats (male) were dosed under a light anaesthesia of 1 L/min O<sub>2</sub>, 2 L/min NO<sub>2</sub> and 5% isoflurane. The animals were held at a 45° angle for dosing and 200 µL of the dose was administered to the trachea 2-3 mm above the bifurcation point using a custom made IT dosing needle.

The rats were then sacrificed immediately after dosing and 15 minutes post dose, the vehicle control rat was also sacrificed 15 minutes post.

The 200 µg/kg dose level was selected so as to deliver a 50 µg topical dose of compound to the lung, to emulate the lung dose given in the published data (Nilsson *et al.*, 2010).

#### 3.2.4. Tissue preparation

The frozen rat lung tissue was mounted to a cryostat stage using a 1% w/v solution of carboxymethylcellulose in water. The frozen tissue was sectioned using a Leica CM3050 cryostat (Leica Microsystems, Wetzlar, Germany) to produce 16 µm thick sections. The sections were transferred and thaw-mounted onto indium tin oxide coated glass slides (Bruker Daltonics, Bremen, Germany) for analysis on the Ultraflex series of mass spectrometers or onto conventional glass microscope slides for the other SYNAPT and QSTAR instruments. The glass slide was then optically scanned in a Nikon Super CoolScan 500ED scanner fitted with a MA-21 slide-mount adapter (Nikon Corporation, Tokyo, Japan) to produce a digital image.

#### 3.2.5. Matrix deposition

The tissue sections were coated either with 7 mg/ml CHCA in 70:30 MeOH: H<sub>2</sub>O with 0.2 % TFA or 20 mg/ml DHB in 50:50 MeOH: H<sub>2</sub>O with 0.2 % TFA using the ImagePrep matrix application device (Bruker Daltonics, Bremen, Germany). Tissue sections were also coated with 5 mg/ml CHCA in 70:30 MeOH: H<sub>2</sub>O with 0.2% TFA using the Suncollect™ automated pneumatic sprayer (Sunchrom, Friedrichsdorf, Germany) in a series of layers. The initial seeding layer and subsequent layers were performed at 10 µl/minute.

### 3.2.6. Instrumentation

#### 3.2.6.1. MALDI-LIFT-MS/MS imaging

Analyses were performed on an Ultraflex extreme MALDI-TOF/TOF mass spectrometer (Bruker Daltonics) equipped with smart beam technology, a more detailed description was described by (Holle *et al.*, 2006). The digital image of the sections was imported into FlexImaging software (Bruker Daltonics), and through the software the instrument was taught the dimensions of the sections. The instrument was operated in LIFT MS/MS mode configuration with a potential of 19.10kV. The spatial resolution was run at 200  $\mu\text{m}$  x 200  $\mu\text{m}$ , with typical laser spot diameters of 75-80  $\mu\text{m}$ . The MS/MS data was acquired in the  $m/z$  range between 100 and 500. The acquisition method was calibrated using a peptide calibration mixture (Bruker Daltonics) before the start of the experiment. MS/MS data was automatically acquired using the FlexImaging software from a total of 200 spectra acquired at each spot position using the proprietary random walk mode in four 50-shot increments at a laser frequency of 1000Hz (Marshall *et al.*, 2010).

#### 3.2.6.2. MALDI-MS and MS/MS imaging

Mass spectra and images were acquired in positive ion mode on an Applied Biosystems/MDS Sciex hybrid quadrupole time-of-flight mass spectrometer (Q-Star Pulsar-*i*) with an orthogonal MALDI ion source (Applied Biosystems, Foster City, California, USA) and a high repetition Neodymium-doped yttrium vanadate (Nd: YVO<sub>4</sub>) laser (5 KHz) (Elforlight Ltd, Daventry, Northamptonshire, UK) a more detailed description is described elsewhere (Trim *et al.*, 2010). Image acquisition was performed at a spatial resolution of 150  $\mu\text{m}$  x 150  $\mu\text{m}$  in "Raster

Image” mode (Simmons 2008); images were generated using the freely available Novartis Biomap 3.7.5.5 software ([www.maldi-msi.org](http://www.maldi-msi.org)).

#### 3.2.6.3. MALDI-IMS-MS imaging

A Waters MALDI HDMS SYNAPT™ G2 mass spectrometer (Waters Corporation, Manchester, UK) was used to acquire mass spectra and images. Prior to MALDI-IMS-MSI analysis the samples were optically scanned using a CanoScan 4400F flatbed scanner (Canon, Reigate, UK) to produce a digital image for future reference, this image was then imported into the MALDI imaging pattern creator software (Waters Corporation) to define the region to be imaged. The instrument was calibrated prior to analysis using a standard mixture of polyethylene glycol (Sigma Aldrich). The instrument was operated in sensitivity mode and positive ion mode, all data was acquired with ion mobility separation in the mass range  $m/z$  100 to 1000. The data was then converted using MALDI imaging converter software (Waters Corporation) and visualised using BioMap 3.7.5.5 software.

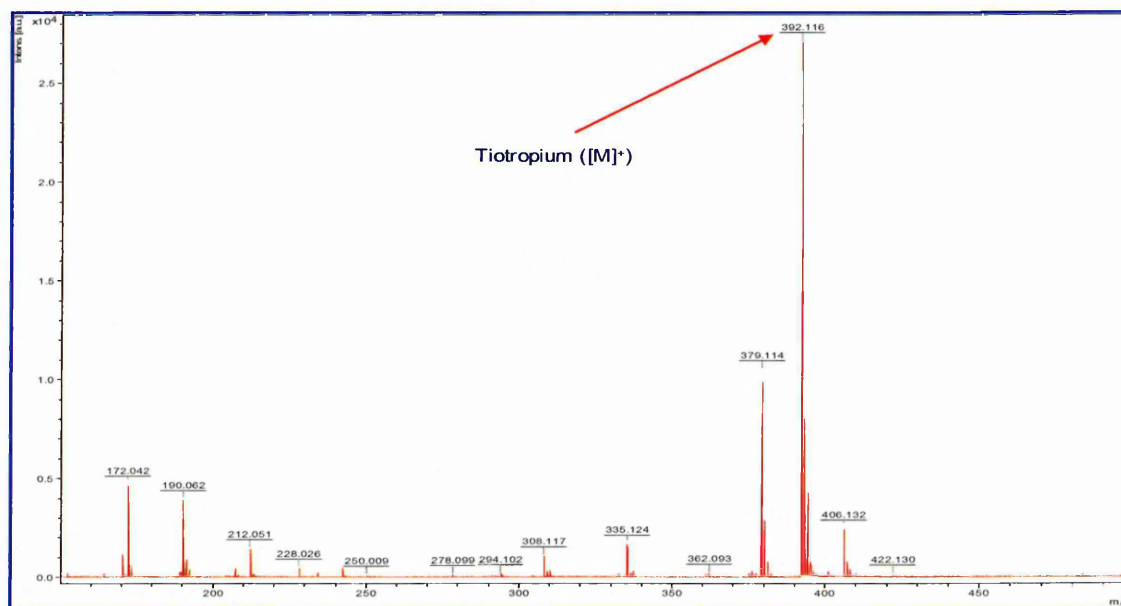
### 3.3. Results and Discussion

#### 3.3.1. Respiratory compound feasibility study

The purpose of the feasibility study was to screen a series of respiratory compounds to determine the on-tissue limit of detection. To begin serial dilutions of each compound were prepared and 1  $\mu\text{l}$  was spotted onto a stainless steel target plate, MS and MS/MS profiles were then obtained. Following this a dilution series of each compound was spotted onto a control rat lung tissue section and MALDI-LIFT-MS/MS imaging was performed.

A selection of the results obtained and later a summary of the results for all the respiratory compounds will be shown.

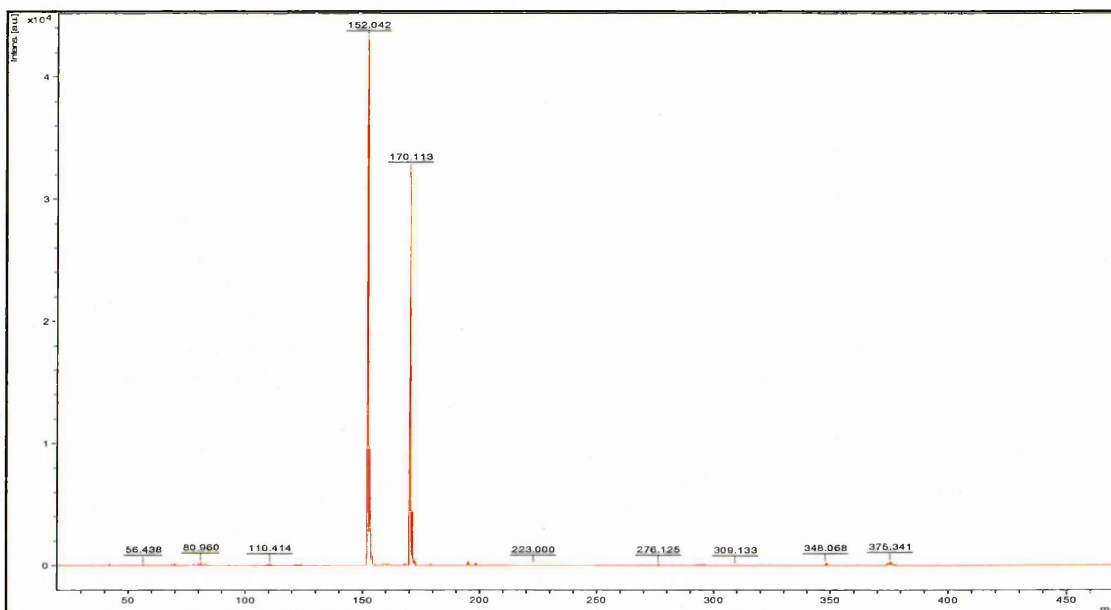
The MALDI-MS spectrum of tiotropium is shown below in Figure 3.2.



**Figure 3.2:** MALDI-MS spectrum showing tiotropium ( $[M]^+$ ) at  $m/z$  392.116 at a concentration of 100  $\text{ng}/\mu\text{l}$ .

The MALDI-MS spectrum of tiotropium bromide obtained from a stainless steel MALDI target plate, is shown in Figure 3.2. The spectrum revealed a strong peak at  $m/z$  392.116 that is clearly visible due to the positively charged nitrogen in the compounds structure.

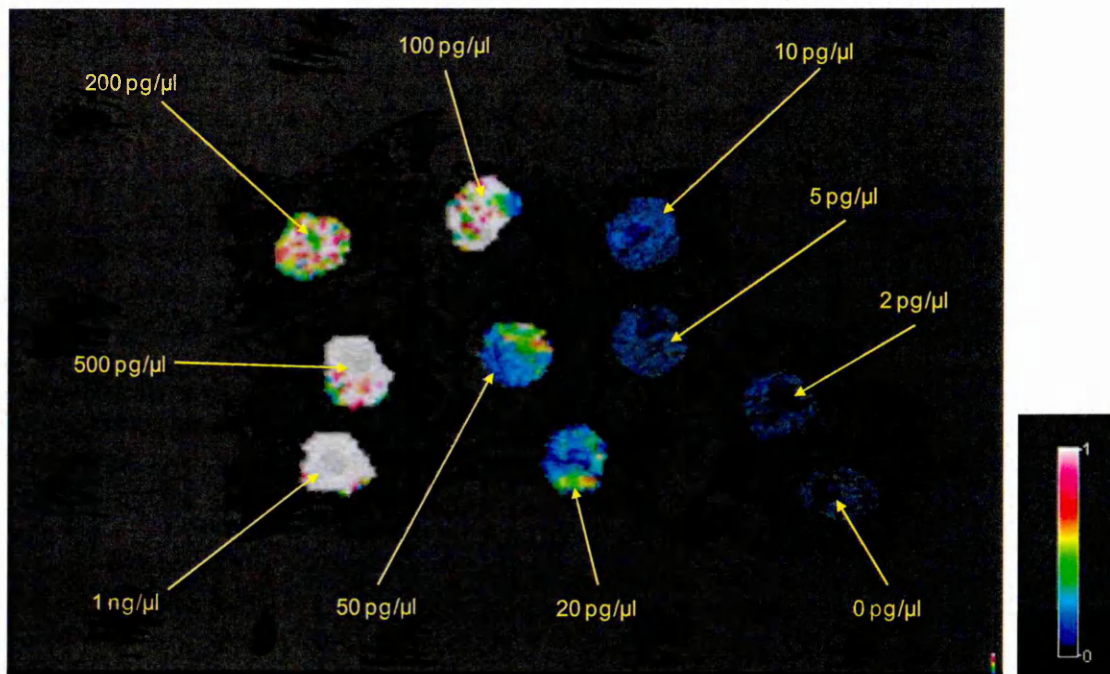
The MALDI-LIFT-MS/MS spectrum of tiotropium is shown below in Figure 3.3.



**Figure 3.3:** MALDI-LIFT-MS/MS spectrum showing the product ions at  $m/z$  152.042 and  $m/z$  170.113, derived from the precursor ion of tiotropium at  $m/z$  392 at a concentration of 100 ng/ $\mu$ l.

The MALDI-LIFT-MS/MS spectrum show in Figure 3.3 shows two product ions at  $m/z$  152.042 and 170.113, derived from the precursor ion of tiotropium at  $m/z$  392.

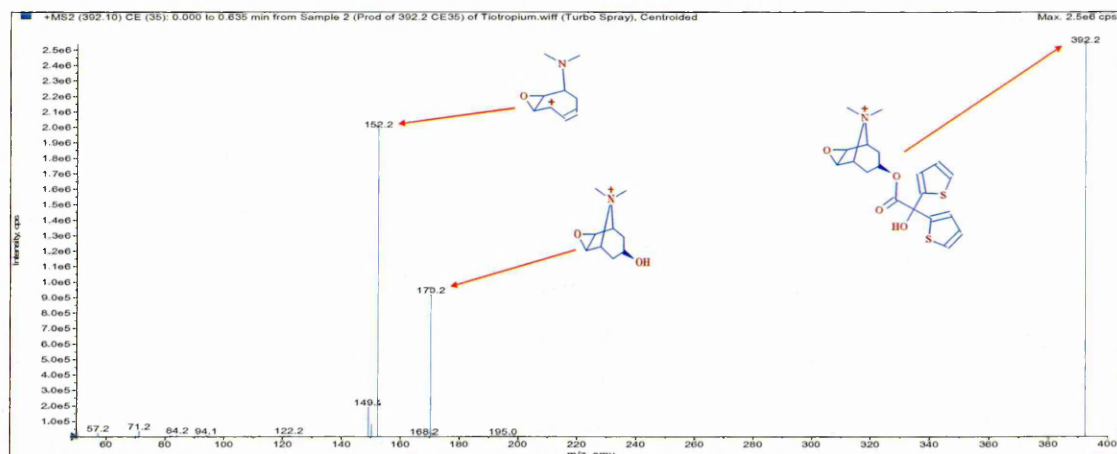
The MALDI-LIFT-MS/MS image of the tiotropium dilution series spotted on tissue is shown below in Figure 3.4.



**Figure 3.4:** MALDI-LIFT-MS/MS image showing the distribution of the product ion at  $m/z$  152, derived from the precursor ion of tiotropium at  $m/z$  392 (200  $\mu\text{m}$  spatial resolution).

The MALDI-LIFT-MS/MS image in Figure 3.4 shows the distribution of the product ion at  $m/z$  152, derived from the precursor ion of tiotropium at  $m/z$  392 to be within the spiked areas on the tissue section. The image shows no interference from the tissue as there is no signal from the blank and the approximate on-tissue limit of detection of tiotropium is 20  $\text{pg}/\mu\text{l}$ .

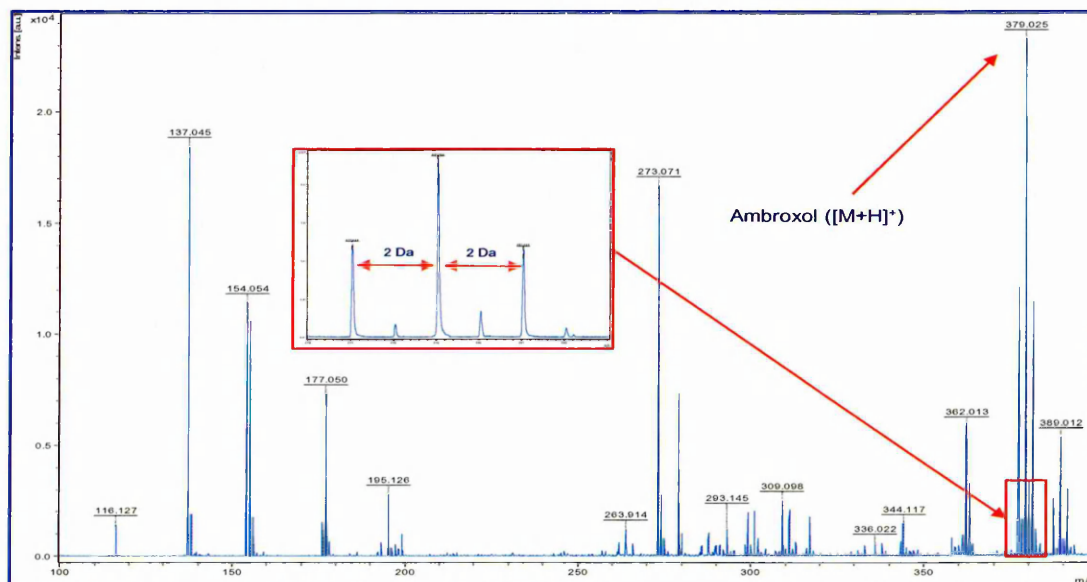
The ESI-MS/MS spectrum of tiotropium is shown below in Figure 3.5.



**Figure 3.5:** ESI-MS/MS spectrum showing the product ions at  $m/z$  152.2 and 170.2, derived from the precursor ion of tiotropium at  $m/z$  392.2 (100 ng/ml).

The ESI-MS/MS spectrum shown in Figure 3.5 shows the product ions at  $m/z$  152.2 and 170.2, derived from the precursor ion of tiotropium at  $m/z$  392.2. The structure of the product ions was determined using Mass Frontier 5.1 software. The two product ions also match those seen in the MALDI-LIFT-MS/MS spectrum.

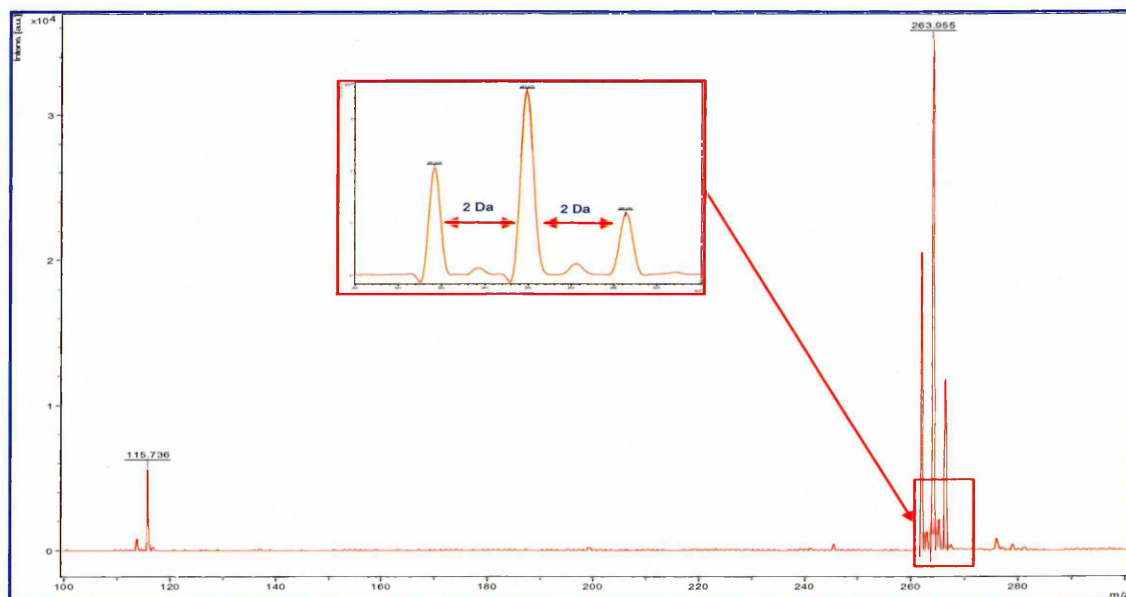
One of challenges in the analysis of low molecular weight compounds by MALDI-MS is spectral noise in the low mass region due to matrix related peaks causing isobaric interference (Krutchinsky and Chait 2002). However with careful matrix selection and sample preparation this problem can be overcome. Isobaric interference was observed for the analysis of one of the respiratory compounds, ambroxol. This compound contains two bromines and there should be a cluster of peaks with a characteristic 1:2:1 ratio, which should be separated by 2 Da (Due to the bromine isotopic distribution for a compound that contains two bromines). There was a peak observed at  $m/z$  379, which was initially thought to be the most abundant ion in this cluster of peaks. However ambroxol was initially analysed using the matrix CHCA which when analysed also has a peak at  $m/z$  379 related to the matrix dimer ( $[2M+H]^+$ ), this isobaric interference was confirmed by MS/MS. Therefore the compound was analysed using the matrix DHB the mass spectrum of which is shown below in Figure 3.6.



**Figure 3.6:** MALDI-MS spectrum showing ambroxol (100 ng/ $\mu$ l) analysed using the matrix 2,5-Dihydroxybenzoic acid (DHB). The spectrum shows the presence of a peak at  $m/z$  379.025.

The MALDI-MS spectrum shown in Figure 3.6 shows a peak at  $m/z$  379.025 the isotopic distribution of this peak shows the compound could possibly have two bromines in structure, which confirms this is the ambroxol ( $[M+H]^+$ ).

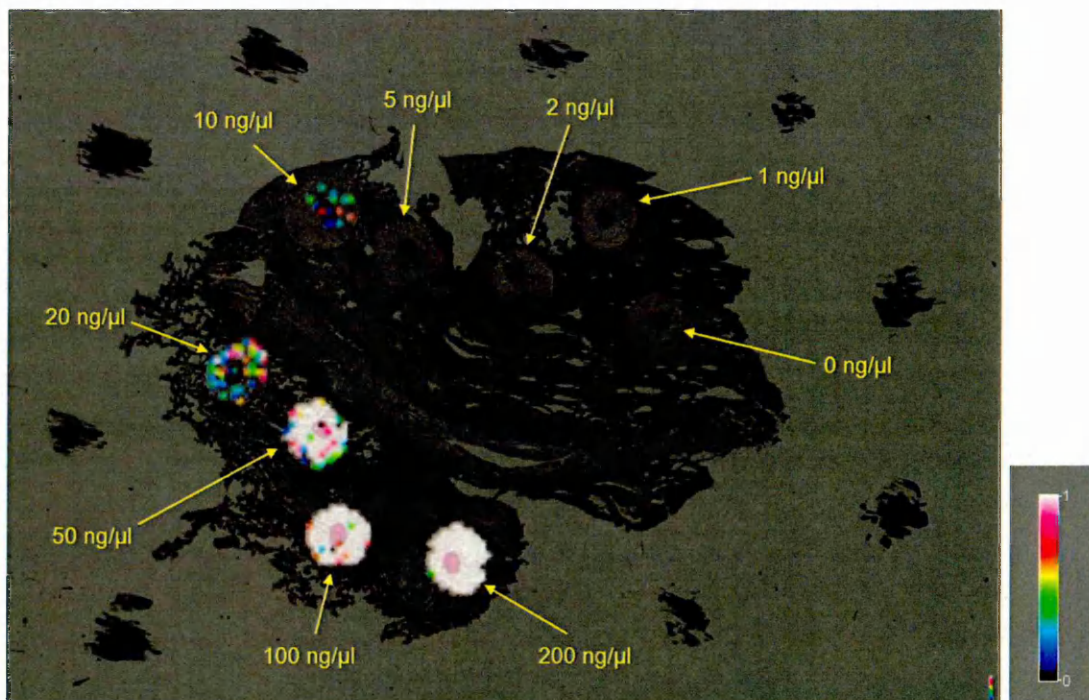
The MALDI-LIFT-MS/MS spectrum of ambroxol is shown below in Figure 3.7.



**Figure 3.7:** MALDI-LIFT-MS/MS spectrum showing the product ions at  $m/z$  115.736 and 263.955, derived from the precursor ion of ambroxol at  $m/z$  379.025 (100 ng/ $\mu$ l).

The MALDI-LIFT MS/MS spectrum shown in Figure 3.7 shows two product ions at  $m/z$  115.736 and 263.955, derived from the precursor ion of ambroxol at  $m/z$  379.025. The product ion at  $m/z$  263.955 has the same isotopic distribution as previous shown in the mass spectrum as shown in Figure 3.6, indicating the presence of two bromine atoms.

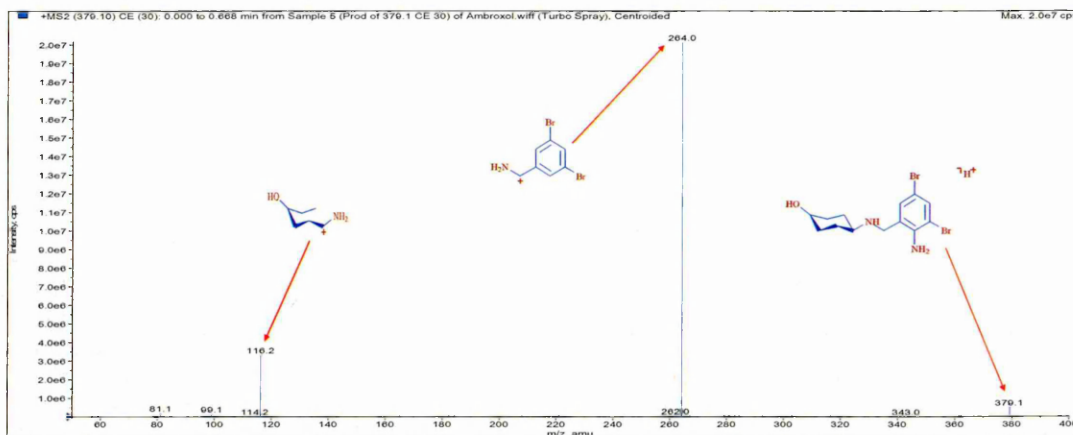
The MALDI-LIFT-MS/MS image of the ambroxol dilution series spotted onto a control rat lung tissue section is shown below in Figure 3.8.



**Figure 3.8:** MALDI-LIFT-MS/MS image showing the distribution of the product ion at  $m/z$  264, derived from the precursor ion of ambroxol at  $m/z$  379.

The MALDI-LIFT-MS/MS image shown in Figure 3.8 shows the distribution of the product ion at  $m/z$  264 derived from the precursor ion of ambroxol at  $m/z$  379 to be located within all of the spiked areas on the tissue section. The lack of signal in the blank region indicates image shows no interference from the tissue, approximate on-tissue limit of detection is 10 ng/μl.

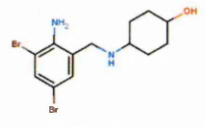
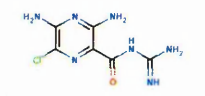
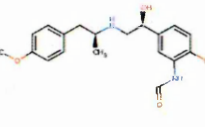
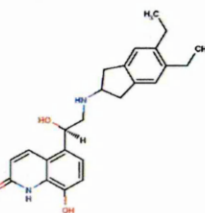
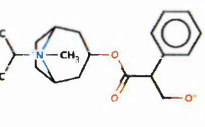
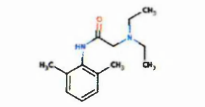
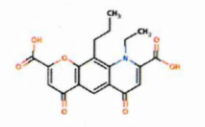
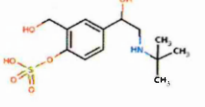
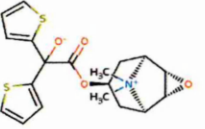
The ESI-MS/MS spectrum of ambroxol is shown below in Figure 3.9.



**Figure 3.9:** ESI-MS/MS spectrum showing the product ions at  $m/z$  116.2 and 264.0, derived from the precursor ion of ambroxol at  $m/z$  379.1 (1  $\mu\text{g/ml}$ ).

The ESI-MS/MS spectrum shown in Figure 3.9 shows the product ions at  $m/z$  116.2 and 264.0, derived from the precursor ion of ambroxol at  $m/z$  379.1. The structure of the product ions was determined using Mass Frontier 5.1 software. The data supports the previous observation in the MALDI-MS/MS spectrum that the product ion at  $m/z$  264 contains two bromines, the two product ions also match those seen in the MALDI-LIFT-MS/MS spectrum.

The results from the feasibility study of the all the respiratory compounds are shown below in Table 3.1.

| Compound Name (IUPAC)  | Compound Structure  | Formula  | Monoisotopic Mass                                     | On-tissue LOD |
|--|---|--|---|---------------|
| Ambroxol<br><i>trans</i> -4-(2-Amino-3,5-dibrombenzylamino)-cyclohexanol   |    | C <sub>13</sub> H <sub>18</sub> Br <sub>2</sub> N <sub>2</sub> O | 375.978585  | 10 ng/μL      |
| Amiloride<br>3,5-diamino-6-chloro-N-(diaminomethylidene)pyrazine-2-carboxamide   |    | C <sub>6</sub> H <sub>6</sub> ClN <sub>6</sub> O                 | 229.047886  | 5 ng/μL       |
| Formoterol<br>N-[2-hydroxy-5-(1-hydroxy-2-[(1-(4-methoxyphenyl)propan-2-yl)amino]ethyl)phenyl]formamide  |    | C <sub>18</sub> H <sub>22</sub> N <sub>2</sub> O <sub>4</sub>    | 344.173608  | 1 ng/μL       |
| Indacaterol<br>5-((1 <i>R</i> )-2-((5,6-diethyl-2,3-dihydro-1 <i>H</i> -inden-2-yl)amino)-1-hydroxyethyl)-8-hydroxy-1,2-dihydroquinolin-2-one  |    | C <sub>27</sub> H <sub>32</sub> N <sub>2</sub> O <sub>3</sub>    | 392.209993  | 1 ng/μL       |
| Ipratropium Bromide<br>(1 <i>R</i> ,3 <i>R</i> ,5 <i>S</i> ,8 <i>R</i> )-3-((3-hydroxy-2-phenylpropanoyl)oxy)-8-methyl-8-(propan-2-yl)-8-azabicyclo[3.2.1]octan-8-ium bromide                        |  | C <sub>23</sub> H <sub>33</sub> BrNO <sub>3</sub>                | 411.140905<br>332.222569 (Observed as free base form) | 0.02 ng/ μL   |
| Lidocaine<br>2-(diethylamino)-N-(2,6-dimethylphenyl)acetamide  |  | C <sub>14</sub> H <sub>22</sub> N <sub>2</sub> O                 | 234.173213  | 5 ng/μL       |
| Nedocromil<br>9-ethyl-4,6-dioxo-10-propyl-4 <i>H</i> ,6 <i>H</i> ,9 <i>H</i> -chromeno[7,6- <i>b</i> ]pyridine-2,8-dicarboxylic acid   |  | C <sub>18</sub> H <sub>17</sub> NO <sub>7</sub>                  | 371.100504  | 10 ng/μL      |
| Salbutamol<br>4-[2-(tert-butylamino)-1-hydroxyethyl]-2-(hydroxymethyl)phenol   |  | C <sub>13</sub> H <sub>21</sub> NO <sub>3</sub>                  | 239.152144  | 10 ng/μL      |
| Tiotropium Bromide<br>(1 <i>R</i> ,2 <i>S</i> ,4 <i>R</i> ,5 <i>S</i> )-7-[[2-hydroxy-2,2-bis(thiophen-2-yl)acetyl]oxy]-9,9-dimethyl-3-oxa-9-azatricyclo[3.3.1.0 <sup>2,4</sup> ]nonan-9-ium bromide |  | C <sub>26</sub> H <sub>27</sub> BrNO <sub>5</sub> S <sub>2</sub> | 471.017364<br>392.099028 (Observed as free base form) | 0.02 ng/ μL   |

**Table 3.1:** A table summarising the results from the feasibility study on a range of respiratory compounds and the determined on tissue limit of detection.

### 3.3.2. MALDI-MS and MS/MS imaging of tiotropium in lung tissue sections

From the results obtained from the feasibility study it was clear that the anticholinergic bronchodilators ipratropium and tiotropium were the best candidates for further study, however the latter was chosen based on recently published data (Fehniger *et al.*, 2011, Nilsson *et al.*, 2010).

#### 3.3.2.1. MALDI-MS and MS/MS images

The MALDI-MS and MS/MS images of tiotropium from consecutive rat lung tissue sections performed on the Q-Star mass spectrometer are shown below in Figure 3.10.

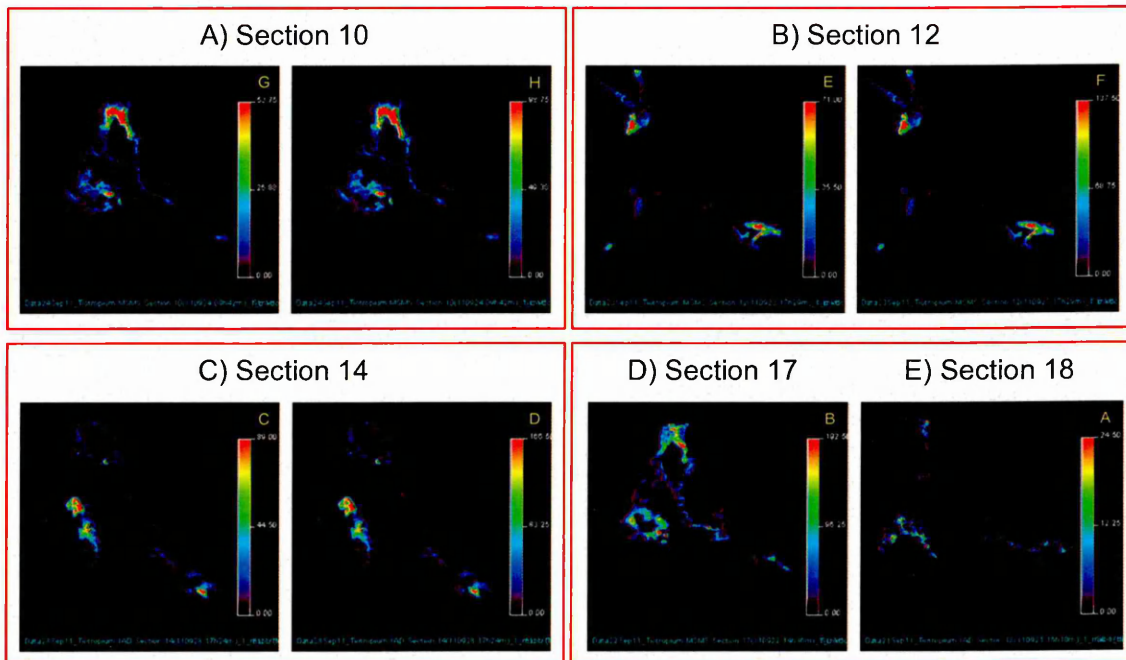


**Figure 3.10:** MALDI-MS and MALDI-MS/MS Images showing the distribution of A) product ions at  $m/z$  152 and 170, B) product ions at  $m/z$  152 and 170, C) product ions at  $m/z$  152 and 170, D) tiotropium ( $[M]^+$ ) at  $m/z$  392 and E) product ion at  $m/z$  152 (Spatial resolution 100  $\mu\text{m}$ ).

The MALDI-MS and MS/MS images shown in Figure 3.10 shows the distribution of tiotropium ( $[M]^+$ ) at  $m/z$  392 and the product ions at  $m/z$  152 and  $m/z$  170,

derived from the precursor ion of tiotropium at  $m/z$  392. The images show the compound is localised in the trachea and major airways.

### 3.3.2.2. MALDI-IMS-MS images

The MALDI-IMS-MS images from a rat lung tissue section acquired on the SYNAPT instrument are shown below in Figure 3.11.

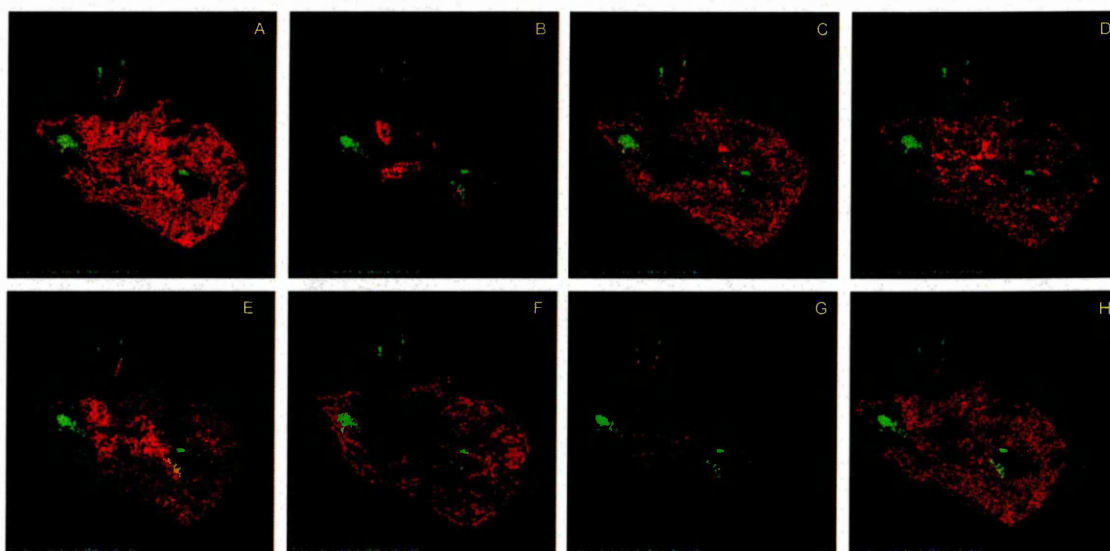


**Figure 3.11:** MALDI-IMS-MS Images showing the distribution of tiotropium ( $[M]^+$ ) at  $m/z$  392 (green) in relation to endogenous species (red) such as A) phosphocholine at  $m/z$  184, B) unidentified species at  $m/z$  241, C) unidentified species at  $m/z$  478, D) heme group of haemoglobin at  $m/z$  616, E) unidentified species at  $m/z$  710, F) unidentified species at  $m/z$  772, G) unidentified species at  $m/z$  380, and H) choline at  $m/z$  104 (Spatial resolution  $100\ \mu\text{m}$ ).

The MALDI-MS images displayed in Figure 3.11 shows the distribution of tiotropium ( $[M]^+$ ) at  $m/z$  392 (green). The images show the compound is localised in the trachea and major airways. The images showing the distribution of the compound have been overlaid onto other MALDI-MS images showing the

distribution of endogenous species (red), to show the location of the drug in relation to the different sub-structures of the lungs, for example the image shown in Figure 3.11G shows the distribution of an unidentified peak at  $m/z$  872 which appears to be related to the cartilaginous rings of the trachea and major airways.

### 3.3.2.3. MALDI-LIFT-MS/MS images

The MALDI-LIFT-MS/MS images of consecutive rat lung tissue sections taken immediately after dosing are shown below in Figure 3.12.

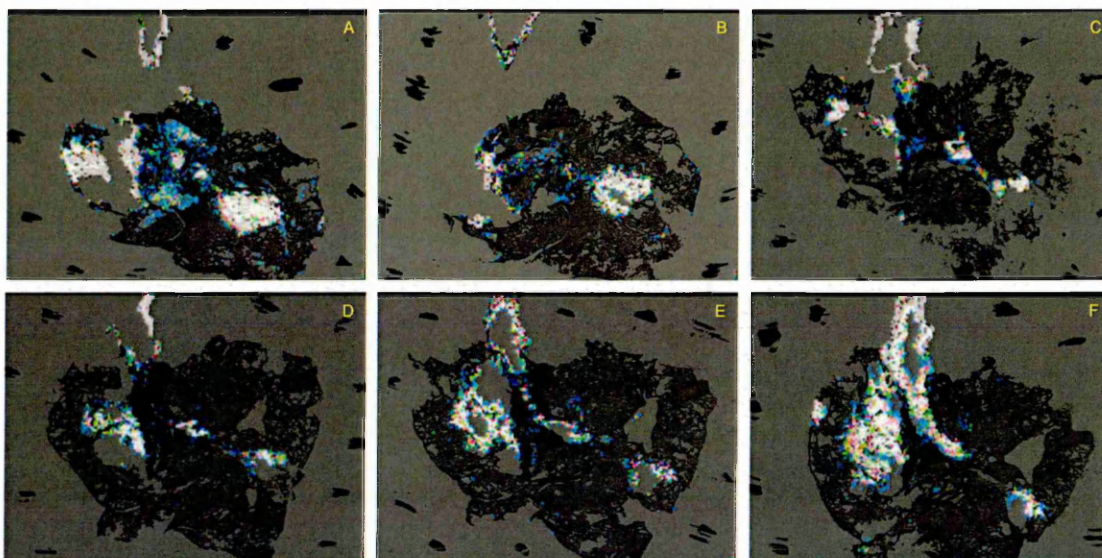


**Figure 3.12:** MALDI-LIFT-MS/MS Images showing the distribution of the product ion at  $m/z$  152, derived from the precursor ion of tiotropium at  $m/z$  392. Consecutive sections showing A) section 11, B) section 12, C) section 15, D) section 16, E) section 17 and F) section 18 (Spatial resolution  $200\ \mu\text{m}$ ).

The MALDI-LIFT-MS/MS images shown in Figure 3.12 shows the distribution of the product ion at  $m/z$  152, derived from the precursor ion of tiotropium at  $m/z$  392 throughout consecutive tissue sections. Again the images shows the compound is localised in the trachea and major airways, the distribution of drug

was overlaid onto the corresponding optical images to show the localisation of the compound within the tissue section.

### 3.3.3. High spatial resolution imaging of tiotropium in lung tissue sections

#### 3.3.3.1. MALDI-IMS-MS images

Following analysis of the lung tissue section, areas of interest were selected and high spatial resolution imaging experiments (30  $\mu\text{m}$ ) were conducted on regions corresponding to the trachea and major airways of consecutive tissue sections, to obtain more detailed information on the drug distribution in these areas. The high spatial resolution MALDI-IMS-MS images of the trachea and major airway acquired on the SYNAPT instrument are shown below in Figure 3.13.

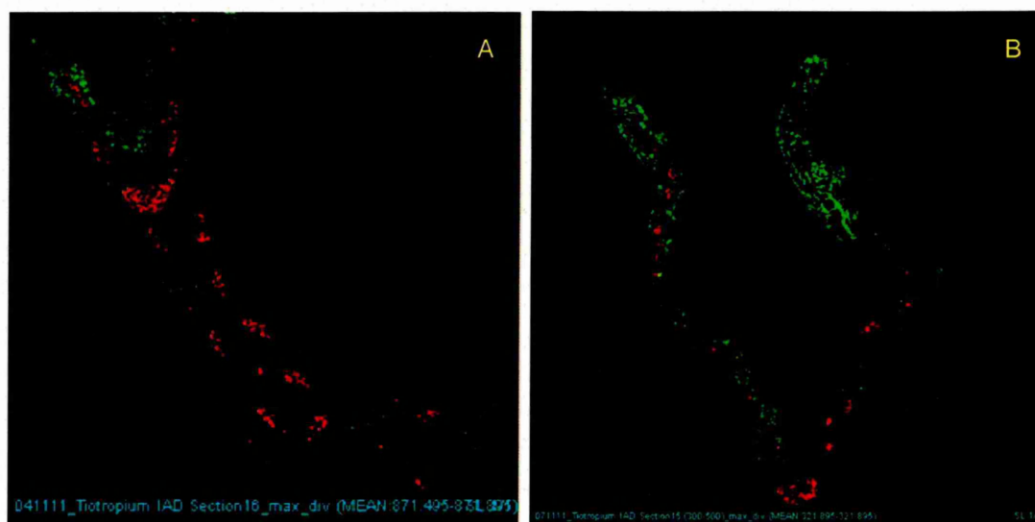


**Figure 3.13:** MALDI-IMS-MS Images showing the distribution of tiotropium ( $[M]^+$ ) at  $m/z$  392 (green) in relation to the endogenous species at  $m/z$  872 (red). (30  $\mu\text{m}$  spatial resolution).

The high spatial resolution MALDI-MS images displayed in Figure 3.13 shows the distribution of tiotropium ( $[M]^+$ ) at  $m/z$  392 (green) overlaid onto the distribution of an unknown endogenous component at  $m/z$  872 (red) that was

localised in the cartilage rings of the trachea and airways. The images were normalised against the protonated CHCA matrix ( $[M+H]^+$ ) at  $m/z$  190.

### 3.3.3.2. MALDI-LIFT-MS/MS images

The high spatial resolution (30  $\mu\text{m}$ ) MALDI-LIFT-MS/MS images of the trachea and major airway of rat lung tissue acquired on the UltrafleXtreme instrument are displayed below in Figure 3.14.

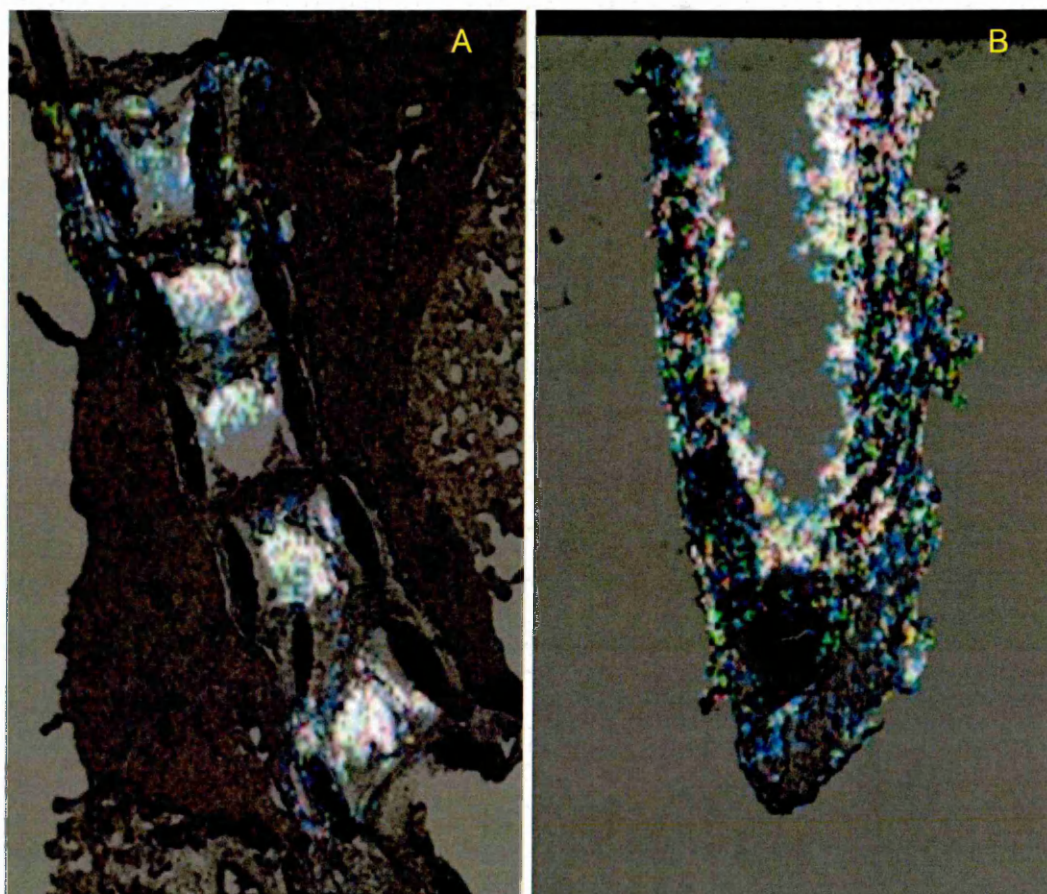


**Figure 3.14:** MALDI-LIFT-MS/MS images showing the distribution of the product ion at  $m/z$  152, derived from the precursor ion of tiotropium at  $m/z$  392 throughout A) the major airway and B) the trachea (30  $\mu\text{m}$  spatial resolution).

The high spatial resolution (30  $\mu\text{m}$ ) MALDI-LIFT-MS/MS images shown in Figure 3.14 shows the distribution of the product ion at  $m/z$  152, derived from the precursor ion of tiotropium at  $m/z$  392 within the trachea and major airways,

the distribution of drug was overlaid onto the corresponding optical images. The image shown in Figure 3.14A shows the drug in the major airway and the image shown in Figure 3.14B demonstrate the compound is localised in the trachea but it appears the drug has begun to diffuse into the surrounding tissue.

### 3.3.3.3. MALDI-MS/MS images

The high spatial resolution (50  $\mu\text{m}$ ) MALDI-MS/MS images obtained on the QSTAR instrument of the trachea are shown below in Figure 3.15.

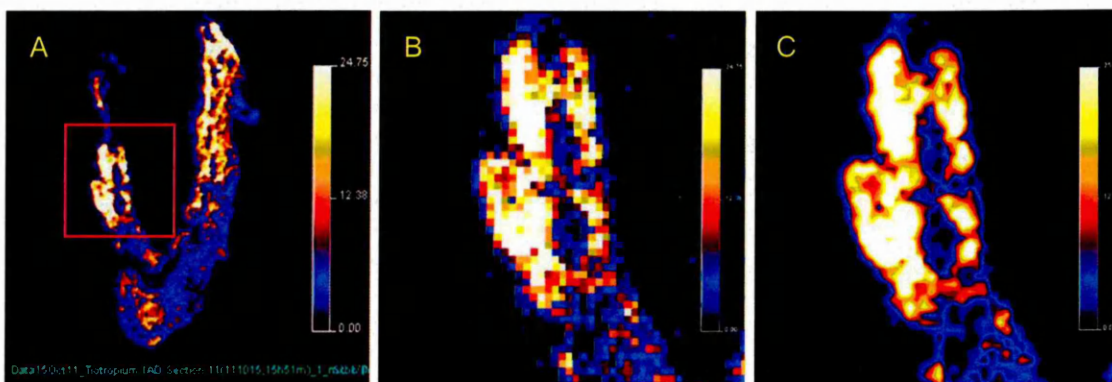


**Figure 3.15:** MALDI-MS/MS images showing A) the distribution of the product ion at  $m/z$  152, derived from the precursor ion of tiotropium at  $m/z$  392. The distribution of the compound is localised in the trachea immediately after intratracheal dosing. The expanded images show B) the data presented prior to smoothing and C) following smoothing (50  $\mu\text{m}$  spatial resolution).

The high spatial resolution (50  $\mu\text{m}$ ) MALDI-MS/MS images shown in Figure 3.15 shows the distribution of the product ion at  $m/z$  152, derived from the precursor ion of tiotropium at  $m/z$  392 within the trachea. The image shown in Figure 3.15A shows the distribution of the product ion at  $m/z$  152 throughout the trachea, the expanded images shown in Figures 3.15B and C shows the selected region before and after smoothing respectively.

### **3.4. Conclusions**

The feasibility study utilising MALDI-MS, LIFT-MS/MS and MSI has enabled the screening of a number of respiratory compounds and has provided information on the on-tissue limits of detection and appropriate matrix to be used for analysis. This information was then used to select the most appropriate respiratory compound in this case tiotropium bromide for further study, this compound was also selected based on recently published data.

One of the challenges with the use of MALDI-MSI in the analysis of pharmaceutical compounds is matrix related peaks causing interference, which was observed with the analysis of ambroxol. In the case of this study careful matrix selection was used to solve this problem.

MALDI-MS and MS/MS imaging has successfully been utilised to show the distribution of the anticholinergic bronchodilator tiotropium throughout the lungs following intratracheal delivery. The drug was found to be localised with the trachea and major airways immediately after dosing. High spatial resolution imaging has enabled a detailed view of the distribution of tiotropium in these areas.

The data sets obtained from the analysis of samples on three different types of instruments correlated well with each other. However due to problems with tissue sectioning of the 15 minute post dose rat lung tissue no data was obtained.

### 3.5. References

FEHNIGER, T.E., VÄGVÄRI, Å., REZELI, M., PRIKK, K., ROSS, P., DAHLBÄCK, M., EDULA, G., SEPPER, R. and MARKO-VARGA, G., 2011. Direct demonstration of tissue uptake of an inhaled drug: Proof-of-principle study using matrix-assisted laser desorption ionization mass spectrometry imaging. *Analytical Chemistry*, **83**(21), 8329-8336.

HOLLE, A., HAASE, A., KAYSER, M. and HOEHNDORF, J., 2006. Optimizing UV laser focus profiles for improved MALDI performance. *Journal of Mass Spectrometry*, **41**(6), 705-716.

HSIEH, Y., CASALE, R., FUKUDA, E., CHEN, J.W., KNEMEYER, I., WINGATE, J., MORRISON, R. and KORFMACHER, W., 2006. Matrix-assisted laser desorption/ionization imaging mass spectrometry for direct measurement of clozapine in rat brain tissue. *Rapid Communications in Mass Spectrometry*, **20**(6), 965-972.

KHATIB-SHAHIDI, S., ANDERSSON, M., HERMAN, J.L., GILLESPIE, T.A. and CAPRIOLI, R.M., 2006. Direct molecular analysis of whole-body animal tissue sections by imaging MALDI mass spectrometry. *Analytical Chemistry*, **78**(18), 6448-6456.

KRUTCHINSKY, A.N. and CHAIT, B.T., 2002. On the nature of the chemical noise in MALDI mass spectra. *Journal of the American Society for Mass Spectrometry*, **13**(2), 129-134.

NILSSON, A., FEHNIGER, T.E., GUSTAVSSON, L., ANDERSSON, M., KENNE, K., MARKO-VARGA, G. and ANDREN, P.E., 2010. Fine mapping the

spatial distribution and concentration of unlabeled drugs within tissue micro-compartments using imaging mass spectrometry. *Plos One*, **5**(7), e11411.

PRIDEAUX, B. and STOECKLI, M., 2012. Mass spectrometry imaging for drug distribution studies. *Journal of Proteomics*, **75**(16), 4999-5013.

PRIDEAUX, B., DARTOIS, V., STAAB, D., WEINER, D.M., GOH, A., VIA, L.E., BARRY, C.E.,III and STOECKLI, M., 2011. High-sensitivity MALDI-MRM-MS imaging of moxifloxacin distribution in tuberculosis-infected rabbit lungs and granulomatous lesions. *Analytical Chemistry*, **83**(6),

REYZER, M., HSIEH, Y., NG, K., KORFMACHER, W. and CAPRIOLI, R., 2003. Direct analysis of drug candidates in tissue by matrix-assisted laser desorption/ionization mass spectrometry. *Journal of Mass Spectrometry*, **38**(10), 1081-1092.

ROHNER, T.C., STAAB, D. and STOECKLI, M., 2005. MALDI mass spectrometric imaging of biological tissue sections. *Mechanisms of ageing and development*, **126**(1),.

SIMMONS, D.A., 2008. Improved MALDI-MS imaging performance using continuous laser rastering. *AB technical note*.

SOLON, E.G. and KRAUS, L., 2001. Quantitative whole-body autoradiography in the pharmaceutical industry: Survey results on study design, methods, and regulatory compliance. *Journal of Pharmacological and Toxicological Methods*, **46**(2), 73-81.

STOECKLI, M., STAAB, D. and SCHWEITZER, A., 2007. Compound and metabolite distribution measured by MALDI mass spectrometric imaging in

whole-body tissue sections. *International Journal of Mass Spectrometry*, **260**(2–3), 195-202.

TRIM, P.J., ATKINSON, S.J., PRINCIVALLE, A.P., MARSHALL, P.S., WEST, A. and CLENCH, M.R., 2008. Matrix-assisted laser desorption/ionisation mass spectrometry imaging of lipids in rat brain tissue with integrated unsupervised and supervised multivariate statistical analysis. *Rapid Communications in Mass Spectrometry*, **22**(10), 1503-1509.

TRIM, P.J., DJIDJA, M., ATKINSON, S.J., OAKES, K., COLE, L.M., ANDERSON, D.M.G., HART, P.J., FRANCESE, S. and CLENCH, M.R., 2010. Introduction of a 20 kHz Nd:YVO<sub>4</sub> laser into a hybrid quadrupole time-of-flight mass spectrometer for MALDI-MS imaging. *Analytical and Bioanalytical Chemistry*, **397**(8),

TROENDLE, F.J., REDDICK, C.D. and YOST, R.A., 1999. Detection of pharmaceutical compounds in tissue by matrix-assisted laser desorption/ionization and laser desorption/chemical ionization tandem mass spectrometry with a quadrupole ion trap. *Journal of the American Society for Mass Spectrometry*, **10**(12), 1315-1321.

## **Chapter 4**

---

Development of methodology for the quantitation of pharmaceuticals in tissue sections by MALDI-MSI

## 4.1. Introduction

### 4.1.1. Traditional methods for the quantitation of drugs in tissue sections

#### 4.1.1.1 Quantitative Whole Body Autoradiography

Quantitative whole body autoradiography (QWBA) is an extension of the WBA technique discussed earlier in Chapter 3, which monitors the distribution of a radio-labelled compound throughout whole body tissue sections of a rat. Quantitation is achieved using commercially available radiolabelled standards or using the method developed by (Schweitzer *et al.*, 1987) in which whole blood is spiked with serial dilutions of the radio-labelled compound and embedded in carboxymethylcellulose with the animal, as shown below in Figure 4.1.

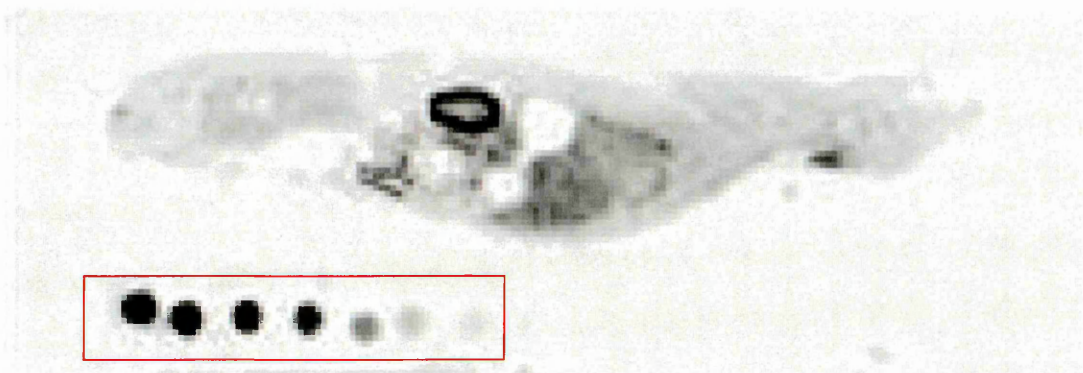


**Figure 4.1:** Whole body autoradiogram showing the distribution of a radio-labelled compound throughout the whole body section of a rat. The highlighted region shows the spiked whole blood standards used for quantitation ([www.biospace.com](http://www.biospace.com)).

The advantages of this technique are that it is quantitative through the use of radio-labelled standards and produces images with good spatial resolution (50-100  $\mu\text{m}$ ). However as previously mentioned the disadvantages of this technique are that it only monitors the distribution of the radio-labelled material; it cannot distinguish between parent compound and its associated metabolites, which

complicates the interpretation of the images. Also the technique is time consuming as images can take several days or up to a week to develop as opposed to MALDI images taking a few hours to produce. It is also a costly technique requiring expensive equipment and the synthesis of the radiolabelled drug (Solon *et al.*, 2009).

#### 4.1.1.2. Tissue homogenisation followed by LC-MS/MS

Liquid Chromatography-Tandem Mass Spectrometry (LC-MS/MS) is a technique routinely employed in the pharmaceutical industry to both identify and quantify drugs and related compounds in biological tissues. This method requires the entire tissue to be homogenised, followed by sample extraction procedures. The ability to monitor the spatial distribution of the parent compound and associated metabolites is then lost during this process. The technique also assumes that the tissue is homogeneous and does not take into account the various compartments of a particular tissue (Castellino *et al.*, 2011, Wang *et al.*, 2005).

#### 4.1.2. Quantitation by MALDI-MSI

The advantages of MALDI-MSI are that it is a label free technique, it can simultaneously monitor the distribution of parent compound and metabolites and produce high spatial resolution images (<30  $\mu\text{m}$ ). The technique also maintains the spatial orientation of the compound and its metabolites within a tissue section and can produce images faster than the QWBA technique. These factors may make MALDI-MSI an amenable technique for the quantitation of pharmaceuticals in tissue sections.

However there are several issues that need to be addressed if quantitative information is to be generated by MALDI-MSI. These include tissue related ion suppression, substance specific ionisation yield and matrix deposition (Stoeckli *et al.*, 2007).

Tissue related ion suppression occurs due to the drug being situated in a complex environment and as a result there is an ionisation competition between the analyte and endogenous species such as lipids (Hamm *et al.*, 2012a, Prideaux and Stoeckli 2012).

This phenomenon has been demonstrated by coating an entire whole body rat section with a compound solution using a pneumatic sprayer, which was then analysed by MALDI-MSI. The resulting image showed differences in ion signal intensity of the compound in different organs (Stoeckli *et al.*, 2007).

In order to correct for this (Hamm *et al.*, 2012a) developed a normalisation factor called the tissue extinction coefficient (TEC) to take into account the ion suppression effect, based on the initial work reported by (Stoeckli *et al.*, 2007).

This method involves homogenously coating a control tissue section with the matrix containing the analyte of interest, the coated tissue section is then analysed. Following analysis regions of interest are selected on and off the tissue section, the TEC is calculated by determining the average intensity of a region on the tissue and dividing it by that of a region off the tissue. A dilution series of the analyte of interest is placed next to the dosed tissue, which are then coated with the matrix and analysed. The average intensity of the analyte of interest in a tissue section is determined and then multiplied by the TEC value. Using the dilution series a calibration curve is then produced and used to determine the amount of drug in the dosed tissue section.

This method was used for the quantitation of olanzapine in rat kidney sections and propranolol in multiple organs of a whole body section of a mouse by (Hamm *et al.*, 2012b). The results showed good correlation to those produced by validated techniques such as LC-MS/MS and QWBA.

Signal variation within a sample can also be caused by inhomogeneous matrix coverage and crystal formation. This can be solved by careful matrix selection and preparation, also by the use of modern matrix deposition devices that are capable of providing reproducible and homogeneous matrix deposition.

Another limitation with the quantitative analysis of pharmaceutical compounds by MALDI-MSI is isobaric interference from the MALDI matrix and/ or endogenous species present in the sample. Such interferences can be overcome by careful matrix selection, the use of mass spectrometers with high resolving power such as Fourier transform ion cyclotron resonance mass spectrometry (FT-ICR-MS) or the use of ion mobility separation (discussed in detail in Chapter 1). The use of FT-ICR-MS for the analysis of pharmaceutical compounds was reported by (Cornett *et al.*, 2008) for the analysis of olanzapine and its two major metabolites within rat liver and kidney tissue sections. The use of ion mobility separation in pharmaceutical research was reported by (Trim *et al.*, 2009). In this work the utilisation of ion mobility separation allowed the differentiation of the anti-cancer drug vinblastine and its metabolites from interfering isobaric ions associated with endogenous species, thus increasing the confidence in the resulting data.

#### 4.1.3. Previous examples of quantitation by MALDI-MSI

MALDI-MSI has always been regarded as a qualitative technique, however several methods showing the possibility of obtaining quantitative information have been published.

It has been shown that spotting serial dilutions of a compound onto a control tissue section can produce a linear calibration curve. The first demonstration of this methodology was by (Nilsson *et al.*, 2010). In this work a dilution series of the respiratory compound tiotropium was prepared and spotted onto a control rat lung tissue section adjacent to a dosed tissue section. Both MS and MS/MS imaging was performed on the spiked and dosed tissue sections, after which a calibration curve was produced and used to determine the amount of the analyte in areas corresponding to low, medium and high intensity regions. The results were shown to correlate well with the results obtained from tissue homogenization and LC-MS/MS experiments.

A different approach has been reported by (Koeniger *et al.*, 2011) this involved the use of a dilution series, created from a range of rat liver samples dosed orally with increasing amounts of the drug olanzapine (0-100 mg/kg). Serial tissue sections, taken adjacent to those analysed by MALDI-MSI, were then homogenised and analysed by LC-MS/MS, the data showed good correlation between the two techniques.

Whilst not an example of quantitative mass spectrometry imaging (Becker *et al.*, 2005) developed a method for the analysis of atomic species by laser ablation inductively coupled plasma-mass spectrometry imaging (LA-ICP-MSI). A dilution series of different atomic species was mixed with tissue homogenate. These were then snap frozen, sectioned and mounted next to tissue sections of human brain. This method was then later adapted by (Hamm *et al.*, 2012a) for

MALDI-MSI and involves the preparation of a dilution series of a drug, which was then mixed with tissue homogenate. The spiked homogenate was snap frozen, sectioned and mounted next to the dosed tissue section.

Pirman and Yost presented a MSI method for the quantitation of endogenous acetyl-L-carnitine in piglet brain tissue sections. In this work a dilution series of acetyl-L-carnitine was spotted onto a microscope slide and allowed to dry, after which deuterated acetyl-L-carnitine was applied on top of the standards using an adapted ink-jet printer. Piglet brain tissue sections were then thaw mounted over the calibration standards and internal standard, matrix was then applied and the sections analysed.

The calibration standards and internal standard were applied under the tissue to mimic the extraction process of the analyte from dosed tissue sections into the matrix crystals. MS/MS imaging was then performed with a wide isolation window to ensure that both transitions for the analyte and the deuterated internal standard were analysed (Pirman and Yost 2011).

This method was used by (Pirman *et al.*, 2013) for the analysis of cocaine in human brain tissue sections, the results were reported to be comparable to those obtained by LC-MS/MS.

Takai *et al.*, recently monitored the distribution of the dopamine D2 receptor selective antagonist raclopride, in whole body mice sections following an intravenous administration. Quantitation of raclopride in multiple organs by MALDI-MS/MS imaging was performed by correlating the response from each organ and comparing this with the tissue concentrations determined by LC-MS/MS. The MALDI-MS/MS images were normalised with a product ion of the matrix DHB, which was used as an internal standard.

It has previously been shown by (Koeniger *et al.*, 2010) that there was a linear relationship between the amount of the drug olanzapine in a single rat liver tissue section analysed by LC-MS/MS and the MSI response in an adjacent tissue section. The MALDI-MS/MS images showing the distribution of raclopride were compared with WBA results showing the distribution of <sup>3</sup>H-raclopride (Takai *et al.*, 2012).

#### 4.1.4. Quantitative MSI software

The increasing interest in this field has prompted the creation of quantitative mass spectrometry imaging software such as the Quantinetix™ software from ImaBiotech ([www.imabiotech.com](http://www.imabiotech.com)).

Quantitative MSI software called “MALDI tools” has been developed recently by Uppsala University (Sweden) and is freely available from [www.maldi-msi.org](http://www.maldi-msi.org). The use of this software was reported by (Kallback *et al.*, 2012) for the quantification of the drugs imipramine and tiotropium in rat brain and lung tissue sections and the quantification of the endogenous neuropeptide substance P in rat brain tissue sections.

#### 4.1.5. Aims and Objectives

The work reported here will evaluate and compare the current methods of quantification for MALDI-MS imaging. Also presented is a novel method for the preparation of standards for use in the quantification of drugs in tissue sections by MALDI-MSI. The standards will be prepared in the form of a homogenate standard array.

## **4.2. Methods**

### **4.2.1. Information**

All animal studies were ethically reviewed and carried out in accordance with Animals (Scientific Procedures) Act 1986 and the GSK Policy on the Care, Welfare and Treatment of Laboratory Animals.

### **4.2.2. Materials**

The reagents alpha-cyano-4-hydroxycinnamic acid (CHCA), gelatin type B, ipratropium bromide monohydrate, fenoterol hydrobromide and trifluoroacetic acid (TFA) were purchased from Sigma Aldrich® (Gillingham, Dorset, UK). Methanol (MeOH) were purchased from Fisher Scientific (Loughborough, Leicestershire, UK). ipratropium bromide and tiotropium bromide were kindly provided by GlaxoSmithKline (Stevenage, UK).

### **4.2.3. Matrix deposition**

Samples were coated with either CHCA (7mg/ml in 70:30 MeOH: H<sub>2</sub>O with 0.2% TFA) using the ImagePrep matrix application device (Bruker Daltonics, Bremen, Germany) or CHCA containing 1 ng/μl of ipratropium as an internal standard.

A 5 mg/ml solution of CHCA in 70:30 MeOH: H<sub>2</sub>O with 0.2% TFA was used for samples sprayed on the Suncollect™ automated pneumatic sprayer (Sunchrom, Friedrichsdorf, Germany) in a series of layers. The matrix application was performed in a series of layers, the initial seeding layer was performed at 2 μl/minute and subsequent layers were performed at 3 μl/minute.

#### 4.2.4. Sample preparation

##### 4.2.4.1. On-tissue standard preparation

Control rat lung tissue was laid out on aluminium foil and frozen at  $-80^{\circ}\text{C}$ . The frozen lung tissue was sectioned using a Leica CM3050 cryostat (Leica Microsystems, Wetzlar, Germany) to produce  $10\ \mu\text{m}$  thick sections. The cut sections were thaw-mounted onto indium tin oxide coated glass slides (Bruker Daltonics, Bremen, Germany).

Standards were prepared from a tiotropium stock solution (1 mg/ml adjusted to free base form) to give the following standards 1 ng/ $\mu\text{l}$ –10 pg/ $\mu\text{l}$  in 50:50 methanol: water. Then 0.5  $\mu\text{l}$  of each standard was spotted onto a control rat lung tissue section.

##### 4.2.4.2. Homogenate standard preparation

During the preparation of the lung tissue sections (see 4.2.4.1) five consecutive tissue sections were taken and placed into an eppendorf tube and stored at  $-80^{\circ}\text{C}$  until required.

In order to account for tissue related ion suppression, the volume of each tissue section collected was calculated and this volume was used to add to the standards. The volume of each tissue section was approximately  $17\ \mu\text{m}^3$ . This was calculated using the FlexImaging software (Bruker Daltonics) and thus 17  $\mu\text{l}$  of water was added for each tissue section. To prepare a control rat lung tissue homogenate 85  $\mu\text{l}$  of water (5 x 17  $\mu\text{l}$ ) was added to five tissue sections. The tissue sections and water were sonicated in an eppendorf tube for approximately 30 minutes.

To prepare standards of ipratropium, the stock solution (1 mg/ml in water adjusted to free base form) was diluted in water to generate the following

standard solutions 100, 50, 20, 10, 5, 2, 1, 0.5, 0.2 and 0.1 ng/μl. 85 μl of these standards was added to the five tissue sections and vortex mixed followed by sonication for approximately 30 minutes. 1 μl of each homogenate standard was spotted onto a conductive glass slide in triplicate.

#### 4.2.4.3. Homogenate standard section preparation

The lung tissue sections were prepared as described earlier in 4.2.4.1. The volume of each tissue section was determined to be approximately 14.6 μm<sup>3</sup> thus, 14.6 μl of water was added for every tissue section. Based upon the above measurement 73 μl of water was added to five tissue sections. The tissue sections and water were sonicated in an eppendorf tube for approximately 30 minutes.

From a stock solution of ipratropium (1 mg/ml in water adjusted to free base form) the following standards 100, 50, 20, 10, 5, 2, 1, 0.5, 0.2 and 0.1 ng/μl were prepared. 73 μl of these standards were added to the five sections of tissue vortex mixed and sonicated for approximately 30 minutes.

In order to prepare the homogenate for freezing 50 μl of a 1 % solution of carboxymethyl cellulose was drawn up into a 200 μl (yellow) pipette tip, after which the pipette tip was placed into dry ice to freeze the CMC in the pipette tip thereby creating a plug. 60 μl of the homogenate was dispensed into the top of the pipette tip as shown in Figure 4.2A and frozen in dry ice to freeze. Once frozen the bottom of the pipette was discarded and the frozen homogenate standard removed from the pipette tip.

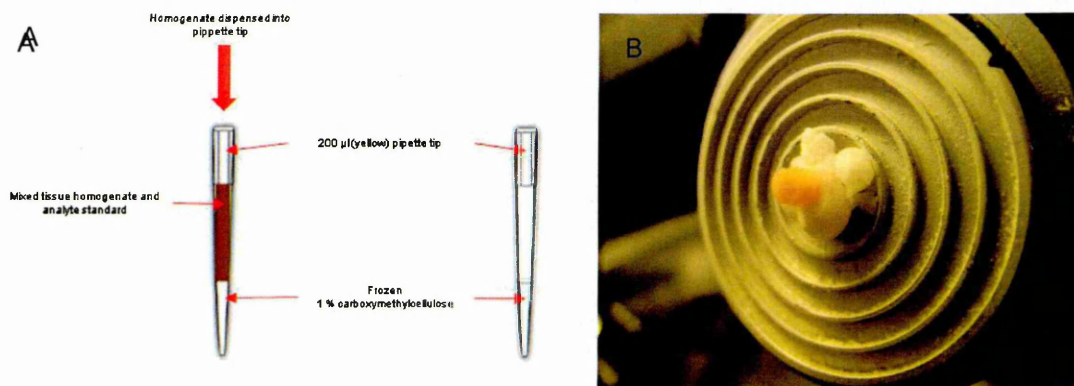


**Figure 4.2:** A) Diagram showing the production of the frozen homogenate standards for sectioning using pipette tips as a mold and B) an optical image showing a frozen homogenate standard mounted to a cryostat stage.

The frozen homogenate standard was then mounted onto a cryostat stage vertically using a 1% solution of carboxymethylcellulose as shown in Figure 4.2B. The frozen homogenate standards were sectioned using a Leica CM3050 cryostat (Leica Microsystems, Wetzlar, Germany) to produce 12 µm thick sections (12 µm thick sections were found to be manipulated easier). The cut sections were thaw-mounted onto indium tin oxide coated glass slides (Bruker Daltonics, Bremen, Germany) in triplicate.

#### 4.2.4.4. Homogenate standard array preparation.

Standards of tiotropium bromide were prepared from a 1 mg/ml stock solution in water adjusted to free base, to give the following standards 100, 50, 20, 10, 5, 2, 1, 0.5, 0.2 and 0.1 ng/µl in water. Control rat lung tissue was snap frozen in liquid nitrogen cooled isopentane and sectioned using a Leica CM3050 cryostat (Leica Microsystems, Wetzlar, Germany) to produce 10 µm thick sections. Five tissue sections were placed in an eppendorf tube, the volume of tissue per tissue section was approximately 28.5 µm<sup>3</sup> (2.85 µm<sup>2</sup> x 10 µm) therefore 28.5 µl of water was added for every tissue section. In order to prepare the

homogenate standards 142.5  $\mu\text{l}$  (28.5 $\mu\text{l}$  x 5 tissue sections) of the standards was added to the contents of the eppendorf tubes, the contents of the eppendorf tube was vortex mixed and sonicated for approximately 30 minutes. The homogenate standards were embedded in pre-frozen gelatin (100 mg/ml aqueous), holes were drilled into the frozen gelatin using a RotaCraft RC12VS mini rotary tool kit (SHESTO Limited, Willesden, London) fitted with a 3 mm diameter drill bit, the holes were then filled with tiotropium homogenate standards using a 1ml glass syringe to produce the homogenate standard array as shown below in Figure 4.3.

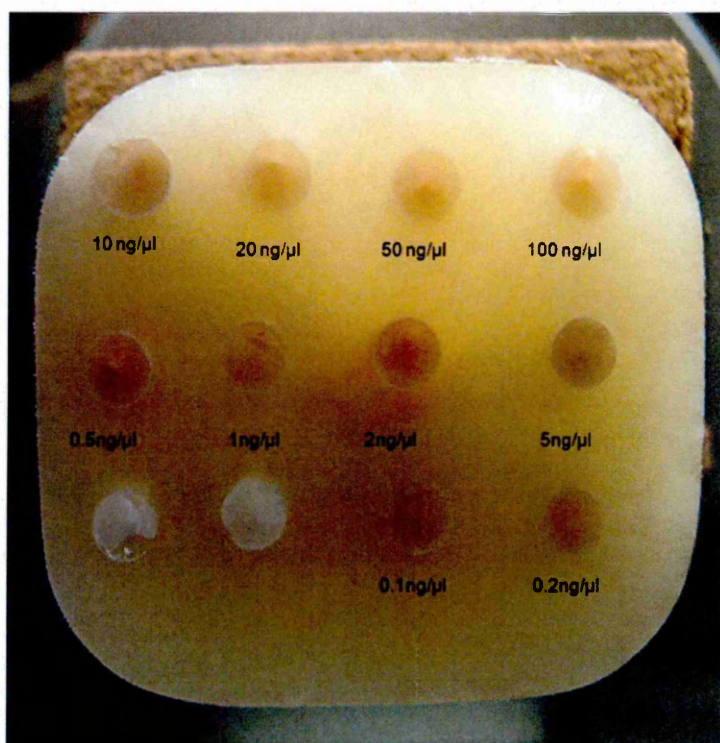


**Figure 4.3:** Optical image showing the tiotropium homogenate standards (100 - 0.1 ng/ $\mu\text{l}$ ) embedded in frozen the gelatin.

The embedded array of homogenate standards was sectioned at a  $-20^{\circ}\text{C}$  using a Leica Cryostat (Leica, Wetzlar, Germany) to produce 12  $\mu\text{m}$  thick sections, which were thaw mounted onto glass slides.

The same sample preparation was used to prepare a second homogenate standard array using fenoterol standards prepared from a 1 mg/ml stock solution in water, to give the following standards 1000, 500, 250, 125, 62.5, 31.2, 15.6, 7.8, 3.9, 1.9 and 0 ng/ $\mu$ l in water.

#### 4.2.5. Instrumentation

##### 4.2.5.1. MALDI-LIFT-MS/MS imaging

Analyses were either performed on an Ultraflex III or UltrafleXtreme MALDI-TOF/TOF mass spectrometer (Bruker Daltonics) equipped with smart beam laser technology. The digital image of the sections was imported into FlexImaging software (Bruker Daltonics), and through the software the instrument was taught the dimensions of the sections.

The instrument was operated in LIFT MS/MS positive mode configuration with a potential of 19.14kV for the Ultraflex III instrument or 19.10kV for the UltrafleXtreme instrument. Data was acquired at a spatial resolution of 200  $\mu$ m, with typical laser spot diameters of 75-80  $\mu$ m. LIFT MS/MS data was acquired in the mass range between 100 and 500 Da. The acquisition method was calibrated using a peptide calibration mixture (Bruker Daltonics) before the start of the experiment. MS/MS data was automatically acquired using the FlexImaging software from a total of 200 spectra acquired at each spot position using the proprietary random walk mode in four 50-shot increments at a laser frequency of 100Hz for the Ultraflex III instrument or 1000Hz for the UltrafleXtreme instrument (Marshall *et al.*, 2010).

#### 4.2.5.2. MALDI-MS and MS/MS imaging

Mass spectra and images were acquired in positive ion mode on an Applied Biosystems/MDS Sciex hybrid quadrupole time-of-flight mass spectrometer (Q-Star Pulsar-*i*) with an orthogonal MALDI ion source (Applied Biosystems, Foster City, California, USA) and a high repetition Neodymium-doped yttrium vanadate (Nd: YVO<sub>4</sub>) laser (5 KHz) (Elforlight Ltd, Daventry, Northamptonshire, UK). Image acquisition was performed at a spatial resolution of 150 μm x 150 μm in “Raster Image” mode; images were generated using the freely available Novartis Biomap 3.7.5.5 software ([www.maldi-msi.org](http://www.maldi-msi.org)).

### 4.3. Results and Discussion

#### 4.3.1. On-tissue standards

The first method evaluated is based upon that proposed by (Nilsson *et al.*, 2010) and involves the spotting of a dilution series of a compound onto a control tissue section.

Here are shown the MALDI-LIFT MS/MS images obtained for a dilution series of tiotropium bromide spotted onto a rat lung tissue section acquired on the Ultraflextreme instrument (Figure 4.4). The tiotropium spotted tissue section was sprayed with matrix containing ipratropium bromide as an internal standard.

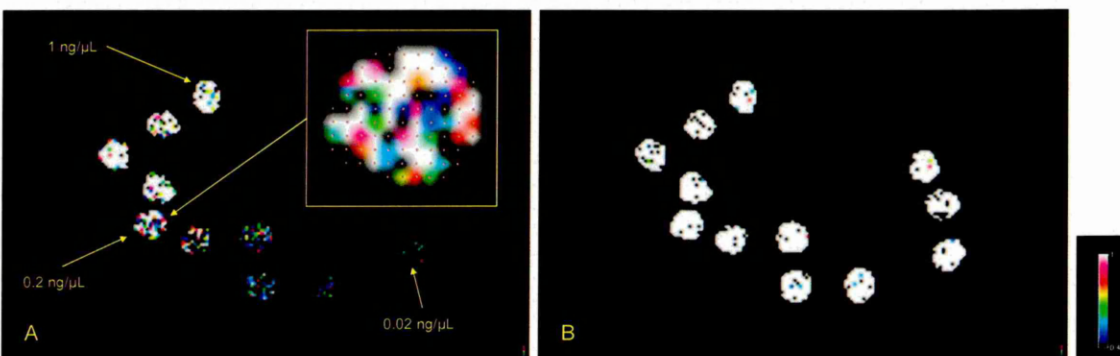


**Figure 4.4:** MALDI-MS/MS images showing A) the distribution of the product ion at  $m/z$  152, derived from the precursor ion of tiotropium at  $m/z$  392 within the deposited standards and B) the distribution of the product ion at  $m/z$  166, derived from the precursor ion of the internal standard ipratropium at  $m/z$  332 within the deposited standards.

The MALDI-LIFT MS/MS images displayed in Figures 4.4A shows the distribution of the product ion at  $m/z$  152, which is derived from the precursor ion at  $m/z$  392 to be within the spiked areas of the tissue section. The image shows that the approximate limit of detection of tiotropium as 20 pg/μl, (which agrees with the results obtained in the initial feasibility study, Chapter 3). The insert shows an expanded view of the sampling points for one of the standards.

Figure 4.4B shows the distribution of the product ion at  $m/z$  166, which is derived from the precursor ion at  $m/z$  332 of the internal standard ipratropium to be within the spiked areas of the tissue section. The image shows the presence of the internal standard in all of the compound spotted areas of the tissue section and the signal intensity is consistent showing no areas of ion suppression on this sample.

The filter data (pixel co-ordinates and the intensity of a selected mass) from the images presented in Figure 4.4 were exported from the FlexImaging software (Bruker Daltonics) in the form of a text file, and opened in an Microsoft excel spreadsheet to be processed and to construct the calibration curve. The average intensity of each region was determined and plotted against the standards respective concentration (see Figure 4.5).

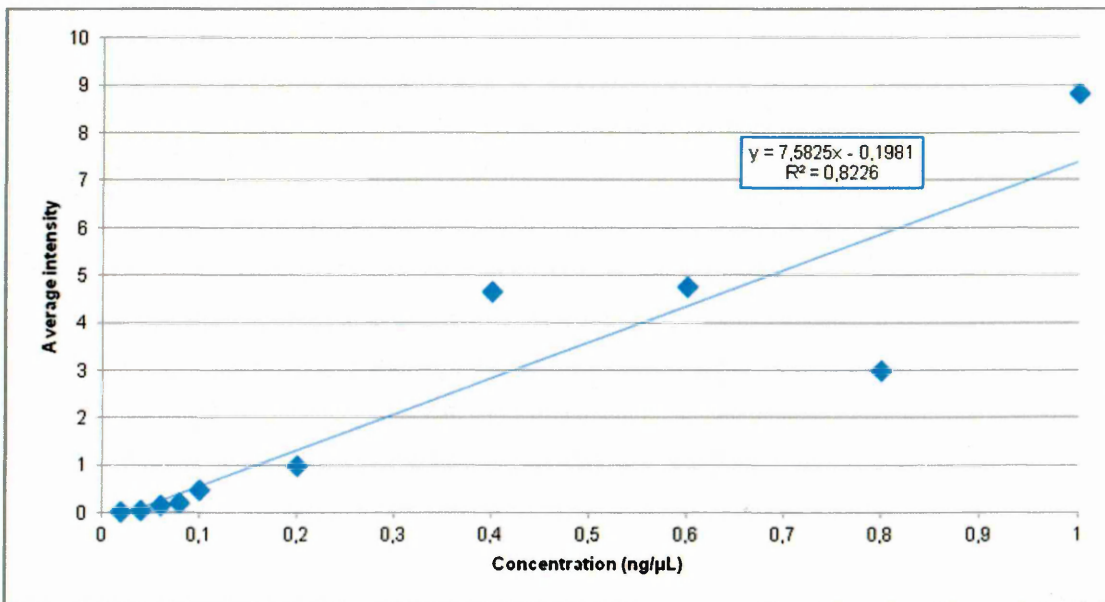


**Figure 4.5:** Calibration curve showing the exported filter data from the MALDI-LIFT MS/MS image showing the tiotropium standards spotted onto the control tissue section.

The calibration curve displayed above in Figure 4.5 shows the filter data from the image shown in Figure 4.4A, which shows the distribution of the product ion of tiotropium at  $m/z$  152. The graph shows a linear response ( $R^2=0.8226$ ) and that values for the 0.8 and 0.4 ng/ $\mu$ l do not fit the line. To determine if these points are outliers, the Grubbs statistical test for outliers was performed. The Q values for the 0.4 ng/ $\mu$ l and 0.8 ng/ $\mu$ l points were calculated at 0.9144 and 0.6187 respectively. As these values are above the tabulated Q value (0.552) for the number of points in the graph with a 95% confidence, these points cannot be classed as statistical outliers and therefore cannot be removed.

The graph shown below in Figure 4.6, is the filter data from the image showing the distribution of the product ion at  $m/z$  152 (Figure 4.4A) following normalisation with the filter data from the product ion of the internal standard at  $m/z$  166 (Figure 4.4B).

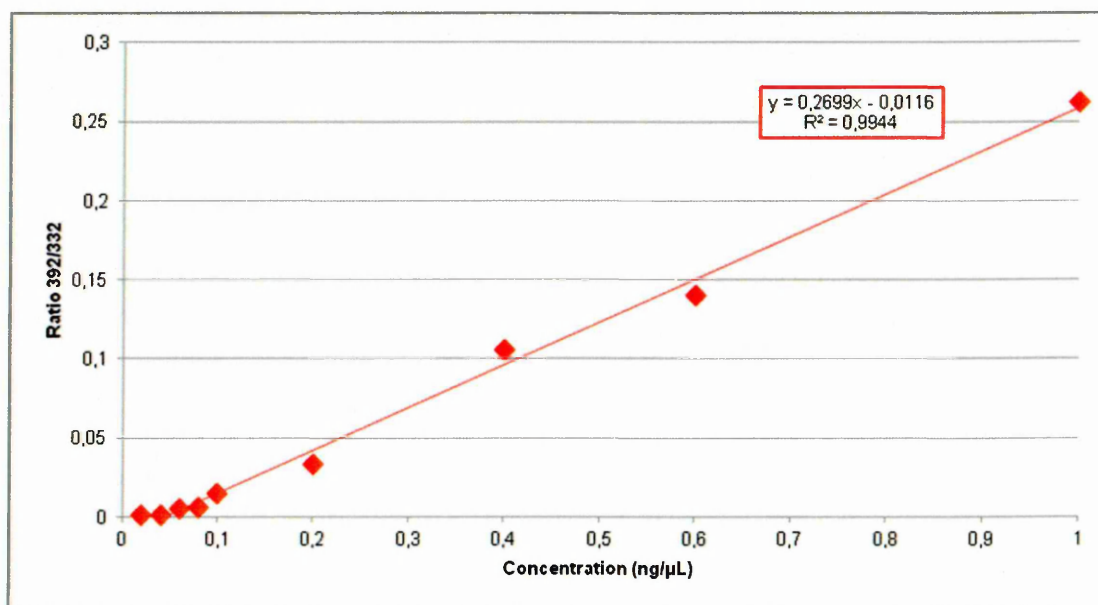


**Figure 4.6:** Calibration curve showing the exported filter data from the MALDI-LIFT MS/MS image showing the tiotropium standards spotted onto the control tissue section following normalisation against the internal standard.

The graph shown in Figure 4.6 shows the filter data from the image shown in Figure 4.4A which shows the distribution of tiotropium ( $m/z$  152) following normalisation against the filter data from the image shown in Figure 4.4B which shows the distribution of the internal standard Ipratropium, the graph shows a linear response ( $R^2=0.9944$ ) and showed that the value for the 0.8 ng/ $\mu$ l did not fit the line. Again, to ascertain if this point is an outlier, the Grubbs statistical test for outliers was performed. The calculated Q value for the 0.8 ng/ $\mu$ l point was 0.5369, because this value is below the tabulated Q value (0.552) for the number of points in the graph with a 95% confidence this point can be classed as a statistical outlier and removed.

The graph in Figure 4.6 shows a significant improvement as a result of the internal standard over that shown in Figure 4.5 based upon the correlation coefficient value. Therefore for future experiments involving Ipratropium shall be used as an internal standard, which shall be incorporated into the matrix as shown here.

Whilst this method can determine the approximate amount of compound in various areas of the sample, the calibration curve may not accurately represent the response obtained from the sample (Koeniger *et al.*, 2011). This could be possibly due to the difference in the matrix extraction efficiency of compound from the sample in comparison to the spiked tissue. Also uncontrolled deposition of standards onto the control tissue section can produce misleading results as all standards will not be uniform due to spreading on the tissues surface (Pirman *et al.*, 2013).

### 4.3.2. Homogenate standards

The second experiment involved mixing the dilution series of ipratropium bromide with tissue homogenate, which is used to mimic the behavior of the compound in a complex environment. The MALDI-LIFT MS/MS image of the mixed ipratropium bromide homogenate standards acquired on the Ultraflex III instrument is shown below in Figure 4.7, the mixed homogenate standards were analysed in triplicate.

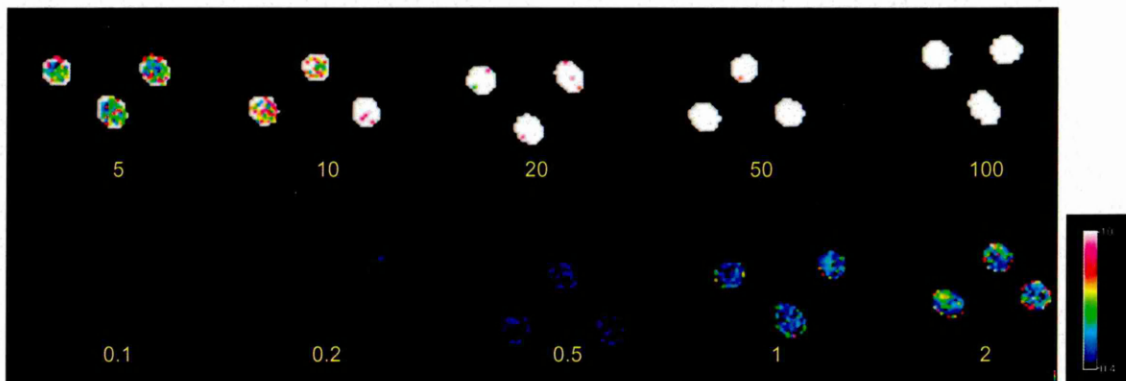


**Figure 4.7:** MALDI-LIFT MS/MS image showing the distribution of the product ion at  $m/z$  166, derived from the precursor ion of ipratropium at  $m/z$  332 within the mixed homogenate standards (200  $\mu\text{m}$  spatial resolution).

The MALDI-LIFT MS/MS image displayed above in Figures 4.7 shows the distribution of the product ion at  $m/z$  166, which is derived from the precursor ion at  $m/z$  332 in the homogenate standards on the glass slide. The images also show that visually the limit of detection is approximately 0.5 ng/ $\mu\text{l}$ .

The calibration curve was constructed from the filter data as described in 4.3.2. The average intensity of each region was calculated and plotted against the standards respective concentration, see Figure 4.8.

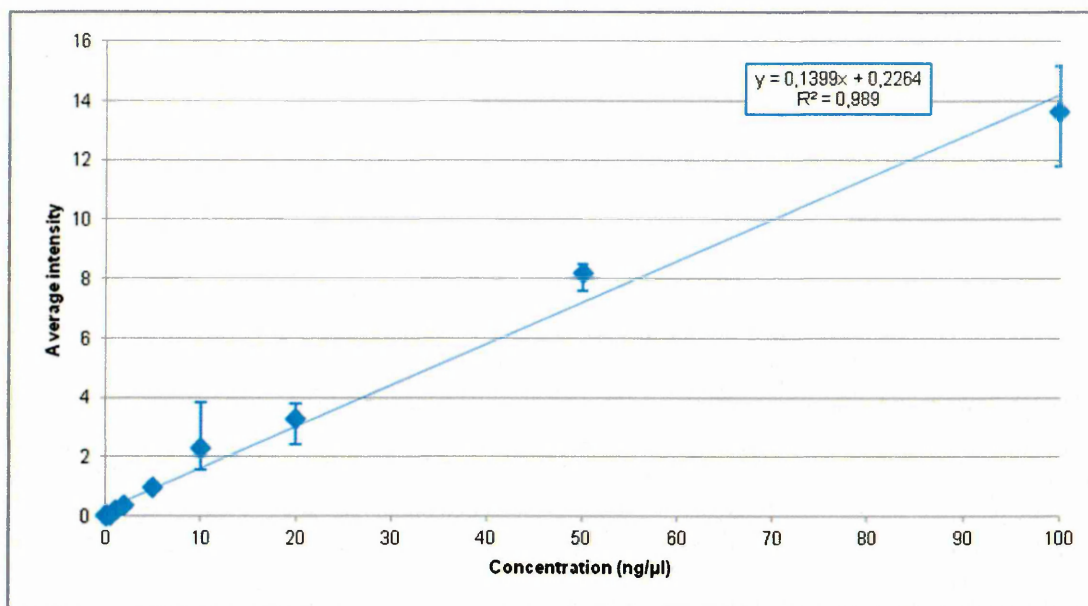


**Figure 4.8:** Graph showing the exported filter data from the MALDI-LIFT-MS/MS image showing the distribution of ipratropium within the mixed homogenate standards.

The calibration curve shown in Figure 4.8 shows a linear response ( $R^2=0.9889$ ) ranging from 0.1-100 ng/μl (three orders of magnitude).

The advantages of this homogenate standard method are that it accounts to tissue related ion suppression due to the homogenate and there is more control over the deposition of these standards, because the homogenate standards were prepared in water with no solvent.

However the disadvantages of this method are it is tissue specific and the deposits may not be fully applicable to the dosed tissue section, and as for the previous method the matrix extraction efficiency may not be the same.

### 4.3.3. Homogenate standard sections

The third method investigated involved the preparation of homogenate standards like the previous method, however in this case the homogenate standards were snap frozen, sectioned and thaw mounted onto a glass slide. This method was demonstrated in the work reported by (Becker *et al.*, 2005).

The MALDI-LIFT MS/MS image of the homogenate standard sections acquired on the Ultraflex extreme instrument are shown below in Figure 4.9, the homogenate standard sections were analysed in triplicate.

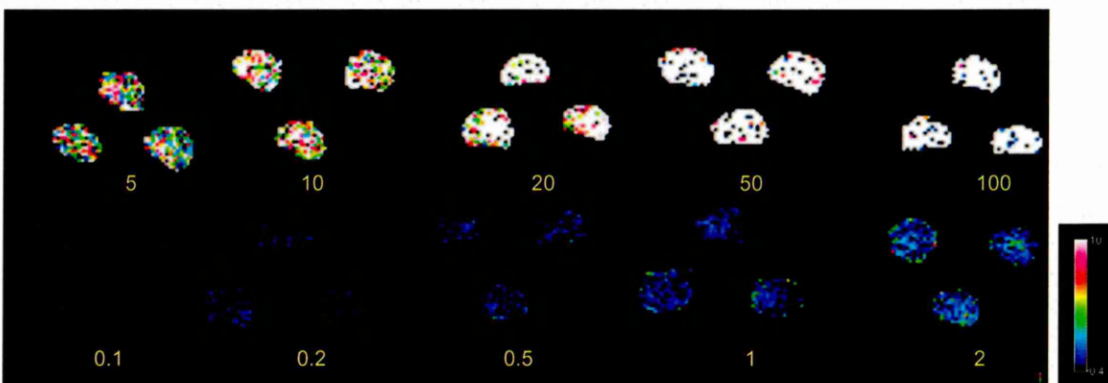


**Figure 4.9:** MALDI-LIFT MS/MS image showing the distribution of the product ion at  $m/z$  166, derived from the precursor ion of ipratropium at  $m/z$  332 within the homogenate standard sections (200  $\mu\text{m}$  spatial resolution).

The MALDI-LIFT MS/MS image displayed in Figures 4.9 shows the distribution of the product ion at  $m/z$  166, which is derived from the precursor ion at  $m/z$  332 to be within the homogenate standard sections. The image shows the distribution of ipratropium ( $m/z$  166) within the homogenate standard sections, the image shows that visually the limit of detection is approximately 0.2 ng/ $\mu\text{l}$ .

The filter data from the above image was exported from FlexImaging software (Bruker Daltonics) in the form of a text file, which was opened in an excel spreadsheet to be processed. The average intensity of each region was

determined and plotted against the standards respective concentration, the results of which are shown in Figure 4.10.

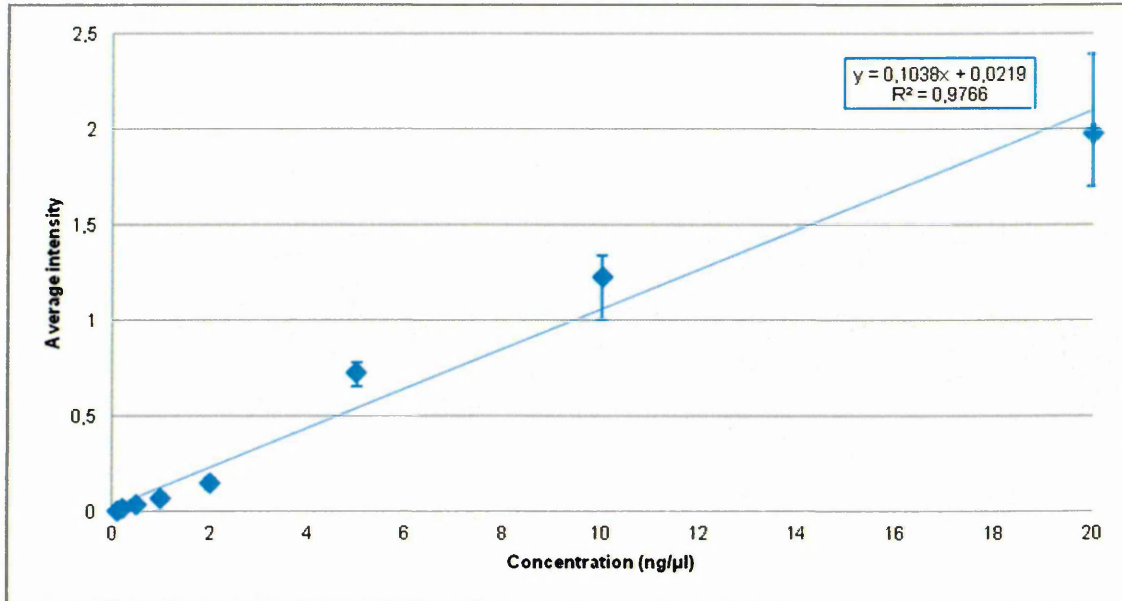


**Figure 4.10:** Calibration curve showing the exported filter data from the MALDI-LIFT MS/MS image showing the three replicates of ipratropium homogenate standard sections.

The calibration curve displayed in Figure 4.10 shows the filter data from the image shown in Figure 4.9 which shows the distribution of ipratropium ( $m/z$  166). The calibration curve shows a linear response for the homogenate standard sections ( $R^2=0.9766$ ) ranging from 0.1 – 20 ng/μl (over two orders of magnitude). The results from the 50 and 100 ng/μl were excluded from the plot as they caused the graph to plateau, this could be due to the dynamic range of the instrument.

The advantages of this method are the standards are matrix matched, also the standard sections are comparable to the dosed tissue sections because like them the compound is within the standard sections and are the same section thickness, and thus should have similar extraction efficiencies. However the

major disadvantage of this technique is that it is time consuming to prepare and section all of the individual standards.

#### 4.3.4. Homogenate standard array

The main disadvantage of the homogenate standard section approach was the lengthy procedure, to overcome this the homogenate standard array was developed. This method consists of a range of homogenate standards embedded in a frozen gelatin block that can be sectioned and placed next to a dosed tissue section.

The MALDI-MS/MS images of the tiotropium bromide homogenate standard array (100-0.1 ng/ $\mu$ l) acquired on the QSTAR instrument are shown below in Figure 4.11.

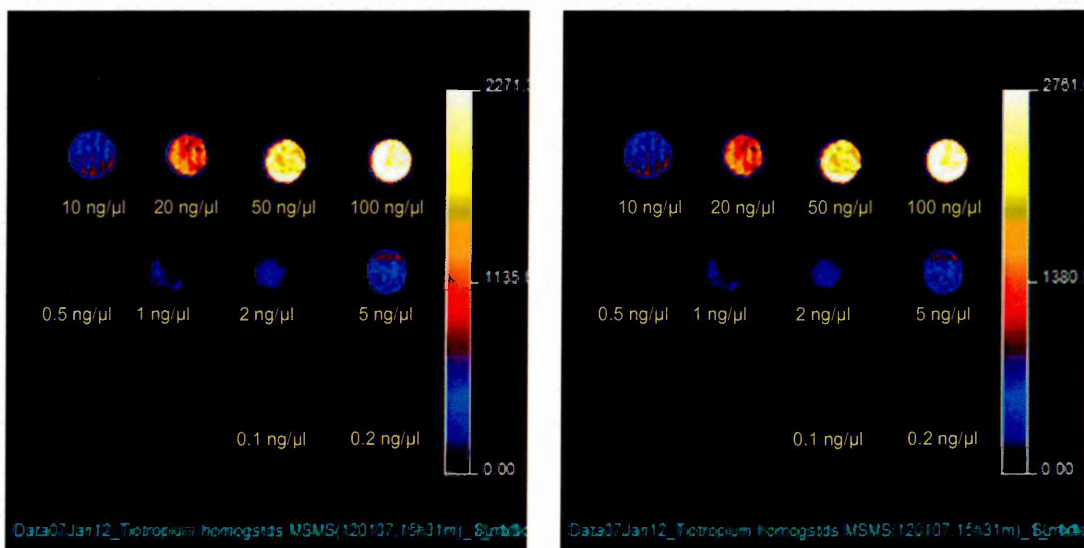


**Figure 4.11:** MALDI-MS/MS image showing the distribution of the product ions at  $m/z$  152 (left) and 170 (right), derived from the precursor ion of tiotropium at  $m/z$  392 (150  $\mu$ m spatial resolution).

The MALDI-MS/MS images displayed in Figure 4.11 shows the distribution of the two product ions at  $m/z$  152 and 170 respectively, derived from the precursor ion of tiotropium at  $m/z$  392 to be within the homogenate standard

array. The images show a decreasing response with respect to the concentration of the standards in the array, also the distribution of the product ions at  $m/z$  152 and 170 appears to be homogenous within each standard.

Utilising the region of interest tool of the BioMap 3.7.5.5 software, the average intensity of each standard was determined and plotted against the standards respective concentration, the results of which are shown in Figure 4.12.

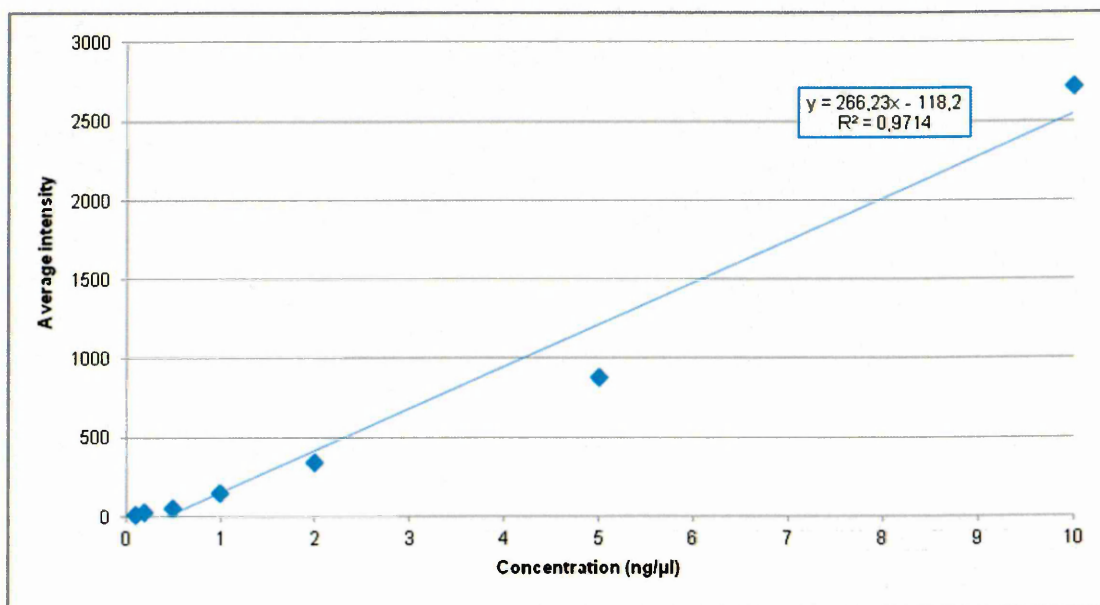


**Figure 4.12:** Graph produced from region of interest analysis on the distribution of the product ion at  $m/z$  172, derived from the precursor ion of tiotropium at  $m/z$  392.

The calibration curve shown in Figure 4.12 shows a linear response ( $R^2=0.9714$ ) ranging from 0.1-10 ng/μl (two orders of magnitude). The results from the 20-100 ng/μl were again excluded since they caused the graph to plateau.

To demonstrate the application of the homogenate standard array method of quantification by MALDI-MSI to different pharmaceutical compounds a second homogenate standard array was made using the long acting  $\beta_2$ -adrenoreceptor agonist fenoterol, which is not as easily ionised by MALDI in comparison to the quaternary ammonium compounds analysed previously.

The MALDI-MS/MS image of the fenoterol homogenate standard array (0-1000 ng/ $\mu$ l) acquired on the QSTAR instrument is shown below in Figure 4.13.

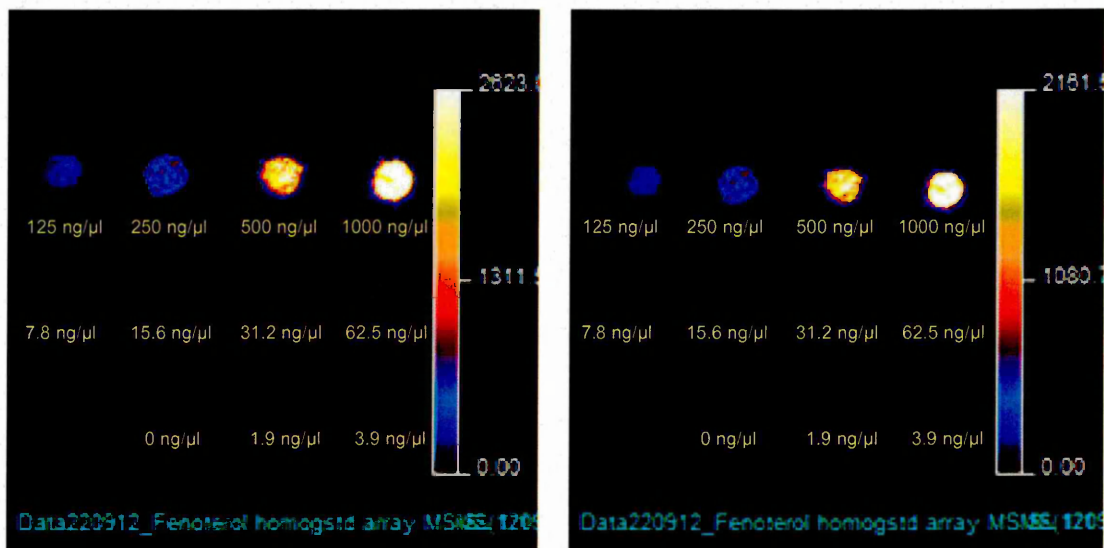


**Figure 4.13:** MALDI-MS/MS image showing the distribution of the product ions at  $m/z$  107 (left) and 135 (right), derived from the precursor ion of fenoterol at  $m/z$  303 (150  $\mu$ m spatial resolution).

The MALDI-MS/MS images shown in Figure 4.13 shows the distribution of two of the most abundant product ions at  $m/z$  107 and 135 respectively, derived from the precursor ion of fenoterol at  $m/z$  303 to be within the homogenate standard array. The images show a decreasing response with respect to the concentration of the standards in the array, also the distribution of the product ions at  $m/z$  107 and 135 appears to be homogenous within each standard.

The calibration curve was constructed using the region of interest data as described in previously, the results of which are shown in Figure 4.14.

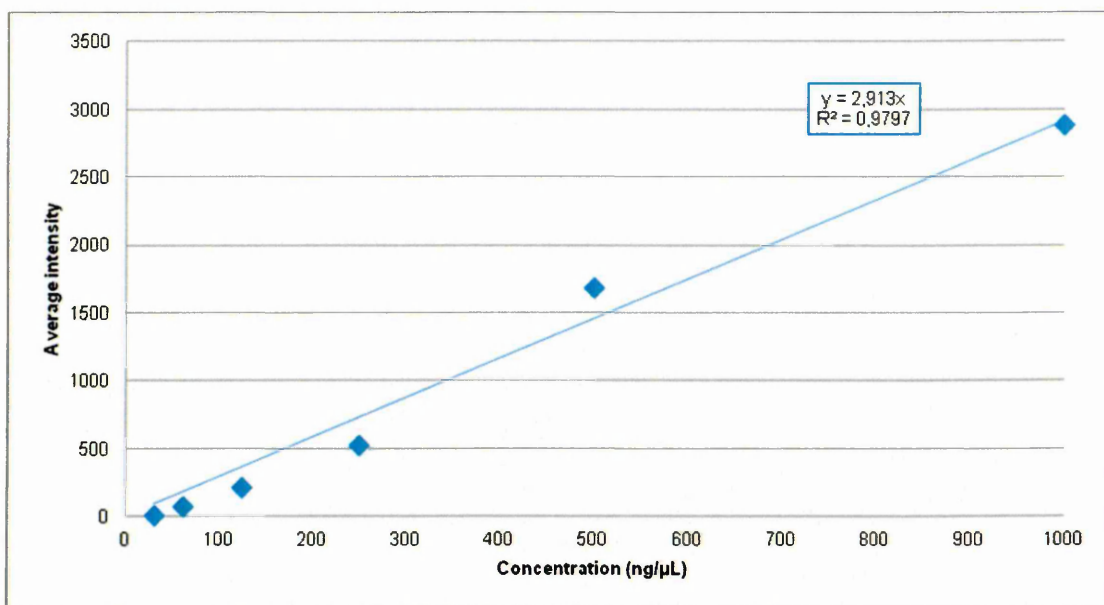


**Figure 4.14:** Graph produced from region of interest analysis on the distribution of the product ion at  $m/z$  107, derived from the precursor ion of fenoterol at  $m/z$  303.

The calibration curve shown in Figure 4.14 shows a linear response ( $R^2=0.9797$ ) ranging from 31-1000 ng/ $\mu$ L.

The advantages of the homogenate standard array method are the standards are comparable to the dosed tissue sections because like them the compound is within the standard sections and are the same section thickness, thus will have similar extraction efficiencies. Another advantage of this approach is that all of the homogenate standards are embedded in a block of frozen gelatin. One section contains all the standards necessary for quantitation which can be placed next to the dosed tissue section and analysed at the same time.

Another envisaged use of the homogenate standard array could be to do quality assurance checks on instruments, to ensure they are operating at optimal performance from day-to-day.

#### 4.4. Conclusion

The purpose of this study was to evaluate the use of the current reported methods for the generation of quantitative information from mass spectrometry images.

There are currently three methods reported for generating quantitative information from mass spectrometry images, the first method involves the spotting of a dilution series of a drug onto control tissue sections to generate a calibration curve, this is then used to determine the amount of the analyte of interest in different areas of the dosed tissue section as recently described by (Nilsson *et al.*, 2010). Whilst this method allows for the approximate amount of a particular compound to be assigned to a specific region on a treated tissue section, the calibration cannot be accurately assigned based upon the difference in extraction efficiencies between standards and sample. The second method involved the preparation of "matrix-matched" homogenate standard sections based upon the work reported by (Becker *et al.*, 2005). The advantage of this technique is homogenate standard sections are the same thickness as the treated tissue section. The standards are located within the section and mimic a dosed compound present in a tissue sample, the extraction efficiencies should be similar. Finally this work has also looked at homogenate standards spotted onto a glass slide.

This study has led to the development of a novel quantitation method in the form of a homogenate standard array, which consists of homogenate standards embedded in a block of frozen gelatin. Sections of the homogenate standard array has the advantage that it can be placed next to a dosed tissue section and analysed at the same time and under the same conditions as the dosed tissue

section and contains all the standards necessary for making an estimate of the drug levels in the tissue.

#### 4.5. Reference

BECKER, J.S., ZORIY, M.V., PICKHARDT, C., PALOMERO-GALLAGHER, N. and ZILLES, K., 2005. Imaging of copper, zinc, and other elements in thin section of human brain samples (Hippocampus) by laser ablation inductively coupled plasma mass spectrometry. *Analytical Chemistry*, **77**(10), 3208-3216.

CASTELLINO, S., GROSECLOSE, M.R. and WAGNER, D., 2011. MALDI imaging mass spectrometry: bridging biology and chemistry in drug development. *Bioanalysis*, **3**(21), 2427-2441.

CORNETT, D.S., FRAPPIER, S.L. and CAPRIOLI, R.M., 2008. MALDI-FTICR imaging mass spectrometry of drugs and metabolites in tissue. *Analytical Chemistry*, **80**(14), 5648-5653.

HAMM, G., BONNEL, D., MICHEL, C., PAMELARD, F., HOCHART, G. and STAUBER, J., 2012a. Towards quantitative imaging mass spectrometry. [Current Trends in Mass Spectrometry](#).

HAMM, G., BONNEL, D., LEGOUFFE, R., PAMELARD, F., DELBOS, J., BOUZOM, F. and STAUBER, J., 2012b. Quantitative mass spectrometry imaging of propranolol and olanzapine using tissue extinction calculation as normalization factor. *Journal of Proteomics*, **75**(16), 4952-4961.

KÄLLBACK, P., SHARIATGORJI, M., NILSSON, A. and ANDRÉN, P.E., 2012. Novel mass spectrometry imaging software assisting labeled normalization and quantitation of drugs and neuropeptides directly in tissue sections. *Journal of Proteomics*, **75**(16), 4941-4951.

KOENIGER, S.L., TALATY, N., LUO, Y., READY, D., VOORBACH, M., SEIFERT, T., CEPA, S., FAGERLAND, J.A., BOUSKA, J., BUCK, W.,

JOHNSON, R.W. and SPANTON, S., 2011. A quantitation method for mass spectrometry imaging. *Rapid Communications in Mass Spectrometry*, **25**(4), 503-510.

MARSHALL, P., TOTEU-DJOMTE, V., BAREILLE, P., PERRY, H., BROWN, G., BAUMERT, M. and BIGGADIKE, K., 2010. Correlation of skin blanching and percutaneous absorption for glucocorticoid receptor agonists by matrix-assisted laser desorption ionization mass spectrometry imaging and liquid extraction surface analysis with nanoelectrospray ionization mass spectrometry. *Analytical Chemistry*, **82**(18), 7787-7794.

NILSSON, A., FEHNIGER, T.E., GUSTAVSSON, L., ANDERSSON, M., KENNE, K., MARKO-VARGA, G. and ANDREN, P.E., 2010. Fine mapping the spatial distribution and concentration of unlabeled drugs within tissue micro-compartments using imaging mass spectrometry. *Plos One*, **5**(7), e11411.

PRIDEAUX, B. and STOECKLI, M., 2012. Mass spectrometry imaging for drug distribution studies. *Journal of Proteomics*, **75**(16), 4999-5013.

PIRMAN, D.A., REICH, R.F., KISS, A., HEEREN, R.M.A. and YOST, R.A., 2013. Quantitative MALDI tandem mass spectrometric imaging of cocaine from brain tissue with a deuterated internal standard. *Analytical Chemistry*, **85**(2), 1081-1089.

PIRMAN, D.A. and YOST, R.A., 2011. Quantitative tandem mass spectrometric imaging of endogenous acetyl-L-carnitine from piglet brain tissue using an internal standard. *Analytical Chemistry*, **83**(22), 8575-8581.

SCHWEITZER, A., FAHR, A. and NIEDERBERGER, W., 1987. A simple method for the quantitation of <sup>14</sup>C-whole-body autoradiograms. *International*

*Journal of Radiation Applications and Instrumentation. Part A. Applied Radiation and Isotopes*, **38**(5), 329-333.

STOECKLI, M., STAAB, D. and SCHWEITZER, A., 2007. Compound and metabolite distribution measured by MALDI mass spectrometric imaging in whole-body tissue sections. *International Journal of Mass Spectrometry*, **260**(2-3), 195-202.

TAKAI, N., TANAKA, Y., INAZAWA, K. and SAJI, H., 2012. Quantitative analysis of pharmaceutical drug distribution in multiple organs by imaging mass spectrometry. *Rapid Communications in Mass Spectrometry*, **26**(13), 1549-1556.

## **Chapter 5**

---

Development of methodology for monitoring the three-dimensional distribution of endogenous species in the lungs by MALDI-MSI

## 5.1. Introduction

### 5.1.1. Traditional 3D imaging techniques

Current well-established bioimaging techniques include positron emission tomography (PET), computed tomography (CT) and magnetic resonance imaging (MRI). These techniques give anatomical information by monitoring the distribution of water or the distribution of a labeled compound. PET is a labeled technique which utilises radiotracers which are isotopes that have a short half-life i.e. Carbon-11 or Fluorine-18, which are often incorporated into glucose or compounds such as Raclopride. MRI and CT are targeted techniques and can recover the anatomy of the body or a specific organ by tracing water or other fluid molecules.

However these techniques do not have the ability to monitor the distribution of unlabelled drugs and metabolites or proteins (Crecelius *et al.*, 2005, Trede *et al.*, 2012). MALDI-MSI has been extensively used to monitor the distribution of pharmaceutical compounds, lipids, peptides and proteins in tissue sections. Expanding this technique with the addition of a third dimension enables a detailed, volumetric visualization of these analytes in an entire organ (Crecelius *et al.*, 2005, Ye *et al.*, 2011).

### 5.1.2. Current approaches to 3D-MSI

There are currently two approaches used for three-dimensional mass spectrometry imaging (3D-MSI), depth profiling and serial-sectioning. In the depth profiling approach, ablation of the sample surface is performed exposing lower layers for analysis. This approach has been reported using SIMS and LAESI (Nemes *et al.*, 2009, Fletcher *et al.*, 2011). For the serial-sectioning approach, the sample is cut into serial sections, each section is imaged and the

images then combined into a 3D model. This approach has been reported using both MALDI and DESI (Crecelius *et al.*, 2005, Ye *et al.*, 2011, Xiong *et al.*, 2012).

### 5.1.3. Previous Examples

#### 5.1.3.1. 3D MALDI-MS Imaging

The first report of the construction of 3D MALDI-MS images came from (Crecelius *et al.*, 2005). In this work a three-dimensional model of the distribution of the myelin basic protein (MBP) in the *corpus callosum* of a mouse brain was constructed. The mouse brain was sectioned into a total of 264 tissue sections, from these sections 10 were selected at equal intervals and analysed by MALDI-MSI. The MALDI-MS images were then co-registered with optical and histological images, as well as anatomical references. The results of this reconstruction are shown below in Figure 5.1.

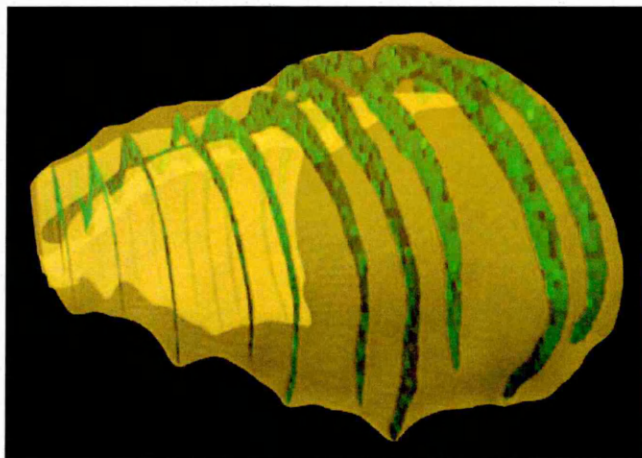


**Figure 5.1:** 3D MALDI-MS image of myelin basic protein in the corpus callosum of a mouse brain. The yellow volume corresponds to the outline of the entire corpus callosum from 264 optical images (Crecelius *et al.*, 2005).

A detailed step-by-step procedure for the production of 3D volume reconstructions of MALDI-MS data was reported by (Andersson *et al.*, 2008).

Here the distribution of peptides and proteins were localized in the substantia nigra and the interpeduncular nucleus of the rat brain. Figure 5.2 shows the co-localisation of PEP-19 and an unidentified protein from four different angles.

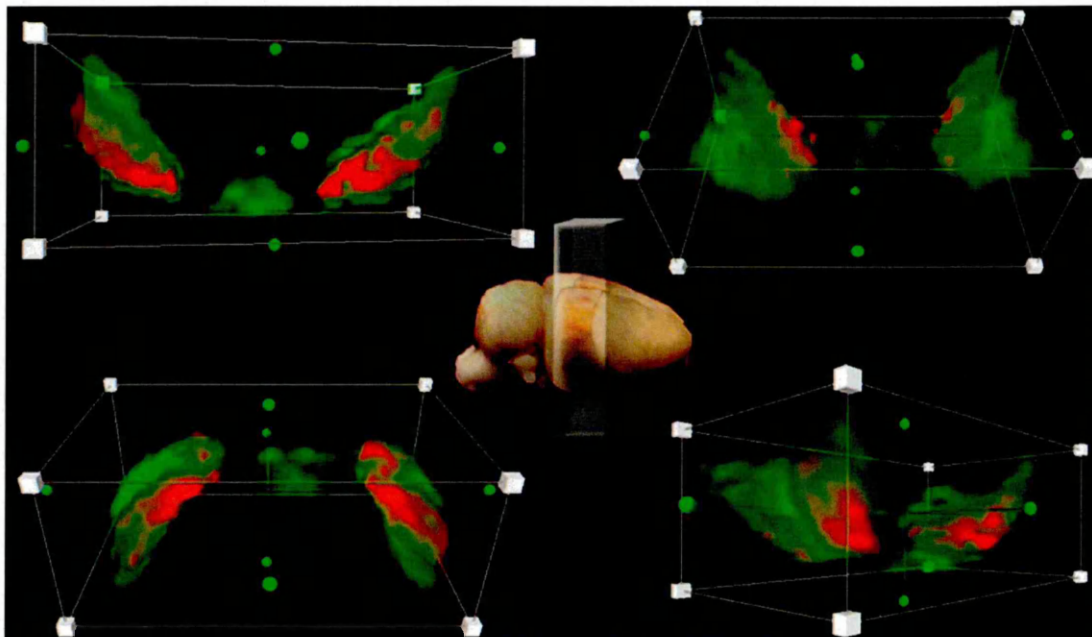


**Figure 5.2:** 3D MALDI-MS images of the substantia nigra and interpeduncular nucleus. The images show the distribution of PEP-19 (green) which is localised in both regions and a protein with  $m/z$  7416 (red) localised in the substantia nigra (Seely and Caprioli 2012).

Later (Sinha *et al.*, 2008) demonstrated the integration of magnetic resonance imaging (MRI) with MALDI-MSI of a whole mouse head into the same three-dimensional model. In this work high resolution MRI of a tumor-laden mouse brain was performed, after which the animals were sacrificed and serial sections were collected and analysed by MALDI-MSI, the data was then co-registered with the MRI data showing the distribution of proteins in relation to anatomical features of the brain as shown in Figure 5.3.

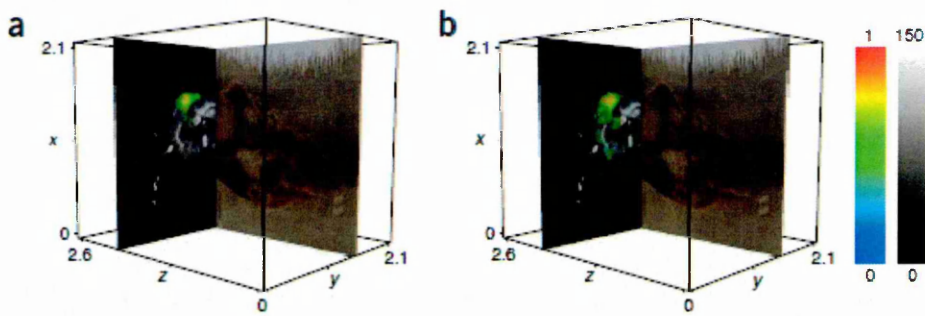


**Figure 5.3:** Co-registered MALDI-MS images and MRI of a whole mouse head. The MALDI-MSI images (colour scale) of A) the astrocytic phosphoprotein (*Pea15*) and B) the fatty acid binding protein 5 (*Fabp5*) are co-registered with the MRI data (grey scale) and an optical image (Sinha *et al.*, 2008).

The distribution of peptides and lipids in the brain of a crab, *Cancer borealis* was demonstrated by (Chen *et al.*, 2009). The brain was embedded in gelatin and sectioned. Seven sections were collected with a spacing of 132  $\mu\text{m}$ . These sections were analysed and the three-dimensional distribution of brain components such as the neuropeptide *C. borealis* tachykinin-related peptide (CabTRP) 1a and the lipid phosphatidylcholine (PC) 38:6 were generated. Figure 5.4 shows the 3D distribution of a lipid and a peptide in a crab brain.

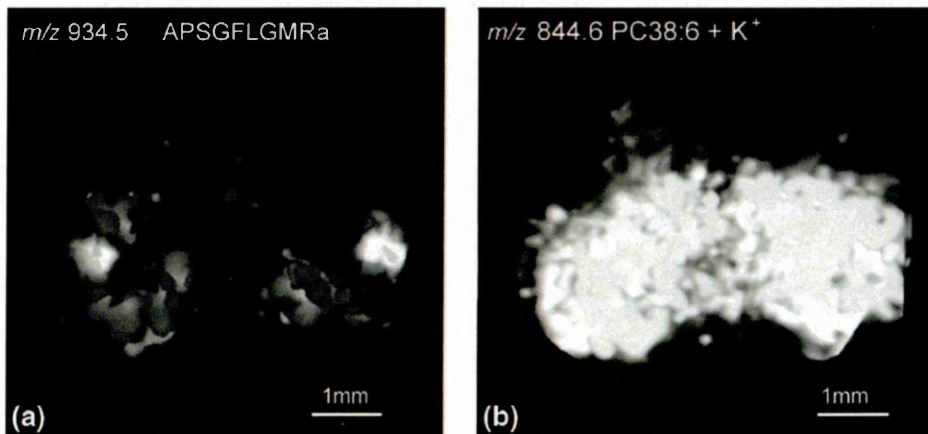


**Figure 5.4:** 3D reconstruction of MALDI-MS images of (A) the neuropeptide *C. borealis* tachykinin-related peptide (CabTRP 1a) and (B) lipid PC 38:6 acquired from the brain of a crab (Chen *et al.*, 2009).

The use of fiducial or registration markers for 3D image alignment and reconstruction was demonstrated by (Chughtai *et al.*, 2012). The use of a fiducial markers comprised of cresyl violet and Ponceau S, was found to be compatible with other imaging modalities such as bright field microscopy, fluorescence, and histological imaging. The use of the fiducial markers enabled data obtained using these techniques to be incorporated into the same 3D images as the MSI data, which is shown below in Figure 5.5.

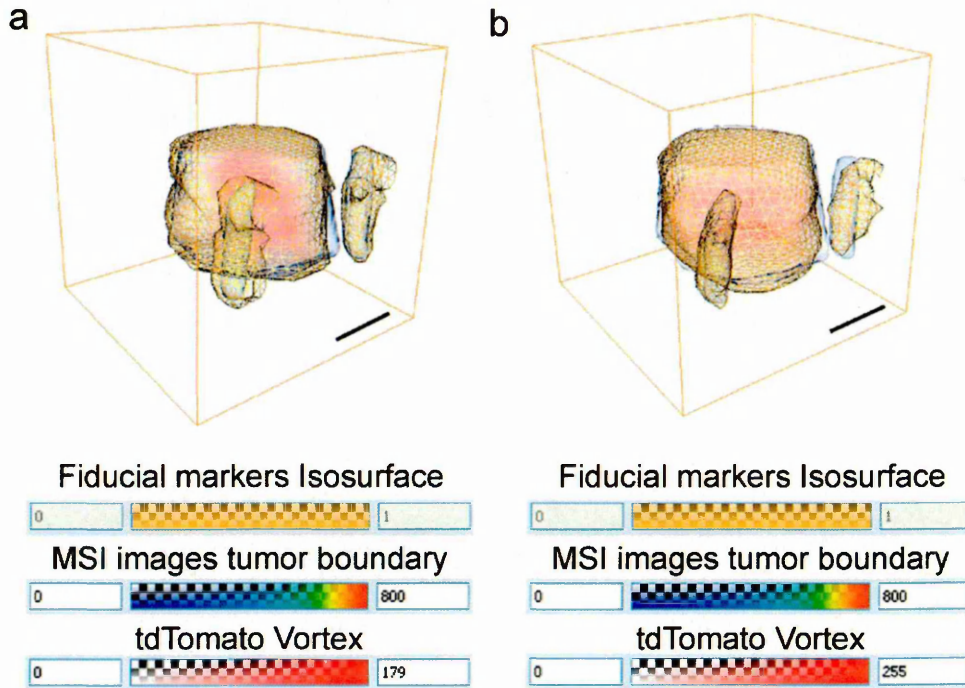


**Figure 5.5:** 3D images showing the co-registration of from optical imaging, H&E imaging, and MSI based on the position of the fiducial markers. (A) co-registration of MSI data (gray), optical imaging data of the tumor boundary (yellow mesh) and the hypoxic region (red). (B) co-registration of MSI data of actin (grey) and tdTomato (red) and H&E imaging data (yellow mesh) (Chughtai *et al.*, 2012).

### 5.1.3.2. 3D LAESI-MS Imaging

The first example of 3D-MS imaging under atmospheric pressure (AP) conditions using LAESI-MS imaging was reported by (Nemes *et al.*, 2009). In this work the distribution of various metabolites such as kaempferol/luteolin, chlorophyll a, acacetin and kaempferol (diacetyl coumarylrhamnoside) were monitored in the leaves of the zebra plant (*Aphelandra squarrosa*). The 3D distribution of metabolites was achieved using both lateral imaging and depth profiling. The results are displayed below in Figure 5.6.

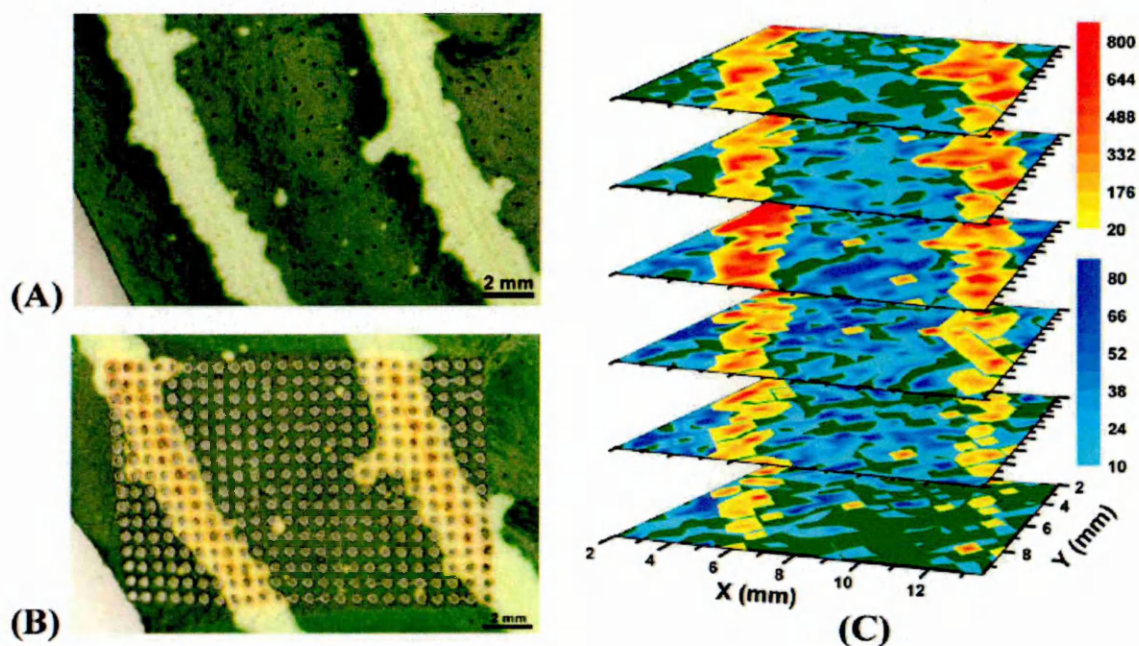


**Figure 5.6:** Optical images of *Aphelandra squarrosa* leaves (A) before and (B) after analysis. (C) 3D LAESI-MS images showing the distribution of kaempferol/luteolin (yellow/orange scale) which follow the variegation pattern and chlorophyll (blue scale) accumulated in the mesophyll layers (Nemes *et al.*, 2009).

### 5.1.3.3. 3D DESI-MS Imaging

The first 3D molecular reconstruction of a mouse brain using DESI-MS imaging was reported by (Eberlin *et al.*, 2010). The distribution of the two lipids (PS and ST) was demonstrated in serial sections of the mouse brain. The distribution of phosphatidylserine (PS) 18:/22:6 and sulfatide (ST) 24:1 were localised in the grey matter and white matter respectively. The distribution of these lipids was overlaid to construct a 3D model, which allowed a complete view of substructures such as the corpus callosum and anterior commissure. As shown in Figure 5.7.

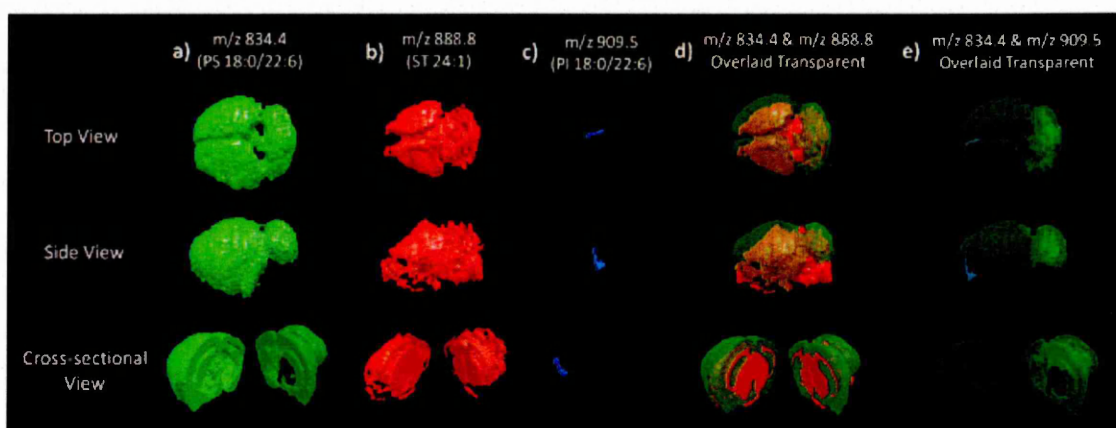


**Figure 5.7:** 3D DESI-MS images of the mouse brain showing (A) PS 18:0/22:6 in green, (B) ST 24:1 in red and (C) PI 18:0/22:6 in blue. The same views are shown for the transparent overlaid distributions of the lipids (D) PS 18:0/22:6 and ST 24:1 and (E) PS 18:0/22:6 and PI 18:0/22:6 (Eberlin *et al.*, 2010).

#### 5.1.3.4. 3D TOF-SIMS Imaging

The application of SIMS for 3D imaging of single cells has recently been demonstrated by Fletcher *et al.*, in 2011. 3D-MS imaging of HeLa-M cells prepared either by formalin fixation freeze-drying (Figure 5.8A) or a hydrated freeze fracture (Figure 5.8B) method was performed. The distribution of adenine at  $m/z$  136 was localised in the nucleus and phosphocholine at  $m/z$  184 was localised in the cell membrane.

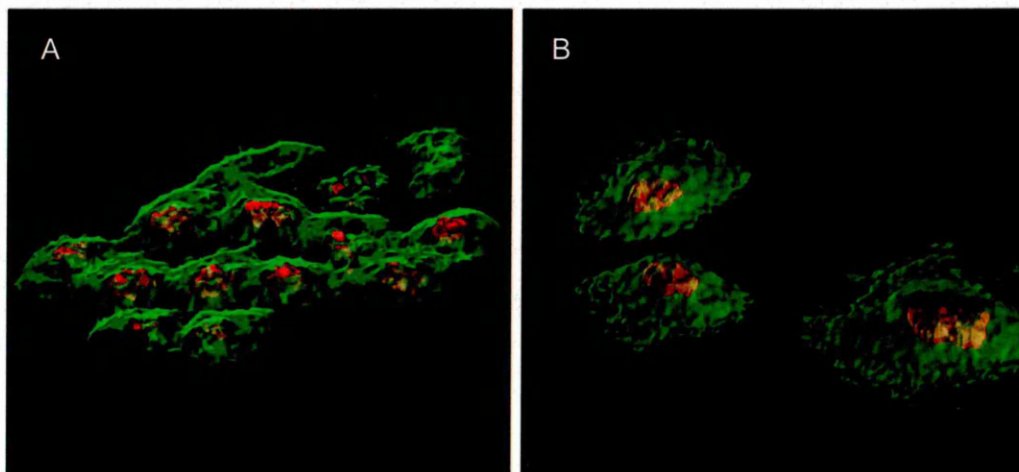


**Figure 5.8:** 3D visualisation of SIMS depth profiling of HeLa-M cells prepared by A) the formalin fixation freeze-drying and B) the hydrated freeze fracture (right). The images show phosphocholine at  $m/z$  184 (green) localised in the cell membrane and adenine at  $m/z$  136 or guanine at  $m/z$  156 localised in the nucleus (Fletcher *et al.*, 2011).

The first 3D molecular reconstruction of a rat heart by SIMS imaging was recently reported by (Fornai *et al.*, 2012). A rat heart was serially sectioned resulting in 40 tissue sections, the sections were then analysed using metal assisted-secondary ion mass spectrometry (MetA-SIMS). The 3D images showed the distribution of sodium at  $m/z$  23 was localised in the atria, potassium at  $m/z$  39 was localised in the ventricles and an endogenous species at  $m/z$  145 was localised in the pulmonary artery, right atrium, and

atrioventricular valve. The reconstruction of the heart is displayed from different angles below in Figure 5.9.



**Figure 5.9:** 3D SIMS-MS images of a rat heart showing the distribution of an endogenous species at  $m/z$  145 (red), sodium at  $m/z$  23 (green) and potassium at  $m/z$  39 (blue) from different angles (Fornai et al., 2012).

#### 5.1.4. Aims and Objectives

The aim of this experiment is to develop methodology to monitor the three-dimensional distribution of endogenous species throughout the lungs using MALDI-MSI. Serial sections were obtained at equal intervals through the control mouse lung tissue and imaged individually; homogenate registration markers were incorporated in order to aid the final 3D image construction.

Using Image J, a freely available software the images were stacked together to generate the 3D distribution of a particular endogenous species throughout the lungs to be displayed, the Volume Explorer software was also used to produced 3D MALDI-MSI images.

## **5.2. Methods**

### **5.2.1. Information**

All animal studies were ethically reviewed and carried out in accordance with Animals (Scientific Procedures) Act 1986 and the GSK Policy on the Care, Welfare and Treatment of Laboratory Animals.

### **5.2.2. Materials**

The reagents alpha-cyano-4-hydroxycinnamic acid (CHCA), gelatin type B and trifluoroacetic acid (TFA) were purchased from Sigma Aldrich® (Gillingham, Dorset, UK). Methanol (MeOH) was purchased from Fisher Scientific (Loughborough, Leicestershire, UK).

### **5.2.3. Tissue Preparation**

A control mouse lung tissue was embedded in gelatin (100 mg/ml aqueous) as shown in Figure 5.10 and placed into a -80°C freezer. Holes were drilled into the frozen gelatin using a RotaCraft RC12VS mini rotary tool kit (SHESTO Limited, Willesden, London) fitted with a 3 mm diameter drill bit. The holes were then filled with control rat lung homogenate, these act as registration markers for later image reconstruction. The embedded tissue was then sectioned at a temperature of -20°C using a Leica Cryostat (Leica, Wetzlar, Germany) to obtain 12 µm sections at 120 µm intervals, which were thaw mounted onto glass slides.



**Figure 5.10:** Optical images showing the control mouse lung tissue embedded in gelatin prior to freezing.

#### 5.2.4. Matrix Application

The matrix solution 5 mg/ml CHCA in 70:30 MeOH: H<sub>2</sub>O with 0.2% TFA was applied using the Suncollect™ automated pneumatic sprayer (Sunchrom, Friedrichsdorf, Germany) in a series of layers. The initial seeding layer was performed at 2 µl/minute and subsequent layers were performed at 3 µl/minute.

#### 5.2.5. Instrumentation

Mass spectra and images were acquired in positive ion mode on an Applied Biosystems/MDS Sciex hybrid quadrupole time-of-flight mass spectrometer (Q-Star Pulsar-*i*) with an orthogonal MALDI ion source (Applied Biosystems, Foster City, California, USA) and a high repetition Neodymium-doped yttrium vanadate (Nd: YVO<sub>4</sub>) laser (5 KHz) (Elforlight Ltd, Daventry, Northamptonshire, UK). Image acquisition was performed at a spatial resolution of 150 µm x 150 µm in “Raster Image” mode; images were generated using the freely available Novartis Biomap 3.7.5.5 software ([www.maldi-msi.org](http://www.maldi-msi.org)).

### 5.2.6. Data Processing

Images generated in the Biomap 3.7.5.5 software were exported in JPEG format and imported into the Image J software (<http://rsbweb.nih.gov/ij/>). Images were orientated and aligned before being integrated as an image stack, which was then viewed as a 3D volume using the 3D viewer option.

Mass spectral post-processing was performed on regions of interest in Biomap, then converted into text files and imported into mMass software (Strohalm *et al.*, 2010).

The Datacube Explorer software ([www.imzml.org](http://www.imzml.org)) was used to further process the raw data in order to create what are known as datacubes. Spectral binning was also performed to reduce the size of the dataset. Then using the Volume Explorer software developed at FOM Institute AMOLF (Amsterdam, The Netherlands) these datacubes were used to create 3D volumes. Individual images were manually aligned with the aid of the registration markers (Klinkert and Heeren 2013).



spectra (obtained from the two regions) were displayed in pairs by flipping one of the spectra as shown in Figure 5.11. In the case of both regions there is an abundance of lipid species such as choline at  $m/z$  104, possible lysophosphatidylcholine at  $m/z$  496 and phosphocholine at  $m/z$  184 which is the most abundant peak in both regions.

The MALDI-MS images obtained for the distribution of various endogenous species in the control mouse lung tissue sections (previously seen in Figure 5.2) are displayed below in Figure 5.12.

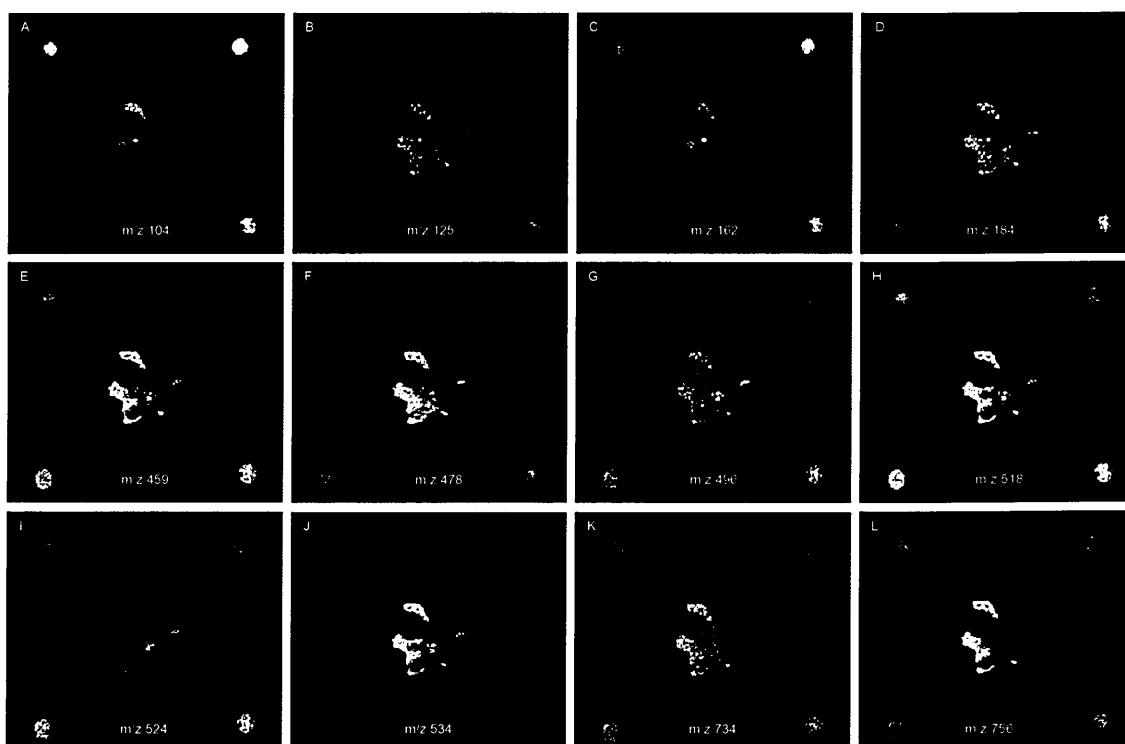


**Figure 5.12:** MALDI-MS images showing the distribution of various endogenous species in the control mouse lung tissue section (150  $\mu\text{m}$  spatial resolution).

The MALDI-MS images displayed above in Figure 5.12 shows the distribution of various endogenous species throughout the control mouse lung tissue. Such as choline at  $m/z$  104 (Figure 5.6A) which is localised in specific regions of the tissue section and phosphocholine at  $m/z$  184 (Figure 5.6D) which is distributed

throughout the control mouse lung tissue section. Other species possibly included a lysophosphatidylcholine at  $m/z$  496 (Figure 5.6G) and phosphatidylcholines at  $m/z$  734 and 756 (Figures 5.6K and 5.6L respectively) are also widespread throughout the lungs tissue sections. All these selected species were observed in each of the homogenate registration markers located in the four corners of the images.

In order to confirm the identity of the lipids MS/MS experiments were performed. The MALDI-MS/MS images showing the distribution of phosphocholine is shown below in Figure 5.13.

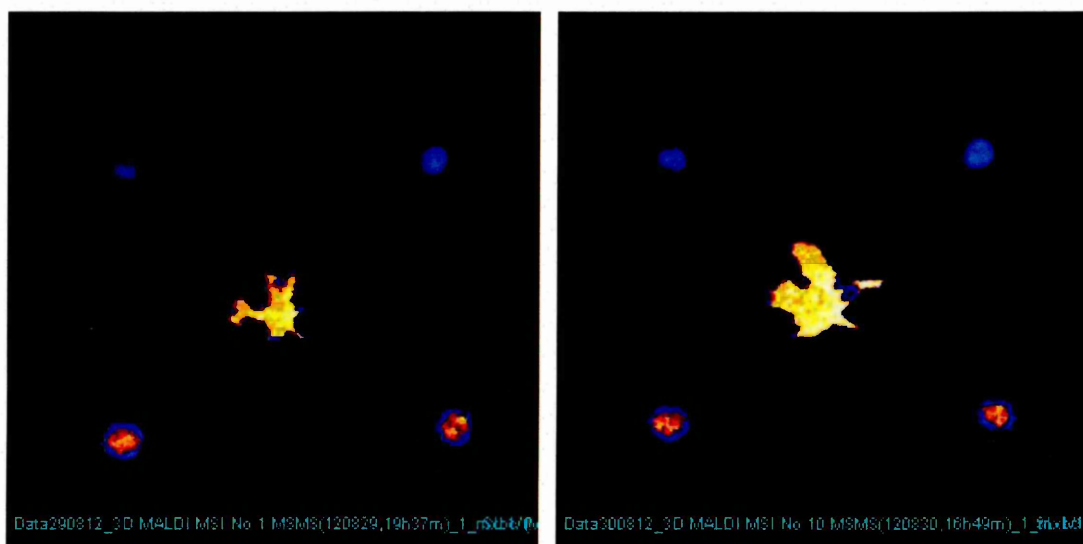


**Figure 5.13:** MALDI-MS/MS images showing the distribution of the product ion at  $m/z$  124, derived from the precursor ion of phosphocholine at  $m/z$  184 (150  $\mu\text{m}$  spatial resolution).

The images displayed above in Figure 5.13 shows the distribution of the product ion at  $m/z$  124, derived from the precursor ion of phosphocholine at  $m/z$  184 (previously shown to be the most abundant endogenous species) to be within the control mouse lung tissue in the centre but also in the four registration markers located in the four corners.

The generation of a three-dimensional image was performed by serially sectioning the mouse lung tissue with defined and measured spatial intervals (z-dimension), a total of 28 sections were collected and analysed by MALDI-MSI. The resulting 2D MALDI-MS images of the first sixteen images generated showing the distribution of phosphocholine in the control mouse lung tissue are presented below in Figure 5.14.

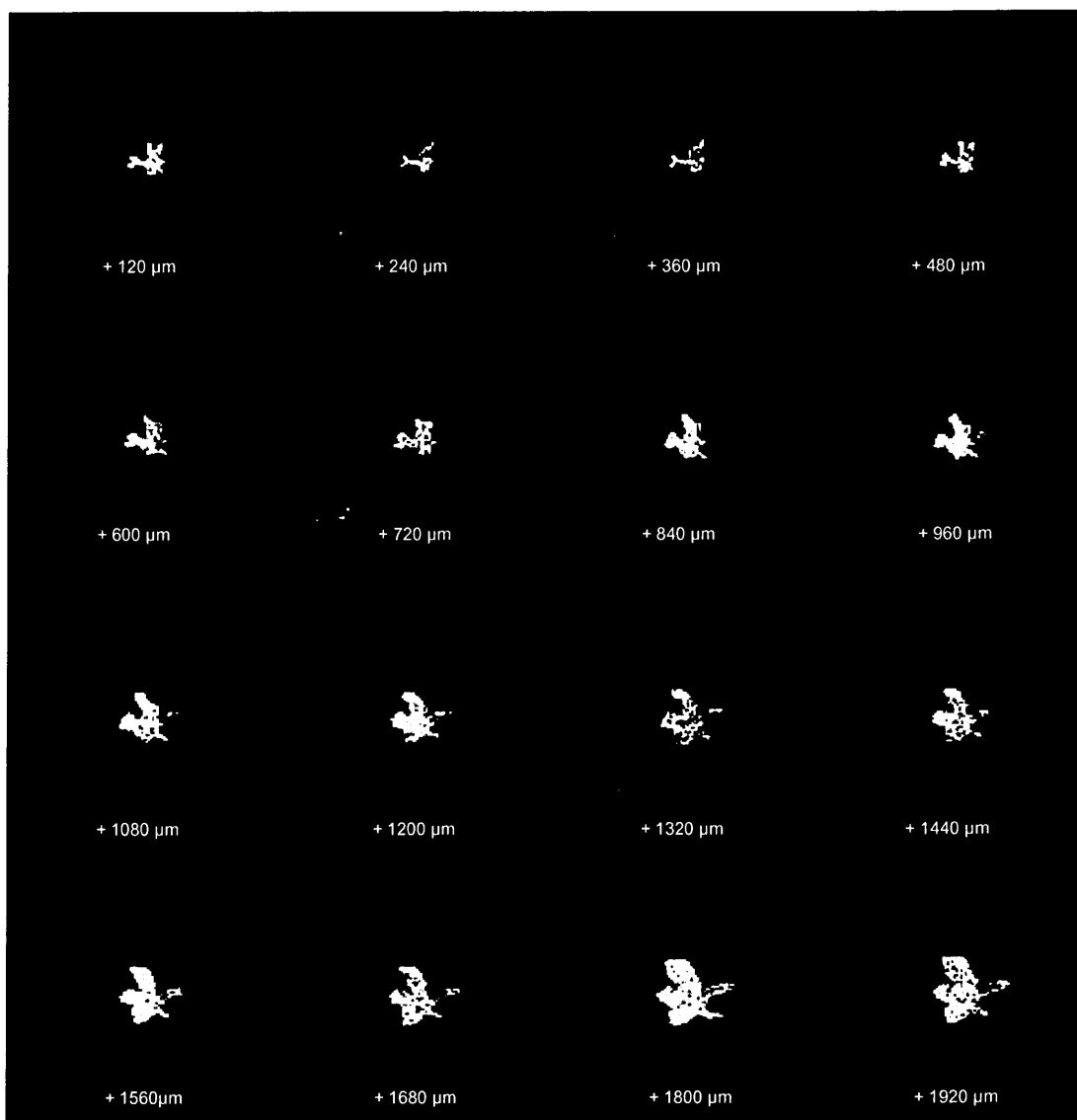


**Figure 5.14:** 2D MALDI-MS images showing the distribution of phosphocholine at  $m/z$  184 following normalization against the protonated CHCA matrix at  $m/z$  190, through the first 16 control mouse lung tissue sections.

The MALDI-MS images displayed above in Figure 5.14 show the distribution of phosphocholine at  $m/z$  184 throughout the first 16 serial tissue sections. The distribution was chosen to show the structure of the tissue sections.

The three-dimensional model of the control mouse lungs was constructed using the first 16 2D MALDI-MS images. The 3D reconstruction of the distribution of phosphocholine at  $m/z$  184 generated using the Image J software is shown below in Figure 5.15 and is displayed from different angles.

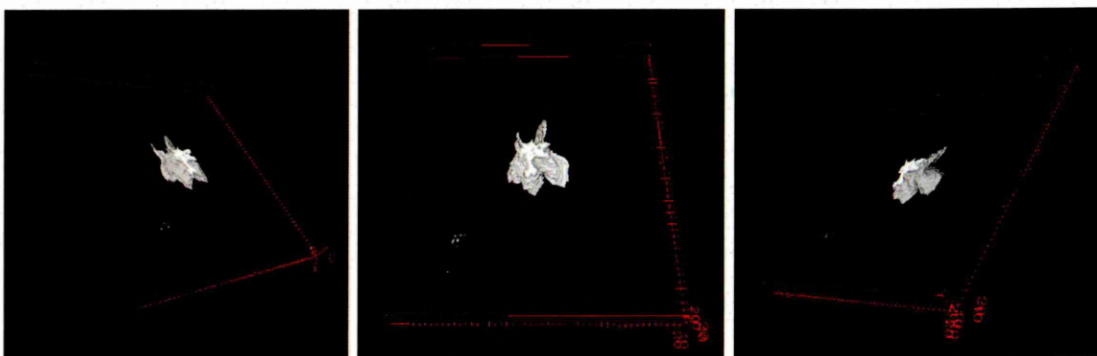


**Figure 5.15:** 3D MALDI-MS images produced using Image J software showing the distribution of phosphocholine at  $m/z$  184 following normalization against the protonated CHCA matrix at  $m/z$  190, throughout the control mouse lung tissue from different angles.

The 3D MALDI-MS images showing the distribution of phosphocholine at  $m/z$  184 (Figure 5.15) is displayed from different angles. The images show that phosphocholine is widely distributed and only shows the external structure of the control mouse lungs, however the images clearly display trachea and the right and left lobes.

The 2D data generated was also processed using the Volume Explorer software, the registration of individual images was performed by manual alignment (offset in the x and y directions) with the aid of the four registration markers. The 3D reconstruction of the distribution of phosphocholine at m/z 184 obtained from the 16 2D images, generated using the Volume Explorer software is displayed from different angles below in Figure 5.16.

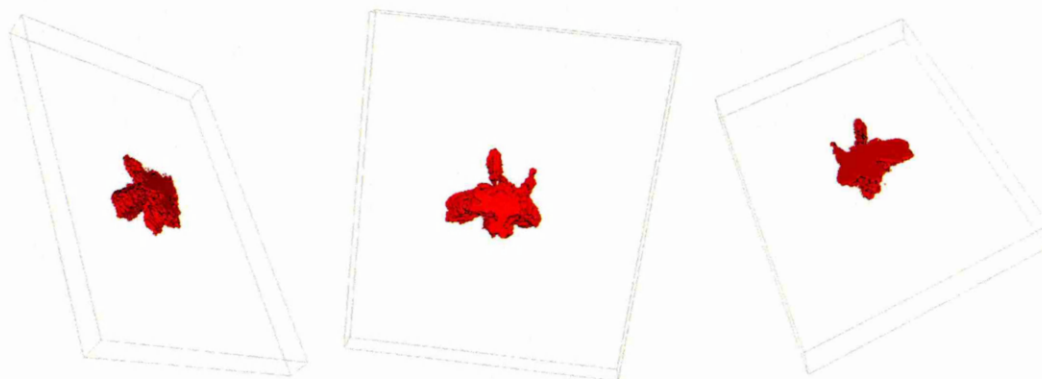


**Figure 5.16:** 3D MALDI-MS images produced using Volume Explorer software showing the distribution of phosphocholine at m/z 184 following normalization against the protonated CHCA matrix at m/z 190, throughout the control mouse lung tissue from different angles.

The 3D MALDI-MS images displayed above in Figure 5.16 shows the distribution of phosphocholine at m/z 184 displayed from different angles. Again the images demonstrate that phosphocholine is widely distributed and only reveals the external structure of the control mouse lungs, such as the trachea and the right and left lobes are displayed.

The Volume Explorer software is also capable of displaying the distribution of up to three masses in the same 3D model, this is demonstrated below in Figure 5.17.

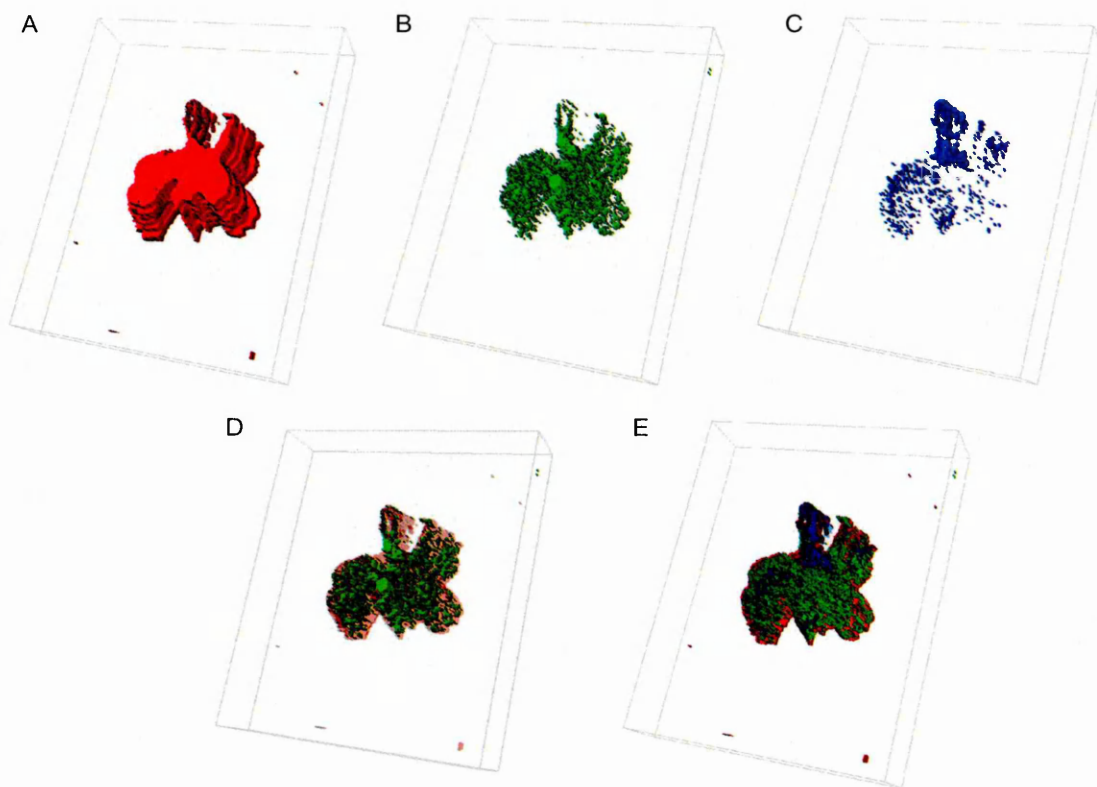


**Figure 5.17:** 3D MALDI-MS images showing the distribution of A) a possible phosphatidylcholine at  $m/z$  756.5, B) the heme group of hemoglobin at  $m/z$  616.2 C) another possible phosphatidylcholine  $m/z$  760, D) an overlay of the phosphatidylcholine at  $m/z$  756.5 and the heme group at  $m/z$  616 and E) an overlay of all three endogenous species.

The 3D models displayed above in Figure 5.17 show the distribution of phosphatidylcholine (possibly the sodium adduct of PC 32:0) at  $m/z$  756 (Figure 5.17A), the heme group of hemoglobin at  $m/z$  616 (Figure 5.17B) and another phosphatidylcholine (possibly PC 34:1) at  $m/z$  760 (Figure 5.17C) throughout the control mouse lungs.

The images show the phosphatidylcholine (PC 32:0) at m/z 756.5 is distributed throughout the control mouse lung tissue, whilst the phosphatidylcholine (PC 34:1) at m/z 760.5 is primarily localised in the trachea of the control mouse lung tissue. The distribution of the heme of hemoglobin at m/z 616.2 shows the network of blood vessels throughout the control mouse lung tissue.

By changing the opacity of the distribution of a particular endogenous species in this case the phosphatidylcholine (PC 32:0) at m/z 756.5, the distribution of other species can be viewed in relation to one another. This is demonstrated in Figure 5.17D which shows the overlaid distribution of phosphatidylcholine at m/z 756.5 (red) and heme at m/z 616.2 (green) similarly Figure 5.17E shows the overlay of all three endogenous species.

#### **5.4. Conclusion**

The work presented here describes a method for monitoring the three-dimensional distribution of endogenous species in the lungs of a mouse. Control mouse lung tissue was serially sectioned resulting in 28 tissue sections obtained at defined intervals, these sections were individually analysed.

The addition of registration markers enabled easier 2D MALDI-MS image alignment and utilising Image J, software the individual 2D MALDI-MSI images of the distribution of a specific endogenous species were stacked together and viewed as a manipulable 3D image. The production of a 3D image was also accomplished using the Volume Explorer software.

Whilst the method requires careful sample preparation and is time consuming, the methodology has the potential to provide information on the 3D distribution of endogenous species or analytes of interest and organ substructures.

Unfortunately a full 3D model of the lung showing the distribution of the endogenous species mentioned here could not be built as sections 17-21 did not reveal any information when analysed.

## 5.5. References

- ANDERSSON, M., GROSECLOSE, M.R., DEUTCH, A.Y. and CAPRIOLI, R.M., 2008. Imaging mass spectrometry of proteins and peptides: 3D volume reconstruction. *Nature Methods*, **5**(1), 101-108.
- CHEN, R., HUI, L., STURM, R.M. and LI, L., 2009. Three dimensional mapping of neuropeptides and lipids in crustacean brain by mass spectral imaging. *Journal of the American Society for Mass Spectrometry*, **20**(6), 1068-1077.
- CHUGHTAI, K., JIANG, L., GREENWOOD, T.R., KLINKERT, I., VAN HOVE, E.R.A., HEEREN, R.M.A. and GUNDE, K., 2012. Fiducial markers for combined 3-dimensional mass spectrometric and optical tissue imaging. *Analytical Chemistry*, **84**(4), 1817-1823.
- CRECELIUS, A.C., CORNETT, D.S., CAPRIOLI, R.M., WILLIAMS, B., DAWANT, B.M. and BODENHEIMER, B., 2005. Three-dimensional visualization of protein expression in mouse brain structures using imaging mass spectrometry. *Journal of the American Society for Mass Spectrometry*, **16**(7), 1093-1099.
- EBERLIN, L.S., IFA, D.R., WU, C. and COOKS, R.G., 2010. Three-dimensional visualization of mouse brain by lipid analysis using ambient ionization mass spectrometry. *Angewandte Chemie-International Edition*, **49**(5), 873-876.
- FLETCHER, J.S., RABBANI, S., HENDERSON, A., LOCKYER, N.P. and VICKERMAN, J.C., 2011. Three-dimensional mass spectral imaging of HeLa-M cells -sample preparation, data interpretation and visualisation. *Rapid Communications in Mass Spectrometry*, **25**(7), 925-932.

FORNAI, L., ANGELINI, A., KLINKERT, I., GISKES, F., KISS, A., EIJKEL, G., AMSTALDEN-VAN HOVE, E.A., KLERK, L.A., FEDRIGO, M., PIERACCINI, G., MONETI, G., VALENTE, M., THIENE, G. and HEEREN, R.M.A., 2012. Three-dimensional molecular reconstruction of rat heart with mass spectrometry imaging. *Analytical and Bioanalytical Chemistry*, **404**(10), 2927-2938.

<http://rsbweb.nih.gov/ij/>

KLINKERT, I. and HEEREN, R.M.A., 2013. Methods for full resolution data exploration and visualization for large 2D and 3D mass spectrometry imaging datasets.

NEMES, P., BARTON, A.A. and VERTES, A., 2009. Three-dimensional imaging of metabolites in tissues under ambient conditions by laser ablation electrospray ionization mass spectrometry. *Analytical Chemistry*, **81**(16), 6668-6675.

SEELEY, E.H. and CAPRIOLI, R.M., 2012. 3D imaging by mass spectrometry: A new frontier. *Analytical Chemistry*, **84**(5), 2105-2110.

SINHA, T.K., KHATIB-SHAHIDI, S., YANKEELOV, T.E., MAPARA, K., EHTESHAM, M., CORNETT, D.S., DAWANT, B.M., CAPRIOLI, R.M. and GORE, J.C., 2008. Integrating spatially resolved three-dimensional MALDI IMS with in vivo magnetic resonance imaging. *Nature Methods*, **5**(1), 57-59.

STROHALM, M., KAVAN, D., NOVAK, P., VOLNY, M. and HAVLÍČEK, V., 2010. mMass 3: A cross-platform software environment for precise analysis of mass spectrometric data. *Analytical Chemistry*, **82**(11), 4648-4651.

TREDE, D., SCHIFFLER, S., BECKER, M., WIRTZ, S., STEINHORST, K., STREHLOW, J., AICHLER, M., KOBARG, J.H., OETJEN, J., DYATLOY, A., HELDMANN, S., WALCH, A., THIELE, H., MAASS, P. and ALEXANDROV, T., 2012. Exploring three-dimensional matrix-assisted laser desorption/ionization imaging mass spectrometry data: Three-dimensional spatial segmentation of mouse kidney. *Analytical Chemistry*, **84**(14), 6079-6087.

[www.maldi-msi.org](http://www.maldi-msi.org)

XIONG, X., XU, W., EBERLIN, L.S., WISEMAN, J.M., FANG, X., JIANG, Y., HUANG, Z., ZHANG, Y., COOKS, R.G. and OUYANG, Z., 2012. Data processing for 3D mass spectrometry imaging. *Journal of the American Society for Mass Spectrometry*, **23**(6), 1147-1156.

YE, H., GREER, T. and LI, L., 2011. From pixel to voxel: a deeper view of biological tissue by 3D mass spectral imaging. *Bioanalysis*, **3**(3), 313-332.

## Chapter 6

---

Conclusions and suggestions for future work

## 6.1. Conclusions and suggestions for future work

The work reported in this thesis demonstrates the successful application of MALDI-MSI to monitor the distribution of respiratory compounds, used for the management of asthma and COPD, within lungs of preclinical species following inhaled delivery. Methodologies have been developed for the analysis of respiratory compounds that are not easily analysed by mass spectrometry. The generation of quantitative information from mass spectrometry images and the production of three-dimensional images have also been demonstrated.

MALDI-MSI has been extensively used for the analysis of pharmaceutical compounds. However the analysis of glucocorticoids remains a challenge as they contain multiple carbonyl functionalities, which are not easily protonated/deprotonated to form charged species under mass spectrometry conditions. The work presented in chapter 2 shows the successful application of hydrazine based reagents such as DNPH, DMNTH and Girard's reagent P to solve this problem. These reagents were utilised for the in-solution and on-tissue derivatisation of selected glucocorticoids improving their sensitivity and detection by MALDI-MSI. It has also been shown that a mixture of the reactive matrices DNPH and DMNTH with the common MALDI matrix CHCA further improves the sensitivity and detection of the glucocorticoid derivatives.

Future studies in this area could be to try different derivatisation reagents such as ethoxyamine to form ethoxime derivatives of the glucocorticoids. Also further optimisation of the methodology reported, with the aim to reduce the derivatisation reaction time to make the ethoxime derivatisation suitable for the in-situ derivatisation of glucocorticoids in order monitor their distribution in the lungs would be useful.

The work presented in chapter 3 relates to the main objective of this work i.e. detecting and monitoring the distribution of respiratory compounds in rodent lungs. MALDI-MSI was successfully employed on several different MS instruments for the screening of a range of respiratory compounds, in order to determine their on-tissue limit of detection.

One of the challenges with the analysis of pharmaceutical compounds by MALDI-MS is isobaric interference due to matrix related peaks below 500 Da. This was observed during the analysis of the respiratory compound Ambroxol. This problem could have been solved by the use of instruments with high mass resolving power or ion mobility separation, however in the case of this work careful matrix selection was used to overcome problem, negating the need for access to other instruments.

MALDI-MSI was employed to determine the distribution of a selected compound, in this case tiotropium bromide throughout the lungs following intratracheal delivery. The use of high spatial resolution imaging (30-50  $\mu\text{m}$ ) enabled a more detailed view of the distribution of tiotropium in the trachea and airways. The analysis of the lung tissue sections was performed on three different types of mass spectrometers enabling the results to be correlated with each other, good agreement was achieved. Now that reliable and reproducible protocols are in place further studies could be performed to determine the distribution of the other respiratory compounds tested in the feasibility study.

Quantitative mass spectrometry imaging is a new field that has recently gained a lot of attention especially in pharmaceutical research. The ability to obtain quantitative information as well as the distribution of pharmaceutical compounds

and associated metabolites offers a distinct advantage over traditional quantitative methods such as LC-MS/MS and QWBA.

The work discussed in Chapter 4 shows the evaluation of the currently accepted methods for obtaining quantitative information from mass spectrometry images and the development of a new method.

The first method involved spotting a dilution series of tiotropium bromide onto a control lung tissue section, this spiked tissue section was then coated with a matrix containing a structural analogue (ipratropium bromide) to act as an internal standard. A calibration curve was produced and the addition of the internal standard was shown to improve the calibration curve based on the correlation coefficient.

The second method of quantitation involved the preparation of dilution series of ipratropium bromide mixed with control tissue homogenate, the homogenate standards were spotted onto a glass slide and analysed. The third method involved the preparation of homogenate standards, only this time they were frozen, sectioned and mounted onto a glass slide and analysed. In both cases the results were shown to produce a linear calibration curve.

The study led to the development of a quantitative technique for MALDI-MSI in the form of a homogenate standard array. This consisted of homogenate standards spiked with drug embedded in frozen gelatin. Sections of the array when cut and mounted for analysis contain all the standards necessary for the quantitation of pharmaceutical compounds in dosed tissue sections. Future work could involve the validation of the homogenate standard array method using traditional quantitative methods such as LC-MS/MS or QWBA. Also worthy of further consideration is to perform qualitative and quantitative

experiments on respiratory compounds in the lungs following inhaled delivery utilising the homogenate standard array.

The use of MALDI-MS imaging has been extensively applied to monitoring the distribution of proteins, peptides, pharmaceutical compounds and lipids in biological tissues sections. This method has been expanded to analyse serial sections from a single specimen and can provide the three-dimensional distribution of endogenous species related to substructures within the tissue to be viewed. The work presented in Chapter 5 describes a method for generating a 3D image of the distribution of endogenous species throughout the lungs of a mouse. The tissue was serially sectioned into 28 sections at defined intervals and each section was individually analysed by MALDI-MSI. The addition of homogenate registration markers enabled easier 2D MALDI-MS image alignment and co-registration and utilising Image J, a freely available software the individual 2D MALDI-MSI images of the distribution of selected endogenous species were stacked together and viewed as a manipulable 3D image. The production of a 3D image was also accomplished using the Volume Explorer software. Whilst the method is time consuming and requires careful sample preparation, the methodology has the potential to provide information on the 3D distribution of endogenous species or analytes of interest within organ substructures. Future work in this area could be to monitor and compare the 3D distribution of respiratory compounds through the lung using the described methodology.

### 7.1. Publications

EVERY, J.L., MCEWEN, A., FLINDERS, B., FRANCESE, S. and CLENCH, M.R., 2011. Matrix-assisted laser desorption mass spectrometry imaging for the examination of imipramine absorption by Straticell-RHE-EPI/001 an artificial model of the human epidermis. *Xenobiotica*, **41**(8), 735-742.

TRIM, P.J., DJIDJA, M., MUHARIB, T., COLE, L.M., FLINDERS, B., CAROLAN, V.A., FRANCESE, S. and CLENCH, M.R., 2012. Instrumentation and software for mass spectrometry imaging—Making the most of what you've got. *Journal of Proteomics*, **75**(16), 4931-4940.

FRANCESE, S., BRADSHAW, R., FLINDERS, B., MITCHELL, C., BLEAY, S., CICERO, L. and CLENCH, M.R., 2013. Curcumin: A Multipurpose Matrix for MALDI Mass Spectrometry Imaging Applications. *Analytical Chemistry*, **85**(10), 5240-5248.

FLINDERS, B., MORRELL, J., MARSHALL, P.S., RANSHAW, L.E., KHAN, M.A. and CLENCH, M.R., 2013. The use hydrazine based derivatisation reagents for improved sensitivity and detection of carbonyl containing compounds using MALDI-MSI (Manuscript in preparation).

### 7.2. Conferences – Poster presentations

FLINDERS, B., MORRELL, J., MARSHALL, P.S., RANSHAW, L.E., KHAN, M.A. and CLENCH, M.R., 2010. The use of derivatisation reagents for improved sensitivity and structure elucidation of carbonyl containing compounds using

MALDI-MS. *Structure 2010, Advances in Structure Elucidation*, Hinckley, Leicestershire, UK, 24th-25th February 2010.

FLINDERS, B., MORRELL, J., MARSHALL, P.S., RANSHAW, L.E., KHAN, M.A. and CLENCH, M.R., 2010. The use of hydrazine based derivatisation reagents for improved sensitivity and detection of carbonyl containing compounds “on tissue” using MALDI-MS. *58th ASMS Conference on Mass Spectrometry and Allied Topics*, Salt Lake City, Utah, USA, 23rd-27th May 2010.

FLINDERS, B., MORRELL, J., MARSHALL, P.S., RANSHAW, L.E., KHAN, M.A. and CLENCH, M.R., 2010. The use of hydrazine based derivatisation reagents for improved sensitivity and detection of carbonyl containing compounds “on tissue” using MALDI-MS. *31st BMSS Annual Meeting*, Cardiff, UK, 5th-8th September 2010.

FLINDERS, B., MORRELL, J., MARSHALL, P.S., RANSHAW, L.E., KHAN, M.A. and CLENCH, M.R., 2011. “Tailor made” reactive matrices for improved sensitivity and detection of carbonyl containing compounds in-situ for MALDI-MS Imaging. *59th ASMS Conference on Mass Spectrometry and Allied Topics*, Denver, Colorado, USA, 5th-9th June 2011.

FLINDERS, B., MORRELL, J., MARSHALL, P.S., RANSHAW, L.E., KHAN, M.A. and CLENCH, M.R., 2012. Development of methodology for the quantitation of pharmaceuticals in tissue sections by MALDI-MSI. *60th ASMS*

*Conference on Mass Spectrometry and Allied Topics, Vancouver, BC, Canada, 19th-24th May 2012.*

FLINDERS, B., MORRELL, J., MARSHALL, P.S., RANSHAW, L.E. and CLENCH, M.R., 2012. Quantification of pharmaceuticals in tissue sections by MALDI-MSI. *Ourense Conference on Imaging Mass Spectrometry*, Ourense, Spain, 3rd-5th September 2012.

SEAMAN, C., HOPCROFT, G., FLINDERS, B., KINSMAN, D. and CLENCH, M.R., 2012. The “after-life” experiment – Mass spectrometry imaging used to demonstrate the “cycle of life”. *60th ASMS Conference on Mass Spectrometry and Allied Topics, Vancouver, BC, Canada, 19th-24th May 2012.*

### 7.3. Conferences – Oral presentations

FLINDERS, B., 2011. Investigation into methods of quantification for MALDI-Mass Spectrometry Imaging. *32nd BMSS Annual Meeting, Cardiff, UK, 11th-14th September 2011.*

### 7.4. Conferences attended

Structure 2010, Advances in Structure Elucidation, *Hinckley, Leicestershire, UK, 24th-25th February 2010.*

58th American Society for Mass Spectrometry Conference on Mass Spectrometry and Allied Topics, Salt Lake City, Utah, USA, 23rd-27th May 2010.

31st British Mass Spectrometry Society Annual Meeting, Cardiff, UK, 5th-8th September 2010.

59th American Society for Mass Spectrometry Conference on Mass Spectrometry and Allied Topics, Denver, Colorado, USA, 5th-9th June 2011.

32nd British Mass Spectrometry Society Annual Meeting, Cardiff, UK, 11th-14th September 2011.

60th American Society for Mass Spectrometry Conference on Mass Spectrometry and Allied Topics, Vancouver, BC, Canada, 19th-24th May 2012.

Ourense Conference on Imaging Mass Spectrometry, Ourense, Spain, 3rd-5th September 2012.